Angle of Arrival Estimation Utilising Frequency Diverse Radio Antenna Arrays

A thesis submitted to the University of Sheffield for the degree of Doctor of Philosophy

Athanasios Vasileiadis

Supervisor: Edward A. Ball

Department of Electronic and Electrical Engineering

September 2020

Live long and prosper

Acknowledgements

Firstly, I would like to express my sincere gratitude to my primary supervisor Edward A Ball, for the continuous support of my research, his patience, motivation, and practical knowledge. His guidance helped me in all the time of research and writing of this thesis. I could not have imagined having a better advisor, mentor, and friend for my research.

My sincere thanks also goes to my secondary supervisor Dr. Wei Liu, and my confirmation review examiner Dr. Jonathan Rigelsford, for their helpful comments in regards of research and professional development. Also I would like express my gratitude to Dr Athanassios Iossifides. Without his support and encouragement I would have not been in the position of producing high quality research independently.

Last but not the least, I would like to thank my life partner Koralia. Without her support, patience and proofreading, the writing quality of this work would be significantly worse. Also, I would like to thank my parents, brother, his wife, and my nephews for increasing my mental fortitude all these years.

Abstract

The purpose of this research is to investigate a novel way of combining carrier signals that are transmitted successively over Multiple Frequencies (MF) and traditional metrics to improve AoA estimation. Every signal contains three metrics, amplitude, phase, and frequency. To achieve localisation, current systems utilise the metrics of amplitude (also known as Received Signal Strength (RSS)) and phase that resolves the AoA. However, the metric of frequency is mostly used with Orthogonal Frequency-Division Multiplexing (OFDM) to increase the number of RSS and AoA metrics, which is not optimal.

This research answers two questions. Can the use of MF improve AoA estimation? Also, how can MF and traditional metrics be combined for AoA estimation? The aim is to prove that the metric of frequency can be utilised more optimally. Therefore, measurements of RSS and AoA are performed in different environments for MF. To perform these measurements, ten frequency diverse Software Defined Radios (SDRs) are employed. A novel technique to time/frequency synchronise the SDRs is developed and presented. Moreover, a ten element Uniform Linear Array (ULA) is designed, simulated and manufactured. The outcomes of this research are two novel algorithms for the MF AoA estimation of a carrier transmitter.

Findings of the first algorithm show that the use of MF with the RSS metric performs equally with current systems that have a higher cost and complexity. The second algorithm that utilises MF with the AoA metric demonstrates a significant reduction in the AoA estimation error, compared to current systems. Specifically, for 50% of the measured cases the AoA estimation error is reduced by 3.7 degrees, while for 95% of the measured cases the AoA estimation error is reduced by 27 degrees. Hence, this research proves that MF with traditional metrics can reduce system complexity and greatly improve AoA estimation.

Contents

List of Figures

List of Tables

List of Algorithms

Nomenclature

A list of the variables and notation used in this thesis is defined below. The definitions and conventions set here will be observed throughout unless otherwise stated. For a list of acronyms, please consult page xvi.

$(\cdot)^{\dagger}$	Hermitian conjugate of $(\cdot)$, page 14
$(\cdot)^{\intercal}$	Transpose of $(\cdot)$, page 14
$\boldsymbol{\Phi}$	Phase shift matrix imposed by the sub-array, page 16
$\boldsymbol{A}$	Steering matrix, see equation (2.7), page 14
$\boldsymbol{a}(\theta)$	Steering vector at angle θ, see equation (2.7), page 14
$\boldsymbol{R_{yy}}$	Covariance matrix of received signal, page 14
$\boldsymbol{U_n}$	Noise subspace of matrix space $\boldsymbol{U}$, page 15
$\boldsymbol{U_x}$	Signal subspace of matrix space $\boldsymbol{U}$, page 15
$\boldsymbol{U}$	Matrix space, page 15
$\boldsymbol{w}(t)$	AWGN in vector form θ, see equation (2.7), page 14
$\boldsymbol{y}(t)$	Received signal in vector form θ, see equation (2.7), page 14
$\Delta\phi$	Phase difference between two rays, paths, or signals, see equation (6.7), page 93
ϵ	Permittivity of the reflective medium, see equation (6.11), page 94
η	Intrinsic impedance of the reflective medium, see equation (6.9), page 93
Γ	Reflection coefficient, see equation (6.4), page 92
κ	Conductivity of the reflective medium, see equation (6.11), page 94
λ	Wavelength of the propagating signal, see equation (6.2), page 88
μ	Permeability of the reflective medium, see equation (6.11), page 94
ω	Angular frequency of the propagating signal, see equation (6.11), page 94

$\overleftarrow{\boldsymbol{R}_l}$	Backward sub-array covariance matrix $l \in [1, L]$, see equation (2.25), page 19
$\overleftarrow{\boldsymbol{R}}$	Backward covariance matrix $l \in [1, L]$, see equation (2.25), page 19
$\overleftarrow{\boldsymbol{y}_l}$	Backward sub-array $l \in [1, L]$, page 19
$\overline{\langle \cdot \rangle}$	Average of $\langle \cdot \rangle$, see equation (6.18), page 107
$\overrightarrow{\boldsymbol{R}_l}$	Forward sub-array covariance matrix $l \in [1, L]$, see equation (2.24), page 19
$\overrightarrow{\boldsymbol{R}}$	Forward covariance matrix $l \in [1, L]$, see equation (2.24), page 19
$\overrightarrow{\boldsymbol{y}_l}$	Forward sub-array $l \in [1, L]$, see equation (2.24), page 19
ϕ	Phase of the received continuous time signal, see equation (2.2), page 12
ρ	Angle of impact at the reflective surface, see equation (6.4), page 92
σ_0^2	Variance of AWGN, page 12
τ	Excess time of travel for the reflective ray, see equation (6.4), page 92
θ	Azimuth angle, also used as AoA, see equation (2.4), page 12
$\varrho(\cdot)$	Correlation of $\cdot$, see equation (6.19), page 107
$\widetilde{RSS}$	Estimated RSS pattern, see equation (6.18), page 107
A^{RX}	Amplitude of the received signal, see equation (2.2), page 12
$B(\cdot)$	Binomial coefficient of $(\cdot)$, see equation (2.5), page 13
c	Speed of light $c = 3\ 10^8$, see equation (6.2), page 88
d	Power of the received signal, see equation (6.2), page 88
d_c	Critical distance , see equation (6.16), page 101
f	Frequency of the propagating signal, see equation (2.2), page 12
G^{RX}	Gain of the receiving antenna, see equation (6.2), page 88
G^{TX}	Gain of the transmitting antenna, see equation (6.2), page 88
h_r	Height of receiver , see equation (6.16), page 101
h_t	Height of transmitter , see equation (6.16), page 101
I_M	Identity matrix with size (MxM), page 14
l	Sub-array index $l \in [1, L]$, page 19
m	Antenna element $m \in [1, M]$, see equation (2.2), page 12
M_{sps}	Antenna elements after the application of spectral smoothing, page 19

P^{LS}	Pathloss between transmitter and receiver, see equation (6.2), page 88
P^{ML}	Power loss due to impedance miss-match between source and load, see equation (4.3), page 61
P^{RX}	Power of the received signal, see equation (6.2), page 88
$p_r(t)$	Propagating continuous time signal for ray r, see equation (6.4), page 92
r	Reflective ray or path $r \in [1, R]$, see equation (6.13), page 98
$Re\{\cdot\}$	Real part of $\{\cdot\}$, see equation (6.4), page 92
s	Distance between two antenna elements, see equation (2.4), page 12
T_s	Sampling interval, see equation (2.3), page 12
$w(t)$	AWGN in continuous time, see equation (2.2), page 12
$y(t)$	Received signal in continuous time, see equation (2.2), page 12
$y[n]$	Sampled received signal, see equation (2.3), page 12

Acronyms

ADC Analogue to Digital Converter. 79, 81

ANN Artificial Neural Network. 144

AoA Angle of Arrival. vi, vii, ix–xi, 1, 4–9, 11–17, 19, 21–25, 28–35, 37–44, 46–57, 62, 63, 68, 74, 80, 83, 101, 105, 106, 109, 111–113, 115–131, 133, 135–137, 139–142, 144

AoD Angle of Departure. 5

AP Access Point. vii, 1, 4–6, 26, 28, 36–38, 47, 51–57, 111

AWGN Additive white Gaussian noise. 11, 12, 21, 47

BLE Bluetooth Low Energy. 4

CDF Cumulative Distribution Function. vii, x, 29, 38, 52, 54, 109–111, 119, 124, 125, 130–132, 134–136

CP Circularly Polarised. x, 142, 143

CPU Central Processor Unit. 48

CRB Cramér-Rao bound. 43

CSI Channel State Information. vii, 25–28, 36, 51–53

CW Continuous Wave. 14, 39, 71, 73, 117, 142

DNN Deep Neural Network. 28, 144, 145

DOF Degrees of Freedom. 43

EA Evolutionary Algorithm. 142

EPC Electronic Product Code. 50

ERP Effective Radiated Power. 72

ESPAR Electronically Steerable Parasitic Array Radiator. vi, 25, 28–31, 110–112, 140

ESPRIT Estimation of Signal Parameters via Rotation Invariance Technique. vi, 8, 11, 14, 16, 17, 34, 35, 55, 139

FB SS Forward-Backward Spatial Smoothing. vi, ix, xii, 8, 11, 17, 19–23, 113–117, 119, 121, 122, 124, 126, 128, 130, 136, 139

FDA Frequency Diverse Array. vii, 39, 42, 43

FFT Fast Fourier Transform. 79–82

FM Frequency Modulation. 145

FTR Forward-looking Threat Research. vi, 3

GA Genetic Algorithm. 141–144

GPS Global Positioning System. 1, 4, 139

IF Intermediate Frequency. 142

IoT Internet of Things. vi, 1, 2, 144

ISM Industrial, Scientific and Medical. 6

ISO International Standards Association. 50

ITU International Telecommunications Union. 85

KNN K-Nearest Neighbour. 26

LAN Local Area Network. 13

LCD Liquid-Crystal Display. vii, 69, 70, 72, 73

LOS Line of Sight. viii, 22, 29, 35, 37, 38, 47, 55, 56, 87, 91, 92, 98, 99, 101, 116, 117, 119, 125, 131, 136

LS Least Square. 48

LSE Least Square Errors. 29

LTE Long Term Evolution. 25, 36

MAC Media Access Control. 25, 40, 53

MCS Monte Carlo Simulation. 26, 43, 47, 48, 50

MF Multiple Frequencies. vii, ix, 5–9, 11, 22, 24, 25, 29–31, 35, 38, 39, 41, 42, 44–47, 51, 56, 57, 63, 87, 91, 101, 106–110, 112, 113, 116, 117, 125, 129, 133, 135–137, 140–142, 144, 145

MF PE Multi-frequency Phase Entanglement. ix, x, xii, 7, 8, 113, 115–117, 125–137, 141

MF SF Multi-frequency Spatial Fusion. ix, xii, 7, 113–116, 125–130, 136, 141

MIMO Multiple-Input and Multiple-Output. 5, 7, 35, 43, 48

ML Maximum Likelihood. 26, 48

MLE Maximum Likelihood Estimation. 32, 49

MSE Mean Square Error. 42

MUSIC Multiple Signal Classifier. vi, ix, xii, 8, 9, 11, 14, 15, 17–23, 34, 35, 37, 38, 51, 53, 55, 113–130, 134, 136, 139, 141, 142

NLOS Non Line of Sight. vii, 37, 47, 48, 53–56

OFDM Orthogonal Frequency Division Multiplexing. 5, 6, 27, 43, 51, 52, 56, 57

OOK On-Off Keying. 77, 78, 142

op-amp Operational Amplifier. 76

PCB Printed Circuit Board. vii, xi, 59–64, 66, 71–73, 95, 140

PIC Peripheral Interface Controller. 71

PLL Phase-Locked Loop. 70

PSU Power Supply Unit. 79

RF Radio Frequency. vi, vii, 1, 4, 5, 7, 13, 32, 40, 44, 46, 56, 70, 73, 79, 80, 139, 142

RFID Radio-Frequency Identification. 5, 32, 33, 35, 36, 39, 48–51, 56

RMS Root Mean Square. ix, 13, 20, 30–32, 48, 107–110, 112, 140, 142

RMSE Root Mean Square Error. 27, 124, 125, 130

RSS Received Signal Strength. vi–ix, 1, 4–9, 12, 25–31, 39–41, 47–51, 53–57, 84, 87–91, 95–98, 101–109, 111, 112, 140, 144

RSVA Random Spherical Volumetric Array. vii, 39, 44–46

RTL Realtek. 6, 7

SAR Synthetic Aperture Radar. vi, 35–37, 48

SBA Switched Beam Antenna. vi, 25, 28, 29, 31, 39–41, 56, 110–112, 140

SDMA Space Division Multiple Access. 39, 40

SDR Software Defined Radio. 6, 7, 12, 36, 74, 75

SF Single Frequency. vii, 6, 9, 46, 112, 113, 117, 119, 121, 122, 125–130, 136, 141

SLAM Simultaneous Localisation and Mapping. 144

SNR Signal to Noise Ratio. vi, xi, 18–24, 29–31, 34, 39, 41–44, 48, 50, 84, 111, 118, 119, 122, 131, 136, 139, 142

SS Spatial Smoothing. 8, 11, 17, 139

SVD Singular Value Decomposition. x, 20, 34, 35, 37, 55, 114–117, 131, 134, 137, 141

SVM Support Vector Machine. 31

TLS Total Least Square. 13, 17

ToF Time of Flight. vii, 5, 47, 52, 53, 56

ULA Uniform Linear Array. vi–ix, xi, 7, 8, 11–17, 19, 21–23, 35, 37, 38, 42–44, 52, 59, 61, 63–68, 83, 85, 88, 89, 95, 97, 101, 102, 104–112, 114, 117, 118, 131, 132, 136, 137, 139–141

USB Universal Serial Bus. 71, 80, 88

VCO Voltage Controlled Oscillator. 70

VHF Very High Frequency. 145

VNA Vector Network Analyser. 63

WiFi 802.11 Wireless Fidelity. 1, 5, 25, 26, 28, 36, 37, 39, 40, 51–53, 55–57, 110, 131

WSN Wireless Sensor Networks. 26

Chapter 1

Introduction

This Chapter serves as an introduction to the research. Section 1.1 provides the motivation for the research, while Section 1.2 provides some commercial examples of localisation systems. Section 1.3 introduces the hypothesis of the research, and Section 1.4 presents the outcomes of this research. The final Section 1.5 concludes this chapter by introducing the following chapters and providing a brief introduction on what they contain.

1.1 Motivation

Localisation of a transmitting node for outdoor and indoor environments has been heavily researched, resulting to the development of various systems for specific environments. For outdoors, the use of Global Positioning System (GPS) [1] has been applied by the majority of the cases, such as airplanes, cars and mobile phones. In reality, the application of GPS demands a high power consumption, and the overall application is expensive. As for indoors, Microsoft has been running competitions [2–4] for Radio Frequency (RF) solutions, and in their latest published results [5] concluded that indoor localisation is still a demanding topic and further research is essential. The majority of indoor systems focus on 802.11 Wireless Fidelity (WiFi) [6–8], since its infrastructure is widely established, and utilise signal metrics such as Received Signal Strength (RSS) and phase to resolve the Angle of Arrival (AoA). Most of those systems make unreasonable assumptions such as high number of Access Point (AP)s per room, e.g. 6. Since there is no system that performs both indoor and outdoor localisation with high accuracy, a novel localisation system will be designed and employed to improve the localisation accuracy.

The proposed novel localisation system will be essential to users in need, or potentially provide solutions to future problems. With the Internet of Things (IoT) expected to grow exponentially as seen in Fig. 1.1, a feasible, low cost, low energy consumption, and physically small transmitter can be designed to allow localisation. Such a device will be worn by a user who wants to be tracked and navigate to an unknown location or greatly benefit certain groups of users in our society, providing the safety that they need. One example is patients with Alzheimer or with other degenerative diseases, who are able-bodied and

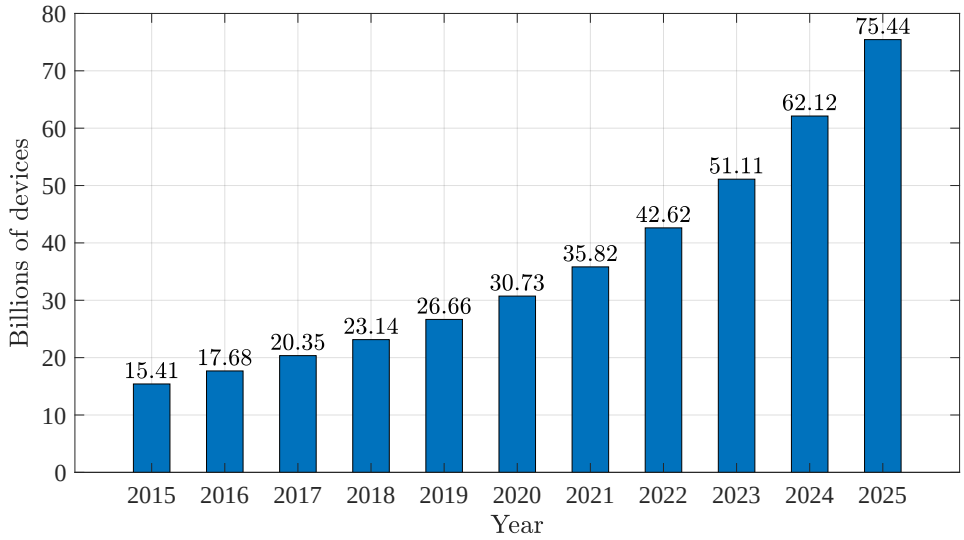

Figure 1.1: Expected growth in IoT devices, data from IHS Markit whitepaper [11].

have a strong desire to be home cared. Children with special needs who need socialisation, but parents and social workers are in fear of their safety outdoors and indoors is another use case.

A technology as the one proposed, could extend even further than providing safety by localisation and potentially include information about the well-being of the patient. This is not the first time that the ethical question of tracking a user is being raised [9, 10]. Such technology can potentially be used to violate the privacy of the user, therefore new regulations should be implemented to protect the user privacy. Some potential solutions to protect the user's privacy is complete anonymity by classifying the user. In one case scenario, such a system could monitor a body able Alzheimer patient that might leave his dwelling, triggering an alarm. Another case scenario could be a special needs school, monitoring the location of the children whose parents have given consent. Such system could potentially disrupt any life-threatening action that is unseen by the social workers. Finally, in every case the user must be aware and agree with the application of tracking technology. For life critical situations that the user is unable to understand or decide, the nearby family could make the decision, if the local law and policies allow it.

1.2 Examples of commercial systems

Even further, an indoor and outdoor localisation system can provide solution to industrial problems, such as monitoring the location of mobile infrastructure or goods and equipment in distribution. An accurate localisation with a low cost, and long battery life would be used to protect high cost products that can be lost or stolen. Moreover, a large scale application of a system could be applied for navigation assistance that is associated with indoor and outdoor environments, museums, national parks (Peak district) or shopping centres (Meadowhall). An ideal grand application would be a smart city like Fig. 1.2,

that could track the movement of busses, taxis and control the traffic. It could help find the nearest parking, enabling one to book a space automatically before arriving. It could offer navigational assistance to tourists that visit the city, giving information about museums, venues, events. A smart city could provide the security for people who require it and the easiness for tourists to have a satisfying experience.

A commercially available system that performs localisation with high accuracy and low cost (hardware cost of a smart-phone), is IndoorAtlas [13]. IndoorAtlas is a geomagnetic hybrid indoor positioning technology that is performing localisation using the magnetic fields of the earth. Specifically, each building's metal construction affect the observed earth's magnetic field, creating a unique pattern. By storing the known data from magnetic fields and inertia sensor data in a finger printing database, each smart phone can perform a comparison of their readings with the finger printing database, estimating their location. This technique has no hardware cost for smart phone users, but the power consumption to perform these measurements significantly reduce the battery life. Even further the process of creating a fingerprinting database is exhausting and environmental changes might require a new set of measurements.

Another commercial system that achieves high accuracy in real-time is Q-Track [14]. This system is a able to measure the relative strengths of E and H fields in near field. To measured the E and H near field the maximum distance of the system is bound to a third of the carriers wavelength λ. Therefor, to maintain a long range the system uses

Figure 1.2: Future smart city example, picture from Trend Micro's Forward-looking Threat Research (FTR) team [12].

low frequencies to increase the overall wavelength. As a result, this allows the system to penetrate walls and materials better than higher frequencies, but due to the near field requirement, the far field of the propagation is not considered. The main problem of using low frequency signals is the size of the transmitter antenna. In fact, the Q-Track transmitters are rugged with a size of a small hand held tool case and have an expected battery life span of 48 hours. Hence, the focus their focus is mainly on industrial applications. In reality the end users would have to carry such a large tracking equipment, making it an unrealistic system for the scope of our application.

A low cost, low power RF solution that is being commercially used by Apple under the name iBeacon [15], is Bluetooth Low Energy (BLE). With BLE transmitters operating at 2.4 GHz, the RSS measurements that are received from 1 AP, per room over 10-20 meter area are used to estimate distance. In case of multiple rooms, multiple APs must be installed making the overall scale inefficient in terms of cost and complexity. The real benefits of a BLE localisation is its low cost and low power consumption. For example, the life span of a BLE system that transmits a 3 ms pulse with a power of 15 mW every 10 minutes can theoretically last up to 68 years. A CR2032 battery could power such a system with no need of replacement until the shelf life of the battery it self, which is 10 years. The real issue of such applications are the system's accuracy, since RSS measurements are very sensitive to multipath propagation. In reality, indoor environments experience intense multipath. The only solution to mitigate the multipath is to place a BLE AP in every room. As the area of localisation increases, the number of BLE AP increases, and so does the cost. Therefore, the application of BLE is unrealistic for a large scale due to cost.

With the purpose of this research being to investigate and create a novel low cost and low energy consumption system, that is able to perform localisation in both indoor and outdoor environments; the most appealing solution of all is the BLE system. The major concerns of such solution are the outdoor availability in terms of range and accuracy. A recent comprehensive survey in localisation systems can be found in [16], while for outdoors the most widely used application is GPS. To further understand the issues of the state of the art systems regarding RF localisation systems, a closer investigation must be performed.

A single metric system that allows low cost, low power, and low complexity solution for localisation is RSS. The main applications of RSS take into consideration fingerprinting, where the measured RSS is compared with a database of known RSS values. The overall accuracy can be in terms of cm, but the overall number of fingerprints required is exhaustive and impractical as an application. Techniques that utilise RSS are investigated in Section 3.1.

Another localisation technique that utilises only a single metric is AoA. To resolve the AoA metric, at least two time/phase antenna elements are required in an array to distinguish the phase difference. Resolving the AoA of a transmitting signal is a complex process and requires a higher cost compared to RSS, but only in terms of the receiver. On the other hand, the transmitter can still be low cost, low power and have a long life span, similar to the BLE system. Techniques that utilise AoA are investigated in Section 3.2.

Apart from the traditional single metric localisation techniques, there is another metric that has been less utilised in modern literature: frequency. Specifically, the use of Multiple Frequencies (MF) is primarily with another metric, either RSS or AoA. Therefore, techniques that apply MF with either metric are investigated in Section 3.3.

Currently, the state of the art in localisation systems are focused on utilising multiple metrics. Different techniques, and diverse algorithms are researched to fuse the metrics of RSS, AoA, Angle of Departure (AoD), Time of Flight (ToF) which is the time that the signal takes to reach the receiver from the transmitter, and the use of MF in terms of Orthogonal Frequency Division Multiplexing (OFDM). A brief investigation of the most popular techniques will be done in Section 3.4.

Finally, with the current research advancements in Multiple-Input and Multiple-Output (MIMO) systems and spatial diversity, state of art systems are now equipped with more antennas, e.g. WiFi, laptops, and mobile phones. With the benefits of spatial diversity being extensively studied in the localisation literature [7] the overall accuracy can be improved with the use of multiple receiving antennas. With the freedom to formulate and develop a new low cost and low power localisation system that is not bounded by any protocols, the hypothesis will be proposed after the literature review.

1.3 Novelty of proposed research

The purpose of this research is to introduce a novel approach to AoA estimation in indoor and outdoor scenarios. Overall, the problem of localisation it is not one dimensional; it is an issue of accuracy, deployment complexity, and hardware specifications. This makes the search of one suitable solution that satisfies every aspect extremely difficult. From the examples of commercial systems presented in Section 1.2, two things are evident. First, that the two most researched metrics use for localisation are RSS and AoA; and second, the majority of RF solutions require multiple APs.

Considering the state of art systems and techniques, the aim of this research is to design a low cost, spatial, and frequency diverse system that utilises the metric of frequency and merge it with the traditional metrics of RSS and AoA. Moreover, the system focuses on having low power requirements by utilising the simplest signal possible, a carrier wave. Also, using MF will provide extended information for the metrics of RSS, and the AoA in different propagating environments [17, 18]. Therefore, with the application of MF, the overall localisation accuracy is expected to increase and at the same the low cost, low power system approach enables a wide range deployment.

State of the art systems mainly utilise the metric of frequency in radars. The main difference between the proposed research is that the radar utilises high microwave and closely spaced frequencies. Currently in research, there is no RF system that utilises large frequency separation to achieve localisation. That is due to the fact that most of the researched systems are bounded by protocol e.g. Radio-Frequency Identification (RFID) and WiFi have a standard frequency band. Moreover, the utilisation of MF has been primarily theoretical in the past, due to the high cost and hardware complexity. With

recent technological advancements of Software Defined Radio (SDR), the overall cost of MF transceivers has been reduced, enabling the development of reliable, low-cost systems.

The utilisation of MF gives rise to plenty of research questions such as: how many frequencies with a high separation are required. Do further smaller frequency separations or (OFDM) provide extended information? These questions are solely dependent on frequency and on the frequency diversity. To answer those questions real environment measurements were performed to understand how efficient and important the frequency diversity is. Furthermore, most of the reviewed systems employ a high number of antennas [7] or a high number of APs [19]. With the introduction of MF it is important to understand how the spatial diversity changes, and how the antennas serve the MF purpose. That creates a whole new research project that raises questions such as: how many antennas are required? Are all the antenna elements necessary to achieve the same accuracy? How close can they be and how different polarisation works? Some of these questions are answered for Single Frequency (SF) systems. For example, the authors in [20] examine the antenna element proximity, while the impact of diverse polarisation has also been researched before [21]. Hence, the emerging question is how the MF affects spatial diversity, and element spacing, as well as how can a novel system utilise MF to increase accuracy, reliability and maintain a low cost. This proposed research answers those questions and proves that MF can greatly increase accuracy by maintaining a low cost.

1.4 Research contributions

The first contribution of this research is a conference publication [22]. In [22] the preliminary results of this research are presented. The paper highlights the importance of localisation and highlights applications such as localising dementia patients. To move forward with the research, a receiver array was required to perform measurements in real environments. The cost of a industry standard ten element receiver array to perform the measurements is £50k [23, 24]. To reduce the overall cost and allow other researchers to perform similar MF RSS and MF AoA measurements, two low cost receivers were designed.

The second contribution of this research is the novel tri-band antenna design presented in Chapter 4. The benefit of the antenna design is that it can be reconfigured to cover a range of multiple bands. In this research three frequencies were used, $f_1 = 434$ MHz, $f_2 = 869$ MHz, and $f_3 = 1595$ MHz. It is evident that f_1 and f_2 are Industrial, Scientific and Medical (ISM) bands, but f_3 is not. That is due to the receiver being unable to utilise the 2.4 GHz band. Utilising the presented antenna design, an antenna able to operate in all three ISM bands which can have wide impact in applied research.

Third contribution of this research are the low cost, time and frequency synchronised SDR receiver arrays designed and employed for measurements. The first receiver array was designed using ten very low-cost Realtek (RTL)-SDRs [25]. Initial results proved

that the RTL-SDR receiver array can be utilised to form an array, resulted to the second conference publication [26]. The overall cost of the first receiver array is £200 and it can be used consistently for MF RSS measurements. On the contrary, for MF AoA measurements the receiver array proved to be questionable due to stability issues. Therefore, the second receiver array employing ten RSP2s [27] was designed and employed. The RSP2 has two RF input ports which can be exploited to achieve time and frequency synchronisation of the SDRs. The overall cost of the second receiver array is £1.7k and it can perform complex measurements, such as AoA estimation in frequencies from 10 KHz to 2 GHz. The developed receiver array is available for researchers and students of the University of Sheffield to develop and test their own algorithms.

The fourth contribution was the result of indoor and outdoor environment simulations to improve AoA estimation accuracy. The research on simulating indoor environments was used to simulate millimetre wave massive MIMO channel, which lead to the third conference publication [28]. Moreover, since the scope of this research is MF AoA estimation, the contributions in the millimetre wave massive MIMO channel is left out.

The sixth contribution of this research is the extraction of AoA from the RSS and it is presented in Chapter 6. Traditionally, extracting the AoA from the RSS required complex phased antenna arrays, that can change or shift their patterns. In early measurements, it was found that the expected RSS was different than the one expected on each antenna element. After further investigation, it was evident that this is due to the indoor propagating environment. Since the transmitted signal reaches the receiver from multiple paths, the different rays that travel in space reach the receiver array in different angles. Since each frequency has a different antenna gain in each angle, the Uniform Linear Array (ULA) formulates diverse antenna patterns for each frequency depending on the transmitter location. The developed system works by performing reference RSS measurements in specific locations for MF. Then the transmitter is placed in random locations and the pattern and the RSS is measured in MF. Then the developed algorithms compare the reference RSS with the measured RSS and a location is estimated. Findings prove that this technique can achieve similar or some times better results compared to complex systems proposed by literature. Therefore, the developed could be easier applied in a wide range, dramatically reducing the overall cost. The results of this contribution are currently under peer review in [29].

The seventh contribution of this research is the benefit of using MF when estimating the AoA and it is presented in Chapter 7. To estimate the AoA, the phase difference between closely spaced antenna elements is utilised. When there is only one propagating path between transmitter and receiver, the phase information is clean. In real environments, this is never true; hence, the phase information is unclear on the actual AoA. When introducing multiple broad spaced frequencies, each frequency experiences different propagating properties due to wavelength difference, uneven surfaces, and the reflection coefficient of the materials. Two novel algorithms were developed Multi-frequency Spatial Fusion (MF SF) and Multi-frequency Phase Entanglement (MF PE) in the scope of this research. Measurement results proved that the developed algorithm MF PE can accurately estimate the

direct AoA even in complex indoor environments, much better than any other system in literature. Specifically, from the measurements performed indoors it was found that compared to the best performing system in literature SpotFi [19], MF PE improves the mean direct AoA estimation error by 6.2 degrees. Moreover, for the for 75% and 95% of the measurements direct AoA estimation error is improved by 12.7 degrees, and 33.1 degrees. The results prove that MF can greatly improve the AoA estimation even in extreme cases were the best systems in literature suffer. The results of this contribution are currently under peer review in [30].

1.5 Thesis organisation

The organisation of this report is as follows:

Chapter 2: Background Theory

This Chapter provides the necessary theoretical background information to understand the fundamentals of the literature review, system model, and algorithms that are implemented in the Chapters that follow. Section 2.1 presents an optimal receiver used for AoA localisation, while Section 2.2 introduces the fundamental technique of estimating the AoA, which is interferometry. Section 2.3 is dedicated to the subspace algorithms that the state of the art localisation systems utilise, Multiple Signal Classifier (MUSIC), and Estimation of Signal Parameters via Rotation Invariance Technique (ESPRIT). Section 2.4 presents decorrelation methods that are required to mitigate reflections such as Spatial Smoothing (SS) and Forward-Backward Spatial Smoothing (FB SS), which are also used by state of the art localisation systems as well. Finally, Section 2.5 introduces three simulations to further comprehend the MUSIC algorithm its spatial power, and why the use of MF can improve AoA estimation.

Chapter 3: Literature review

This Chapter presents the literature review performed on systems or techniques that perform localisation with one or more metrics. Section 3.1 presents systems or techniques that perform localisation with the RSS metric, while the following Section 3.2 is dedicated on systems or techniques that perform localisation with the AoA metric. Section 3.3 focuses on localisation that utilises MF as a metric. Section 3.4 concludes the literature review by presenting systems that use multiple metrics, while Section 3.5 performs a distillation out of the literature review performed in the previous subsections and presents a table comparing all the systems.

Chapter 4: Novel antenna array design, simulation and measurements

This Chapter provides information regarding the novel antenna design and its performance as a ULA. Section 4.1 introduces the prototype tri-band antenna design with measurement of the return loss and simulation of the radiation pattern. Then Section 4.2 presents a performance evaluation of the antenna as a ULA receiver with measurements of the return loss, the mutual coupling, and simulation of the radiation patterns.

Chapter 5: System design simulation, measurements, and characterisation This Chapters provides the design, measurements, simulations, and characterisations of the trans-

mitter and receiver used for the measurements in Chapters 6 and 7. Section 5.1 introduces the transmitter design, while Section 5.2 is dedicated to the transmitter characterisation, which is very important to understand the capabilities of the transmitter. Section 5.3 presents the RSP2 receiver array prototype and the necessary procedure to perform frequency and time synchronisation. Finally, Section 5.3 is dedicated to the receiver characterisation, which provides an insight on the receiver performance and capabilities.

Chapter 6: Novel technique extracting AoA from frequency diverse RSS patterns

This Chapter presents a novel technique for performing localisation utilising the RSS. Section 6.1 serves as an introduction to the first RSS measurements in an anechoic chamber, while Section 6.2 presents the second set of measurements performed outdoors to confirm the idea. Section 6.3 shows the effect of a theoretical indoor environment on the RSS, while Section 6.4 is dedicated on the novel technique of estimating the AoA using RSS, and presents the results and comparison with the state of the art systems. Finally, Section 6.5 discusses the overall results and draws conclusions on how MF can be used to produce similar results with the state of the art but to reduce the complexity and overall cost.

Chapter 7: Novel direct AoA estimation utilising frequency diverse antenna array

This Chapter presents two novel techniques for performing localisation utilising MF and estimating the direct ray AoA. Section 7.1 is dedicated to the introduction of MF algorithms. Section 7.2 serves an introduction to indoor environment used for measurements, while Section 7.3 presents the performance of the SF MUSIC subspace algorithms, and explains the importance of MF. Section 7.4 presents the performance evaluation of the MF direct ray AoA algorithms and its robustness in terms of frequencies, antenna elements and methods of matrix decomposition. Section 7.6 presents the comparison of the proposed system and algorithm with state of the art systems, that were discussed in Chapter 1, SpotFi [19], LTEye [31] and CUPID [32]. Finally Section 7.7, discusses the overall results and draws conclusions on why MF is the only way on detecting the direct ray AoA with high certainty.

Chapter 8: Conclusions and future research

This Chapter summarises the findings of this research, draws conclusions based on the findings and highlights potential future research. Section 8.1 presents the findings of each Chapter with detailed results and explanations, while Section 8.2 provides a brief description on future research this research could generate.

Chapter 2

Background Theory

This Chapter provides the necessary theoretical background information to understand the fundamentals of the literature review, system model, and algorithms that are implemented in the Chapters that follow. Section 2.1 presents an optimal receiver used for AoA localisation, while Section 2.2 introduces the fundamental technique of estimating the AoA, which is interferometry. Section 2.3 is dedicated to the subspace algorithms that the state of the art localisation systems utilise, MUSIC, and ESPRIT. Section 2.4 presents decorrelation methods that are required to mitigate reflections such as SS and FB SS, which are also used by state of the art localisation systems as well. Finally, Section 2.5 introduces three simulations to further comprehend the MUSIC algorithm its spatial power, and why the use of MF can improve AoA estimation.

2.1 Optimal receiver for AoA detection

This Section presents the mathematical model of an optimal receiver for AoA detection. Such mathematical model is well defined in the literature [33–35] but also it is also important in the context of localisation.

Therefore, before this research progresses to the literature review and more complex concepts, the trivial equations must be explained to establish a mathematical background. First, a received sinusoidal signal as a function of time, for a single antenna is defined as [35],

$$y(t) = A^{\mathrm{RX}} \cos(2\pi f t + \phi) + w(t) \tag{2.1}$$

where, A^{RX} is the received amplitude, f is the frequency of the transmitted signal, ϕ is the phase of the received signal, $w(t)$ is the Additive white Gaussian noise (AWGN) in continuous time, and t is time. To test the hypothesis, a ULA with M elements is defined and the received sinusoidal signal is expressed as [35],

$$y_m(t) = A_m^{\mathrm{RX}} \cos(2\pi f t + \phi_m) + w_m(t) \tag{2.2}$$

where, y_m is the received continuous time signal for element $m \in [1, M]$, A_m^{RX} is the

received amplitude at element m, ϕ_m is the received phase for element m, and w_m is the AWGN in time of zero mean and variance σ_0^2 for element m.

Finally, the representation of a discrete-time pass-band received sinusoidal signal of element m is defined as [35],

$$y_m[n] = A_m^{\mathrm{RX}} \cos(2\pi f T_s n + \phi_m[n]), \tag{2.3}$$

where, $n = [1, 2, \ldots, N]$ are the samples in a frame with N samples, T_s is the sampling interval, and $\phi_m[n]$ is the phase at element m in sample n.

In practice, a SDR receives the signal as seen in (2.3). The received signal is then used to perform the localisation with different techniques. RSS localisation techniques use the received amplitude A_m^{RX} from multiple receivers and attempt to determine the transmitter location. AoA localisation techniques on the other hand, use the phase information ϕ_m. During this research both methods were investigated, with the utilisation of the RSS being presented in Chapter 6, and the utilisation of the AoA being presented in Chapter 7.

2.2 Interferometry

This Section presents the basic principle of AoA detection, interferometry. Interferometry requires a ULA system with at least two antenna elements resolving the phase difference between the two elements. An example of such ULA is presented in Fig. 2.1, where both angles θ_1 and θ_2 are part of a (red) triangle. To do so, the receiving system requires to have all the antenna elements frequency locked and time aligned, receiving samples simultaneously without any drift over the time period.

By setting the phase of the first element as reference (2.3), the phase difference between elements can be defined as a phase difference $\Delta\phi_m$, where, $\Delta\phi_1 = 0$, $\Delta\phi_2$ is the phase difference between elements 1 and 2, $\Delta\phi_M$ is the phase difference between elements 1 and M. By using Euclidean geometry in the red triangle of Fig. 2.1, the angles θ_1 and θ_2 can be resolved. The hypotenuse is the distance between the two elements s, while the side adjacent to θ_1 is the extra distance L travelled by the wave to reach element 1 compared to element 2, causing the phase difference. The distance L is determined by the speed of light c, and time of travel τ, $L = c\tau$. Time of travel τ can be seen as the phase difference between the two elements, taking into consideration the frequency f of the wave, defined as $\tau = \Delta\phi/2\pi f$. By substituting frequency f to the wavelength as $f = \lambda c$, the side is now $L = \lambda\Delta\phi/2\pi$. Finally, angles θ_1 and θ_2 can be defined by the trigonometric functions [36],

$$\theta_1 = \cos^{-1}\left(\frac{\lambda\Delta\phi_2}{2\pi s}\right) \qquad \theta_2 = \sin^{-1}\left(\frac{\lambda\Delta\phi_2}{2\pi s}\right). \tag{2.4}$$

For the scope of this research, the number of possible AoA detections from M antennas was formulated as an equation. With multiple antennas, a multiple AoAs (θ) can be estimated between pairs. Using binomial coefficient the number of estimated AoAs can

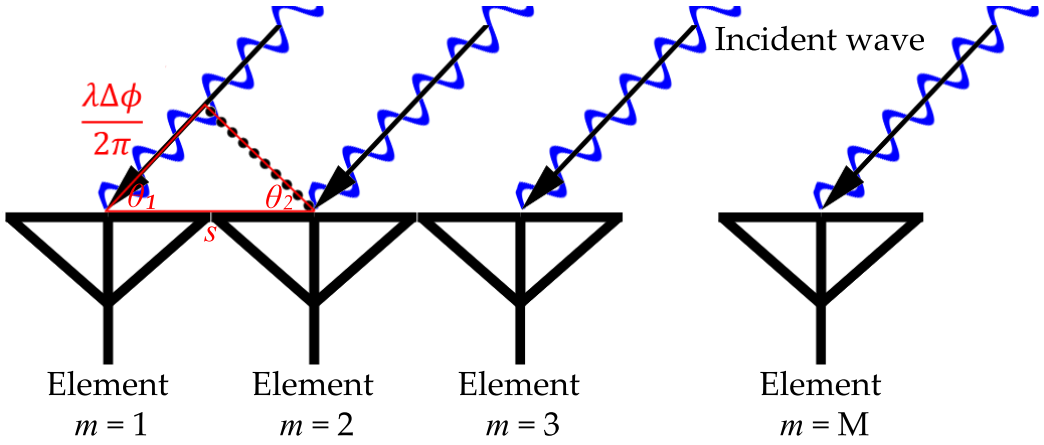

Figure 2.1: Example of a ULA with M elements with an incident wave at angle θ_1.

be found by,

$$B\binom{M}{2} = \frac{M!}{2(M-2)!}, \tag{2.5}$$

where, M is the number of antennas, and 2 is the minimum set of elements required to estimate the AoA θ. For example, having 4 antenna elements using equation (2.5) we can see that 6 pairs of antenna elements can be made. Therefore, 6 AoAs can be estimated from each pair. To combine the different AoA estimations there are different techniques, such as Root Mean Square (RMS) or Total Least Square (TLS).

Having two or more receiving systems in known positions and by acquiring multiple AoA a central processor can use the AoA and triangulate the source of the signal. This requires a back-haul connection, such as Local Area Network (LAN) or internet connection and a central processor. This is the most basic RF application of interferometry which is also applied in many fields; such as, astronomy, fiber optics and spectroscopy.

As the signal propagates through space, depending on its wavelength, it will reflect and/or pass through objects. These reflections are very likely to be picked up from the receiver and the outcome will be a mixing of direct signal and the different reflections, which is the same signal delayed in time. Thus, the process of extracting the true $\Delta\phi_m$ is not straightforward and the result will contain errors. In applications such as astronomy, the transmitting source is located extremely far away and there are few reflections; these reflections have a huge delay in time due to the extreme distance.

2.3 High resolution subspace algorithms

The concept of subspace is the existence of one space inside another space, meaning that its points, elements, or signal are part of another space. In practice, the received signal contains both signal and noise, thus, both signal and noise are subspaces of the received signal. Subspace algorithms are fundamental to localisation and used by the majority of the state of the art localisation systems. The two most researched subspace algorithms

are the spectral, MUSIC [37], and the parametric, ESPRIT [38], which are presented in Subsection 2.3.1, and Subsection 2.3.2 respectively. Both algorithms are presented later in literature review, Chapter 3, but most importantly the most important research outcome is based on MUSIC, Chapter 7.

Furthermore, both MUSIC and ESPRIT are able to obtain the AoA from multiple K independent narrow band sources, offering a high spatial resolution compared to other AoA techniques. The narrow band sources can be either Continuous Wave (CW) in different frequency i, or a frequency modulated signal at the same frequency i. Typically, a received continuous time signal $y_m(t)$ intercepted by a ULA with M elements, such as (2.3), can be expressed in a vector form $\boldsymbol{y}(t)$ as [39],

$$\boldsymbol{y}(t) = \begin{bmatrix} y_1(t) \\ y_2(t) \\ \vdots \\ y_M(t) \end{bmatrix} = \begin{bmatrix} 1 \\ \exp\left(\frac{-j2\pi s\cos\theta}{\lambda}\right) \\ \vdots \\ \exp\left(\frac{-j2\pi(M-1)s\cos\theta}{\lambda}\right) \end{bmatrix} x(t) + \begin{bmatrix} w_1(t) \\ w_2(t) \\ \vdots \\ w_M(t) \end{bmatrix} \Leftrightarrow$$

$$\boldsymbol{y}(t) = \boldsymbol{a}(\theta)x(t) + \boldsymbol{w}(t), \tag{2.6}$$

where, $\boldsymbol{y}(t)$ is the received vector in time t, $\boldsymbol{a}(\theta)$ is the steering vector, and $\boldsymbol{w}(t)$ is the added noise in vector form. In the case of K sources, the steering vector $\boldsymbol{a}(\theta)$ will be a MxK matrix $\boldsymbol{A} = [\boldsymbol{A}(\theta_1), \ldots, \boldsymbol{A}(\theta_K)]$ and the the signal matrix will be a Kx1 vector $\boldsymbol{x}(t) = [s_1(t), \ldots, s_K(t)]^\intercal$, where $^\intercal$ is the transpose of the vector. Thus, the received signal with a vector representation and multiple sources is described as [39],

$$\boldsymbol{y}(t) = \boldsymbol{A}\boldsymbol{x}(t) + \boldsymbol{w}(t). \tag{2.7}$$

2.3.1 The MUSIC algorithm

The MUSIC algorithm begins by computing the MxM covariance matrix $\boldsymbol{R_{yy}}$ to attain the spectral and spatial information of the received signals, as per [39],

$$\boldsymbol{R_{yy}} = E\{\boldsymbol{y}(t)\boldsymbol{y}^\dagger(t)\} = \boldsymbol{A}\boldsymbol{R_{xx}}\boldsymbol{A}^\intercal + \sigma_0^2\boldsymbol{I}_M, \tag{2.8}$$

where, $\boldsymbol{R_{xx}} = E\{\boldsymbol{x}(t)\boldsymbol{x}^\intercal(t)\} = \text{diag}\{\sigma_1^2, \ldots, \sigma_K^2\}$ is the eigenvalues of the K transmitted signals of the K uncorrelated sources, and $\boldsymbol{I}_M$ is the identity matrix with size MxM. In case the signals are correlated, the $\boldsymbol{R_{xx}}$ is not diagonal. This is due to reflections; since correlation tries to find similarities, if two identical signals appear as one. Further information can be found in [39]. Subspace algorithms attain the optimal results only if $\boldsymbol{R_{xx}}$ is a full rank matrix. The rank of a matrix represents the maximum number of linearly independent columns. When that hold true, the dimension of the space spanned in its

rows is identical as well, the matrix has a full rank [40]. Furthermore, the matrix rank is important because it defines the dimension of the signal subspace. When the signals are correlated (multipath propagation), then $\boldsymbol{R_{xx}}$ rank is deficient and a decorrelation technique needs to be applied, such as spectral smoothing [41] or forward/backward spectral smoothing [42], which will be further discussed in the following Section 2.4.

In case that $M \leq K$, the signal and noise subspace are part of the same subspace and the subspace algorithms can not detect all the K signals. For $M > K$, $\boldsymbol{AR_{xx}A^\intercal}$ is singular thus, $\det[\boldsymbol{AR_{xx}A^\intercal}] = \det[\boldsymbol{R_{yy}} - \sigma_0^2] = 0$. This implies that σ_0^2 is an eigenvalue of $\boldsymbol{R_{yy}}$, the noise that scales all over the eigenvectors. Since the dimensions of the null space of $\boldsymbol{AR_{xx}A^\intercal}$ are non-negative, their eigenvalues are K such as $\sigma_K^2 > \sigma_0^2 > 0$. Thus, if the signal variance is higher than the noise variance, the signals' AoA can be resolved. Let u_k be the kth eigenvalue of $\boldsymbol{R_{yy}}$ corresponding to σ_k^2 [39].

$$\boldsymbol{R_{yy}}u_k = [\boldsymbol{AR_{xx}A^\intercal} + \sigma_0^2\boldsymbol{I}]u_k = \sigma_k^2 u_k; \begin{cases} \sigma_k^2 > \sigma_0^2 > 0 \text{ for } k = 1, \ldots, K \\ \sigma_k^2 = \sigma_0^2 \qquad \text{for } k = K+1, \ldots, M \end{cases} \tag{2.9}$$

Moreover, (2.9) can be further expanded as [39].

$$\boldsymbol{AR_{xx}A^\intercal}u_k = (\sigma_k^2 - \sigma_0^2)u_k, \quad k = 1, 2, \ldots, M$$

$$\boldsymbol{AR_{xx}A^\intercal}u_k = \begin{cases} (\sigma_k^2 - \sigma_0^2)u_k, & k = 1, \ldots, K \qquad \text{(case 1)} \\ 0, & k = K+1, \ldots, M \qquad \text{(case 2)} \end{cases} \tag{2.10}$$

That means the M dimensional matrix space of $\boldsymbol{U}$ can be partitioned into the signal subspace $\boldsymbol{U_x}$ and the noise subspace $\boldsymbol{U_n}$ [39],

$$\boldsymbol{U} = [\boldsymbol{U_x} \quad \boldsymbol{U_n}] = [\boldsymbol{u}_1, \ldots, u_K \quad \boldsymbol{u}_{K+1}, \ldots, \boldsymbol{u}_M] \tag{2.11}$$

Furthermore, (2.10) case 1, shows that the K linear combinations of columns $\boldsymbol{A}$ are equal to the signal subspace which is spanned over the columns of $\boldsymbol{U_x}$, while (2.10) case 2, shows that the linear combinations of columns $\boldsymbol{A}$ are orthogonal to $\boldsymbol{U_n}$. That means that the steering vector $\boldsymbol{A}(\theta)$, which is in the signal subspace, is orthogonal to the noise subspace, $\boldsymbol{A^\intercal}(\theta_k)\boldsymbol{U_n} = 0$. Utilising the steering vector which can be formulated for each individual AoA, the MUSIC algorithm searches through all angles θ and plots the spatial spectrum $P(\theta)$ using,

$$P^{\text{MUSIC}}(\theta) = \frac{1}{||\boldsymbol{A^\intercal}(\theta)\boldsymbol{U_n}||} = \frac{1}{\boldsymbol{A^\intercal}(\theta)\boldsymbol{U_n}\boldsymbol{U_n^\intercal}\boldsymbol{A}(\theta)}, \tag{2.12}$$

where, wherever $\theta = \theta_i$, $P(\theta)$ exhibits a peak depending on the σ_i^2. The MUSIC algorithm can be altered to work for different shapes other than ULA, but it is very sensitive to antenna positioning, phase errors and gain; thus accurate calibration is required. The issue of MUSIC is that it is required to search throughout all θ, which can be computationally expensive.

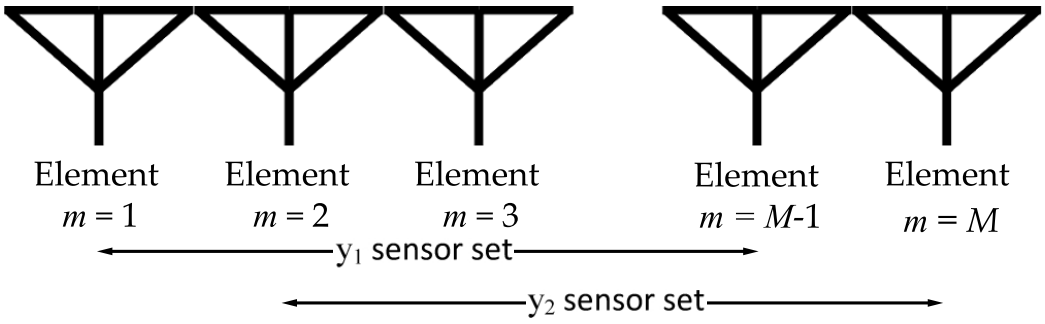

Figure 2.2: Example of a two sensor pair $\boldsymbol{y_1}$ and $\boldsymbol{y_2}$ for a ULA ESPRIT.

2.3.2 The ESPRIT algorithm

ESPRIT [38] algorithm was developed to analytically estimate the AoA θ without requiring to search all the possible angles. A ULA is split into two equally spaced identical sensor pairs s as shown in Fig. 2.2. To form the two identical sub arrays, $\boldsymbol{y}_1$ and $\boldsymbol{y}_2$, the M element ULA is split into one sensor set, $\boldsymbol{y}_1$ from elements $(1 : M-1)$, and a second set, $\boldsymbol{y}_2$ from elements $(2 : M)$. This one element shift creates a phase difference between each pair of $\boldsymbol{\Phi}$. The identical sub arrays from the ULA have a received time signal in matrix form such as [39],

$$\begin{aligned} \boldsymbol{y}_1(t) &= \boldsymbol{A}x(t) + \boldsymbol{w}_{\boldsymbol{y_1}}(t) \\ \boldsymbol{y}_2(t) &= \boldsymbol{A\Phi}x(t) + \boldsymbol{w}_{\boldsymbol{y_2}}(t), \end{aligned} \tag{2.13}$$

where, $\boldsymbol{\Phi} = diag\{e^{\gamma_1}, \ldots, e^{\gamma_K}\}$, and $e^{\gamma_k} = 2\pi s \cos(\theta_i))/\lambda$. The purpose of ESPRIT is to estimate $\boldsymbol{\Phi}$, which contains the information regarding θ_k. In matrix form is formulated as [39],

$$\mathbf{Z}(t) = \begin{bmatrix} \boldsymbol{y_1}(t) \\ \boldsymbol{y_2}(t) \end{bmatrix} = \begin{bmatrix} \boldsymbol{A} \\ \boldsymbol{A\Phi} \end{bmatrix} x(t) + \begin{bmatrix} \boldsymbol{w}_{\boldsymbol{y_1}}(t) \\ \boldsymbol{w}_{\boldsymbol{y_1}}(t) \end{bmatrix} = \overline{\boldsymbol{A}}x(t) + \boldsymbol{W_Z}(t), \tag{2.14}$$

with $\overline{\boldsymbol{A}}$ being the new steering vector. The covariance matrix $\boldsymbol{R_{ZZ}}$ with matrix size $2(M-1)$x$2(M-1)$ is obtained from,

$$\boldsymbol{R_{ZZ}} = E\{\mathbf{Z}(t)\mathbf{Z}^{\dagger}(t)\} = \overline{\boldsymbol{A}}\boldsymbol{R_{xx}}\overline{\boldsymbol{A}}^{\mathsf{T}} + \sigma_0^2\boldsymbol{I}. \tag{2.15}$$

As per (2.11) the matrix is split in the signal subspace $\boldsymbol{U_x}$ with size of $2(M-1)$xK and the noise subspace $\boldsymbol{U_n}$ with size $2(M-1)$x$2(M-1) - K$. Now, the steering vector that spans over the same subspace as $\boldsymbol{U_x}$ is defined as$\overline{\boldsymbol{A}}$. Therefore, there must be a matrix $\boldsymbol{T}$ that satisfies, $\boldsymbol{U_x} = \overline{\boldsymbol{A}}\boldsymbol{T}$. Partitioning $\boldsymbol{U_x}$ to satisfy the form of (2.14) as [39],

$$\boldsymbol{U_x} = \begin{bmatrix} \boldsymbol{U_x} \\ \boldsymbol{U_y} \end{bmatrix} = \begin{bmatrix} \boldsymbol{AT} \\ \boldsymbol{A\Phi T} \end{bmatrix}. \tag{2.16}$$

Both $\boldsymbol{U_x}$ and $\boldsymbol{U_y}$ are linear combinations of $\boldsymbol{A}$, so each of them has a column rank K and defines a $(M-1)$x2K matrix with rank K, $\boldsymbol{U_{xy}} = [\boldsymbol{U_x} \quad \boldsymbol{U_y}]$. Therefore, $\boldsymbol{U_{xy}}$ has a null space of K, thus there is a 2KxK matrix $\boldsymbol{F}$ that $\boldsymbol{U_{xy}F} = 0$. Expanding to [39],

$$[\boldsymbol{U_x} \quad \boldsymbol{U_y}] \begin{bmatrix} \boldsymbol{F_x} \\ \boldsymbol{F_y} \end{bmatrix} = \boldsymbol{U_x F_x} + \boldsymbol{U_y F_y} = 0. \tag{2.17}$$

Substituting from (2.16) gives [39],

$$\boldsymbol{ATF_x} + \boldsymbol{A\Phi TF_y} = 0 \leftrightarrow \boldsymbol{A\Phi TF_y} = -\boldsymbol{ATF_x}. \tag{2.18}$$

Since $\boldsymbol{T}$ is a known full column rank matrix (if the sources are uncorrelated), it results to [39],

$$\boldsymbol{\Phi} = \boldsymbol{TF_x F_y^{-1} T^{-1}}. \tag{2.19}$$

Overall, the final result is always equal or worse to spectral based MUSIC, since its analytical process does not consider every possible AoA. Imperfect element distances can result to a large error which can be calibrated out only by altering the distances of the physical elements. To further improve the result, ESPRIT is commonly combined with TLS. This estimation is a single procedure and the computational complexity is much less than MUSIC. In practice, MUSIC spectral search in a 180 degrees spectrum is executing (2.12) 181 times for one degree resolution, or 1801 for .1 degree resolution, while ESPRIT is executed only once.

2.4 Decorrelation techniques for coherent signals

This Section is dedicated to present decorrelation techniques to mitigate the effect of reflections. As it was pointed in Section 2.3, the covariance matrix of the transmitted signal $\boldsymbol{R_{xx}}$ should not be rank deficient. When a matrix is rank deficient the information that reside within the matrix is insufficient and therefore, the MUSIC algorithm to perform an accurate estimation. In presence of multipath, the transmitted signal is reflected at the receiver multiple times, which leads to a rank deficient $\boldsymbol{R_{xx}}$. Since the success of the subspace algorithms are dependant on the non singular covariance matrix $\boldsymbol{R_{yy}}$, SS [41] or FB SS [42] must be applied. Both techniques are used by state of the art systems, such as SpotFi [19] and ArrayTrack [7]. Therefore, Subsection 2.4.1 presents the SS algorithm, while 2.4.2 presents the FB SS algorithm.

2.4.1 Spatial Smoothing

Spatial smoothing divides a ULA with M antenna elements to a new ULA with the of size M_{sps} overlapping antenna elements. The first set of antenna elements will be [1,...,M_{sps}], second set [2,...,$M_{sps}+1$], as seen in Fig. 2.3. The overall number of subarrays are $L = M - M_{sps} + 1$, and $\boldsymbol{y}_l$ denotes the vector of the received signal at the subarray

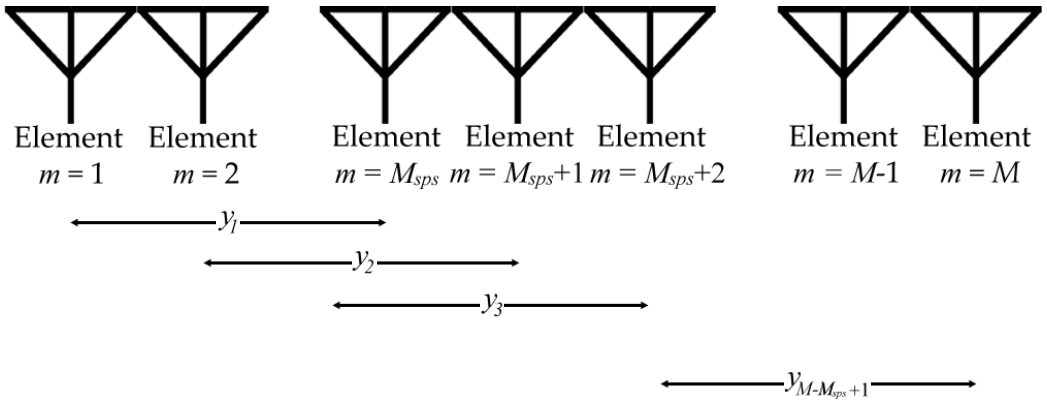

Figure 2.3: Sub-array example of spatial smoothing with M antenna elements, and M_{sps} spatial smoothing elements.

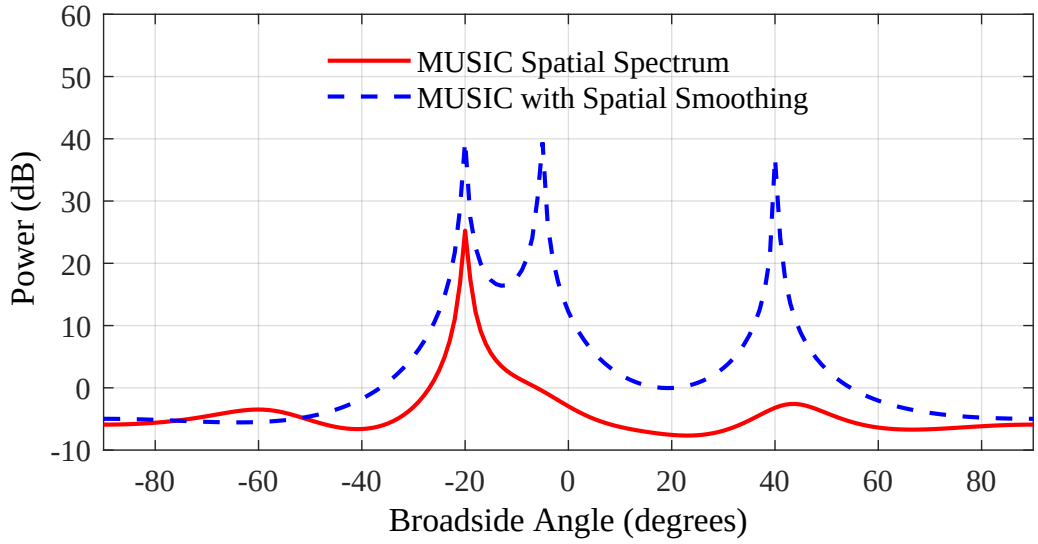

Figure 2.4: MUSIC spatial spectrum for no spatial smoothing (red) and spatial smoothing (blue) with a subarray size M_{sps} = 4, and M = 6 antenna elements, Signal to Noise Ratio (SNR) = 3 dB, two coherent sources at -5 degrees, -20 degrees and one incoherent source at 40 degrees.

l. Following the notation of (2.7), the new received vector is defined as [41],

$$\boldsymbol{y}_l(t) = \boldsymbol{A}\boldsymbol{D}^{(l-1)}x(t) + \boldsymbol{w}_l(t). \tag{2.20}$$

where, K is the number of incident signals, and $\boldsymbol{D}^{(l)}$ denotes the $l-1$ power of the (KxK) diagonal matrix defined as [41],

$$\boldsymbol{D} = \text{diag}\{e^{-j2\pi s\cos\theta_1/\lambda}, e^{-j2\pi s\cos\theta_2/\lambda}, \ldots, e^{-j2\pi s\cos\theta_K/\lambda}\}. \tag{2.21}$$

Furthermore, the covariance matrix of the subarray l is expressed as [41],

$$\boldsymbol{R}_l = \boldsymbol{A}\boldsymbol{D}^{(l-1)}\boldsymbol{R}_{\boldsymbol{xx}}\boldsymbol{D}^{(l-1)^\intercal}\boldsymbol{A}^\intercal + \sigma_0^2\boldsymbol{I}_m, \tag{2.22}$$

The spatial smoothed covariance matrix $\overline{\boldsymbol{R}_l}$ is finally defined by averaging the set of l subarray as [41],

$$\overline{\boldsymbol{R}} = \frac{1}{L}\sum_{l=1}^{L}\boldsymbol{R}_l. \tag{2.23}$$

For sake of space, the full proof that covariance of the transmitted signals is non singular when $L \geq I$ is not shown here, but it is presented in [41]. Instead, Fig. 2.4 presents an example with the effects of spatial smoothing for a ULA with M = 6 antenna elements, SNR = 3 dB, two coherent sources at -5 degrees, -20 degrees and one incoherent source at 40 degrees.

The red line in Fig. 2.4 proves that in the presence of coherent signals MUSIC is unable to determine the AoA and only registers the one at -20 degrees. By applying spectral smoothing, blue line in Fig. 2.4, reduces the subarray size to M_{sps} = 4 elements. Now the MUSIC algorithm is able to distinguish all incoming AoA.

2.4.2 Forward-Backward Smoothing

Spatial smoothing is able to reduce the size of the array to M_{sps}, thus reducing the maximum number of signals that MUSIC can identify. FB SS [42] is able to identify K signals with a $M \geq \lceil 3K/2 \rceil$ antenna elements. Thus, in an indoor environment where there are multiple coherent reflections, FB SS helps to decrease the requirements for the overall number of elements. Moreover, FB SS follows the same principle as spatial smoothing, starting from (2.20), the vector of the forward received signal $\overrightarrow{\boldsymbol{y}_l}$ is used to defined the forward covariance matrix $\overrightarrow{\boldsymbol{R}_l}$ as in (2.22). Now, the forward spatial smoothed covariance matrix is defined similarly to (2.23) as,

$$\overrightarrow{\boldsymbol{R}} = \frac{1}{L}\sum_{l=1}^{L}\overrightarrow{\boldsymbol{R}_l}. \tag{2.24}$$

Furthermore, the backward subarray is defined by the same antenna elements but backwards, as seen in Fig. 2.5. The backward subarray $\overleftarrow{\boldsymbol{y}_l}$ is used to calculate the backward covariance matrix $\overleftarrow{\boldsymbol{R}_l}$, as (2.22). Finally, backward spatial smoothed covariance matrix is defined as,

$$\overleftarrow{\boldsymbol{R}} = \frac{1}{L}\sum_{l=1}^{L}\overleftarrow{\boldsymbol{R}_l}. \tag{2.25}$$

The forward-backward covariance matrix is the average between the forward $\overrightarrow{\boldsymbol{R}_l}$ and the backward $\overline{\boldsymbol{R}_l}$. The final spatially smoothed covariance matrices is estimated as,

$$\overline{\boldsymbol{R}} = \frac{\overrightarrow{\boldsymbol{R}} + \overleftarrow{\boldsymbol{R}}}{2}. \tag{2.26}$$

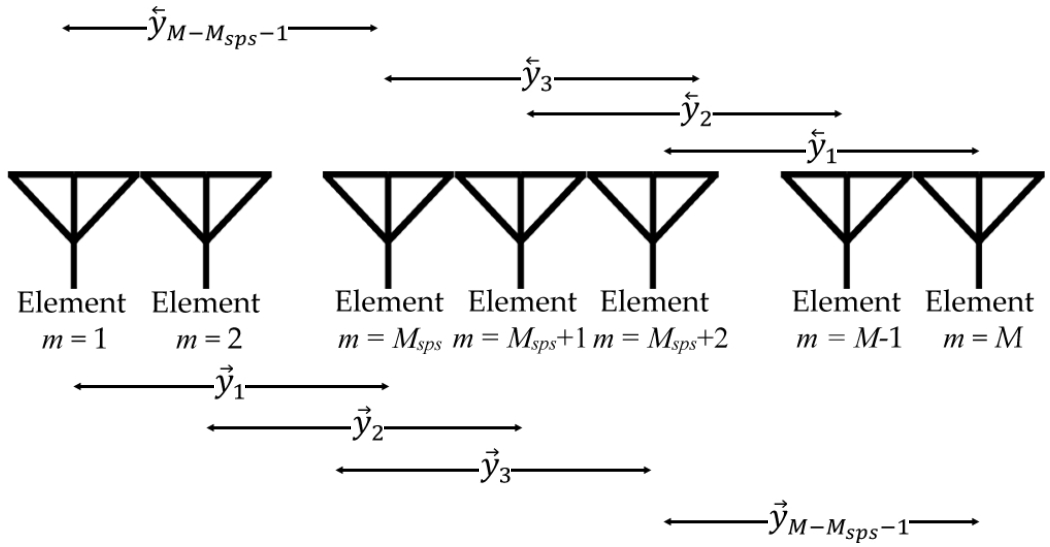

Figure 2.5: Sub-array example of FB SS with M antenna elements, and M_{sps} spatial smoothing elements.

The FB SS covariance matrix contains more information as it averages the covariance matrix in two ways and it can identify K signals with $M \geq \lceil 3K/2 \rceil$ antenna elements. Again for sake of space proof is not presented here but it can be found in [42].

An example of the FB SS performance can be seen in Fig. 2.5, where it is compared with the standard MUSIC spatial spectrum, and the MUSIC with spatial smoothing. The number of antenna elements is M = 6, the spatial smoothing subarray is M_{sps}, the SNR = 5 dB, and there are four coherent sources at -60 degrees, -30 degrees, -5 degrees, and 35 degrees. The figure shows that both standard MUSIC and MUSIC with spatial smoothing are unable to detect all the sources. On the other hand, the MUSIC with forward-backward spectral smoothing is able to detect all the sources at angles -57 degrees, -33 degrees, -3 degrees, -35 degrees. The RMS error is 3.4 degrees, which is good for being at the border line of required elements, $M \geq \lceil 3K/2 \rceil$.

The main disadvantage of FB SS over spatial smoothing and MUSIC is the complexity. When FB SS is implemented, the noise subspace must be obtained twice (forward and backward). Taking into consideration that all literature implements Singular Value Decomposition (SVD) to obtain the noise subspace, the overall complexity increases even further. As explained in Subsection 3.2.1 the SVD complexity is higher than QR decomposition. Therefore, if SVD is replaced by QR decomposition, the complexity can be reduced and that is why it is studied extensively in Subsection 7.5.3. Finally, in terms of performance comparison, it is evident that FB SS outperforms the other algorithms and that it is featured later, in Section 7.1.

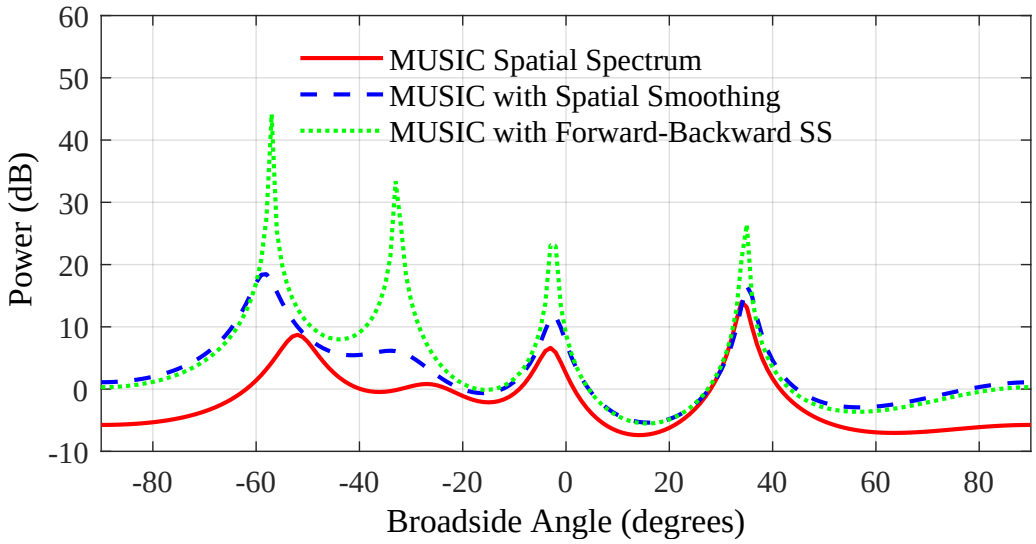

Figure 2.6: MUSIC spatial spectrum for no spatial smoothing (red), spatial smoothing (blue) with a subarray size M_{sps} = 5, FB SS (green), and M = 6 antenna elements, SNR = 5 dB, four coherent sources at -60 degrees, -30 degrees -5 degrees and 35 degrees.

2.5 Comprehending the MUSIC power spectra estimation

This Sections presents simulations to provide insight on the estimation of the FB SS MUSIC power spectra. In Subsection 2.5.1 the FB SS MUSIC power spectra is presented as a function of SNR, while in Subsection 2.5.2 the FB SS MUSIC power spectra is presented as a function of number of elements M in the ULA. Finally, Subsection 2.5.3 introduces the FB SS MUSIC power spectra as a function of AoA noise. The three different scenarios were simulated and the results are presented in Fig. 2.7.

2.5.1 MUSIC power spectra as a function of SNR

The first simulation investigates the FB SS MUSIC power spectra as a function of SNR. The number samples of the received signal was set to 1000, the AoA was set to 75 degrees, and the number of ULA elements was set to $M = 6$. To simulate different SNR conditions a complex AWGN was added on the simulated received signal to investigate its effect on received AoA estimation. The FB SS MUSIC power spectra is presented in Fig. 2.7a, with the SNR being 10 dB, 0 dB -10 dB, -20 dB.

From Fig. 2.7a it was evident that that for the high SNR cases of 20 dB and 10 dB the measured floor imposed by noise was below -30 dB. On the contrary, for SNR -10 dB and -20 dB, the measured floor imposed by noise was at -25 dB and -10 dB respectively. Therefore, it was evident that as the SNR deteriorates the performance of FB SS MUSIC decreases. Moreover as the SNR decreases the FB SS MUSIC power spectra peak becomes less sharp, leading to broader peak. That means that the phase information of the transmitted signal was affected by the complex noise, making the direct AoA estimation more difficult. Finally, the accuracy of AoA estimation under low SNR was a broad space of

research, development, and improvement of algorithms [43]. For the scope of this research it was made sure that the SNR was kept above 0 dB.

2.5.2 MUSIC power spectra as a function of ULA elements

The second simulation investigates the FB SS MUSIC power spectra as a function of number for elements in the ULA. The number of samples of the received signal was set to 1000, the AoA was set to 75 degrees, and the SNR was set to -20 dB. The FB SS MUSIC power spectra is presented in Fig. 2.7b, with the ULA elements being $M = 6, 8, 10, 12$.

From Fig. 2.7b it was evident that as the number of elements increase, the measured floor imposed by noise decreases but also the peak becomes sharper. For $M = 6$ the measured floor imposed by noise was circa -10 dB, while for $M = 8$ and 10, the measured floor imposed by noise was reduced to circa -12 dB. The only difference between $M = 8$ and 10 was that for $M = 8$ a false peak was formed at circa 40 degrees. Finally, for $M = 12$ the measured floor imposed by noise was reduced to circa -14 dB.

Comparing Fig. 2.7a with Fig. 2.7b it was evident that the increase of elements can improve the SNR. As the number of elements increase both noise floor was reduced and the spectral peak becomes sharper. The reason was because the amount the covariance matrix at the start of MUSIC was increased in size. Therefore, the number of eigen values was increased and therefore, the phase information attained by the receiver was increased. This was another reason why ten ULA elements were selected for the receiver array. A detailed comparison on the effect that the size of the ULA element has on the developed MF algorithms and the the state of the art systems presented in Subsection 7.5.2.

2.5.3 MUSIC power spectra as a function of AoA noise

The third simulation investigates the FB SS MUSIC power spectra as a function of AoA noise. This simulation is established to understand cases when the receiver is unable to identify multiple rays that are closely spaced in angle domain. This scenario can occur when a ray traverses through a wall or in a Line of Sight (LOS) scenario when the phase of the direct AoA and reflection are added destructively. This effect is studied in literature and it is defined as when the steering matrix is tainted [44].

To simulate AoA noise the direct AoA steering vector was averaged with two steering vectors, one with a positive offset in degrees, and one with negative offset in degrees. To simplify the notation the symbol $\pm$ is used, with the offset in degrees. For example, a 5 degree offset, is notated as ± 5 degrees. The number of samples of the received signal was set to 1000, the AoA was set to 75 degrees, the SNR was set to 10 dB, and the number of ULA elements was set to $M = 6$. The FB SS MUSIC power spectra is presented in Fig. 2.7c, with the AoA noise being $\pm 0, 5, 10, 15$ degrees.

From Fig. 2.7c it was evident that phase noise does have a constructive effect on the FB SS MUSIC power spectra. For a AoA noise of ± 5 degrees the noise floor was circa -25 dB; while for a AoA noise of ± 10 degrees the noise floor was circa -13 dB; and for a AoA noise of ± 15 degrees the noise floor was circa -5 dB. Moreover, as the AoA noise

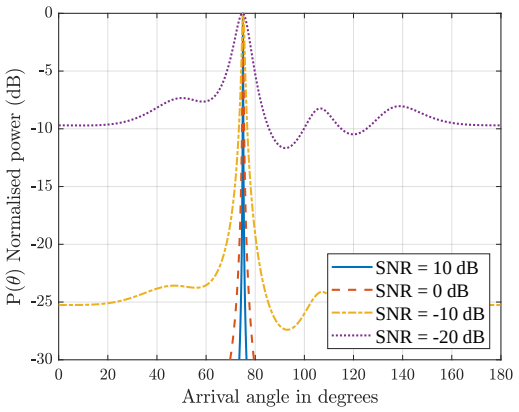

(a) FB SS MUSIC power spectra as a function of SNR, and $M = 6$.

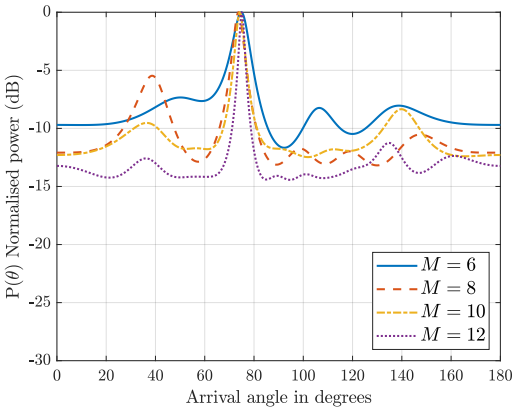

(b) FB SS MUSIC power spectra as a function of number of ULA elements, and SNR $= -20$ dB.

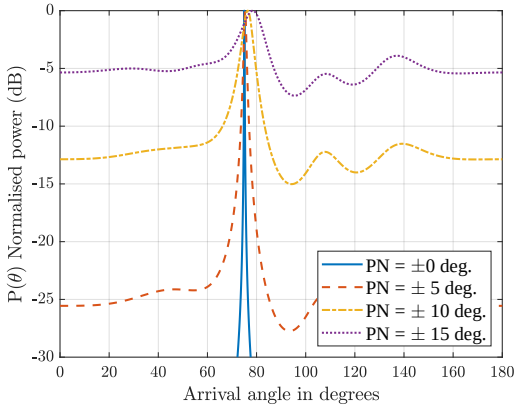

(c) FB SS MUSIC power spectra as a function of AoA noise, $M = 6$, and SNR $= 10$ dB.

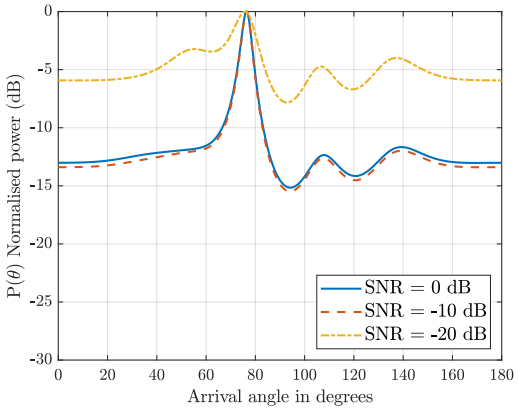

(d) FB SS MUSIC power spectra as a function of SNR, ± 10 degrees AoA noise, and $M = 6$.

Figure 2.7: Simulation of MUSIC power spectra with AoA $= 75$ degrees for three different cases, as a function of SNR in Fig. 2.7a, as a function of ULA elements in Fig. 2.7b, as a function of AoA noise in Fig. 2.7c, and as a function of AoA noise and SNR in Fig. 2.7d.

increases the peak becomes broader, because the phase information was tainted. Also, as the AoA noise increases the direct AoA estimation was offsets toward the centre of the ULA. Specifically for AoA noise of $\pm 0, 5, 10, 15$ degrees, the direct AoA estimations were 75, 75.3, 76.4, and 78.5 degrees respectively.

The main objective of this simulation was to comprehend the effects of AoA noise. With this simulation taken into consideration two conclusions were made. First, when destructive interference of rays occurs, or a wave traverses through a wall, the direct AoA estimation error was expected to be increased. Second, as see from Fig. 2.7a in cases where the SNR was low, and the performance of the FB SS MUSIC was worse in terms of peak sharpness and measured floor. Since SNR degradation and AoA noise occurs due to multiple walls, the effect of both could be destructive. To validate this conclusion another simulation was conducted where the AoA noise was ± 10 degrees, and the SNR was 0, -10, -20 dB. The results are presented in Fig. 2.7d. From the results it was evident that the AoA noise formulates a new measured floor for SNR=0, -10 dB. When the SNR

was decreased even further, the peak becomes broader and the measured floor imposed by noise was increased even further, similar to Fig. 2.7c when the AoA noise was ± 15 degrees. Therefore, with low SNR and high AoA noise, the estimation of direct AoA is even harder. But in real environments since the phase noise is random across frequencies, the employment of MF will mitigate the effect.

Finally, to analyse results of the measurements the term "phase information" is utilised. AoA and phase are directly related to the steering matrix, since the steering matrix is the phase translation of the AoA. Hence, the term phase information refers to the AoA noise, and if the steering matrix is tainted or not. Since all the measures are made with an SNR$>$ 0; when a measurement has a broad AoA power spectra peak it means that the steering matrix is tainted, there is AoA noise, and therefore, the phase information is uncertain and poor. In cases that the AoA power spectra peak is sharp; the steering matrix is clean, there is no AoA noise, and therefore, the phase information is clear.

Chapter 3

Literature review

This Chapter presents the literature review performed on systems or techniques that perform localisation with one or more metrics. Section 3.1 presents systems or techniques that perform localisation with the RSS metric, while the following Section 3.2 is dedicated on systems or techniques that perform localisation with the AoA metric. Section 3.3 focuses on localisation that utilises MF as a metric. Section 3.4 concludes the literature review by presenting systems that use multiple metrics, while Section 3.5 performs a distillation out of the literature review performed in the previous subsections and presents a table comparing all the systems.

3.1 Techniques or systems that utilise the RSS metric

This Section serves as the literature review of this research in systems or techniques that utilise RSS for localisation. Subsection 3.1.1 presents and discusses RSS and Channel State Information (CSI) fingerprinting techniques. The last presented paper is the the best performing state of the art localisation system, DeepFi [8], which is also highlighted in the final Section of this Chapter, where the presented papers are compared and final conclusions are drawn. Moreover, Subsection 3.1.2 introduces systems that utilise diverse arrays, such as Switched Beam Antenna (SBA) [45, 46] and Electronically Steerable Parasitic Array Radiator (ESPAR) [47, 48] which are used to directly compare the results of this research in Chapter 7.

3.1.1 Fingerprinting with RSS or CSI

Modern literature offers plenty of localisation techniques that rely on RSS or CSI. The difference between RSS and CSI is the level where they are extracted; the former is known on a Media Access Control (MAC) level, while the latter on a physical level. Moreover, the use of CSI mainly refers to WiFi or Long Term Evolution (LTE), and it contains additional information such as scattering, fading and power decay.

The first and most widely researched use of RSS or CSI, is the creation of indoor maps

with measurements taken at specific locations, known as fingerprints [49, 50]. When a signal is received from a node, the RSS or CSI is compared with the fingerprint database and with the appropriate (researched) technique, a location is estimated. In terms of fingerprint technique, in [49, 50] the authors proposed a deterministic method that use K-Nearest Neighbour (KNN) position estimates and it utilises more than one WiFi AP to gather RSS. Specifically in [50] they use 5 APs in an indoor office area that spans over 22 by 42 m, and 49 locations for fingerprints. The mean and 90% error performance with 5 APs are 2.37 m and 5.97 m respectively. The 90% error performance is very important because it conveys that in the majority of the cases, the error will be less than the presented number.

Moreover, modern systems such as Horus [6] are a more advanced fingerprinting method. To evaluate Horus's performance the authors have taken measurements in two testbeds, first in an area of 68.2 by 25.9 m with 6 APs, and second in an area of 11.8 by 35.9 m with 4 APs. The mean and 90% error performance of the first testbed was 39 cm and 89 cm; while for the second testbed was 51 cm and 132 cm. To achieve these results, Horus required 110 measurements as part of fingerprinting for each testbed.

Overall, from the results of Horus [6], it is evident that fingerprinting is a high accuracy technique. But there are two issues in practical applications. First is the high cost, since the process of taking fingerprinting is exhaustive it requires highly trained people, and second, the indoor environment changes, meaning that the fingerprints do not remain static and change as well. Furthermore, even the presence of people in an office area can change the fingerprints enough to reduce the accuracy. The fundamental issue of the fingerprinting technique, which is accuracy uncertainty, is investigated in [51]. The authors in presented a general probabilistic model to provide an answer regarding on what are the accuracy limits of indoor RSS fingerprinting localisation. Also, the authors presented an optimal fingerprinting reporting strategy to improve accuracy as a function of reliability and the number of RSS measurements. Therefore, based on their model, an optimal fingerprinting system could be designed, specific for the application environment. On the contrary its application in real environments is questionable, but interesting and it could be investigated in greater detail.

Furthermore, there are other techniques in literature that perform localisation using RSS and require no fingerprints. Tomic *et al.* in [52] proposed a RSS localisation technique for Wireless Sensor Networks (WSN) which applied a convex optimisation problem based on RSS. The proposed technique took into consideration both non cooperative and cooperative localisation between multiple WSN. The passive receiving nodes collected noisy RSS and formulated a relaxed convex estimation that was closely related to the non convex Maximum Likelihood (ML) estimator. This allowed the search of the global minimum since the problem was relaxed to a convex estimation. Also the proposed estimation was expected to be very accurate, since it was related to ML. The performance was evaluated using Monte Carlo Simulation (MCS) for both non cooperative and cooperative localisation of the transmitting location. The results were evaluated with the transmit power being known and unknown. For non cooperative localisation and known transmit power the

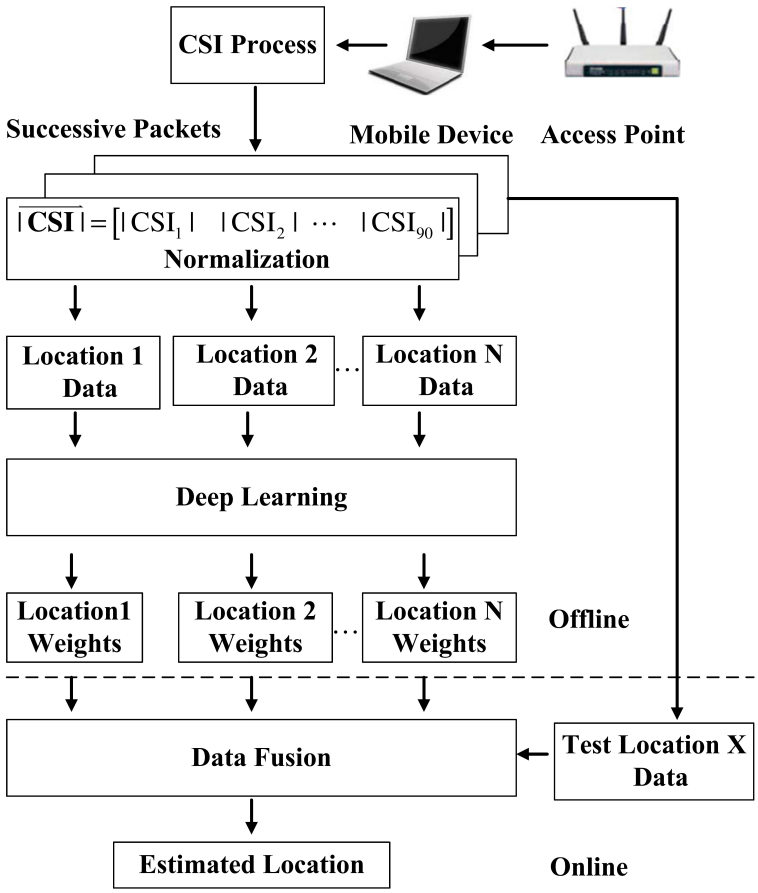

Figure 3.1: System model of the DeepFi [8].

proposed technique had an improved performance in terms of complexity and accuracy, with an Root Mean Square Error (RMSE) of circa 1 m. Also, with the proposed three-step procedure for cases of unknown transmit power and pathloss estimation, the authors managed to achieve an RMSE of 3.4 m, which was a 15% improvement compared to the state of the art techniques. For cooperative localisation and known power, the proposed technique imposes a 0.5 m improvement compared to other techniques. For unknown power and pathloss the mean error for 50% of the cases was less, circa 2.5 m. Overall, the authors in [52] provided analytical results, and their system was not applied under real environments. Even if their results prove that RSS with no fingerprinting can have high accuracy, taking into account the complexity of convex optimisation and multiple nodes, it is uncertain that this remains true in real environments.

DeepFi [8] is a state of the art localisation system that utilises CSI fingerprinting with a deep learning approach algorithm. The authors performed OFDM measurements with 3 antennas and 30 subcarriers, acquiring 90 CSI values per measurement. By utilising the CSI DeepFi [8] attains information regarding scattering, fading and power delay. Utilising the power delay measured from the CSI, the authors hypothesised and proved that the CSI

values, compared with the RSS values, exhibit greater stability for continuously received packets at a fixed location. The DeepFi's [8] architecture is presented Fig. 3.1 and is broken down into two phases, the offline which is the Deep Neural Network (DNN) training and the online which is the localisation. The offline process begins by acquiring and normalising the raw CSI values from multiple locations and packets. Then, it proceeds to the offline DNN training, where the weights for each location are generated. In the online localisation phase, a probabilistic data fusion method was applied on the location weights derived from the offline phase, based on the radial basis function to obtain the estimated location.

For the validation, the authors performed measurements in two environments, a living room, and computer laboratory, comparing the results with other WiFi localisation methods. The overall setup allowed measurement of 400 CSI values per second, which were used for the offline training phase. For the online localisation phase the authors set a distance of 50 cm, because they to maintain a balance between pre-process cost and localisation accuracy. Although the author made such compromise, this was not practical for a real application. When the area for localisation interest increases, the number of fingerprints increases linearly as well, leading to an exhaustive number of measurements. Finally, the authors compared their results with FIFS [53], a WiFi finger printing system, Horus [6], that explores different channel distributions and was presented above, and ML [54], a WiFi statistical learning theory algorithm.

The results show that DeepFi [8] is able to attain close to centimetre level of accuracy on a living room environment. Furthermore, the authors claim that the training phase is acceptable but in truth it is unrealistic for a real scenario, when an application wants to cover a large area. For example, in the living room used for experiments which is 7 by 5 m, 50 measurements are required. Furthermore, the accuracy required for these measurements is extremely high, as a small measurement error will result to an accuracy error. With the obvious issue of DeepFi's ability to scale, the mean run time of the algorithm is at 2.5679 s for a single AP. Scaling even further, for instance by adding more rooms, the support of more AP's will be required increasing the computational time exponentially. It is evident that for the purpose of centimetre localisation results, the DeepFi [8] system is not applicable as a real system solution. Finally, this paper is also presented in Subsection 3.5 where the results are compared with other localisation techniques or systems.

3.1.2 RSS metric from diverse antennas patterns

More recent techniques utilise RSS signals received from diverse arrays such as, SBA and ESPAR. Cidronali *et al*. [55] introduced the first hemispherical SBA for the purpose of positioning based on RSS. The SBA enables AoA estimation employing six planar antenna elements as seen in Fig. 3.2a. The proposed SBA also supports polarisation diversity and it utilises a switch to alter antenna plane and polarisation, also seen in Fig. 3.2a. Due to the 3-D antenna element placement, the proposed system can locate a target in both

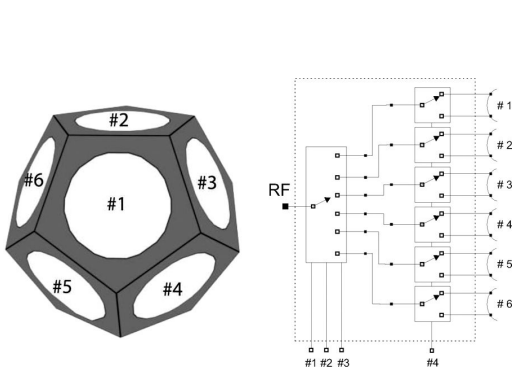

(a) Six element SBA and schematic used in [55].

(b) Four element SBA used in [45].

Figure 3.2: Examples of the diverse antenna arrays, SBA (3.2a) and ESPAR (3.2b).

azimuth θ and elevation ϕ. In this paper, the receiver measured the RSS in all elements and polarisations and searched for the θ and ϕ that minimised the objective function. The authors performed 24 RSS measurements in a 7.2 by 8 m room, with the system placed on the ceiling. The average error over the entire plane reported is 1.7 m.

More recently, Ahmed *et al*. proposed a SBA with four elements and the application of a neural network [45] to extract the AoA from RSS. A picture of the SBA can be seen in Fig. 3.2b. The applied neural network algorithm was a Levenberg-Marquardt with five hidden layers. The Levenberg-Marquardt algorithm applied Least Square Errors (LSE), and it worked with a loss functions that take the form of a sum of squared error. It does not compute the Hessian matrix; but instead it utilises the gradient vector and the Jacobian matrix. The benefits were, good accuracy with the cost of high memory, and low complexity in terms of training speed. The authors performed measurements in an indoor room and its and its peripheral corridors, with the transmitter moving at a slow speed. They measured the RSS in 75 random placed, indoors and outdoors. For training, they used 50 measurements, and to test the system, the remaining 25 measurements. The mean Cumulative Distribution Function (CDF) error reported was 7 degrees, with a standard deviation of 4 degrees. Even though the results were not as impressive as [55], the authors in this paper reduced the overall array requirements. The elements were reduced from six to four, and there were no requirements for diverse polarisation. Also, the authors performed measurements in peripheral corridors without LOS, which no other paper presented in this Section does. The results of this paper are compared with the contributions of this research in MF RSS in Subsection 6.4.4.

Moreover, Taillefer *et al* first proposed the use of ESPAR to estimate AoA through RSS [56]. An ESPAR antenna is consisted of a single feed element which is surrounded by a ring of reactively loaded parasitic elements. The loading reactances are controlled electronically, formulated directional beams and nulls which can be steered through the azimuth plane. By providing adaptive beam forming and control of the radiation pattern, ESPAR antennas can increase the overall channel capacity and improve SNR by reducing

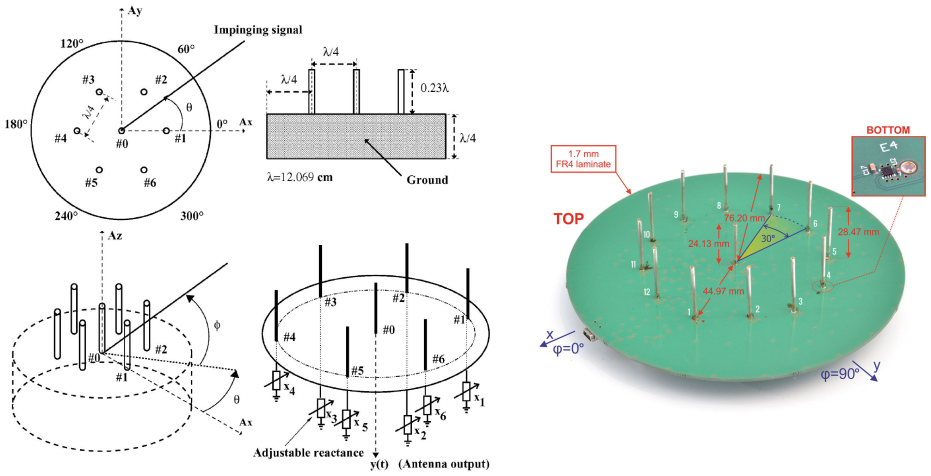

(a) Seven element ESPAR schematic used [56]. (b) Twelve element ESPAR used in [47, 48, 57].

Figure 3.3: Examples of ESPAR used for extracting AoA information from RSS.

the interference. The schematic of the seven element ESPAR with the central single feed and outer elements used in [56] can be seen in Fig 3.3a. To extract the AoA from RSS, the authors cross correlated the power output and antenna pattern diversity from a set of known pre-measured power radiation patterns. They proposed an "estimator condition" which was used to determine the most appropriate pattern shape. For the experimental results, they measured and stored the patterns for 36 equally spaced AoAs as part of pre-measurements. Then the AoA error was estimated for the different reactance vectors. For 4 reactance vectors the mean estimation error and standard deviation were less than 1.6 degrees and 1.28 degrees respectively. For 6 reactance vectors, the mean estimation error and standard deviation were 0.7 degrees and 0.6 degrees respectively.

More recently, localisation with ESPAR has been a major research focus of Kulas and his research group [47, 48, 57]. In all instances, the authors employ the 12 element ESPAR, shown in Fig. 3.3b. Rzymowski *et al* in [47] proposed an ESPAR fingerprinting method, measuring the RSS with 24 different antenna configurations, at 100 locations in a 4.5 by 4.5 m room. Using 25 out of the 100 measurements as fingerprints resulted to a mean error of 1.6 m, while reducing the fingerprints to 9 out of 100, the mean error was increased to 1.86 m. The overall technique exhibits very high accuracy, but the amount of pre-measurements required and the fact that a single anchor was limited to perform localisation only in a single room room, makes the overall system expensive and not practical. The results of this paper are compared with the contributions of this research in MF RSS in Subsection 6.4.4.

In [48] Kulas, introduced interpolation to reduce the ESPAR calibration phase maintaining the same accuracy on AoA estimation. For measurements in an anechoic chamber, without interpolation, 20 dB SNR, and 360 measurements the RMS error was reported to 2 degrees, while for 10 measurements the RMS error was reported to 10.6 degrees. With interpolation and 10 measurements, the reported RMS error was 2.5 degrees, an increase

of 0.5 degree compared to 360 measurements. The calibration time required was reduced from 33 minutes to 15.7 minutes. The overall decrease in calibration time and the 2 degree RMS error performance make the ESPAR approach even more attractive, but again, this system and technique are not tested in real environments. The results of this paper are compared with the contributions of this research in MF RSS in Subsection 6.4.4.

Tarkowski and Kulas in [57] applied Support Vector Machine (SVM) to improve the AoA estimation accuracy with a RSS and ESPAR. The authors utilised 12 radiation patterns and perform 360 measurements, one for each degree in an anechoic chamber. These measurements were used as a training set in the learning process of the SVM. For the test set, the ESPAR was rotated in the horizontal plane with a 5 degree angular step, resulting to 72 test directions. The results for 30 dB SNR report an RMS error performance for SVM to be 0.74 degrees, while for the correlation technique used in previous papers 1.55 degrees. For 0 dB SNR, the RMS error performance was increased to 1.87 degrees and 2.59 degrees, for SVM and correlation respectively. Overall, it was evident that the SVM approach improves the overall accuracy, but the issue of performance in real world still remains. Since the technique was tested in an anechoic chamber, the technique has not been tested under the effects of multipath.

Concluding this Subsection, it was evident that the proposed ESPAR implementations can achieve good accuracy on estimating the AoA based on RSS compared to the SBA. The overall estimation improvement is achieved with a higher cost, since ESPAR implementation is more complex than SBA. Since the cost is higher than SBA, the single receiver in every room approach will always favour SBA. Hence, the application of an ESPAR indoors for commercial use is not as attractive as SBA. Finally, both SBA and ESPAR have not been applied to outdoor environments. Therefore, the overall use of diverse RSS patterns can be low cost, but requires complex receivers for single room, and its application is not tested for outdoors.

3.2 Techniques or systems that utilise the AoA metric

This Section serves as the literature review of this research in systems or techniques that utilise AoA for localisation. Subsection 3.2.1 is dedicated to interesting AoA novel novel systems, giving further emphasis on the technique presented by author Tayem in [58]. Furthermore, Subsection 3.2.2 presents state of the art localisation systems that utilise AoA and complex system techniques. Further emphasis is give on ArrayTrack [7] since it is the best performing system. Finally, both the technique presented by Tayem in [58] and ArrayTrack [7] are featured in the final Section of this Chapter for comparison and to draw conclusions but also to compare the findings of this research in Chapter 7.

3.2.1 AoA novel techniques

Scherhäufl *et al*, first in [59, 60], and more recently in [61, 62] proposed the localisation

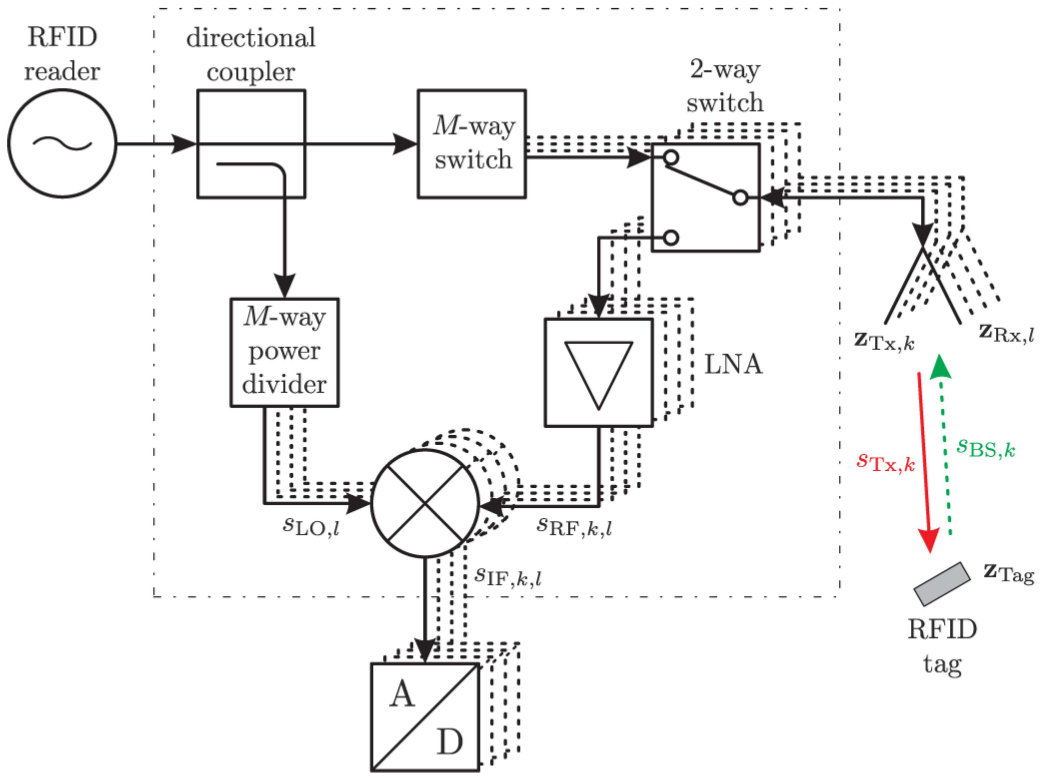

Figure 3.4: Schematic of the measurement system used in [59–62], with K RF front ends.

of RFID tags using AoA. In all of their papers, the authors utilised a single RFID reader with an 8 port switch for 8 antennas. The reader was able to transmit and then receive the signal backscattered from the RFID tag from 8 different antennas. The schematic of the system is shown in Fig. 3.4. Specifically in [59, 60], the location of the RFID tag was determined by defining a grid search algorithm and estimating the received phase based on each grid point. The received phase was compared with every grid point, and the grid point that was closest to the equation was determined as the transmitted location. With measurements in a 3.5 m by 2.5 m indoor environment, and 645 grid positions, the RMS error was reported to be 0.558 m. Instead of a grid search, the same authors with the same system, propose a Maximum Likelihood Estimation (MLE) approach in [61, 62]. Performing measurements in the same environment, with the MLE approach, they reduced the accuracy estimation to 0.11 m. This technique is impressive due to the high accuracy, but unrealistic to be applied in a larger scale. It would be interesting to see what effect on accuracy if the detection area was increased.

Cremer *et al* in [63] proposed the use of beamforming for AoA detection of an RFID. Their technique is based on pivoting the main lobe of the antenna array in the azimuth plane and formulate a sensitive threshold of detection. The authors employed three circularly polarised patch antennas as an array with a dedicated phased shifter on each patch antenna. In the first stage, the system initialised by setting the transmit power to max and then pivots the beam to the azimuth plane. If a tag was detected, the transmit power was

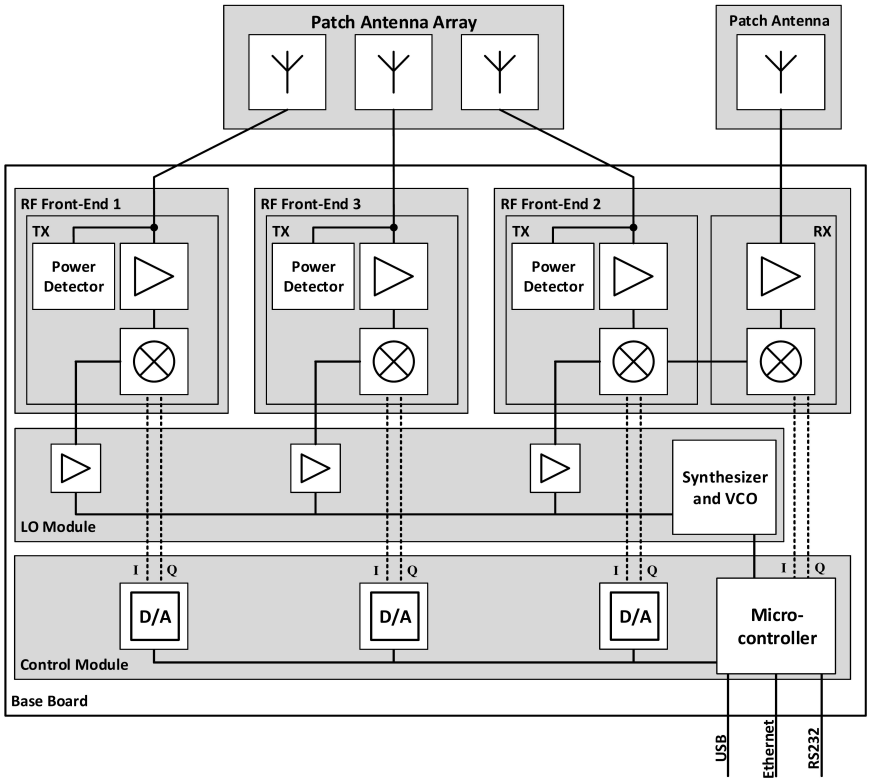

Figure 3.5: Block diagram of the system used in [63].

reduced and the pivoting continues until the tag was not readable. Without changing the recorded power from stage one, the second stage initiates, where the azimuth angle resets and attempts to read the tag n times before pivoting. Each time a tag detection was made, the angle was stored. The process was completed when the beamformer reaches the final activation angle at the azimuth plane. The final AoA was computed by averaging the first and final activation angles. The authors reported a mean accuracy of 1.2 degrees in an anechoic chamber, 1.9 degrees in basic multipath environment, and 2.5 degrees in real world environment. By placing 4 systems in a 3 by 3 m grid and performing triangulation with the AoA estimation, the mean localisation accuracy was 7 cm. The technique used in this system allowed the overall application to achieve high accuracy. On the contrary, an issue arises with the use of multiple RFID tags. Stage one will detect the first RFID tag by reducing the power, and potentially ignoring other tags that are further away, or close together. This technique could be potentially applied in modern systems to improve the overall localisation accuracy, but the complexity of the system increases the overall cost. Therefore, it is unsuitable for the purpose of this research.

In [58] Tayem presents a summary of his work [64, 65] summarising multiple novel methods that use QR decomposition for AoA. QR decomposition is the decomposition of a matrix **A** into a product **A**=QR, where matrix **Q** is orthonormal and contains both signal and noise subspace [66]. While **R** is an upper triangular matrix that contains both signal

and noise information, the true rank of the matrix and it is easier to solve. In modern literature SVD is preferred even though its computational process might be more complex because it results to a clearer representation of noise and signal subspace. Moreover, QR is unable to handle rank deficiency, and the performance depends on the upper triangular matrix. The overall complexity of QR is characterised as $\mathcal{O}((mn2 - n3)/3)$, using the Householder transform [66]. On the contrary, the SVD has a characterised complexity of $\mathcal{O}(mn2 + n3)$ [66].

The performance of SVD is always expected to be better since it can solve rank-deficient matrices and more complex data problems, but the reason why QR is the reduced complexity for practical application. Therefore, this paper is highlighted because in can reduce the hardware complexity and as the author claims achieve equal performance in some cases. To prove that claim, five different methods to estimate the AoA were introduced.

Method 1 [58], is a straight forward application of MUSIC, where it utilises the noise subspace representation of $\mathbf{Q_n}$. It is an attractive solution due to the low complexity, compared to more complex matrix decomposition such as SVD. Both decomposition methods could be used to obtain the noise subspace and estimate the AoA. The downside of QR is that it can not handle rank deficiency matrices. The presence of reflections formulate matrices that are rank deficient. Therefore, the performance with QR decomposition is expected to be worse than utilising SVD. Another downside of QR is that the orthogonal matrix contains a lower SNR compared to SVD. This is the cost of reducing the complexity of the estimation, resulting to an equal or worse performance than SVD. The performance difference is dependent to the overall system SNR. In cases that the received SNR is high, the difference is negligible.

Method 2 [58], performs a rank revealing using the **R** matrix. The benefit of the rank revealing is that it attempts to reveal the true rank of the matrix. Correlated sources such as reflections and multipath, severely affect subspace algorithms. Thus, the application of rank revealing RRQR attempts to reduce the sources correlation from multipath. In theory, this method should result to a higher SNR estimation than **Method 1** in cases of strong multipath.

Method 3 [58], exploits the shift invariant property, same as ESPRIT. It performs the rank revealing RRQR like **Method 2** and gives a parametric result rather than spectral. The results are expected to be equal or worse than **Method 2**, but since its a parametric estimation, the complexity is far lower.

Method 4 [58], utilises the signal subspace of the covariance matrix (2.11), where compared to **Method 3**, utilises the upper triangular matrix. Using the signal subspace, the accuracy results are expected to be improved, when the signal sources are not correlated and the SNR is high. In practice, **method 4** is the exact application of ESPRIT algorithm using the signal subspace.

Method 5 [58], follows the same logic as **Method 3** and **Method 4**, utilising both **R** and **Q** matrices. The purpose is to benefit from the rank revealing **R** matrix and then utilise the signal subspace of its newly formed data matrix. In theory this algorithm should perform better than the other in cases of high SNR.

Table 3.1: Experimental AoA results for two sources at 37 and 115 degrees, with four element ULA [58].

	MUSIC SVD	ESPRIT SVD	**Method 1**	**Method 2**	**Method 3**	**Method 4**	**Method 5**	
AoA 1: 37	36.5	36.2	34.9	37.6	36.3	37.6	36.3	deg.
AoA 2: 115	115.1	114.2	114.5	114.9	115	114.9	113.6	deg.

The environment that the measurements took place was a flat rooftop in order to decrease possible multipath and has a direct LOS. Unfortunately this scenario is not applicable for many applications. Hence, the results are not appropriate to take into consideration for indoor applications as they do not experience heavy multipath. Table 3.1 presents the experimental results for all five methods with two sources, 37 and 115 degrees. The results prove that for an ideal environment, (small number of multipath propagation) and LOS conditions the QR decomposition methods can have the same results with MUSIC or ESPRIT. Some doubt for the performance of QR decomposition algorithms in a multipath scenario still remains, because of the way that the experimental tests were performed. Although the QR is a complexity reducing algorithm compared to SVD, the results show that QR can produce quality results under low multipath scenarios.

The contributions of this paper are taken into consideration to the MF AoA research, Chapter 7. The performance of the developed algorithm within the scope of this research is evaluated and compared utilising SVD and the two QR decomposition methods 1 and 2 in Subsection 7.5.3. Moreover, this paper is also presented in Subsection 3.5 where the results are compared with other localisation techniques or systems.

3.2.2 State of art AoA localisation systems

In [67] Miesen *et al*. utilised the movement of a robotic arm to formulate a Synthetic Aperture Radar (SAR) to localise a RFID tag. SAR systems work similarly as the phased arrays, but movement is required. To localise a transmitter samples are collected from each receiver in multiple time snapshots, and positions. In order to have the transceiver in different positions, a mechanical movement with a known speed is required. As the transceiver changes positions mechanically, it emulates the existence of an array. In [67] the robotic arm rotated on the x and y axis, the RFID tag backscatters passively a phase modulated signal. The received signal was then used to synthesise the SAR. Experimental results from indoor environments, reported that an aperture (x-y-axis movement) of 0.8 m was required to achieve an error of 0.9 m and a standard deviation of 0.02 m. The novelty of this paper could be applied on moving readers, for example hand held readers mounted on vehicles. With a known trajectory and speed, the moving vehicle could scan an area to locate a missing person that carries a passive RFID tag.

Furthermore, in [68] the authors proposed the utilisation of SAR with multiple readers that scan a RFID tag indoors. Instead of having a moving transceiver, the authors used a MIMO system where the 8 transceivers took turns on transmitting and receiving, as seen

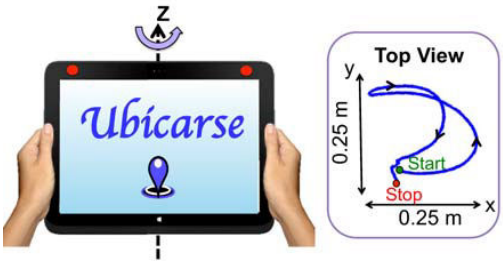

(a) Example of the user twisting the mobile device on the vertical (z) axis, at left. The red circles indicate antenna locations. On the right, the top view with the trajectory measured by a Vicon motion capture system. [69].

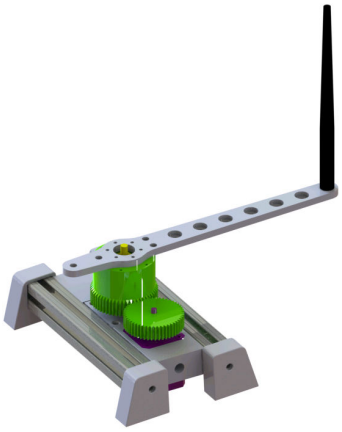

(b) LTeye prototype sniffer [31].

Figure 3.6: Examples of SAR systems used in in Ubicarse and LTEye.

in [59–62]. This allowed the formulation of a virtual array as if a single transceiver was moving on each location collecting data. Results in an indoor room with a size of 2.5 by 3.5 m and 8 transceivers reported an accurate localisation with a root median deviation below 0.1 m and an error of 0.01 m. Overall, this specific application is not practical for tracking people in need. The cost and complexity requirements are huge for a large scale application, but if the overall transceivers were reduced and placed in different rooms it would be more practical. Combining the application of [67] with [68] in a very large scale, in theory, a person in need could be located in both indoor and outdoor only by carrying a RFID tag.

Kumar *et al.* in [69] introduced UbiCarse, a SAR based system where, instead of a mechanically moving transceiver, the movement is simulated by a hand held device on the user side. When the user rotates the hand held device on the z-axis, the device records WiFi data from known locations, gyroscopic data, and camera information, Fig 3.6a. In practice, the WiFi data served as the transmitting signal of the traditional SAR systems, the gyroscopic data served as a correction of the mechanical movement, and the camera information was used for geotagging to improve the overall accuracy. Without geotagging, in a 10 by 15 m indoor environment, UbiCarse achieved an accuracy of 80 cm error with 3 APs, 50 cm error with 4 APs, and 30 cm error with 5 APs. By applying geotagging, the accuracy was decreased to 15 cm error with 5 APs.

Moreover, the same authors in [31] introduced LTEye, a SAR localisation system for LTE 4G cellular network. With the cellular network evolving to the use of pico and femto cells, they employed an SDR as a passive sniffer, and capture CSI information with a static and a mechanically moving antenna. LTEye employed a passive sniffer, and requires no support from cellular providers; a picture of the prototype is shown in Fig. 3.6b. It utilises the LTE control channels that contain downlink and uplink data, without accessing encrypted or private data. They evaluated the performance in two scenarios, in a classroom

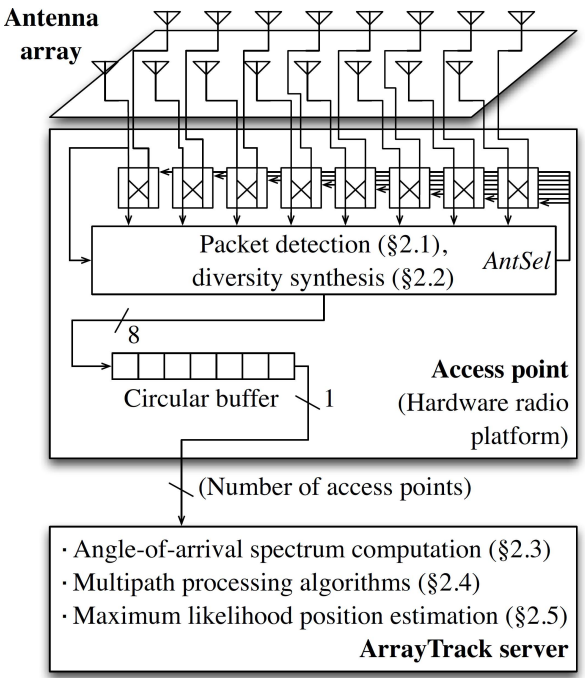

Figure 3.7: ArrayTrack high-level block diagram of the front end, access point, and server [7].

(24 by 17 m) where the LOS is dominant with 2 APs, and in a Non Line of Sight (NLOS) office (60 by 34 m) with 5 APs. For the first scenario, the mean error in localisation was 34 cm for each dimension, and 61 cm for 3 dimensional placement; while for the second scenario the mean error was 43.7 cm for each dimension and 84.6 cm in 3-D displacement. The results of LTEye [31] are compared with the contribution of this research in Section 7.6.

Overall, the performance of UbiCarse [69] is LTEye [31] are impressive, but in fact it is not applicable for all cases. In terms of tracking people in need, it is not sure that the users will be able to use the mobile phone. Moreover, the battery life of the hand held devices is low, requiring daily charging. Finally, both methods have not been tested in outdoor environments, where the distances are greater, and the number of APs is low.

ArrayTrack [7] is an AoA detection system with a passive ULA that requires no movement, outperforms the SAR systems, and it can be applied for indoor localisation using WiFi. The system utilises 16 receiving antennas where 8 are used for spectral estimation using SVD. Compared to commercial WiFi router, the implementation of 16 receiving antennas is unrealistic, while the use of 8 antennas is practical. The overall system design is a combination of multiple signal processing algorithms to eliminate multipath, even when there is little to no energy from the direct path. The reason ArrayTrack is highlighted in this Section is because it is the best performing single metric system that utilise only AoA.

The block diagram of the ArrayTrack is presented in 3.7, with all the related algorithm performed in each step. For each individual AoA estimation on the ArrayTrack server, spatial smoothing is applied first, before MUSIC [41], as presented in Subsection 2.1. After

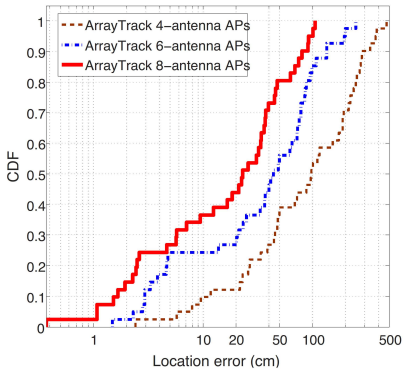

(a) CDF plot of location error for different number of antennas [7].

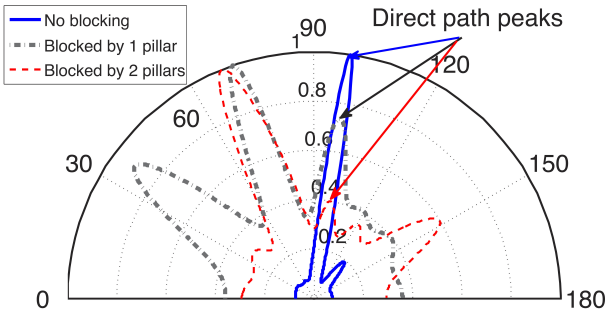

(b) AoA spectra for 3 clients in a line with AP [7].

Figure 3.8: ArrayTrack results of a CDF and AoA spectra [7].

spatial smoothing and MUSIC, the system continues by applying a windowing function over the AoA angles which is proportional to the confidence on the AoA. Furthermore, the system removes the 360 degrees uncertainty, with the back of a ULA mirrored to the front forming a 180 degree spectrum. Furthermore, multipath suppression aims to remove or reduce peaks that do not belong in the direct path. The algorithm is grouping two to three AoA spectra from frames taken closer than 100 ms in time. Then one AoA spectrum is chosen arbitrarily as the primary, and the peaks that do no pair with the other AoA spectra are removed. In the final step, the spectra synthesizer algorithm lays down all N APs in a map, and their corresponding calculated spectrum estimated $P_i(\theta_i)$, and assigns a likelihood. The location with the highest likelihood, is the estimated location of the transmission.

Fig. 3.8a shows that the number of antennas is vital to the ArrayTrack performance. The mean accuracy is at 10 cm, 40 cm and 23 cm with four, six and eight antennas respectively. Furthermore, the improvement from four to eight antennas was higher than the improvement from six to eight. Fig. 3.8b demonstrates the direct path peak changes over different scenarios. At first the transmitter was at LOS, then it was being blocked by one pillar, and finally blocked by two pillars. Even with the two pillars blocking the LOS, there was still a direct path although it was not the strongest. Finally, the authors recommended the use of a ULA with six (30.5 cm long) or eight antennas (43 cm long). These results proved that acquiring the direct path is possible, even with 2 pillars blocking it. Hence, forming a platform to attempt and resolve the true path, with lower cost and complexity will bring novelty in the AoA estimation; which is where this research is focused on.

The results of this paper provide the majority of evidence for the research and novelty of this research and MF AoA estimation in Chapter 7. The authors utilise a 16 element ULA, complex hardware and appropriate signal processing the authors proved that the direct AoA is detectable even when the LOS is blocked by two pillars. The research presented in Chapter 7 attempts to improve the performance by reducing the hardware complexity and developing a novel MF algorithm. Finally, this paper is also presented

in Subsection 3.5 where the results are compared with other localisation techniques or systems.

3.3 Techniques or systems utilising MF and a single metric

This Section serves as the literature review of this research in systems or techniques that utilise MF and one more metric for localisation. The first Subsection 3.3.1 is dedicated techniques and systems that utilise MF and RSS, with the highlight being the SBA of Maddio *et al.* [46]. Furthermore, Subsection 3.3.2 presents techniques and systems that utilise MF and AoA, such as Frequency Diverse Array (FDA)s, and coprime arrays. The highlighted paper is from Rigelsford and Tennant [70] with an acoustic Random Spherical Volumetric Array (RSVA). Both papers are featured in the final Section of this Chapter, but also the results of [46] are used for comparison with the findings of this research in Chapter 6.

3.3.1 Novel utilisation of MF and RSS metric

In [71] Viikari *et al.*, proposed a MF based method to determine the distance of RFID tags with unknown properties. The reader measured the tag's response at different discrete frequencies at the power threshold of the RFID tag. The tag's modulated reflection coefficient was estimated through the received measured power and by measuring distance compensation. The authors performed measurements in a anechoic chamber. Both reader and tag were placed at the same height and the tag was placed at different distances, 1 meter, 2 meters, and 3 meters. The frequency modulated CW that the reader used for measurements operated at frequency from 840 to 875 MHz with a step of 3 MHz. First the author attempted to estimate the parameters of the RFID tag at different distances, 1, 2, and 3 m. The best result was achieved at 1 m due to the high SNR, but even in 3 m the deviation was small that it could be ignored. Then the resonance frequency of the RFID tag was estimated. The average of the estimated resonance was at 864 MHz, with deviations of -4 and + 10 MHz. Furthermore, the results report that by using MF and by estimating the properties of the tag, a 1.4 meters improvement was achievable. For measurements in an anechoic chamber, the mean distance error was reported to be 0.068 meters. In this paper, it was evident that the MF can provide further information regarding the tag properties, allowing better estimation. The issue is that the performance of this system is that it's untested in real environments with strong multipath effect. This technique is very interesting and it could be used by mobile units that can attempt to localise a target.

As presented in the Subsection 3.1.2, Cidronali *et al.*, where the first authors to propose the use of a SBA to distinguish AoA from RSS [55]. More recently, Maddio and Cidronali have focused on utilising dual-band signals from WiFi to improve the overall accuracy of estimation [46]. As with every SBA, Maddio and Cidronali applied Space Division Multiple Access (SDMA) where they enhanced the effectiveness of the RSS measurements,

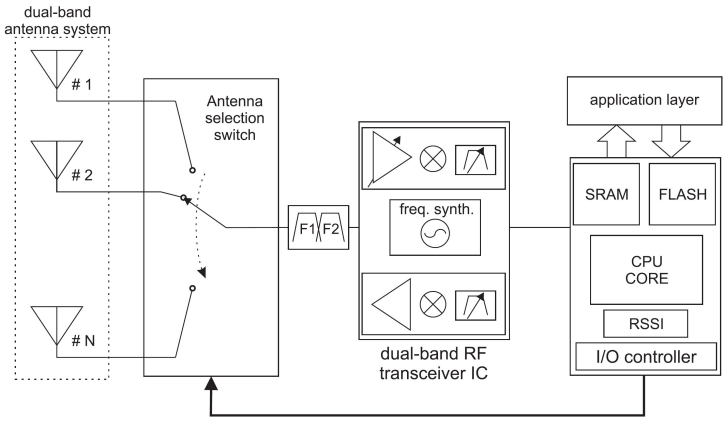

(a) System architecture of the dual-band node used in [46, 80].

(b) Picture of the dual-band SBA prototype used in [46, 80].

Figure 3.9: System architecture and prototype of the dual-band node used in [46, 80].

coping with the multipath problem. In practice, SDMA is selecting the signal reception from only a specific angular region, instead of all the elements simultaneously. This helps mitigating the uncertainty caused by the multiple path reception [72, 73]. In [46] the authors extended their work presented in [74] where the SBA operates in two uncorrelated frequencies, 2.45 and 5.2 GHz.

A schematic of the system architecture is depicted in Fig. 3.9a. There is a single dual-band transceiver connected to an antenna switch and then to the dual-band antennas. The microcontroller was programmed to serve as the IEEE 802.11x WiFi MAC layer. To enable SDMA, the dual-band RF transceiver was responsible to electronically control the antenna, pointing in different space sectors by selecting a predefined beam. The SBA arrangement with 8 printed patch antennas in an octagonal prism can be seen in Fig. 3.9b. The geometry allowed the signal distribution in the $x - y$ plane to be optimal. The patch antennas were circularly polarised to allow robust communication regardless the transmitting antenna orientation. Moreover, it was shown in [75–77] that circular polarisation increased robustness against the effect of multipath, allowing more precise RSS data [78, 79]. The employed patch antennas were able to have two radio patterns, left-hand and right-hand, for both proposed frequencies, 2.45 and 5.20 GHz.

The estimation of AoA was mathematically expressed as follows: with a set of measured RSS data $\mathbf{S}^i$, it was necessary to know the gain pattern $\boldsymbol{G}^i(\theta)$, therefore, the azimuth angle θ was the angle that fits best the analytical expression found [46]. Moreover, to mitigate multipath noise, the dual-band approach was exploited. For a each frequency, the received signal is consisted of multiple repetitions (reflections) of the transmitted signal. Hence, lack of variance in in different angles, makes it more likely that the AoA (θ) is the true AoA.

Since the the multipath effect was unlikely to be similar on both frequencies, one of the two frequencies was used for the estimation. Thus, it was unlikely that both received signals to be affected by the same multipath fading. Since the antenna gains $G^1(\theta)$ and

Table 3.2: Summary of the AoA estimation for different SNR

	Mean error			90% error performance			
	MF	2.45 GHz	5.2 GHz	MF	2.45 GHz	5.2 GHz	
SNR = 32 dB	2.6	4.5	6.4	5.4	9.3	12.7	deg.
SNR = 3 dB	4.9	9	7.8	10.5	18.3	17.4	deg.
SNR = 0 dB	7.1	13	9.5	15.1	23.6	21.4	deg.

$G^2(\theta)$ for the two frequencies had different shapes, also supported the fact. Furthermore, to combine the two gain sets $G^1(\theta)$ and $G^2(\theta)$, a corrective factor and it can be found in[46].

To evaluate the performance of the proposed system, the authors performed measurements in an anechoic chamber. The proposed SBA was placed on a rotor that was controlled by the target node on a tripod at the same height. A third device was employed to provide interference to the direct communication link and to serve the purpose of controlled multipath. A detailed table with the mean and the 90% error performance with different SNR is presented in Table 3.2. From Table 3.2 is evident that MF was able to reduce the 90% error more effectively. Specifically, for SNR = 32 dB the error was reduced by 3.9 degrees, for SNR = 3 dB the error was reduced by 6.9 degrees, and for SNR = 0 dB the error was reduced by 6.3 degrees.

In every case, it was evident that the MF outperforms the use of a single frequency. Regardless of which frequency was the worst performing, the MF was always performing better than both of them. Since in the real world is not possible to predict the environment in signal reception, the proposed system is an improvement to the AoA estimation regardless the environment, and with no prior knowledge. The only case that the dual-band system will not perform better, is when both frequency bands are affected by sever distortion, but in this case, AoA estimation is considered impractical and impossible for any system. Even if the results are part of measurements in an anechoic chamber, it is evident that MF can improve the overall AoA estimation.

Finally, this paper is presented in Subsection 3.5 where the results are compared with other localisation techniques or systems. Moreover, the results of this paper are also compared with the contributions of this research in MF RSS in Subsection 6.4.4.

3.3.2 Novel utilisation of MF and AoA metric

The authors in [81] were the first to propose and investigate the use MF radar. Specifically, they proposed a MF array that achieves high accuracy with multiple coherent signals. The main problem of radar was that during the transmission of the first burst the transmitted signal that was affected by the multipath reflects back to the receiver as a coherent signal. The authors proposed a MF array that allowed a decorrelation technique to enable correct AoA estimation. A flowchart of the proposed system architecture was presented in Fig. 3.10. The flowchart depicts the two processes that enabled localisation;

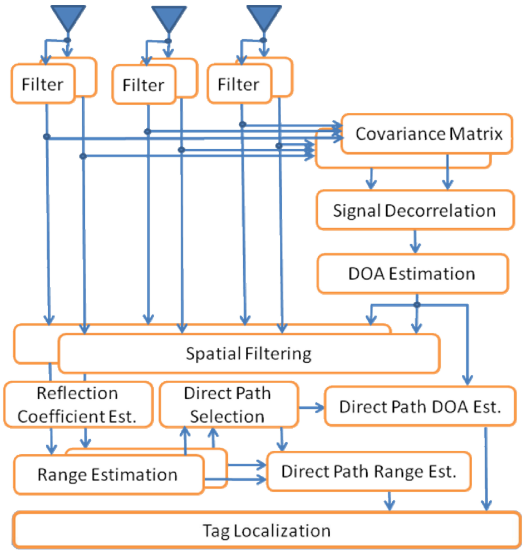

Figure 3.10: Flowchart representation of the proposed system architecture in [81].

the covariance matrix with decorrelation enabled the AoA estimation, while on the other hand, the reflection coefficient estimation that enabled the range estimation for each path. These two processes enable both direct AoA and the direct path estimation for the final localisation. To evaluate the proposed system, the authors formulated a simulation with a three element ULA, and utilised the frequencies of $f_1 = 905$, $f_2 = 914$ and $f_1 = 925$ MHz, with the SNR set to 6 dB. With the true path at -15 degrees and a reflection at 40 degrees, the Mean Square Error (MSE) was 0.066 meters, but when the reflection was moved to 10 degrees, the error increased to 0.14 meters. The authors remarked that as the direct path and reflection came closer, it was harder to distinguish which one was true. Moreover, the authors investigated the estimation accuracy, when the distance of the reflective path changed. They concluded that, as the path increased, the direct path detection became easier (since the reflection amplitude decreases and the phase offset was greater). The proposed system was able to utilise both the MF and the spatial diversity to achieve impressive results. The issue with the proposed paper is that the results are theoretical and they take into consideration only a single reflection, while in real environments more than a single reflections exist.

The majority of the MF research is focused on the co-prime frequencies and the FDA. A recent review in [82] highlights the performance improvement in terms of SNR, range resolution, angle resolution, and improved tracking performance using FDA. The use of ULA phase arrays is based on controlling the phase of each element as seen in Fig. 3.11a, allowing constructive or destructive interference at specific angles. Therefore, beam steering is enabled as the different phased arrays allow different patterns to be generated, however, this also generates side lobes at undesired angles [83]. Beam steering can also provide high gain, allowing the localisation of weak transmission, and also the ability to suppress interference from other directions [84].

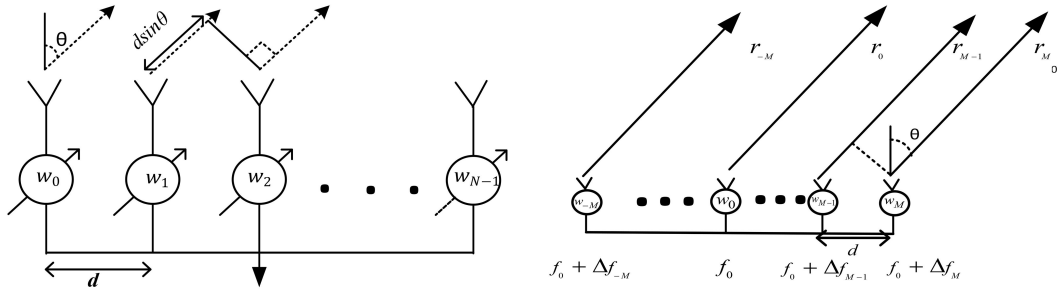

(a) Example of a ULA phased array with N elements as show in [82].

(b) Example of a FDA with N elements as shown in [82].

Figure 3.11: Examples of ULA (3.11a) and FDA (3.11b) with N as shown in [82].

Frequency diversity in radars was first presented in [85], where a single element transmit frequency diverse pulses in sequence. Modern FDAs are different from MIMO radar systems, as they transmit overlapping signals in close spaced frequencies. Meanwhile, MIMO radar utilises orthogonal signals from the different antenna elements received from the multiple paths to stipulate spatial diversity [86]. Furthermore, in some cases MIMO radar utilises waveform diversity also known as collocated MIMO [87], and even OFDM [88]. FDAs have a similar physical structure as the ULAs, with the same element separation but different operational frequency, as seen in Fig. 3.11b. When it comes to localisation, the application difference is that the FDA beam forming provides a global maximum and a number of local maximum with diverse ranges and angles [89]. This enables the detection of multiple targets at the same direction but in different range distances, also known as angular resolution. The angle/phase capabilities have been proven to be dependant on the transceiver number of elements [90]. As with the ULA, a FDA can apply beam forming to reduce interference, and improve the SNR, enabling longer range. One issue that FDAs face is that as the range increases, a range/angle ambiguity is formulated due to the range/angle coupling. A recent paper, [91] addresses this issue and it will be presented next.

More recently, in [92] the authors presented a performance analysis of a sparse ULA that utilises two co-prime frequencies. The use of co-prime frequencies has gained attention in literature after being proposed in [93]. Traditionally, co-prime arrays have different spacing on their elements, depending on the distance of the co-prime frequencies. The benefits are that the received narrow band signal can be decorrelated with fewer receiving elements, increasing the Degrees of Freedom (DOF) of the system. DOF of a system is defined as the number of parameters that may vary independently in the system. In this paper, the authors analysed the performance of a ULA instead of a co-prime array, and presented the effects of the different frequencies on phase. Since the received signals have an unknown phase, the Cramér-Rao bound (CRB) was derived for a conventional sparse ULA. To evaluate the performance of utilising two co-prime frequencies with a ULA, the authors performed a MCS. They considered a ULA with 4 elements, two co-prime frequencies and two sources with equal transmit power and SNR. To estimate the AoA, they

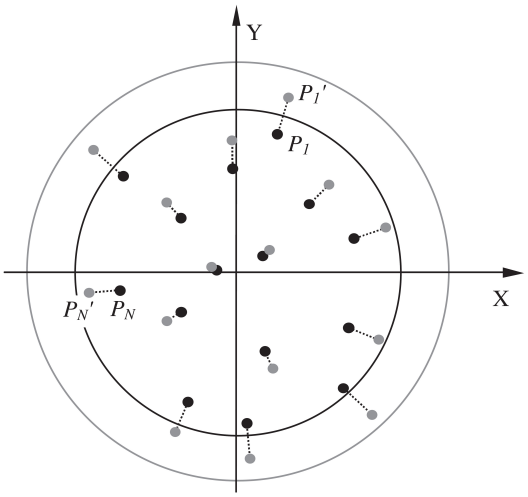

Figure 3.12: Example of a RSVA that is employed in [70], N elements placed in pseudo-random x, y, z locations.

used the group LASSO method presented in [94], which was specifically developed for sparse ULA arrays. Results showed that by using two co-prime frequencies and a ULA, two sources could be resolved as long as they were 2 degrees apart and their phase difference was over 0.7π. Finally, they distribute various number targets between -60 and 60 degrees with 20 dB SNR and 2000 snapshots. Results proved that more targets could be resolved when two signals from co-prime frequencies were present with phase differences. Overall, this papers highlights the multiple benefits of MF with co-prime frequencies, even though the results are a product of simulation and not a real system.

The final paper even though it utilised acoustic frequencies and not RF, Rigelsford and Tennant [70] showed the benefits of MF when it comes to AoA estimation. The authors employed a RSVA to present a method that reduces the sidelobe level, utilising multiple frequencies. The proposed technique combines data that were measured in different discrete frequencies over a wide bandwidth. The final estimation produced a spectral result with the average sidelobe level reduced, depending on the number of discrete frequencies used. This technique was applied to estimate the location of an unknown source, utilising enhanced holographic imaging. Results showed superior image resolution, with the MF decreasing the noise from unwanted directions.

An example of a RSVA used in this paper is shown in Fig. 3.12. RSVA is named as such, because the elements of the array are positioned pseudo-randomly in different locations within a spherical region, in a three dimensional space. The use of RSVA is common in both acoustic systems [95, 95] and communication applications [96–98]. The benefit is that it removes statistical possibility from large lobes, and can provide a full scan in both azimuth and elevation with constant beamwidth and gain. As the number of elements increases, the spherical region increases inversely proportional, but that allows the reduction of the sidelobes in the final estimation. Applying MF to reduce the sidelobes can allow the employment of fewer elements, thus decreasing the overall hardware complex-

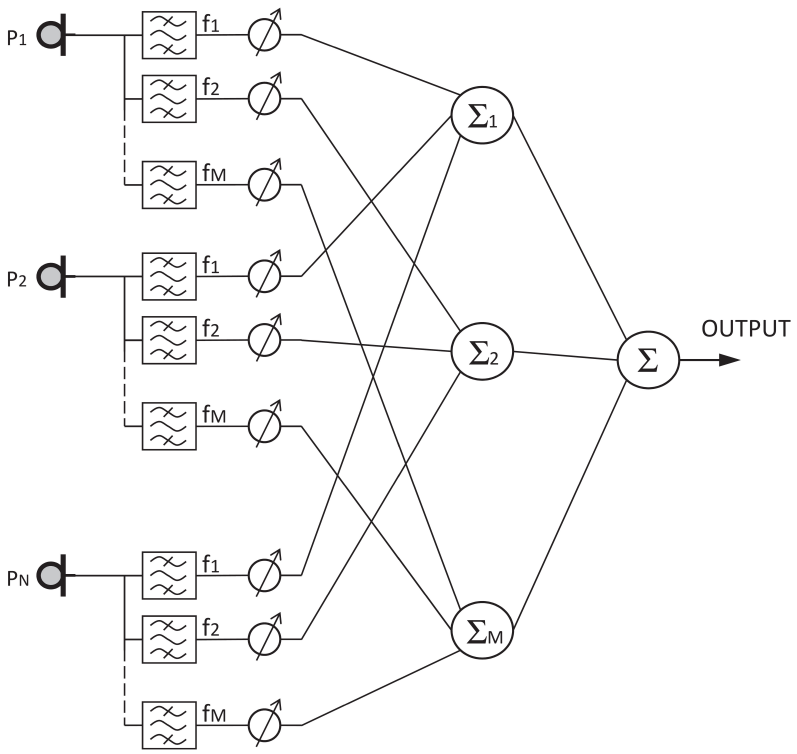

Figure 3.13: Schematic of the system used in [70].

ity. The method introduced is a sub-array beamforming that syntheses multiple patterns. Further signal processing can applied to reduce the sidelobes even further.

A schematic of the employed system is shown in Fig. 3.13, where P_N represents the Nth acoustic element. Every element is connected with a band-pass filter F_1 to F_N, and the phase can be independently changed to steer the main beam direction. For every frequency, the output is combined in the form of narrow band beamformers but then these outputs are further combined, providing an array broadband response. The difference between every frequency measured is large enough for the sidelobe structures of each data to remain uncorrelated, hence it is possible to synthesise a RSVA result by combining the uncorrelated data sets.

To evaluate the performance of the proposed technique, the authors performed measurements using an experimental three dimensional RSVA. The array consisted of N=64 omni directional microphones arranged at a pseudo random location within a 86 cm diameter. The array operated in audio frequencies between 50 Hz and 13 KHz and applied electronic beamforming to provide a directional pattern. Measurements were performed in an anechoic chamber lined with absorbing foam. The sound source was an 8 cm loud speaker driven by a signal generator and audio amplifier. For both experiments, the speaker location was 2.3 meters in front and 0.22 meters below the centre of the RSVA.

Fig. 3.14a depicts the response patterns of the RSVA with m=6 frequencies. It was evident that the MF method reduced the sidelobe level from -18 dB to -26 dB. Also, the

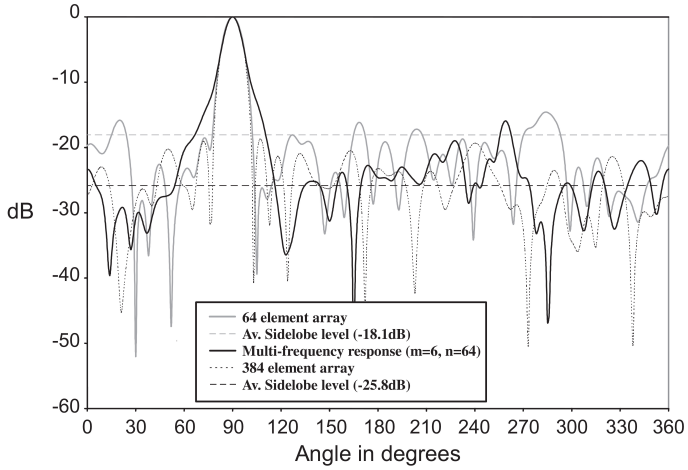

(a) Comparison of spectral performance with a SF and MF ($m = 6$) with the $N = 64$ element RSVA, employed in [70].

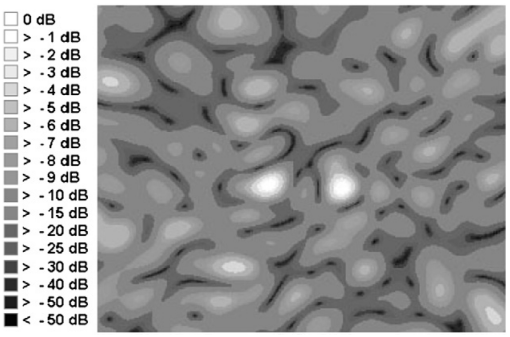

(b) Holographic imaging with SF at 6 KHz with SF [70].

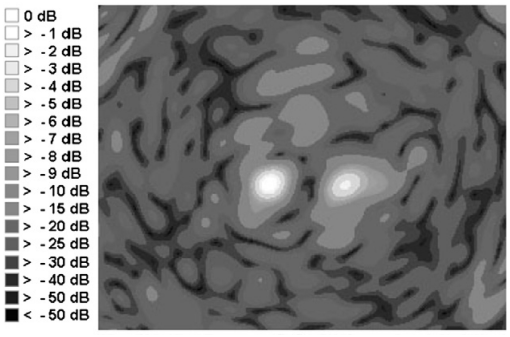

(c) Holographic imaging with MF from 3 KHz to 7 KHz [70].

Figure 3.14: A comparison of two holographic images of two sources, with SF at 3 KHz Fig. 3.14b, and MF starting from 3 kHz to 7 kHz in 500 Hz steps Fig. 3.14c.

theoretical response with 384 element array is given in Fig. 3.14a to show that MF can produce the same results utilising only 6 frequencies and 64 elements. The following result confirms the authors' suggestion that MF can reduce the average sidelobe level by $-10\log(1/M)$ dB. Moreover, Fig. 3.14b shows the holographic imaging of two sound sources at 6 KHz with single frequency, while Fig. 3.14c with multiple frequencies. Both images were taken with the 64 element array, with the MF measured with signals from 3 kHz to 7 kHz in 500 Hz steps. The sidelobes were shown to be reduced by 9.6 dB, which is equivalent that of a 576 (64 by 9) element array. In Fig. 3.14b, the reflections can be distinguished in the holographic imaging with high intensity, while in Fig. 3.14c, the reflections are reduced.

The main concerns with this technique is that it is proven experimentally on acoustic frequencies, not RF, and that bands of different frequencies are tightly spaced. On the contrary, this paper proves that MF can be extremely beneficial to AoA estimation in acoustic frequencies. It also serves as a great example for the benefits of RSVA, providing 360 degree of detection in both azimuth and elevation. The authors prove with measurements,

that the application of MF can reduce the average sidelobe level by $-10\log(1/M)$ dB. The real advantage of MF is that it does not require additional hardware complexity or complicated software to improve the overall performance. Furthermore, this technique can be applied with additional signal processing techniques to further suppress the sidelobes, with the cost of angular resolution degradation. The proposed technique is ideal for noisy or rich acoustic multipath environments. Finally, this paper is presented in Subsection 3.5 where the results are compared with other localisation techniques or systems.

3.4 Techniques or systems that utilise multiple metrics

This Section serves as the literature review of this research in systems or techniques that utilise multiple metrics for localisation. The first Subsection 3.4.1 presents novel techniques and highlights the work of Scherhäufl *et al.* [99] for the smart fusion of RSS and AoA. Moreover, Subsection 3.4.2 presents novel systems and it highlights the best performing system, SpotFi [19] which utilises the AoA, ToF and RSS metrics. Both papers [19, 99] are featured in the comparison at the end of this Chapter, but also the results of SpotFi [19] are used to directly compare the results of this research in Chapter 7.

3.4.1 Novel techniques that utilise multiple metrics

In [100] the authros present a selective hybrid weighting algorithm to localise a transmitter in a NLOS case scenario utilising both AoA and RSS metrics. This paper and its improved version [101], introduced a simple concept of fusing different metrics and localise transmitter over long range of 350 m. In the first step of the algorithm, the effect of the NLOS in RSS was corrected. The three APs that encircle the transmitting node were selected, by being the ones that measure the highest RSS. Then, the RSS was adjusted using weights to mitigate the NLOS effect and to approximate the expected LOS RSS. At the second step, using the weighted RSS the interception point between AP one and two was estimated, and then the interception point between AP one and three was estimated. Assuming an AoA deviation the final estimation could be then performed. If both interception points were within the limit of that assumed AoA deviation, an average of the two points was assumed to be the location of the transmitter. If they were not, then the process was restarted and the weight factors of the RSS were updated. The same authors in [101] improved the algorithm by estimating the interception points between all APs. If the average of all locations were within the weighted RSS and AoA, then this was the estimated location. If not, then the process was restarted and the weight factors of the RSS were updated. To demonstrate the performance of the proposed algorithm, a MCS was presented, with 1000 trials. The pathloss exponent was set to 2, the AoA variance was set to 10 degrees, and the variance of the AWGN was set to 3 dB. The presented mean distance error of the proposed selective hybrid weighting algorithm was 52 meters, while without weighting the mean error was circa 95 meters. This paper proposed a low complexity algorithm to improve the estimation error over long ranges, such as cellular

communications. Unfortunately, the evaluation that the authors perform was theoretical and not with measurements. This approach would be interesting to be tested in real environments under real NLOS conditions.

Tomic *et al* introduced two low complexity techniques to merge RSS and AoA in [102, 103]. In [102] the authors presented an algorithm that requires multiple receivers to localise a transmitter with unknown power. The benefits is that it does not require a Central Processor Unit (CPU), the processing can be done locally by each receiver, and the initialisation is computation free. The location estimation was performed by formulating a non-convex ML estimator. Moreover, the use of anchor nodes was required, as the ML required signals from known locations. That allowed the estimator to resolve information such as pathloss and AoA. To solve the non-convex problem, the authors transformed it in to a second order cone programming problem [104]. To evaluate the performance of the simplified algorithm, the authors performed a MCS with 50 K runs, 20 anchor nodes, 15 target nodes, and a pathloss exponent of 3. Results showed a RMS error of 2 m with 5 dB SNR, while for the same scenario an algorithm that utilised only the RSS metric a RMS error of 4.7 m.

Moreover, the same authors in [103] presented an improved version of [102]. They proposed the use of weights based on the total RSS. For example, the received signal that had higher power would have the highest weight. By weighting all the signals in the estimator, the signal with the higher SNR score was prioritised. Furthermore, the authors now apply a weighted Least Square (LS) estimator, which they proved that was less computationally complex. Similarly to the previous paper, the authors performed a MCS with 50 k runs, 4 anchor nodes, one target node, and a pathloss exponent of 2.5. Results showed a RMS error of 2.2 m with 5 dB SNR, a slight increase of 0.2 m than [102]. The reason was that the weighted LS is less complex estimator than the ML, which is computationally demanding. Overall, both papers show that the utilisation of RSS and AoA metrics can achieve good localisation results with low complexity. The major concern regarding this two papers is that they have not been tested in real environments. Therefore, it is uncertain to know if they perform similarly in a practical application.

Scherhäufl *et al.* in [99] presented an algorithm that locates a RFID tag utilising both RSS and AoA metrics for the back scattered signals. The same authors have presented similar work in the past utilising only the AoA metric [61, 62], and formulating a SAR [68]. The system used K transceiver front-ends. The transponders communicated through back scatter modulation where the refection coefficient of the RFID tag switches between two stages according to the transmitted data. When one of the K transceivers transmitted, the remaining $K-1$ front-ends received the back scattered signal forming a MIMO system with 1 transmitter, $K-1$ receivers. The AoA and RSS of the back scattered signal depended on the tag location, and the combination of both metrics improved the accuracy and the robustness of the localisation. The proposed technique processed each metric differently and combines them with a joint likelihood function.

The AoA of each transmission depended on the length and direction of the propagating path; from the transmitter, to the RFID tag and to the receiver. For the first metric, the

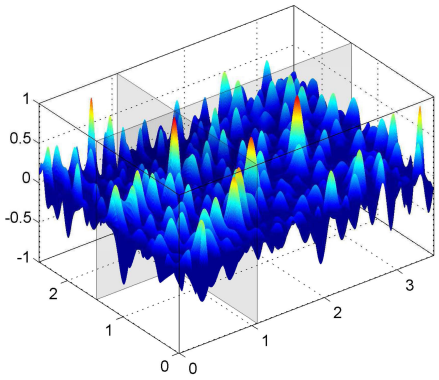

(a) AoA utility function example used for localisation of a passive RFID tag using the AoA metric, as shown in [99].

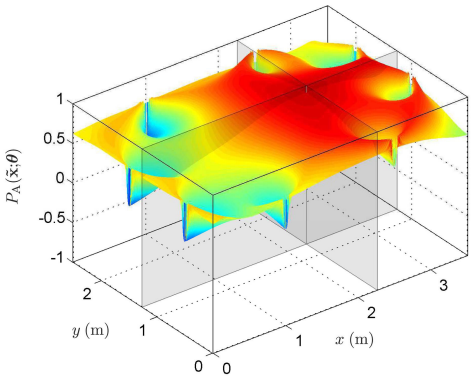

(b) RSS utility function example used for localisation of a passive RFID tag using the RSS metric, as shown in [99].

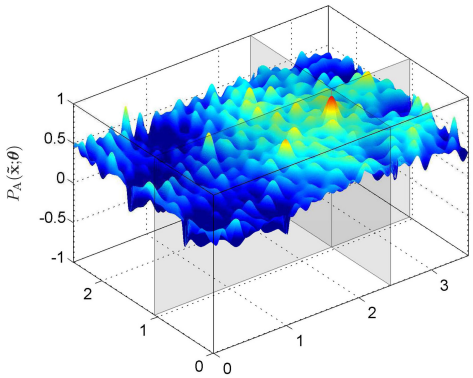

(c) AoA and RSS utility function example used for localisation of a passive RFID tag using both AoA and RSS metrics, as shown in [99].

Figure 3.15: Examples of localisation using single metrics Fig. 3.15a and Fig.3.15b the improvement with multiple metrics Fig. 3.15c, as reported in [99].

authors formulated a grid and applied MLE using the phase information of the received signal. That enabled the formulation of the utility function $\mathbf{P}_\phi$ [99]. This utility function is practically the likelihood of the transmitter to be in the exact position of the designed grid, with two unknowns, the signal $\tilde{x}$ and an AoA θ [99]. The AoA utility function $\mathbf{P}_\phi$ by it self creates multiple peaks in the grid and even if they are distinguishable there is an uncertainty on which location contains the correct phase information.

The RSS localisation estimation was performed in a similar fashion. This time, the authors formulated a utility function $\mathbf{P}_A$ using the RSS [99]. The utility function is once more applied on the same grid by applying the MLE, searching for the most probable signal $\tilde{x}$ with an AoA θ [99]. The process of finding the maximum value of the utility function solely by the RSS is inaccurate due to the flat curve progression.

The merging of both utility functions RSS $\mathbf{P}_A$ and AoA $\mathbf{P}_\phi$ was done by a multiplication of both utility functions, such as, $\mathbf{P} = \mathbf{P}_\phi \mathbf{P}_A$, formulating a combined MLE. Again, following a grid search approach the algorithm searches for the possible signal $\tilde{x}$ and AoA

θ in each grid position. The result is an improvement compared to single metrics, due to the fact that the RSS is able to eliminate peaks formed by the AoA utility function due to phase uncertainty.

The authors presented theoretical results with a MCS and real measurements as well. For sake of space, only the experimental results are presented for AoA and RSS combination only. The environment used for measurements was an indoor office and $K = 8$ transceiver front-ends were employed. The linearly polarised antennas were distributed at a height of 1.6 m above floor, two on each side of the room, forming a 3.5 meters by 2.5 meters grid; the RFID tag was an Electronic Product Code (EPC) global Class-1 Gen-2/International Standards Association (ISO) 18000-6C compliant. The authors moved the tag into 645 positions located inside the defined grid. Such scenario is unrealistic for a practical system, but it would be interesting case if the transceivers where placed at the outer walls of a house instead. The purpose of their paper was the localisation of a single tag in a close space, thus, the performance of their technique for localisation in general indoor and outdoor environments is unknown. The RFID tag was configured to backscatter at 866.9 MHz with a signal level of 2 watts of radiated power. The 2 watts of radiated power is very high compared to other systems that operate in dBm and its also the maximum power allowed for RFID. One time phase calibration was required to remove the phase uncertainty by performing 10 measurements in known positions.

Fig. 3.16 presents the results for the absolute error. In Fig. 3.16a AoA metric results, the absolute error was less than 0.05 m for 92.6% of the measurements, while for the majority of the observations the absolute error was less than 0.02 m; In Fig. 3.16b RSS metric results, the estimation performance was overall inaccurate with the majority of the observations having over 0.3 m absolute error. Finally, in Fig. 3.16c both metrics, the results were even better than the single AoA metric. Specifically, only one estimation out of 645 had an absolute error of 0.4 m and, overall, the majority of estimations showed an error below 0.04 m.

As mentioned before, the work performed by the authors could be potentially applied on a larger scale enabling localisation of a wearable RFID tag. Even though the authors performed measurements, the environment is close to ideal and they employ multiple antennas in a very close space. Also the transmit power of 2 watts would be unrealistic for a practical system, therefore the performance of such system is unknown when the SNR was reduced. On the contrary, this paper presents a low complexity algorithm that performs an accurate RFID tag localisation, merging both AoA and RSS metrics. The visual results in Fig. 3.15 are insightful on the impact that each metric has on localisation. It would be interesting to see this technique applied in the future, in real indoor and outdoor scenarios, and investigate if the effect of merging the two metrics would be the same. Finally, this paper is presented in Subsection 3.5 where the results are compared with other localisation techniques or systems.

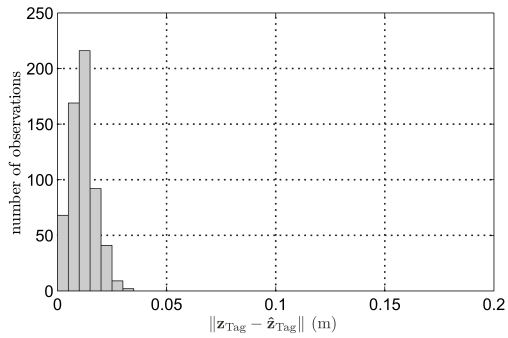

(a) Utility function example used for localisation of a passive RFID tag using the AoA metric, as shown in [99].

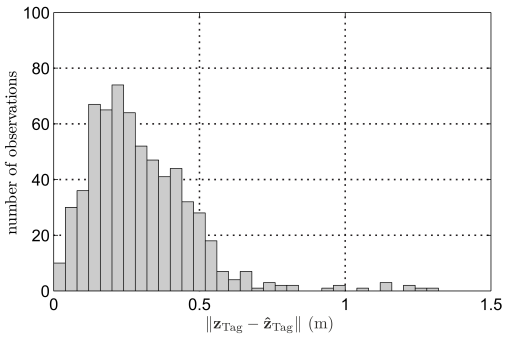

(b) Utility function example used for localisation of a passive RFID tag using the RSS metric, as shown in [99].

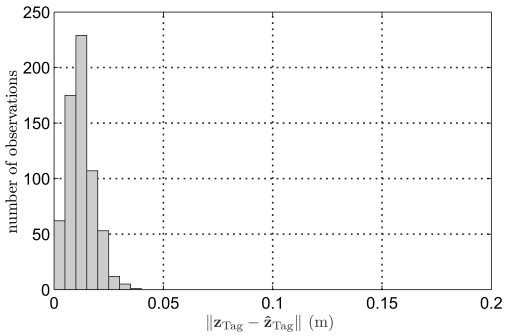

(c) Utility function example used for localisation of a passive RFID tag using both AoA and RSS metrics, as shown in [99].

Figure 3.16: Examples of localisation using single metrics Fig. 3.15a and Fig.3.15b the improvement with multiple metrics Fig. 3.15c, as reported in [99].

3.4.2 Novel systems that utilise multiple metrics

The system CUPID was the first that fused MF, RSS, and AoA [32]. Also, CUPID has been one of the first systems that utilise the WiFi OFDM signal to acquire multiple RSS, and AoA metrics. The main application of this system is indoor navigation with a mobile phone or tablet, with multiple WiFi APs utilising the CSI metric. The process of the CUPID algorithm is presented in Fig. 3.17. The CSI metric was used to produce a distance estimation and an angle estimation. The pathloss exponent was estimated from the CSI and the distance was estimated using the received power from the primary path. Concurrently, the AoA was estimated through MUSIC. If the angle estimation is the same as with previous measurements then this angle is the direct AoA. If not, then the angle from the MUSIC spectra that was close to the previous measurement is selected as direct AoA. This approach is used to stop a reflective AoA that might appear stronger than the true direct AoA. Since the movement of the user is limited indoors, big jumps in the direct AoA are possible only if the transmitter is really close to the receiver which is detectable from the RSS measurements. The final estimation of the transmitter location was performed by taking into consideration the location of the AP, the distance estimation and the AoA es-

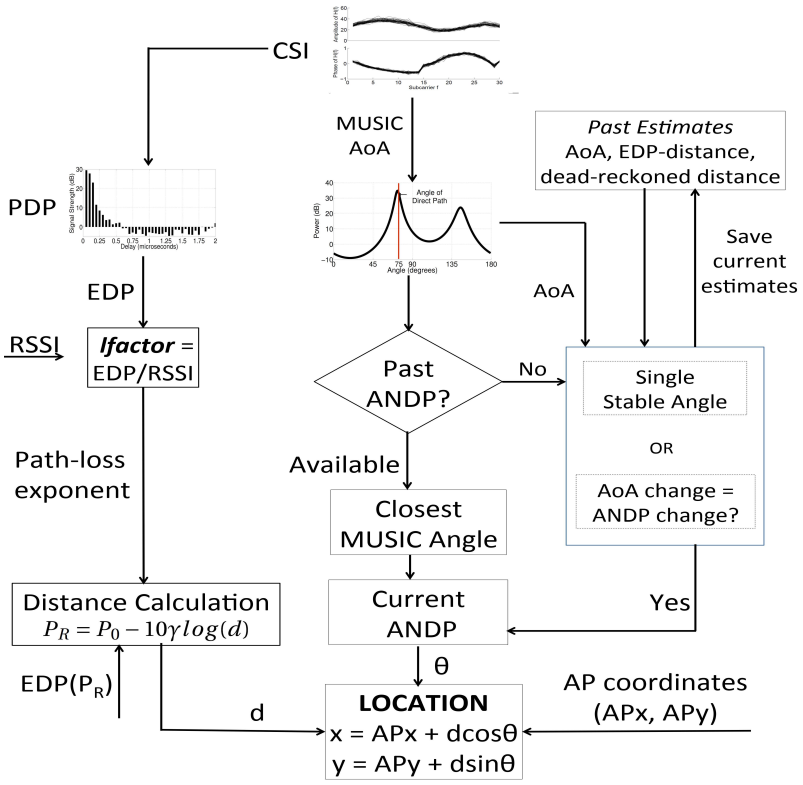

Figure 3.17: CUPID system architecture [32].

timation. To test the performance of CUPID, the authors performed measurements in an indoor environment with a total size of 76 by 60 meters, and five APs placed randomly in the area. Empirical CDF showed a mean error of circa 4 m, while for 75% of the measurements circa 6 m error. Moreover, an empirical CDF for direct AoA estimation error was presented, which is compared with the findings of this research in Subsection 7.6. Overall, the results of CUPID show that the utilisation of multiple metrics can utilised to formulate a simple yet accurate system. It would be extremely interesting to see if the estimation could be improved if the OFDM signal was used differently instead of collecting multiple metrics.

Furthermore, SpotFi [19] is the only WiFi based system that claims to deliver decimetre level of localisation under certain indoor environment. It utilises CSI information, already existing from the WiFi chips, and it does not require any modifications to the hardware or firmware of existing routers. As with DeepFi [8], the authors used an Intel IWL5300 [105] equipped with three antennas formulating a ULA receiver, and utilise exclusively the CSI to derive all the metrics. Using each sub-carrier from each antenna allowed the system to combine the CSI data in order to form a virtual array, and then perform the final localisation estimation.

The authors claimed that the multipath affects the CSI values across the sub-carriers due to ToF. By ToF, the authors mean the time it takes for the signal to reach the AP from the source. By utilising the CSI, they were able to attain the AoA and ToF for

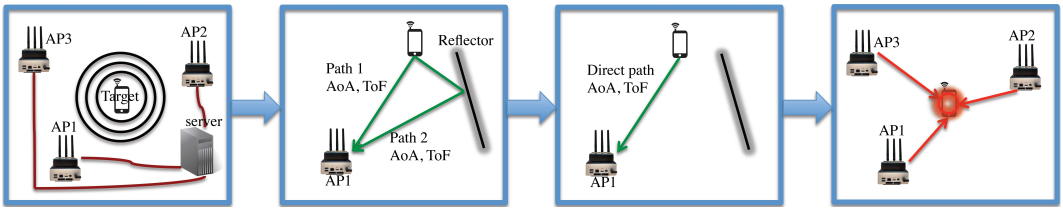

Figure 3.18: SpotFi system procedure: APs that can hear the target collect CSI and upload into the server. 1) Calculate AoA and ToF. 2) Resolve the propagation paths from the target to each individual AP. 3) Decide the direct path between the target and each AP. 4) The location of the target is estimated using the RSS and direct AoA information from all the APs [19].

each received path. The ToF measurements were not considered to be universal for all APs since there was no synchronisation between all the APs; thus, this was a metric concerning each individual AP. The system employed MUSIC to estimate the incoming AoA but in order to do so, the CSI values need to be reshaped. IWL5300 produces 30 CSI values, 3 for each antenna and 10 for each sub-carrier and since the sub-carriers were closely spaced, the phase change due to frequency displacement was considered very small. Thus, each one of the sub-carriers can be used to create a super-resolution AoA estimation forming a virtual array. Since the system was able to measure the small phase shift between the two sub-carriers, the algorithm could find the ToF difference between those two sub-carriers. By utilising antennas and sub-carriers, each propagation in a multipath environment introduced a different phase shift at each antenna and sub-carrier, which was measured and utilised by SpotFi. An overview of the SpotFi system procedure can be seen in Fig. 3.18.

An experimental evaluation was performed using an off the shelf Intel's 5300 WiFi NICs connected into a laptop for each one of the AP. The authors used 802.11a WiFi operated at 5 GHz that provided CSI values for 30 sub-carriers, although data were sent to 116 sub-carriers, due to firmware limitations. The use of 5 GHz was beneficial due to the high frequency and high bandwidth but the problem was the transmission distance. They deployed SpotFi in different locations inside the building, a high NLOS environment with 6 APs and a corridors environment with 14 APs. The overall number of APs was unrealistic, thus SpotFi could not be applied with the same results, unless the number of APs in a room was increased. They compared their results with ArrayTrack [7] with three antennas as it was the only known system that does not require hardware modifications to the WiFi infrastructure and it could operate only with 3 antennas. The source transmitted 500 packets with 100ms interval and the nearby APs recorded the CSI and the MAC address. The same data measured were used for the ArrayTrack and SpotFi.

The results at Fig. 3.19 shows the comparison between SpotFi [19] and ArrayTrack [7] with three antennas. In Fig. 3.19a, the indoor office environment, SpotFi's median localisation error was at 0.4 meters compared to 1.8 meters of the ArrayTrack. For the 80% of the measurements SpotFi achieved 1.8 meters error, ArrayTrack achieved an error of 4 meters. It is obvious that SpotFi outperforms ArrayTrack since the latter mainly

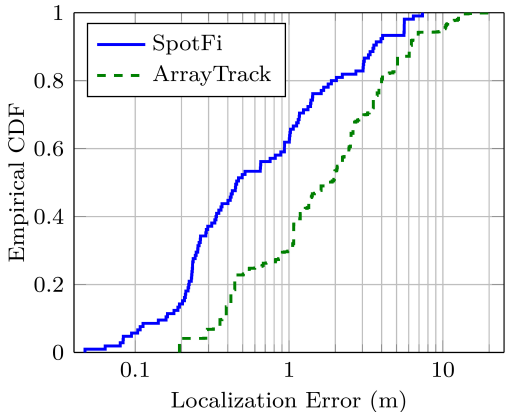

(a) SpotFi empirical CDF compared to ArrayTrack in an indoor office deployment [19].

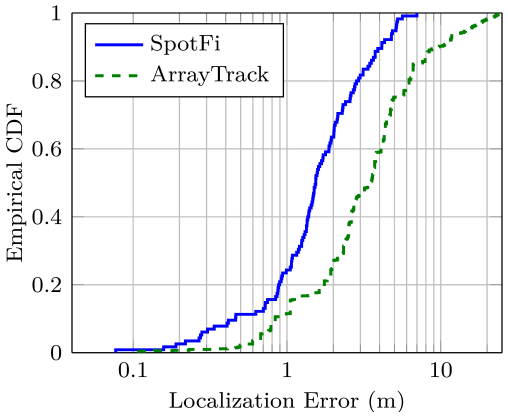

(b) SpotFi empirical CDF compared to ArrayTrack in an high NLOS deployment [19].

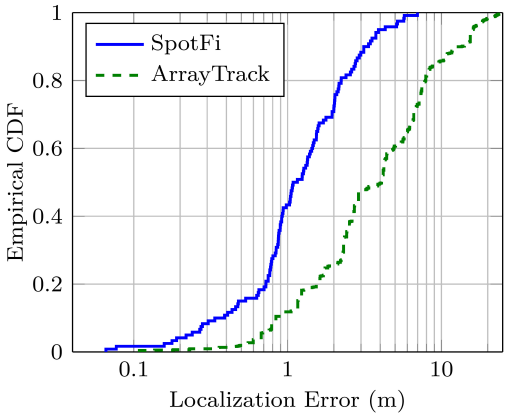

(c) SpotFi empirical CDF compared to ArrayTrack in an corridor deployment [19].

Figure 3.19: Plots of empirical CDF of SpotFi localisation error with different scenarios, in an office employment, Fig. 3.19a, high NLOS deployment Fig. 3.19b, and a corridor deployment Fig. 3.19c, as reported in [19].

used a higher number of antennas in order to perform localisation. Thus, a combination of RSS and AoA can improve the overall result with the use of less antennas. Previous authors, normally did not perform a stress test for their systems, but the authors in this paper performed measurements for a high NLOS environment in Fig. 3.19b. The same localisation experiment was performed; the median accuracy of the SpotFi was at 1.6 m while for ArrayTrack was at 3.5 m. It is obvious that the overall performance of both systems degrades but SpotFi was still able to outperform ArrayTrack when three antennas are considered. In high NLOS deployment, finding the direct path can be extremely difficult, but SpotFi was able to perform localisation with a good result. Moreover, the corridor measurements shown in Fig. 3.19c were the most challenging due to the fact that APs were not be densely deployed, but also they were not located at advantageous points. Performing the same experimental process, the median localisation error for SpotFi was around 1 m, while ArrayTrack was degraded to 4 m. This result proves that SpotFi is able

to resolve the multipath effect more accurately than ArrayTrack and providing a higher likelihood to the direct path.

Overall, SpotFi proves that the combination of RSS and AoA can improve the localisation accuracy with the same number of antennas. This proves that the utilisation of multiple metrics is as important as spatial diversity. On the contrary, SpotFi makes an unrealistic use on the number of APs in an area. For the NLOS case the authors employ 6 APs, while for the corridor case 14 APs. In real environment, employing such large number of APs in unrealistic, as it increases the overall cost and computational complexity, merging metrics from multiple APs. Finally, SpotFi shows that utilisation of metrics is the correct approach to improve localisation accuracy. Therefore, it is presented in Section 3.5 where the results are compared with other localisation techniques or systems. Also the results of SpotFi [31] are compared with the contribution of this research in Section 7.6.

3.5 Comparison and conclusions

The purpose of this Section is to summarise the theoretical or experimental systems presented previously in this chapter and provide a solid statement for the hypothesis that comes next. Table 3.3 presents the previously highlighted papers, to allow easy evaluation and comparison. The comparison is performed by comparing the overall number of metrics used, their accuracy, the environment, area covered, number of APs and the antennas employed. It is impossible to find one optimal solution for each situation but this will help to reason with the choices before proceeding with a novel research.

In [8], the authors delivers a very good result at 93 cm with a single AP. The platform they used is commercially available since it requires a laptop and an IWL53000 WiFi board. The main concern with this technique is that it requires a very large set of pre-training, high power and an overall high application cost. The problem with such situations is that each environment requires 50 measurements in a room, in specific pre-determined positions. These measurements must be very accurate as a small deviation might result in a high error. Furthermore, when applying this algorithm in a new environment, a set of new measurements must be taken. Applications such as DeepFi are effective but unrealistic in a real world environment; for example, in a large house with multiple rooms, the training requires time and trained manpower to achieve a reliable measurement accuracy. Also, if any changes occur in the environment, such as change in the position of a couch or a painting, the channel conditions change and re-training is required.

Furthermore, [58] offers very good theoretical and practical low complexity AoA results but only in an ideal environment. The rooftop environment offers few to no reflections and the LOS gives a dominant direct path. The main reason this paper is cited is that it provided information about a reduced complexity AoA and the alternative ways to apply the subspace algorithms MUSIC and ESPRIT. The findings of this paper could be utilised to reduce the complexity of the SVD used primarily for MUSIC. ArrayTrack [7], is the first WiFi based system that has the best performance using the AoA metric. It offers 31 cm of accuracy in an indoor environment with 8 antennas and 6 APs. The exceptional

Table 3.3: Comparison of localisation systems and techniques

Reference	Evaluation type	Metrics	Accuracy (Mean)	Environment Measure Zone	APs	Antennas	Notes
DeepFi, [8]	Application WiFi	RSSI	94 cm	Living Room 4 m x 7 m	1	3	Exceptional results, requires exhaustive training.
Tayem, [58]	Application NI-PXI	AoA	$\pm 0.35^{\circ}$	Rooftop LOS N/A	1	4	Ideal environment, reduce complexity.
ArrayTrack, [7]	Application WiFi	AoA	31 cm	Indoor office N/A	6	8	Exceptional results, unrealistic hardware.
J. Rigelsford, A. Tennant, [70]	Experimental Acoustic	AoA & MF	N/A	Anechoic Chamber	1	64	Good result, anechoic chamber but MF proves improvement
Maddio *et al.* [46]	Application SBA WiFi	RSS & MF	2.4°	Anechoic Chamber	1	8	Good result, anechoic chamber, proves that MF improves accuracy.
Scherhäufl, *et al*, [99]	Application RFID	RSS & AoA	2 cm	Indoor office 3.5 m x 2.5 m	8	1	Unrealistic environment, good algorithmic fusion
SpotFi, [19]	Application WiFi	RSS & AoA with ToF using OFDM	40 cm	Indoor office 10 m x 16 m	6	3	Good result and algorithm. Requires plenty AP's.

accuracy is native to the spatial diversity. The practical issues with ArrayTrack are two. First, there are very few WiFi APs that employ 8 antennas and they have a very high cost. Second, the system takes into consideration the case of 6 APs in an indoor office, which is unrealistic. The overall results of this paper are still exceptional as they reduce the number of antennas into a reasonable level, compared with SpotFi [19].

In regards to MF, in [70] the authors propose the use of multiple frequencies to reduce the sidelobe level. Results prove that a significant reduction of sidelobes is achieved, equal to as if the antenna array size is increased. Unfortunately, the test case of an anechoic chamber, and the use of acoustic frequencies creates uncertainty whether the same happens at RF frequencies in real indoor or outdoor environments. Therefore, it is hard to directly compare this paper with the rest of the papers, but it does proves that closely spaced frequencies can indeed increase the overall system accuracy. Moreover, in [46] the authors continue their research in SBA nodes for indoor localisation. They investigate the use of the RSS metric from both frequencies associated with WiFi, 2.45 and 5.2 GHz. Their findings prove that MF can greatly improve not only the mean localisation accuracy, but also greatly increase the 90% accuracy. Specifically, the mean accuracy achieved with the dual-band SBA is 2.4 degrees, 2 degrees improvement from single frequency, and for the 90% of the measurements, 5.4 degrees, 4 degrees improvement compared to single frequency. Even though the measurements were performed in an anechoic chamber, the benefits of MF are proven once again and highlighted even more for difficult cases. Unfortunately, the system is not tested in NLOS cases, therefore it is unknown what the performance is in real environments.

Finally, for systems that utilise multiple metrics, in [99] the authors employ a system that localises RFID tags, utilising both RSS and AoA. Specifically, by comparing the use of multiple metrics (RSS and AoA) they achieved an accuracy of 2 cm. The result might seem very accurate, but it is under ideal circumstances. Even though the measurements are done in an indoor environment, they employ a high number of APs in a small grid. Also, ten reference measurements are required to achieve these results. Compared to DeepFi,

ten reference measurements is not a big number, but it still makes the deployment of the system more costly in regards to man-power. The reason that this paper is highlighted is the way that the authors combine the RSS and AoA metrics. SpotFi [19], is another WiFi localisation system that uses off the shelf equipment, hardware and commercially available firmware. It forms a super resolution algorithm utilising the multiple sub-carriers that exist in the OFDM. Furthermore, SpotiFi has the best performance compared to all the other systems with a 40 cm accuracy. The downside of SpotFi is that it needs the unrealistic number of 6 APs in a 10 meters by 16 meters indoor office to achieve this result.

Overall, the literature review shows that the best results are achieved by combining different techniques. The spatial diversity is definitely a key factor, as ArrayTrack [7] proves, but the overall system diversity such as SpotFi [19] can reduce the unrealistic number of antennas. As shown in [99], as well as in [19], the fusion of both RSS and AoA outperforms each one individually. Everything points into that utilising the available information, thus, formulating a system that is able to extract the maximum information from the measured data. The extra information can be gathered from multiple antennas, diverse AP information synthesis or multiple frequencies. To the best of my knowledge the MF AoA approach, has not been studied with a great extent. Since different frequencies provide a different set of results for both RSS and AoA, the system information is increased even further than prior systems. That leaves room for algorithmic development, hardware implementations and tests to develop a competing state of the art system.

Chapter 4

Novel antenna array design, simulation, and measurements

This Chapter provides information regarding the novel antenna design and its performance as a ULA. Section 4.1 introduces the prototype tri-band antenna design with measurement of the return loss and simulation of the radiation pattern. Then Section 4.2 presents a performance evaluation of the antenna as a ULA receiver with measurements of the return loss, the mutual coupling, and simulation of the radiation patterns.

4.1 Antenna design and performance evaluation

This Section provides information related to the novel tr-band antenna design, measurements and simulations. The first Subsection 4.1.1, is dedicated to the tri-band PCB antenna design, while Subsection 4.1.2 presents the measurements and simulation of the antenna return loss. Third and final Subsection 4.1.3, depicts the results of the simulated far field patterns of the antenna.

4.1.1 Novel tri-band PCB antenna design

As part of a system design, the design of a tri-band antenna was required. There are different types of antennas in the modern literature: dipoles, monopoles, loops, patches, with each one having benefits and negatives [106, 107]. But designing an antenna that is operable in three different frequency bands, with good performance in each frequency, is a new research topic on its own, which is discussed further in Subsection 8.2.1.

Before designing a tri-band Printed Circuit Board (PCB) dipole there was a major issue that needed to be addressed. The lower frequency $f_1 = 434$ MHz results to a high length dipole, $l_d = \lambda_{f_1}/2 = 0.345$ meters; resulting to a PCB that it would have been too long. Therefore, to decrease the overall length of the PCB the track of the lowest frequency was meandered. In the antenna design, the placement of a meander is important because it can have a negative effect on the return loss or the radiation patterns. Hence, different

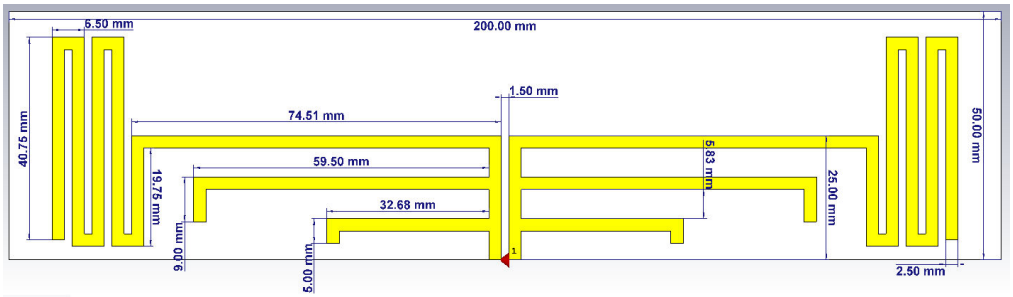

(a) Designed tri-band PCB antenna.

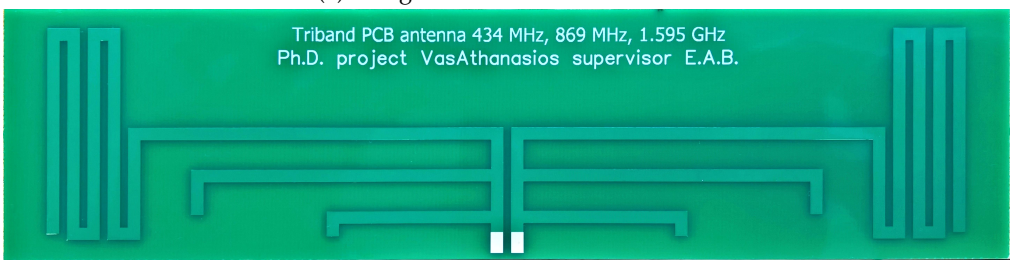

(b) Manufactured tri-band PCB antenna.

Figure 4.1: Designed and manufactured tri-band PCB antenna for frequencies $f_1 = 434$, $f_2 = 869$, $f_3 = 1595$ MHz.

locations were simulated before selecting the optimal placement that has the minimum effect.

The designed PCB antenna is presented in Fig. 4.1. The PCB that the antenna was designed has a thickness of 0.8 mm; the substrate is FR-4 with permittivity $\epsilon = 4.3$, and the copper thickness is 0.035 mm. The dimensions of the PCB are 200 mm by 50 mm, with the two dipoles placed in the middle of the long side; the gap between them is 1.5 mm and the track of the PCB is 2.5 mm. The top arm is the longest, serving f_1 with the highest point in the middle of the PCB, at 25 cm. The arm extends for 74.51 mm and meanders two times, for an overall length of circa 283 mm. The second arm, serving f_2, starts in the middle, extends for 59.5 mm and bends for 9 mm. Finally, the third arm, serving f_3, starts closer to the feed position, extends for 32.68 mm and then bends for 5 mm. The length of the arms for each frequency is tuned to obtain a simulated return loss of $S_{11} \leq -10$ for each corresponding frequency. The simulated PCB antenna can be seen in Fig. 4.1a, while the actual manufactured tri-band PCB antenna can be seen in Fig. 4.1b.

4.1.2 Measured return loss

The return loss, also known as S-parameter, describes the input and output relationship between two ports (S_{12}), or between one single connection (S_{11}). S_{11} represents the reflected power that occurs when it is transferred to the antenna due to impedance missmatch. In practice, the return loss is the reflection coefficient squared [106]. The reason that the reflection coefficient is squared, is because it deals with complex impedances.

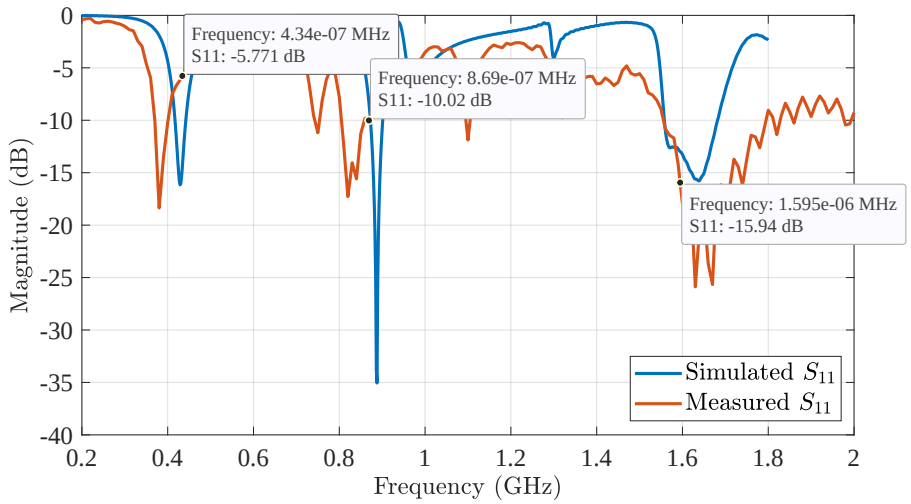

Figure 4.2: Simulated and measured return loss S_{11} for the tri-band PCB dipole antenna.

Therefore, the reflection coefficient is defined as [106],

$$|\Gamma| = \left| \frac{Z_l - Z_s}{Z_l + Z_s} \right| \tag{4.1}$$

where, Z_s is the impedance of the source, and Z_l is the impedance of the load. Therefore, the return loss S_{11} is described in dB by [106],

$$S_{11} = -20 \log |\Gamma|, \tag{4.2}$$

while the overall loss between impedance miss-match is given by [106],

$$P^{\mathrm{ML}} = -10 \log \left(1 - \Gamma^2\right). \tag{4.3}$$

To minimise power loss, it is evident that Γ should be close to zero. Hence, for efficiency purposes it is required to have a very low S_{11} at the targeted frequencies, ideally $S_{11} \leq -10$ dB, which translate to a miss-match loss of 0.5 dB or less.

Fig. 4.2 presents the simulated and measured return loss S_{11} of the PCB antenna at all three frequencies. The first thing noticed, is the overall shift of large return loss nulls, due to the effect of the substrate [107]. The return loss for f_1 is -5.7 dB, for f_2 is -10 dB, and for f_3 is -15.9 dB. It was evident that two out of three frequencies still have a return loss less than -10 dB. Using (4.3), we can see that the missmatch loss for f_1 is $P^{\mathrm{ML}}_{f_1}$1.3 dB, while for f_2 is $P^{\mathrm{ML}}_{f_2}$0.5 dB, and for f_3 is $P^{\mathrm{ML}}_{f_3} = 0.1$ dB.

In this point of the research, changes on the length of the f_1 arm could be performed to achieve a better match, but the $P^{\mathrm{ML}}_{f_1}$1.3 dB loss was judged to be sufficient for the scope of this research. Therefore, the PCB dipole design was not altered and was used for the receiving ULA, which is presented in following Section.

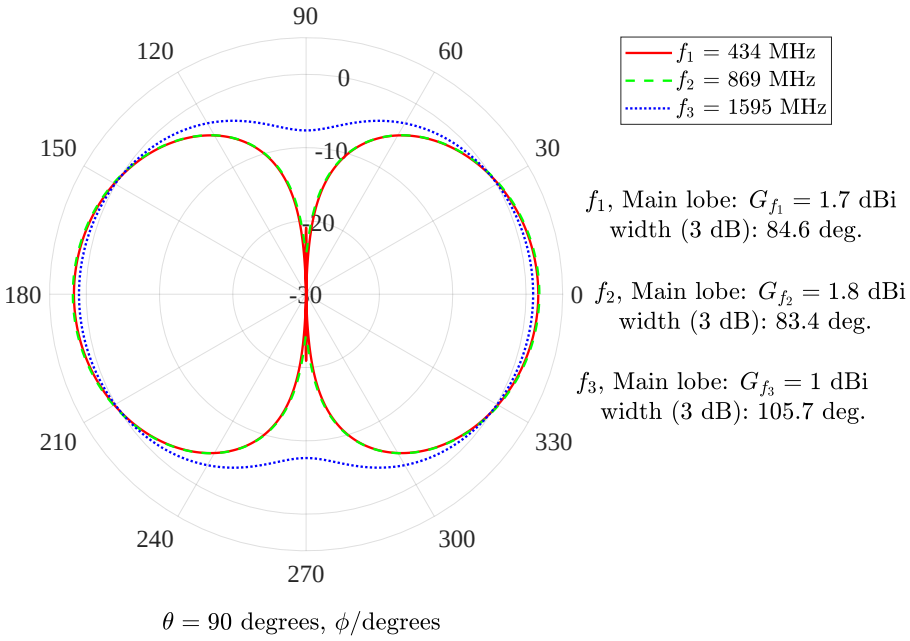

Figure 4.3: Simulated far field gain patterns of the PCB dipole of f_1, f_2, f_3, for azimuth $\theta = 90$ degrees, and variable elevation φ 0 to 360 degrees.

4.1.3 Simulated far field patterns

Next, the simulated far field radiation patterns of the simulated antenna are investigated. The far field region of the antenna comes after the near field radiation [107]. In the far field region, the electromagnetic field are dominated by the E and H radiating field. E and H field are orthogonal to the direction of propagation and to each other. The far field region is used to transfer signals at large distances, and the radiation pattern presents the antennas' overall directivity and gain at specific angle.

Fig. 4.3 presents the simulated radiation patterns in CST, with the corresponding gains, and the 3 dB main lobe width, for the three frequencies at an azimuth angle $\theta = 90$ degrees, and variable elevation φ. In these results, a difference for f_3 in both gain and width compared with f_1 and f_3 was evident. Specifically, the gain for f_1 and f_2 was 1.7 dBi and 1.8 dBi respectively, while the 3 dB width was 84.6 and 83.4 degrees, obtaining a similar performance with the first designed dipole. In regards to f_3, the gain was reduced to 1 dBi but the -3 dB width was increased to 105.7 degrees. The transition from wire to PCB seems to have the biggest effect on the highest frequency f_3; the gain reduction of 0.7 dBi was characterised insignificant, and the overall width was increased by 28.4 degrees, which was convenient for the scope of this research.

Moreover, the simulated far field gain patterns for the PCB dipole, when the elevation $\varphi = 90$ degrees, and the variable azimuth θ 0 to 360 degrees are presented in Fig. 4.4. The varying azimuth angle θ is the AoA that the this research investigates, therefore it was important to understand how the antenna gain affects the AoA. For f_1 and f_2, both gain and -3dB width remain the same, while for f_3 we can see that the width changes even

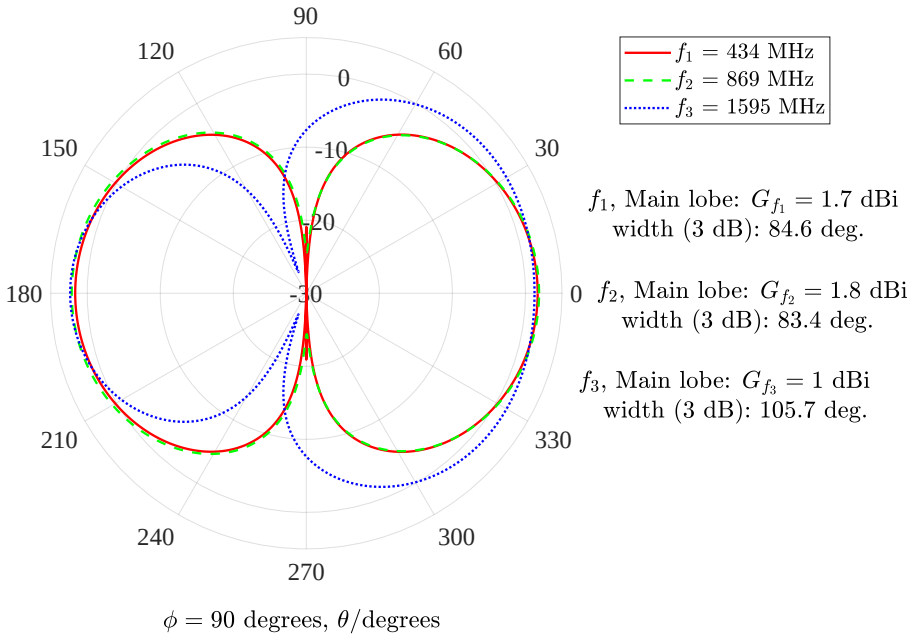

Figure 4.4: Simulated far field gain patterns of the PCB dipole of f_1, f_2, f_3, for elevation $\varphi = 90$ degrees, and variable azimuth θ 0 to 360 degrees.

further to 133 degrees. That means that the antenna orientation when used a transmitter or receiver has a small gain difference for each AoA.

Finally, the results prove the meander placement does not affect the radiation patterns, since the performance is typical compared to a typical dipole [107]. Moreover, it is expected that as the frequency increases, the dipole size and the directivity decreases as well [107]. What is not typical, is that the radiation pattern is not equal for both lobes. The result of the uneven lobes on the two sides is due to the *MF* support of the dipole. Overall, it is evident that the uneven lobes have very small effect, and it can be ignored.

4.2 Performance evaluation of the antenna as a ULA

This Section presents a performance evaluation of the tri-band antenna as a ULA. The first Subsection 4.2.1, is dedicated to the measured return loss, while Subsection 4.2.2, explains the effects of mutual coupling and presents measurements performed on the ULA. Finally, Subsection 4.2.3 demonstrates the simulated far field patterns of the ULA.

4.2.1 Measured return loss of the ULA

To measure the return loss of the array, a 4 port Vector Network Analyser (VNA) is employed. Since the VNA had 4 ports, and ten measurements were required, the following process was followed. First, all the VNA ports were calibrated for a 50 Ω input, and a worm connector was used to perform the pass through measurement, connecting every port to every other. Then, the antennas 1 to 4 were connected to the VNA ports 1 to

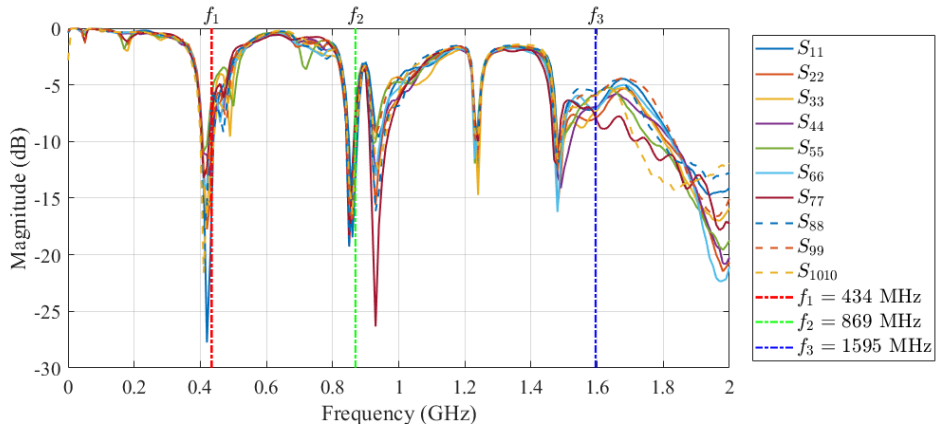

Figure 4.5: Return loss S_{11} of the antenna as a ULA elements 1 to 10.

Table 4.1: Detailed view of the return loss S_{11} for frequencies $f_1 = 434$ MHz, $f_2 = 869$ MHz, $f_3 = 1595$ MHz.

	Ant. 1	Ant. 2	Ant. 3	Ant. 4	Ant. 5	Ant. 6	Ant. 7	Ant. 8	Ant. 9	Ant. 10	
f_1	-15.9	-12.2	-9.8	-10.9	-6.2	-7.1	-7.7	-6.8	-8.7	-13.2	dB
f_2	-13.2	-8.8	-8.1	-9.4	-7.0	-8.3	-7.7	-7.7	-9.0	-10.5	dB
f_3	-7.0	-7.9	-7.3	-6.9	-5.7	-7.1	-7.8	-5.6	-5.9	-5.9	dB

4. A flexible foam was cut and used to keep equal distance of $s = 0.9$ cm to the antenna elements and it was placed as close as possible to the remaining ULA elements, to emulate a functioning receiver array. This process was repeated, measuring the antenna sets of, 3 to 6, 5 to 8, and 7 to 9.

Fig. 4.5 presents the return loss S_{11} of all ULA elements. Vertical lines were placed for each frequency of interest, red for f_1, green for f_2, and blue for f_3. Comparing with the return loss of a single PCB antenna with the return loss in a ULA in Fig. 4.5, it was evident that f_1 and f_3 were most affected. But even though the return loss was now lower, none of the return loss was above -5 dB. For a detailed view of the return loss S_{11} for frequencies $f_1 = 434$, $f_2 = 869$, $f_3 = 1595$ MHz, Table 4.1 is presented.

From Table 4.1 it is evident that for the f_1 antenna elements 5 to 8 suffered the most, but a return loss of -6.2 dB was still considered acceptable. Moreover, f_2 seems to be affected the least. The worst performing antenna element was located in the middle, with a return loss of -7 dB. Finally, f_3 was the worst performing out of all three frequencies. Antenna element 5 had a return loss of -5.7 dB, while elements 8 to 10 also had a return loss of circa -5.8 dB. Compared with the measurements presented in the previous Section, the performance of the return loss was reduced significantly. Even if the performance was not optimal ($S_{11} \leq -10$ dB), the overall performance seemed to be within the acceptable boundaries for the research needs.

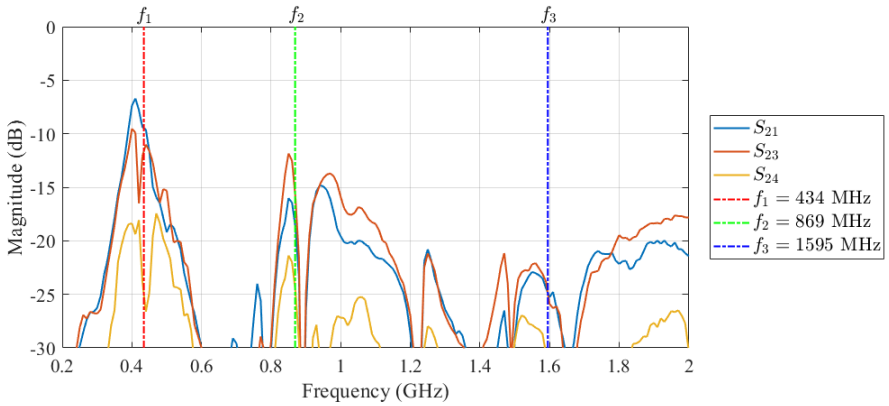

(a) Mutual coupling between ULA element 2, and elements 1, 3, 4.

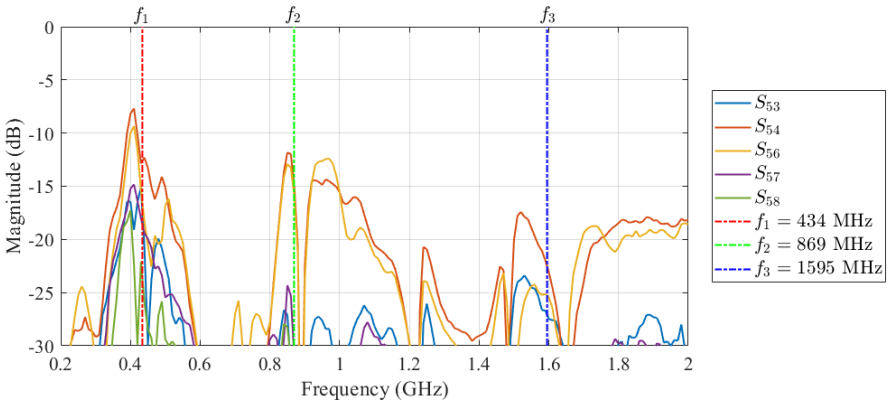

(b) Mutual coupling between antenna element 5, and elements 3, 4, 6, 7, 8.

Figure 4.6: Mutual coupling between ULA element 2, and elements 1, 3, 4 in Fig. 4.6a, and the mutual coupling between ULA element 5, and elements 3, 4, 6, 7, 8 in Fig. 4.6b.

4.2.2 Measured mutual coupling of the ULA

Mutual coupling describes the energy absorbed by a nearby antenna, close to the one that operates [107]. Mutual coupling is of course undesirable, since the energy that is supposed to be radiated away, is absorbed by a nearby element. Also, the antenna is supposed to capture the energy and not transfer it to nearby element. Therefore, the antenna efficiency is reduced. For a perfectly radiating ULA, there is no effect from nearby elements and materials. The purpose is to maximise the power that is radiated in, or away the element. Closely spaced antennas collect the radiated energy, but also radiate it to nearby elements. This is undesirable because the antenna impedance changes, creating an energy loss due to coupling. The more energy is absorbed by the nearby elements, the less power is received and also the far field pattern of the antenna can be affected. In cases that the mutual coupling is strong, an application of the algorithm that authors present in [20] can solve the issue.

Mutual coupling is measured similarly as the return loss. Instead of measuring the S_{11}, which is the return loss, the mutual coupling between port 1 and 2 is shown by the

measurement of S_{12}. For sake of space only the mutual couplings of antenna elements 2 and 5 is presented in Fig. 4.6.

Specifically, in Fig. 4.6a, the mutual coupling between ULA element 2 and elements 1, 3, 4 is presented. The highest values of mutual coupling for f_2 and f_3 were for S_{23}, at -15.8 dB and -23 dB respectively. In fact these values in both frequencies suggest that mutual coupling was very low. On the contrary, for f_1, the S_{21} and S_{23} were -9.4 dB and -11.5 dB respectively. For example, when a signal was received at element 2, the same signal was reflected to element 1, attenuated by -9.4 dB, and to element 3 attenuated by -11.5 dB. Overall, this level of mutual coupling was acceptable, since a signal reflection attenuated by -9.4 dB was judged to be weak and not affect the phase of the received signal.

Moreover, The mutual coupling between the antenna element 5 and elements 3, 4, 6, 7, 8 is presented in Fig. 4.6b. Similarly with the mutual coupling of antenna element 2 presented above, f_2 and f_3 were well below -10 dB, at -15 dB and -22.6 dB respectively. Moreover, for f_1 the mutual couplings for both S_{54} and S_{56} was circa -12 dB.

Overall, it was evident that even if the elements were in the middle of the ULA, the coupling seemed to be reduced. In practice, small errors in the placement of antenna elements (e.g. 0.5 cm difference) might had a small effect in the measurements. But what is important to note, is that for the worst measurement, the mutual coupling was -9.4 dB. Therefore, it was evident that effect of the mutual coupling to the designed ULA could be ignored and the second RTL-SDR design could not had suffered from it. Hence, it was concluded that the second RTL-SDR issues were mainly due to drivers, and not mutual coupling.

4.2.3 Simulated far field patterns of the ULA

To understand the effect of ULA to the far field pattern of the elements, a CST simulation was conducted. For sake of space, only the radiation patterns of antenna elements 1, 4, 7, and 10, with varying azimuth angle θ, elevation $\phi = 90$ and $\phi = 45$ degrees are presented in Fig. 4.7. From the results, it was evident that the overall gain for each element was increased, and the main beam width of -3 dB was decreased. This were expected changes, since the single element is part of a ULA [107].

Specifically, for the antenna element 1 of the ULA in Fig. 4.7a, the gain increased to 4.5 dBi, 7.8 dBi, and 8.9 dBi for frequencies f_1, f_2, and f_3 respectively. The -3 dB width beam of element 1 and $\theta = 0$ was 40 degrees for f_1, 21 degrees for f_2, and 12 degrees for f_3. Contrary to gain, the beam width of element 1 was reduced significantly, compared to the single PCB antenna. The -3 dB width at frequency f_1 was reduced by 44.6 degrees (from 84.6 degrees), while for f_2 was reduced by 62.4 degrees (from 83.4 degrees), and for f_3 was reduced by 93.7 degrees (from 105.7).

Looking at element 10 of the ULA in Fig. 4.7a, both gain and -3 dB beam width were the same. What changes, was the overall shape of the beam from the element. For f_1 and antenna element 10, the highest gain was at $\theta = -7$ degrees, while for the same frequency but antenna element 1, the highest gain was at $\theta = 7$ degrees. This effect was caused by

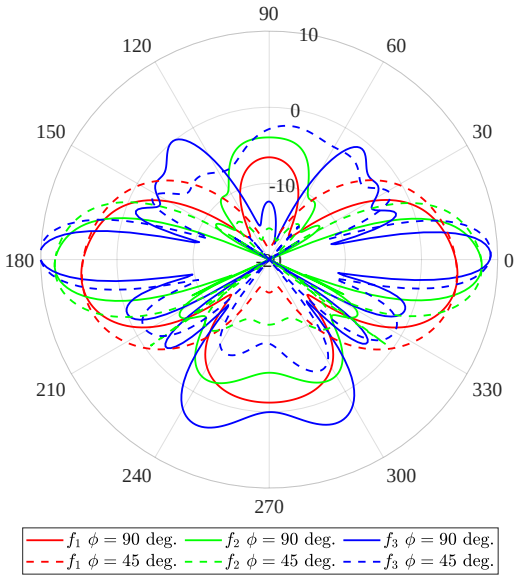

(a) Simulated far field gain patterns of ULA element 1 for f_1, f_2, f_3, elevation $\phi = 90$, $\phi = 45$ degrees, and variable azimuth $\theta \in [0, 360]$.

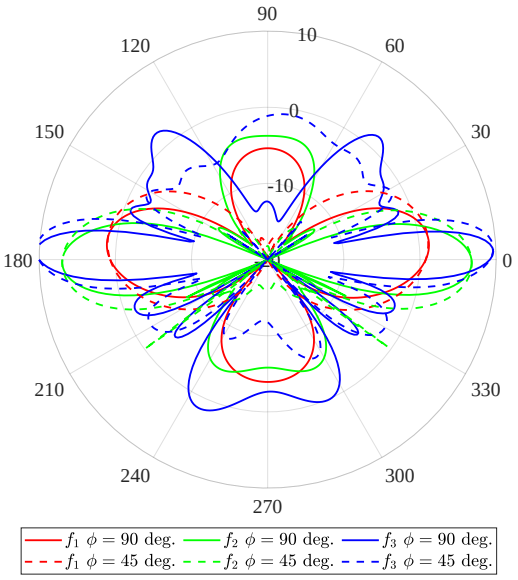

(b) Simulated far field gain patterns of ULA element 4 for f_1, f_2, f_3, elevation $\phi = 90$, $\phi = 45$ degrees, and variable azimuth $\theta \in [0, 360]$.

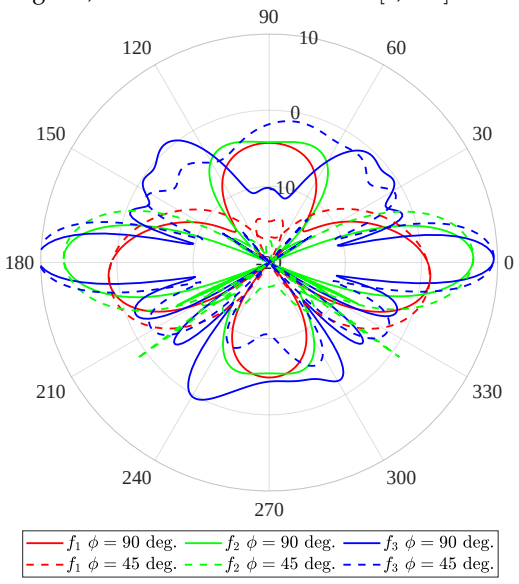

(c) Simulated far field gain patterns of ULA element 7 for f_1, f_2, f_3, elevation $\phi = 90$, $\phi = 45$ degrees, and variable azimuth $\theta \in [0, 360]$.

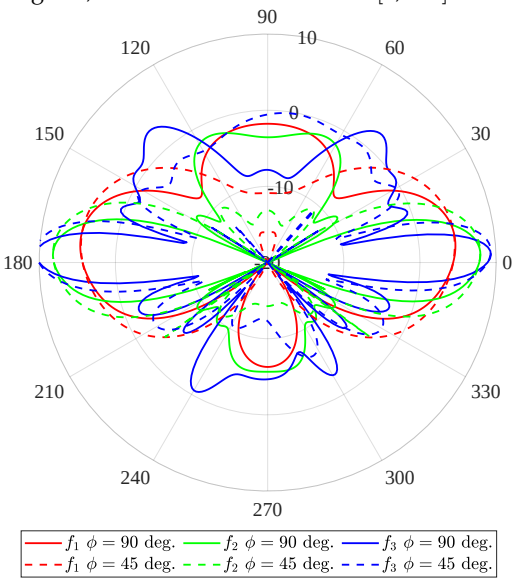

(d) Simulated far field gain patterns of ULA element 10 for f_1, f_2, f_3, elevation $\phi = 90$, $\phi = 45$ degrees, and variable azimuth $\theta \in [0, 360]$.

Figure 4.7: Simulated far field gain patterns of ULA element 1 in Fig. 4.7a, element 4 in Fig. 4.7b, element 7 in Fig. 4.7c, element 10 in Fig. 4.7d.

the ULA array [107].

The same effect was evident in elements 4 and 7, in Fig. 4.7b, and Fig. 4.7c respectively, but the antenna gains and -3 dB width were not the same. The gains were 0.8 dBi, 6.8 dBi, and 9.2 dBi, for f_1, f_2, and f_3 respectively. For f_1 the gain reduced by 3.7 dBi, while for f_2 reduced as well by 1.6 dBi. On the contrary, for f_3 the gain increased by 0.2 dBi.

Table 4.2: Detailed view of the antenna gains for f_1, f_2, f_2, and azimuth $\theta = 0$ degrees, and elevation $\phi = 90$ degrees.

	Ant. 1	Ant. 2	Ant. 3	Ant. 4	Ant. 5	Ant. 6	Ant. 7	Ant. 8	Ant. 9	Ant. 10	
$G_{f_1}(0,90)$	4.5	1.1	0.1	0.8	1.4	1.4	0.8	0.1	1.0	4.4	dBi
$G_{f_2}(0,90)$	7.8	5.7	6.6	6.8	5.7	5.6	6.7	6.6	5.7	7.8	dBi
$G_{f_3}(0,90)$	9.0	9.3	8.8	9.2	9.1	9.1	9.4	9.1	9.6	8.9	dBi

The increase or decrease was in fact the lobe shift, as explained before. That was why the antenna element experienced similar changes.

Overall, the gain of the far-field patterns seemed to be well within a -20 dB range, therefore the AoA estimation would have no issues at receiving the transmitted signal. What is noted in this section is the fact that each ULA element has different gains in the two elevations and frequencies. This triggered the research that is presented in Chapter 6. A table that presents the gains of all elements, frequencies, and two elevation is presented in Table 4.2.

Chapter 5

System design simulation, measurements, and characterisation

This Chapters provides the design, measurements, simulations, and characterisations of the transmitter and receiver used for the measurements in Chapters 6 and 7. Section 5.1 introduces the transmitter design, while Section 5.2 is dedicated to the transmitter characterisation, which is very important to understand the capabilities of the transmitter. Section 5.3 presents the RSP2 receiver array prototype and the necessary procedure to perform frequency and time synchronisation. Finally, Section 5.3 is dedicated to the receiver characterisation, which provides an insight on the receiver performance and capabilities.

5.1 ADF4351 Multi-Frequency transmitter prototype

This Section is dedicated to presenting the prototype of the transmitter used for the measurements performed in Chapters 6 and 7. The low cost programmable transmitter is based on the ADF4351 [108], with an Adafruit trinket Pro to control it. A block diagram of the transmitter schematic that includes the trinket, ADF4351, and an Liquid-Crystal Display (LCD) display screen can be seen in Fig. 5.1. A battery pack of 6 V was used to power the circuit, and it was controlled by an on-off switch (SW1). Pins 3 to 6 were used to connect the trinket with the ADF4351 controlling registers 1 through 5. The supply power of the ADF4351 was from the voltage regulated source, on board the trinket at pin 8. Pins 18 to 21 were connected with a rotary switch, which controls the transmitted frequency; modes 1-3 were for f_1, f_2, f_3 respectively, while f_4 was set for a 1 second rotating transmission of each frequency. For a visual output, a generic LCD was connected with pins 22 and 23, and operated to a I^2C protocol. A back-light control switch (SW3) was connected to pins 5 and 6 of the LCD display screen to reduce the overall energy

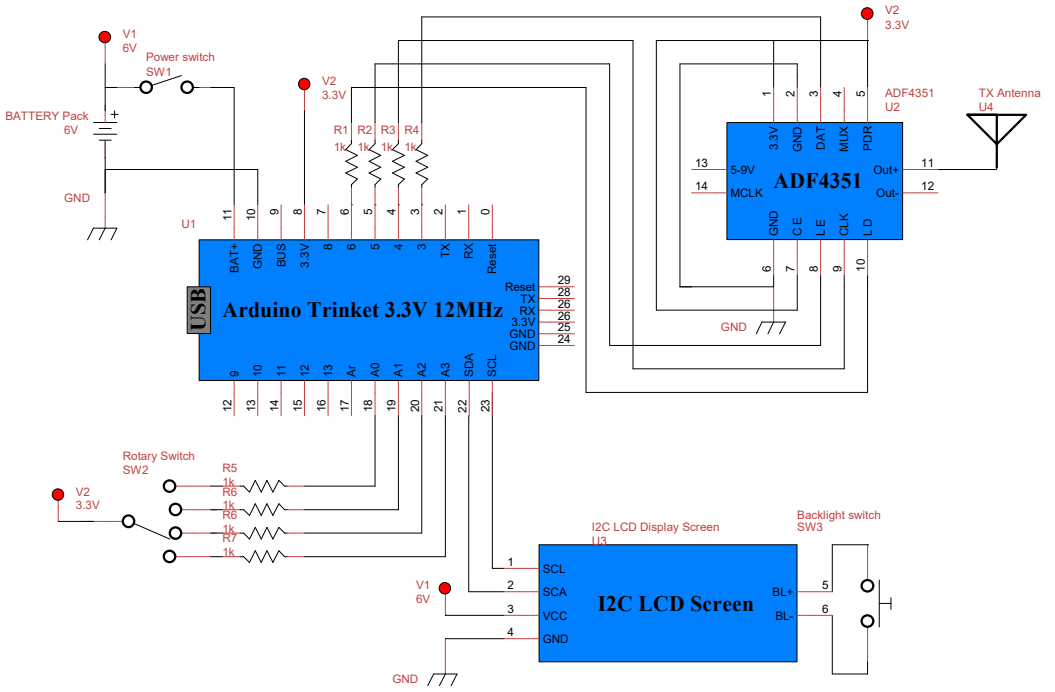

Figure 5.1: Transmitter schematic that operates with a 6 V battery pack, an Arduino Trinket (3.3 V, 12 MHz), an ADF4351, an I2C LCD display screen, and a rotary switch to select mode of transmission.

consumption.

Specifically, the ADF4351 [108] can be used as a fractional-N or integer-N Phase-Locked Loop (PLL) frequency synthesizer with an external loop filter and external reference frequency. Furthermore, ADF4351 has an integrated Voltage Controlled Oscillator (VCO), with a fundamental output frequency ranging from 2.2 to 4.4 GHz and can divide the output by 1/2, 1/4, 1/8, 1/16, 1/32, and 1/64, allowing the RF output frequency as low as 35 MHz. The control of the on-chip registers is done by a simple 3-wire interface, with a mute function that is controlled by pin and software, for RF output isolation. The output power can be set to -4 dBm, -1 dB, 2 dB, and 5 dB using the on-chip registers. For the scope of this application was set to 2 dB. The chip requires a voltage of 3 to 3.6 V and it consumes circa 112 mA when RF output is on and 7 uA on low power sleep mode.

The RF output is controlled by the programmable registers as [108],

$$RF_{OUT} = [INT + (FRAC/MOD)] \times (f_{PFD}/RF_{Divider}) \tag{5.1}$$

where, RF_{OUT} is the RF frequency output, INT is the integer division factor, $FRAC \in [0, MOD-1]$ is the numerator of the fractional division, $MOD \in [2, 4095]$, $RF_{Divider}$ is the output divider that divides the VCO frequency, and f_{PFD} is the phase frequency detector. Furthermore, f_{PFD} is controlled by [108],

$$f_{PFD} = REF_{IN} \times [(1+D)/(R \times (1+T))] \tag{5.2}$$

where, REF_{IN} is the reference frequency input, D is the $REF_{IN} \in [0,1]$ doubler bit, $R \in [1,1023]$ is the RF reference division factor, and $T \in [0,1]$ is the reference divide by 2 bit.

For the scope of this research, the doubler was set to $D = 1$, the reference division was set to $R = 10$, and the divider was set to $T = 0$. Therefore, using (5.2), $f_{PFD} = 2.5$ MHz. With f_{PFD}, the rest of the values was calculated using (5.1). Furthermore, to transmit a CW at $f_1 = 434.1$ MHz the values were: $INT = 1389$, $FRAC = 12$, $MOD = 100$, and $RF_{Divider} = 8$. These values were converted into binary and translated to registers 1 through 5 using a microcontroller. Each register is 32 bits, where each value matches a specific bit position. For example, the bit positions 3-14 of register R0 represent $FRAC$ in binary, while positions 15-30 represent INT in binary.

To send the registers and control the ADF4351, an Adafruit trinket Pro with an Atmel 8-bit Microcontroller was employed [109]. The process of sending data is not fully explained here but it can be found in [108]. The benefit of using the trinket instead of a Peripheral Interface Controller (PIC) was that the communication with the device is done directly through Universal Serial Bus (USB) and the programming language of Arduino, which is a simplified version of C. The trinket operates at 3.3 V, 12 MHz clock, and has 20 programmable inputs or outputs.

5.2 Transmitter characterisation

This Section is dedicated to the transmitter characterisation and discussion regarding its performance. Designing or incorporating different off the self components can become very complicated and unmanageable. Real world systems do not abide to idealisation or assumptions that simulations do. Therefore, characterisation is very important because first, it proves that the real world system works as it is expected; and second, it highlights advantages or disadvantages.

First, the smith chart of the ADF4351 [108] is presented in Fig. 5.2. The input impedance is presented as the conjugate, since the vector analyser that performs the measurement sees the ADF4351 [108] as the load. Since the ADF4351 [108] is the transmitter (source), the correct impedance is the conjugate of the measured (load). Therefore, the measured impedance of the ADF4351 for f_1 was $Z^*_{434} = 0.99 - 0.11j$, for f_2 was $Z^*_{869} = 0.84 + 0.03j$, while for f_3 was $Z^*_{1595} = 0.88 + 0.1$. Moreover, the measured impedance of the designed PCB dipole for f_1 was $Z_{434} = 0.84 - 0.78j$, for f_2 was $Z_{869} = 0.52 + 0.08j$, while for f_3 was $Z_{1595} = 0.88 + 0.2j$.

From Fig. 5.2, it was evident that the ADF4315 [108] maintains an output impedance very close to 50 ohm match. On the contrary, the tri-band antenna from Chapter 4 was designed to operate in specific frequencies. In Table 5.1, the transmitter characterisation is presented. The ADF4351 [108] was programmed to transmit a 2 dBm CW signal. Using a spectrum analyser it was found that the transmit power was 0 dBm on f_1, -0.5 dBm on f_2, and 0.5 dBm on f_3. Also, the impedance missmatch losses were estimated using (4.3). Furthermore, the antenna transmit gain at azimuth $\theta = 90$ degrees and the elevation $\varphi = 90$ degrees were used as an indicator to calculate the transmit power at the specified

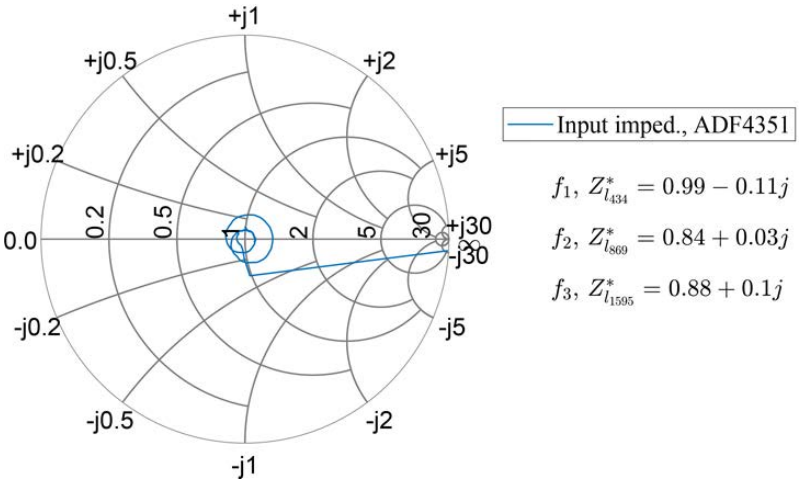

Figure 5.2: Smith chart showing the input impedances of the ADF4351.

Table 5.1: Transmitter characterisation displaying the ADF4351 transmit power and impedance, the PCB dipole impedance, the missmatch loss, the antenna gain at azimuth $\theta = 90$ degrees, elevation $\varphi = 90$ degrees, and the expected transmit power $P^{\text{TX}}(90, 90)$.

	ADF4351 Tx power	ADF4351 impedance	PCB dipole impedance	Missmatch loss	$G^{\text{TX}}(90,90)$	$P^{\text{TX}}(90,90)$
f_1	0 dBm	$0.99 - 0.11j$	$0.84 - 0.78j$	-0.5 dB	1.7 dBi	1.2 dBm
f_2	-0.5 dBm	$0.84 + 0.13j$	$0.52 - 0.08j$	-0.3 dB	1.8 dBi	1 dBm
f_3	+0.5 dBm	$0.88 + 0.10j$	$0.88 - 0.20j$	-0.1 dB	1.0 dBi	1.4 dBm

angle $P^{\text{TX}}(\theta, \varphi)$. The transmit power of circa 1 dBm for all the frequencies was efficient when the actual transmit power of the ADF4351 [108] is 2 dBm.

Moreover, a Effective Radiated Power (ERP) measurement was performed to validate the simulated gain of the manufactured antenna. The transmitter was placed in an anechoic environment connected with the designed antenna. For a receiver a spectrum analyser was used, connected to a log periodic antenna with 6.5 dBi gain in f_1, 7.3 dBi gain in f_2, and 7.2 dBi gain in f_3. The height of both transmitting and receiving antennas was set to 2 m and the distance between them was measured to be 5 m. Using the free space model losses model [106] the pathloss was estimated; for f_1 it was 39.2 dB, for f_2 it was 45.2 dB, and for f_3 it was 50.5 dB. Using the spectrum analyser as a receiver, the measured power for f_1 was -31.9 dBm, for f_2 was -37.4 dBm, and for f_3 was -42.5 dBm. Known the transmitted and received powers, the missmatch loss, the antenna gain of the receiver, the measured transmitting antenna gain was 1.3 dBi at f_1, 1.3 dBi at f_2, and 0.4 dBi at f_3. The difference between theoretical and transmitted gain was circa 0.5 dB. Taking into consideration that the cable losses of the RG-316 cable are circa 0.6 dB for the half meter cabling, the measured antenna gain $G^{\text{TX}}(90, 90)$ was as expected from the simulation.

The current consumption of the transmitter was measured on the 6 V power rail, and was found to be 157 mA with the LCD back-light turned on and 112 mA with the LCD back-light turned off. Powering the transmitter with 4 high performance AA alkaline

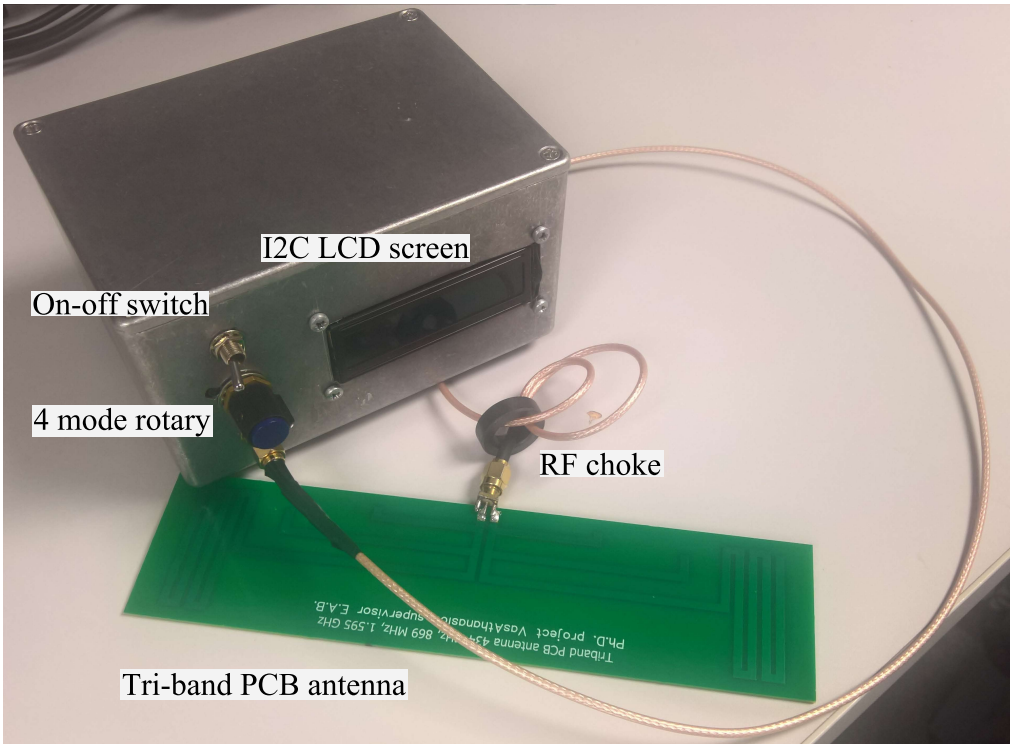

Figure 5.3: Picture of the final transmitter design with the ADF4315, Arduino Trinket inside the box, and the tri-band PCB antenna with an RF choke.

batteries in series to supply the 6 V, the available energy is 2000 mAh. Therefore, the maximum operational time when the ADF4351 [108] can be powered on continuously is 12.7 hours with the LCD turned on, and 19.6 hours with the LCD turned off. The operational hours were enough to perform multiple measurements without the need to turn the power off to conserve power. The overall power consumption could be reduced by turning the ADF4351 [108] on and off for pulse transmission instead of a CW.

Finally, the overall performance of the transmitter was adequate for its purpose. The antenna design could be improved to reduce the missmatch loss, but the overall improvement would be circa 0.3 dB. Moreover, the 19.6 hour of battery life for the transmitter enabled extensive measurements, for both indoor and outdoors. Thus, the overall transmitter design and implementation was efficient in terms of power consumption and portability. Fig. 5.3 presents a picture of the actual transmitter implementation and its portability. The metallic box contains the battery pack, ADF4315 [108], and the Arduino trinket. The on-off switch is on the top, followed by the 4 mode rotary switch, and then the RF output, where the RG316 cable was attached to connect the ADF4315 [108] with the designed tri-band PCB antenna. An RF choke was placed next to the antenna preventing common mode, which shields the cable from radiation, and prevent the cable it self from radiating. This transmitter was used in measurements performed in Chapters 6 and 7.

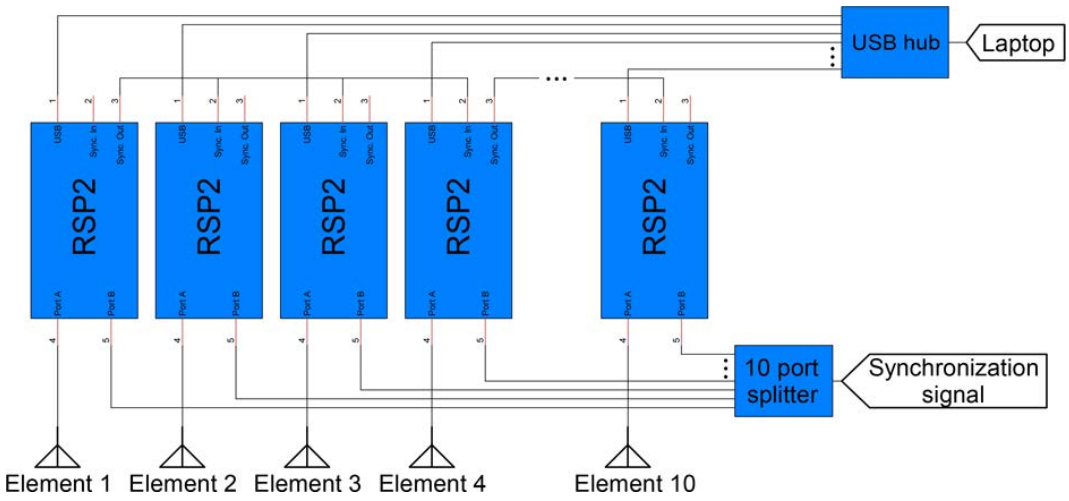

Figure 5.4: Block diagram of the RSP2 receiver array used for measurements, showing both frequency and time synchronisation.

5.3 RSP2 receiver array prototype

This Section is dedicated to the RSP2 receiver array which is employed and used for the measurements performed in Chapters 6 and 7. The RSP2 is a SDR that can tune to all frequencies from 1 kHz up to 2 GHz, with a maximum bandwidth of 10 MHz [27]. Moreover, it employs two 50 Ω antenna inputs, Port A and Port B, and an input with a high impedance for low frequency signals. Furthermore, every RSP2 has a sampling clock input and output, allowing the connection of multiple RSP2s sharing the same clock. The employed receiver array utilises ten RSP2s, requiring a specific process of initialisation and operation to achieve time and frequency synchronisation, which is explained in the following subsections. A block diagram of the RSP2 receiver array is presented in Fig. 5.4.

To enable control of the RSP2 from Matlab environment, driver development was required. To access a single RSP2 device, the installation of drivers was required, as a first step. The library (.dll) and header (.h) files were used from the software to interact with the device. Once the library file was accessed once, the file could not be accessed again to allow the control of a second device. Therefore, multiple library files were required, one for each RSP2. Moreover, Matlab is able to access a single library file, but not multiple at the same time. Hence, the appropriate multi-threaded MEX/C file was written, with each thread opening a library file, enabling the support of multiple RSP2 devices. With the MEX file, Matlab could now directly communicate with every RSP2. To ensure that the communication was done properly an object function was created. The object function is initialised when a RSP2 device is loaded in Matlab, and contains the parameters of the device, such as sampling rate and frequency of operation. A detailed example on how to connect the RSP2 devices, and achieve frequency synchronisation is presented on my GitHub page [110].

Moreover, enable the receiver array to perform AoA measurements two necessary steps

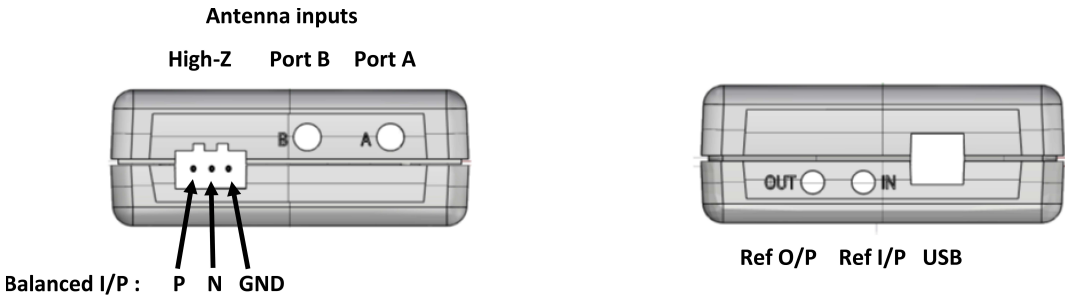

Figure 5.5: Inputs and outs of the RSP2 [27].

are required. First is frequency synchronisation which tunes all the RSP2s in the same sampling clock. That process is described in Subsection 5.3.1. That processes to time synchronise the receiver array with a synchronisation signal is explained in Subsection 5.3.2. Furthermore, Subsection 5.3.3 depicts the first measurements performed to show how two RSP2s can be time and frequency synchronised, and the final Subsection 5.3.4 is dedicated to showcasing the ten RSP2 receiver array.

5.3.1 Frequency synchronisation of two RSP2s

The RSP2 SDR allows the output or the input of a sampling clock without any modifications. A picture of the RSP2 inputs and outputs is presented in Fig. 5.5. Ref I/P is the input of the sampling clock, while Ref O/P is the output of the internal sampling clock that the RSP2 uses. Moreover SDRplay, has released documentation on how to achieve frequency synchronisation through connecting and initialising the RSP2s in a daisy-chain [111]. Thus, in theory, the frequency synchronisation is straight forward by enabling the clock output of the first RSP2 and connecting its output with the input of the second RSP2. Then the output of the second RSP2 is connected to the input of the third, and so forth for all the remaining RSP2s. Unfortunately, that was not the case.

While connecting three RSP2 devices in a daisy-chain, the fourth device seemed that it did not accept the input of the third, and used it's internal sampling clock. To further investigate this, the clock signal was measured for each stage with an oscilloscope, as presented in Fig. 5.6. The output clock of the RSP2 that was the input to the RSP2 can be seen in Fig. 5.6a. The sampling clock has a frequency of $f = 10$MHz, and $V_{pp} = 2.1$ V. The output of the second RSP2, which was the input of the third RSP2, is presented in Fig. 5.6b. Here it was evident that the frequency was the same, but peak to peak voltage increased to $V_{pp} = 2.47$ V. Finally, the output of the third RSP2, which was the input of the fourth RSP2 is presented in Fig. 5.6b. In this figure, the peak to peak voltage is $V_{pp} = 2.76$ V. It was evident that each RSP2 induced a small gain on the sampling clock. As a result, when the sampling clock reaches the fourth RSP2 it was amplified to a level that the fourth RSP2 does not accept as an input and therefore does not use the common sampling clock.

Fortunately, the solution for this problem was straightforward. Instead of connecting them to a single daisy-chain, a block daisy-chain was implemented. Since the output and

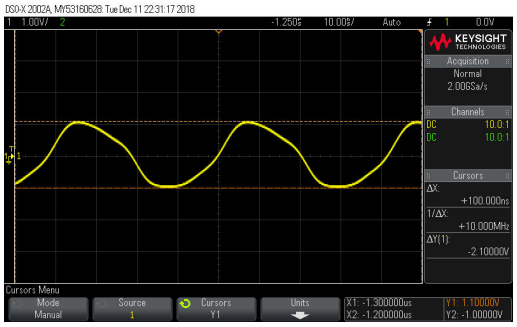

(a) Sampling clock output of the first RSP2, input of second RSP2.

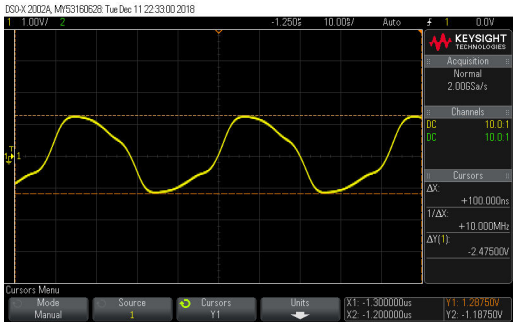

(b) Sampling clock output of the second RSP2, input of third RSP2.

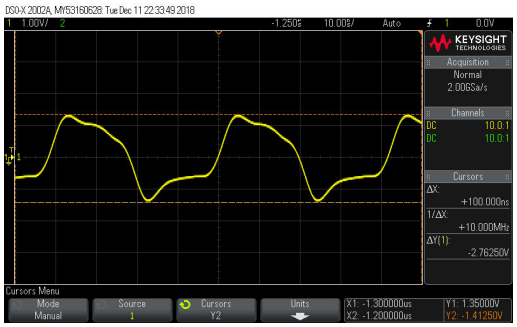

(c) Sampling clock output of the third RSP2, input of fourth RSP2.

Figure 5.6: Output and input synchronisation clocks for RSP2s, one to two Fig. 5.6a, two to three Fig. 5.6b, three to four Fig. 5.6c.

input of the RSP2 has an Operational Amplifier (op-amp) buffer circuit, a single RSP2 clock output can support the clock input of multiple RSP2s. Hence, different cables were cut and soldered to connect the sampling clock of the first RSP2 to the output of the RSP2s two, three and four. An example of the block daisy-chain can be seen in the RSP2 receiver array block diagram presented in Fig. 5.4. The output of the RSP2 number four was used to supply the sampling clock to the RSP2s five, six and seven; and finally, the output of RSP2 seven, supplied the sampling clock to RSP2 eight, nine and ten.

The results of this configuration showed that all the RSP2 devices were successfully initialised with a common sampling clock. Another positive aspect of this configuration, was that the sampling clock was attenuated, instead of amplified. Meaning that even more RSP2 devices can be connected in a similar fashion, increasing the overall size of the array.

5.3.2 Time synchronisation of two RSP2s

To time align multiple RSP2s a series of measurements was performed. Each RSP2 has two 50 Ω ports, which can be selected thought the developed MEX file. The first idea was to receive a signal at the Port B of two RSP2s, and time synchronise them. After the synchronisations, both RSP2s switched to Port A and received a new frame. If the process was done correctly, in theory, the two RSP2s should see the same signal with no phase

Table 5.2: Detailed information of target node and anchor node for the first RSP2 time and frequency synchronisation proof of concept.

	Target node	Anchor node
Frequency (MHz)	869.3	869.1
Sample Rate (k sps)	1	1
Power (dBm)	-70	-40
Port	A	B
Modulation	On-Off Keying (OOK)	OOK

shift. Unfortunately, it was discovered that switching ports imposed a random delay at the received signal at Port A, hence time synchronisation was impossible.

Since port switching was not an option, the amplitude and phase difference was measured next. For the amplitude difference, the process was simple. A signal was conductively fed to Port B, while the RSP2 was set to receive at Port A. A block diagram of the RSP2 receiver array with the synchronisation signal being fed on the Port B and the antenna element at Port A can be seen in Fig. 5.4. Measurements found a 14 dB attenuation between the two ports. Therefore, to receive a signal at -60 dBm at Port A, a -54 dBm signal should be conductively fed at Port B. For the phase difference the measurement process was complex. Using a zero phase splitter in the signal generator, a signal was fed conductively through cables toboth Port A and Port B. To create a phase difference between the two signals, the two cables that connected the splitter to the RSP2 ports had different lengths. By measuring the phase difference $\Delta\phi_2 = 157.8$ degrees the length of the cable can be estimated by using the following equation [106],

$$\Delta L = \frac{f\Delta\phi_2}{360c}\chi \tag{5.3}$$

where, $\chi = 0.6$ and is the transmission coefficient of the copper track on the FR4 PCB. Therefore, with $\Delta\phi_2 = 157.8$ the cable length is estimated to be $\Delta L = 50$ mm, which confirms that the two RSP2s are time synchronised. After performing such measurements, with a signal power of -30 dBm at both ports, but with different cable length, the received signal was found to be the addition of the two signals. Signal one was at -30 dBm, while signal two was at -44 dBm, with a phase difference of circa 157 degrees. Hence, this proves that the two ports have a zero phase offset, and -14 dB attenuation.

5.3.3 Frequency and time synchronisation measurements of two RSP2s

With the knowledge that the two ports have a zero phase difference and a 14 dB attenuation, the following test was conducted to prove that two or more RSP2s can be synchronised. The test setup was consisted of two RSP2s, an anchor node, and a target node. To achieve phase synchronisation, the two RSP2 were initialised as a daisy-chain [111], where the clock of the first RSP2 acts as a clock master on the second RSP2. For both anchor node and target node SPIRIT1 a low data rate, low power transceiver [112]

(a) Picture of the first time and frequency synchronisation conductive test.

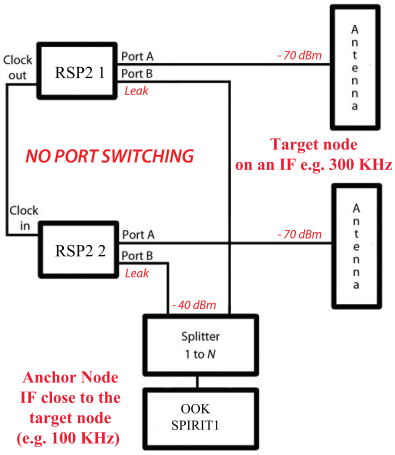

(b) Conceptual block diagram of time and frequency synchronised array.

Figure 5.7: Picture of the first time and frequency synchronisation conductive test 5.7a, and conceptual block diagram of time and frequency synchronised array 5.7b.

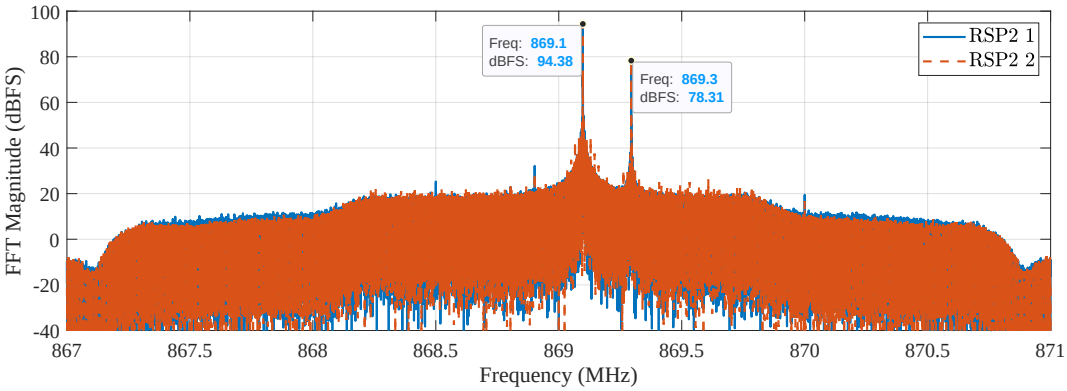

Figure 5.8: FFT of the raw captured data for two RSP2s.

was used. The anchor node transmitted a OOK modulated signal at 869.1 MHz. A two-way splitter and two cables with equal length allowed a zero-phase difference feed to the two RSP2 at Port B. Similarly, the target node transmits was a OOK modulated signal at 869.3 MHz. As described above, a zero-phase difference feed reaches port A of both RSP2. For detailed information regarding the setup see Table 5.2 and a picture of the setup in Fig. 5.7a.

Since it was found that port switching introduces a random phase offset between the two RSPs, the two port approach was implemented. The cable length between the RSP2s and the target node at port A or anchor node and port B was recommended to be the same, in order avoid unnecessary pre-calibration. Both RSP2s were set to Port A, and Port B was fed with a strong synchronisation signal, which leaked to port A. For time synchronised, phased array applications the target node (conductively feed in this test) were replaced with an antenna, Fig. 5.7b.

In Matlab environment, the two RSP2s were initialised in a daisy-chain for phase synchronisation, and both RSP2s were set to RF frequency of 869 MHz, sample rate of 4 M sps, gain reduction of 50 dB, and bandwidth of 1.5 GHz. An Fast Fourier Transform (FFT) of the raw captured data can be seen in Fig.5.8. The two FFT peaks are highlighted, showing the transmission frequencies 869.1 and 869.3 MHz, with the received powers, 94 and 78 dBFS respectively. To convert dBFS to dBm or vise versa, the following simple equation is used,

$$P^{\text{TX}}_{\text{dBm}} = P^{\text{RX}}_{\text{dBFS}} + x \tag{5.4}$$

where, x is an unknown offset introduced by the Analogue to Digital Converter (ADC) in the RF input. To find x, a signal of known power was injected in the RSP2 RF input $P^{\text{TX}}_{\text{dBm}}$, and the received power in dBFS $P^{\text{RX}}_{\text{dBFS}}$ was recorded. Solving (5.4) for x, the offset is now known. Using (5.4), the dBm values presented in Table 5.2, and dBm values presented in Fig.5.8, the two offsets were estimated to be $x_1$148.3 and $x_2 = 134.3$. By subtracting the two values, the attenuation was confirmed to be 14 dB.

Both target signal synchronisation signal (leaked from port B) fell within the RSPs IF bandwidth (100 and 300 kHz). To distinguish the anchor node and the target signal, two FIR filters for each IF (100 and 300 KHz) were created in Matlab. To preserve the phase of the recorded signals, zero-phase digital filtering was used. The phase offset of the anchor node in the two RSP2s was measured in two stages. The first stage uses a cross-correlation to detect the coarse time offset, which was then applied. The second stage was a phase offset measurement between the two RSP2s' signals using FFT, which was rounded and converted into samples, to completely align the two RSP2s. The unsynchronised high frequency anchor node signals is presented in 5.9, while the synchronised low frequency target node signals is presented in Fig. 5.10. Both figures contain a snapshot at the start and at the end of the frame to prove that the frame was unsynchroned or synchronised, depending on the frequency.

Thereafter, the time offset measured remained the same while the devices were streaming data. That means that the anchor node could be turned off after the initial calibration. If any setting changed on any device, a random unknown offset is added, hence re-synchronisation is required. It was theorised that this might be due to the internal switching in random indices and its effect in the phase of the received signal. Further investigation is required to determine the source of this random offset and a possible solution.

5.3.4 Frequency and time synchronised RSP2 array receiver

Knowing how frequency and time synchronisation was achieved for two RSP2s, now the ten RSP2 receiver array and the process to synchronise ten RSP2s is presented. Fig. 5.11 presents the front and the back of the ten RSP2 receiver array.

Starting from the front of the receiver array in Fig. 5.11a, the E4437B signal generator provides a signal to the ten port splitter, that is conductively fed to Port B of the RSP2. A Power Supply Unit (PSU) was required, to supply power to every RSP2 through the

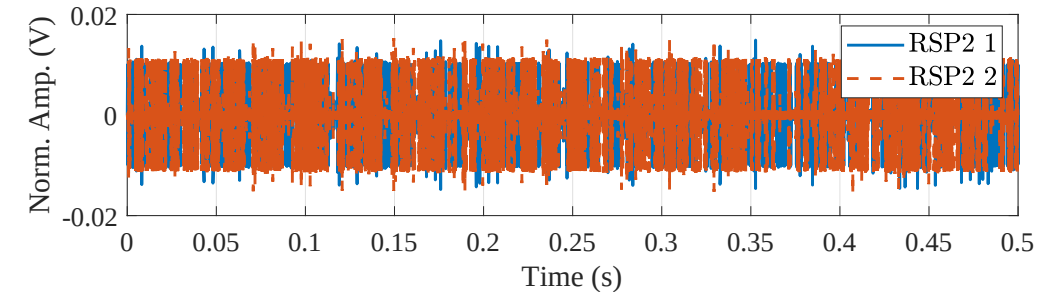

(a) Unsynchronised high frequency target node signals.

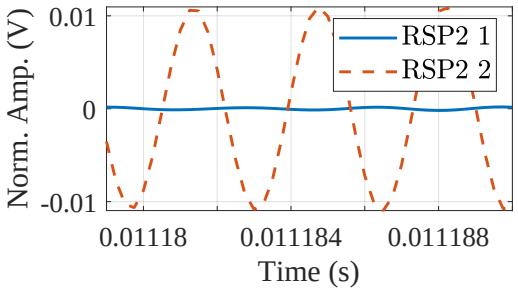

(b) Start of the frame.

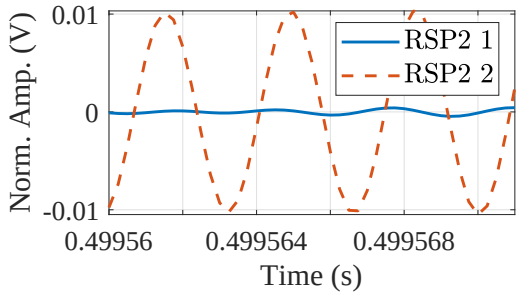

(c) End of the frame.

Figure 5.9: Unsynchronised high frequency anchor node signals Fig. 5.9a, the start of the frame in Fig.5.9b, and the end of the frame in Fig.5.9c.

USB. The current requirement of a single RSP2 when streaming is circa 160 mA. With four RSP2s in a single USB hub the overall required current is 640 mA, which exceeds the maximum USB current output. The USB hubs had 5 ports, and they were modified to enable external power option. Moreover, the external monitor shows the Matlab 2018a environment that was used to interface with the RSP2s.

In the back of the receiver array in Fig. 5.11b, the distributed time synchronisation signal and the block daisy-chain can be seen. The ten cables were bundled together at the start, to minimise phase change due to movement. The cables were then split and with the help of adhesive tape and cable grips were lead to the 90 degree SMA connector. Each cable had a RF choke close to Port B to prevent the common mode, which shields the cable from radiation, and prevent the cable it self from radiating. Moreover, the block daisy-chain cables for frequency synchronisation can be seen in the same figure. The block chain starts from the clock output of RSP2 one, and feeds the input of RSP2 two, three, and four, as described in Subsection 5.3.1.

Finally, to enable AoA estimation, the phase uncertainty caused by the splitter and cables had to be estimated. To do so, the process starts by initialising the RSP2s in frequency f_1, connected in a block daisy-chain, and the continuous data stream started. Without interrupting the data stream, a zero phase two port splitter was attached to the signal generator, and the two outputs of the splitter connected to the Port B of RSP2 one and RSP2 two, with cables that had an equal length. Then the two RSP2s were time synchronised through correlation and FFT. The cable that was attached to the Port B of the RSP2 two was then removed, and attached to the Port B of the third RSP2. The process

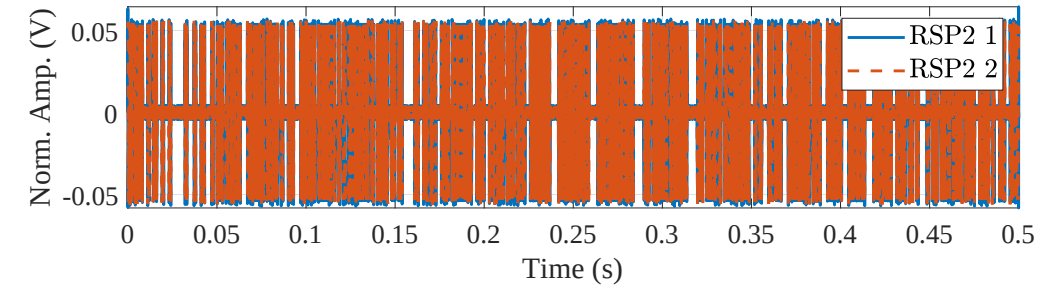

(a) Synchronised low frequency target node signals.

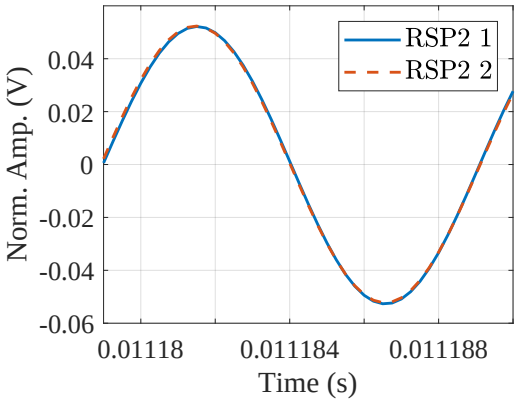

(b) Start of the frame.

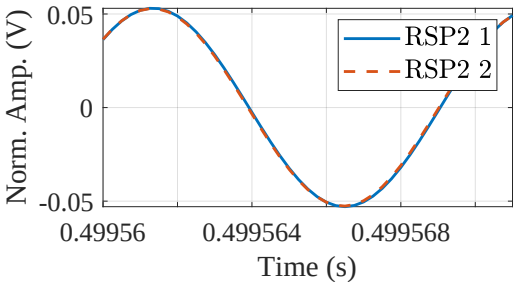

(c) End of the frame.

Figure 5.10: Synchronised low frequency target node signals Fig.5.10a, the start of the frame in Fig.5.10b, and the end of the frame in Fig.5.10c.

was then repeated until all nine RSP2 were time synchronised with the first RSP2. Then, the the zero phase two port splitter and cables were removed, and all the cables from the ten port splitter were attached to all the Port B. By measuring the new phase difference between the first RSP2 and every other RSP2 (two to ten), the unknown phase uncertainty of the splitter and cable could be estimated. Therefore, all ten RSP2 could now be time aligned for frequency f_1 with the time synchronisation signal coming from the ten port splitter. The same process needed to be repeated for all frequencies, since the phase delay of the cables and splitter was frequency dependant.

5.4 RSP2 receiver array characterisation and conclusions

Similarly to Subsection 5.2, in this Section the receiver array is characterised. The characterisation of the receiver is important because it provides an insight on the receiver performance and abilities. For example, dynamic range shows the saturation point but more importantly allows the user to convert the ADC dBFS range to real power of dBm. Therefore, without characterisation a receiver output can not be interpreted, making it essential for proper operation.

First, the sensitivity is presented in Table 5.3 and Fig. 5.12. The received signal in dBFS was measured by applying FFT to the received signal, converting the Fourier spectrum

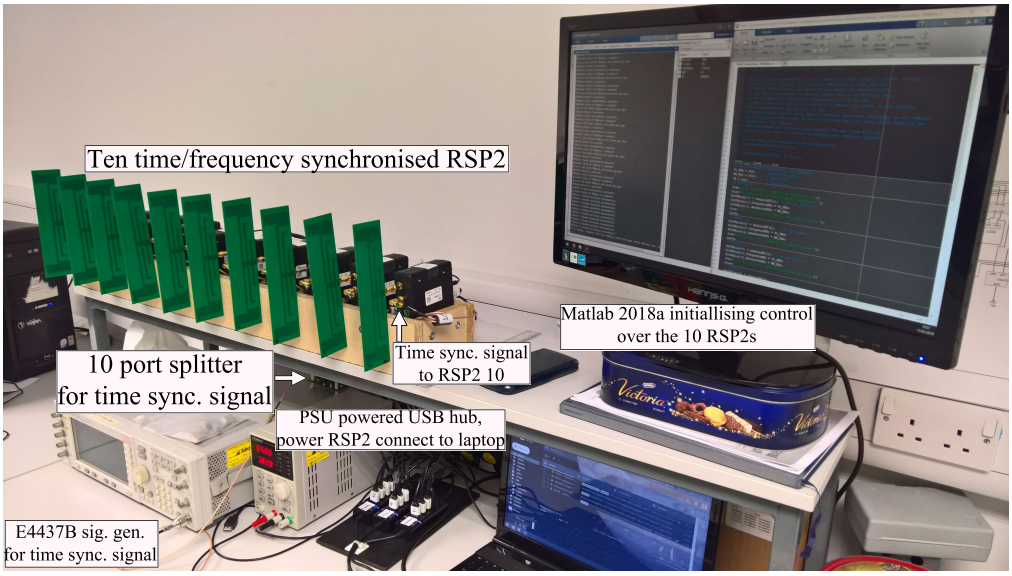

(a) The front view of the ten RSP2 time and frequency synchronised receiver array.

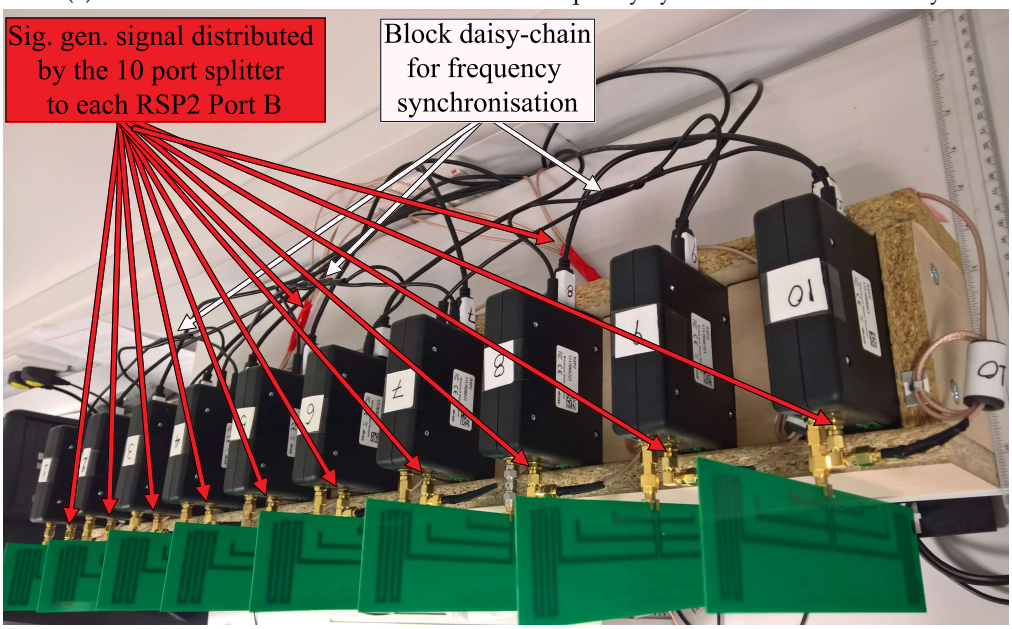

(b) The back view of the ten RSP2 time and frequency synchronised receiver array.

Figure 5.11: The ten RSP2 time and frequency synchronised receiver array, front view in Fig. 5.11a, and back view in Fig.5.11b.

to dB and selecting transmitted frequency. Instead of using the time signal, FFT has a better performance because it eliminates the noise found in the time domain. Also, because the absolute values change between each RSP2, instead of presenting maximum and minimum for each RSP2, an average is presented.

Table 5.3 presents the dynamic range, which is the maximum and minimum power the receiver array can have in its input. For example, if a signal was received at f_1 that

Table 5.3: Measured dynamic range, from -130 dBm to -40 dBm and frequencies f_1, f_2, and f_3 for the first RSP2.

	-130	-120	-110	-100	-90	-80	-70	-60	-50	-40	-30	dBm
f_1	1.9	10.2	19.4	27.6	37.5	47.0	57.2	67.1	78.2	81.7	81.8	dBFS
f_2	0.8	4.6	14.4	24.4	32.9	44.1	54.6	64.5	74.1	81.3	81.5	dBFS
f_3	0.1	0.3	7.8	18.3	25.2	38.0	47.4	57.4	64.1	75.5	81.2	dBFS

was over -40 dBm would saturate at the input and the received signal would be clipped. This would create an error in phase estimation, therefore the AoA estimation would be impossible. On the other hand, the sensitivity of the receiver array for the same frequency was found to be at -130 dBm. Moreover, for f_2 the sensitivity was measured to be circa -120 dBm, and for f_3 circa 110 dBm. Overall, the receiver array is very sensitive to signals at f_1, and f_2 provides a high dynamic range of circa 80 dB. Finally, in Fig. 5.12 presents a good visual example of the RSP2's dynamic range and its low sensitivity.

Next, the smith plots of all RSP2s are presented in Fig. 5.13. During the measurements, it was evident that the input impedance was different between frequencies f_1, f_2, and f_3. Therefore, the input impedance of the first RSP2 in frequencies f_1 and f_2 is presented in Fig. 5.13a, and for f_3 in Fig. 5.13b. A detailed table of the input impedances of all RSP2 in the three frequencies is presented in Table 5.4. Overall, from the figures it was evident that the performance of all RSP2s was on average the same. Therefore, the mean impedances were derived from Table 5.4 and for f_1 it was found to be $33 + 39.2j\Omega$, while for f_2 it was $18.2 - 7.5j\Omega$, and for f_3 it was $36.1 - 3.2j\Omega$.

Furthermore, the measurements used for the return loss and the mutual coupling measurements in Section 4.2, are now presented as antenna impedances. A detailed table of all the measurements for every antenna element in all three frequencies is presented in Table 5.5. The input impedance of a single antenna, as show, in Section 4.1, were $42 - 39j\Omega$ for f_1, $26 - 4j\Omega$ for f_2, and $44 - 10j\Omega$ for f_3. Comparing these single element impedances with the ULA impedances, it was evident that the ULA had an effect on the impedances in all frequencies. For example the input impedance at f_1 of antenna element 5 increased to, $111.4 + 43.2j\Omega$, while a similar increase was evident for f_2 as well. As expected, due to element spacing, f_3 suffered the least with the worst performance being in the antenna element 5 again, where the impedance reduced to $36.8 + 50.4j\Omega$.

Moreover, Table 5.6 presents the missmatch losses of the impedances between the RSP2s and the antenna elements using (4.3). Compared to the transmitter missmatch losses, which were circa 0.5 dB, the ULA antenna effect increased the losses significantly. Specifically, for f_1 the biggest loss was at 2.9 dB in antenna element 1, while for f_2 was 5.1 dB in antenna element 4. This magnitude of loss, could have an potential affect on the overall system design. Looking at the dynamic range measures that was presented in Table 5.3 and Fig. 5.12, the system had a large dynamic range with low sensitivity. Therefore, the change in the receiver range and sensitivity was ignored. With the biggest missmatch loss measured to be circa 4 dB for both f_1 and f_2, the overall dynamic range was reduced

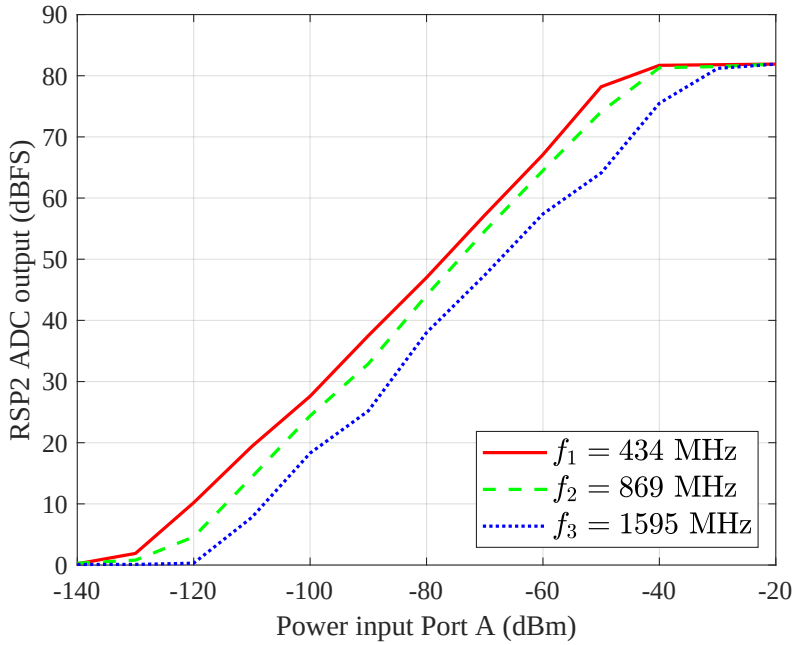

Figure 5.12: Measured dynamic range, from -140 dBm to -20 dBm and frequencies f_1, f_2, and f_3 for the first RSP2.

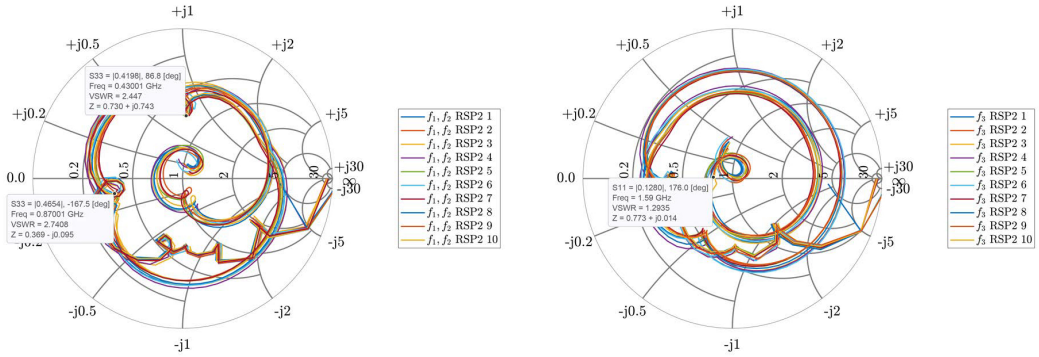

(a) Smith charts of all 10 RSP2 for frequencies f_1 and f_2.

(b) Smith charts of all 10 RSP2 for frequencies f_3.

Figure 5.13: Smith charts showing the input impedances of all 10 RSP2 for frequencies f_1 and f_2 in Fig. 5.13a and for frequency f_3 in Fig. 5.13b.

to 76 dB and sensitivity to -126 dBm and -116 dBm respectively. Furthermore, the biggest missmatch loss for f_3 was measured to be 2 dB, therefore, the dynamic range was reduced to 78 dB and sensitivity was reduced to -108 dBm. The overall measured missmatch losses were applied on the received RSS measurements as part of the calibration, to acquire the correct RSS.

With the receiver sensitivity being estimated with the missmatch loses, the maximum indoor range was estimated next. The transmit power was set to -30 dBm and the SNR was assumed to be above zero. To take into consideration attenuation for the walls the

Table 5.4: Input impedances of the RSP2s, at frequencies f_1, f_2, and f_3.

	RSP2 1	RSP2 2	RSP2 3	RSP2 4	RSP2 5	RSP2 6	RSP2 7	RSP2 8	RSP2 9	RSP2 10	
f_1	$32.9+41j$	$34.8+37.6j$	$29.8+40.1j$	$28.8+40.8j$	$33+36.7j$	$33.2+43.4j$	$35.7+37.5j$	$33.4+37.8j$	$35.1+39j$	$33.1+38.1j$	Ω
f_2	$17.1-7.4j$	$19.1-7.1j$	$17.8-11j$	$16.5-9.1j$	$18.8-6.8j$	$17-6.5j$	$18.3-4.9j$	$18.4-8.7j$	$19.4-5.2j$	$19.4-8.3j$	Ω
f_3	$34.8-5.9j$	$34.8-0.5j$	$33.7-6.2j$	$34.5-3.1j$	$34.1-3.3j$	$35.7-2.7j$	$37.5-2.7j$	$37.1-6.5j$	$38.8+1.4j$	$40.3-2.7j$	Ω

Table 5.5: Input impedances of the ULA elements, at frequencies f_1, f_2, and f_3.

	Ant. 1	Ant. 2	Ant. 3	Ant. 4	Ant. 5	Ant. 6	Ant. 7	Ant. 8	Ant. 9	Ant. 10	
f_1	$49.7+17.1j$	$59.1+9.4j$	$77.8+3.9j$	$65.8-14.5j$	$111.4+43.2j$	$82+4.6j$	$60.9+20.8j$	$78.6+8.6j$	$80.9+15.4j$	$76.9-10.2j$	Ω
f_2	$40.6-17.4j$	$34.4-28.1j$	$39.7-36.1j$	$37-26.4j$	$35-38j$	$32.9-30.1j$	$26.6-22.7j$	$29.7-28.4j$	$34.9-29.8j$	$32.7-19.1j$	Ω
f_3	$51+50.2j$	$55.5+46.5j$	$53.9+49.8j$	$49.8+51.1j$	$36.8+50.4j$	$68.9+55j$	$50.1+45.1j$	$44.5+58.9j$	$50.1+59.9j$	$36.5+48.8j$	Ω

Table 5.6: Table of the impedance missmatch between the conjugate impedances of RSP2s and the antennas, at frequencies f_1, f_2, and f_3.

	P_1^{ML}	P_2^{ML}	P_3^{ML}	P_4^{ML}	P_5^{ML}	P_6^{ML}	P_7^{ML}	P_8^{ML}	P_9^{ML}	P_{10}^{ML}	
f_1	2.9	1.5	1.7	0.8	3.9	1.6	2.4	1.6	1.9	0.9	dB
f_2	1.8	2.6	5.1	3.3	3.9	3.2	1.9	3.6	2.3	1.7	dB
f_3	1.0	1.2	1.0	1.2	1.4	1.4	0.9	1.3	1.9	1.2	dB

International Telecommunications Union (ITU) model was used [113]. For all frequencies the signal attenuation by two walls was set to 19 dB, by three walls was set to 24 dB, and by four walls was set to 29 dB. The maximum distances that the sensitivity criterion was met, are presented in Table 5.7. This table provides a coarse expectation of the system performance under different circumstances. For example, in an indoor environment for frequencies f_1 and f_2, a link between transmitter and receiver would be possible even for four rooms apart. On the contrary for f_3 the expectation of four walls and 13.4 m distance is unrealistic. Therefore, the three walls assumption would be more suitable.

Finally, the characterisation proved that the designed RSP2 receiver array was able to provide a suitable sensitivity, dynamic range, and ability to cover large distances for indoor measurements. The overall design could be improved to reduce the missmatch losses by designing specific matching circuit for each antenna, but this would impose issues with the mutual coupling at the lower frequencies. Therefore, in this stage the receiver array performance was judged to be adequate to proceed with the final measurements performed for Chapters 6 and 7.

Table 5.7: Maximum distances with the transmitter with the power of -30 dBm placed in a straight line from the receiver, for different frequencies, number of rays, and walls between them.

	$f_1 = 434$ MHz			$f_2 = 869$ MHz			$f_3 = 1595$ MHz			
Walls	2	3	4	2	3	4	2	3	4	
Max distance with 1 ray	1238.8	696.6	391.7	195.4	109.9	61.8	42.4	23.8	13.4	m
Max distance with 2 rays	696.6	407.4	237.7	158.9	108.9	75.3	36.5	19.6	17.7	m
Max distance with 3 rays	391.7	268.5	170.6	139.0	99.1	69.5	37.8	32.7	14.9	m
Max distance with 5 rays	195.4	206.1	154.2	151.7	111.7	80.9	21.5	13.3	18.7	m

Chapter 6

Novel technique extracting AoA from frequency diverse RSS patterns

This Chapter presents a novel technique for performing localisation utilising the RSS. Section 6.1 serves as an introduction to the first RSS measurements in an anechoic chamber, while Section 6.2 presents the second set of measurements performed outdoors to confirm the idea. Section 6.3 shows the effect of a theoretical indoor environment on the RSS, while Section 6.4 is dedicated on the novel technique of estimating the AoA using RSS, and presents the results and comparison with the state of the art systems. Finally, Section 6.5 discusses the overall results and draws conclusions on how MF can be used to produce similar results with the state of the art but to reduce the complexity and overall cost.

6.1 Anechoic chamber RSS measurements

This Section presents the theoretical model and the results of the first RSS measurements performed in an anechoic chamber. First, 6.1.1 presents the free space theoretical model which represents the anechoic chamber and it is used to compare with the measured results. Subsection 6.1.2 is dedicated to presenting the measurement environment, while Subsection 6.1.3 presents the results from the the RSS patterns measured in the anechoic chamber and compares them with the theoretical model.

6.1.1 Free space theoretical model

The simplest scenario is the single ray communication between transmitter and receiver, referred to as the LOS. The Friis transmission formula is used to obtain the received

power such as [106],

$$P^{RX} = P^{TX}\left(\frac{\lambda}{4\pi d}\right)^2 G^{TX} G^{RX} \tag{6.1}$$

where, P^{RX} is the received power, G^{RX} and G^{TX} are the gains of receiving and transmitting antennas respectively, and d is the distance between receiving and transmitting antennas. Thus, the actual pathloss P^{LS} is determined by $(\lambda/4\pi d)^2$, assuming ideal isotropic antennas with $G^{RX} = G^{TX} = 1$ dBi, it can be is defined as [106],

$$\begin{aligned} P^{LS} &= 10\log_{10}\left(\frac{P^{TX}}{P^{RX}}\right) = 20\log_{10} d - 20\log_{10}\lambda + 21.98 \Longleftrightarrow \\ P^{LS} &= 20\log_{10} d + 20\log_{10} f - 147.6 \qquad \text{(dB)}, \end{aligned} \tag{6.2}$$

where, the wavelength λ is expressed as $\lambda = c/f$, $c = 3\,10^8$ is the speed of the propagating wave, and f is the operating frequency. Therefore, pathloss is proportional to distance and frequency.

The primary use of the free space model is for satellite or space communications, and anechoic environments without reflections. In this Section, the free space model was used to simulate the anechoic environment and compare it with the measurements presented in the following Section.

6.1.2 Anechoic chamber measurement environment

This Subsection presents the first RSS measurements that were performed in an anechoic chamber. The purpose of the anechoic chamber is to provide a controlled environment and eliminate any reflections that might exist in real environments. The transmitter employed was an E4437B signal generator connected to a UHALP 9108 log periodic antenna, as seen in Fig. 6.1a. The transmit power was set to -50 dBm, while the gains of the log periodic antenna for frequencies f_1, f_2, and f_3 were 6.4 dBi, 7.3 dBi, and 7.2 dBi respectively. The employed receiving ULA was the initial RTL-SDR receiver but it is not presented in this research, since it was later replaced by the RSP2 receiver presented in Section 5.3. The ten element ULA and two RTL-SDR boxes with the USB cables can be seen in Fig. 6.1b.

A detailed map of the receiving ULA in a static static position, and the four different transmitting locations can be seen in Fig. 6.1c. The ULA was set in the middle of the bottom side at a height of 0.9m, while the transmitter always had an offset from the centre of -0.7 m. The height of the transmitting antenna was 1.2m, and different length offsets were chosen, 4 m in location A, 3 m in location B, 2 m in location C, and 1 m in location D. The different length offsets were chosen to show the affect of the receiving RSS patterns in the three different frequencies.

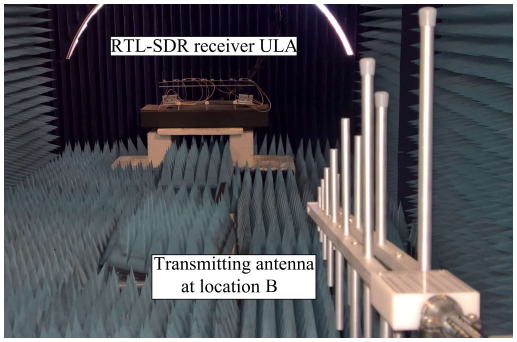

(a) The log periodic transmitting antenna.

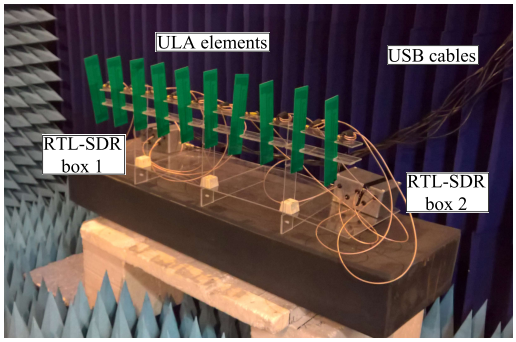

(b) The ULA receiver employing 10 RTL-SDRs.

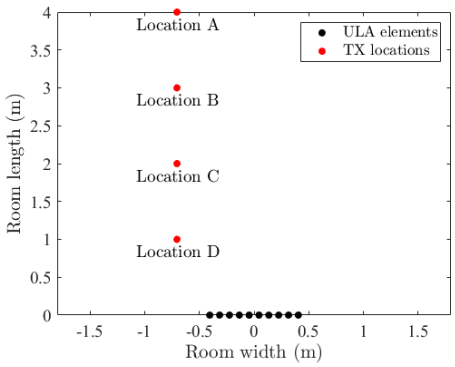

(c) Map of the anechoic chamber, with the exact locations of the transmitter and the ULA.

Figure 6.1: Details of the first RSS measurements in an anechoic chamber. Fig. 6.1a presents the transmitting antenna, Fig. 6.1b presents the receiving ULA, and Fig. 6.1c shows a detailed map of the receiving ULA and the different transmitting locations.

6.1.3 Measurement results

This Subsection presents the RSS patterns of the measurements. For every location and frequency in Fig. 6.2, three RSS patterns are presented. First, is the measured RSS in the anechoic chamber, then the theoretical RSS without the receiving ULA gain patterns, and finally the theoretical RSS with the receiving ULA gain patterns taken into consideration. The theoretical RSS is estimated with the free space loss equation (6.2). The RSSs are presented vertically, with the top being the farthest, and bottom being the closest to the ULA.

Fig. 6.2a presents the RSS patterns for frequency f_1 and locations A, B, C, and D. Comparing the RSS in location D, which is close to the ULA, it is evident that the gain antenna patterns affect the received signal RSS patterns. Moreover, the measured RSS pattern match with the theoretical RSS therefore the far filed radiation patterns of the ULA presented in Section 4.2 are accurate. The maximum difference of the theoretical RSS between with and without the received gain pattern is circa 15 dB. Therefore, even with a 3 dB variance in the measured RSS a pattern can be easily determined. As the transmitter gets farther away from the receiver, in location C, the maximum difference of

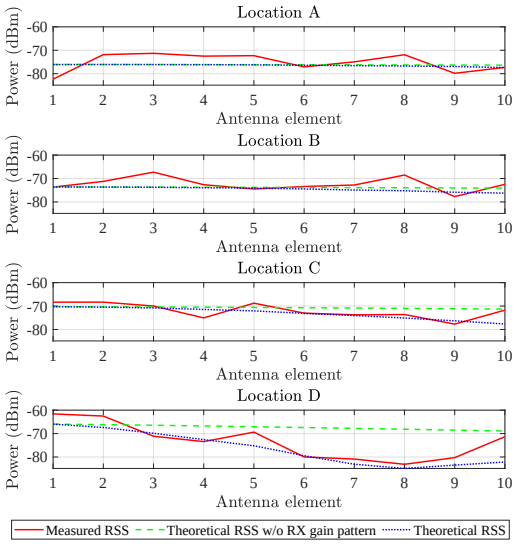

(a) RSS patterns for $f_1 = 434$ MHz in four locations A, B, C, and D.

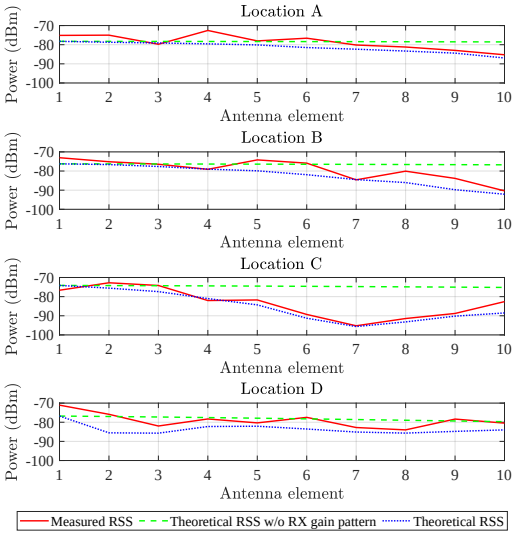

(b) RSS patterns for $f_2 = 869$ MHz in four locations A, B, C, and D.

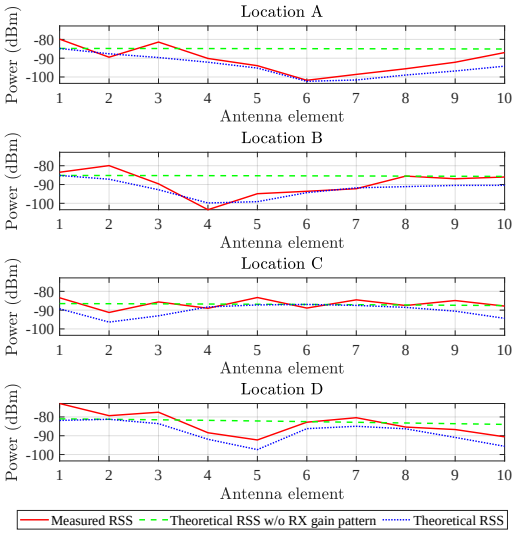

(c) RSS patterns for $f_3 = 1595$ MHz in four locations A, B, C, and D.

Figure 6.2: RSS patterns of the four locations A, B, C, D, and the three frequencies, f_1 in Fig. 6.2a, f_2 in Fig. 6.2b, and f_3 in Fig. 6.2c.

the theoretical RSS between with and without the received antenna gain is reduced to circa 6.3 dB, while for location B is reduced even further to 2.1 dB. Hence, apart from location D, the RSS pattern is indistinguishable.

Fig. 6.2b presents the RSS patterns for frequency f_2 and locations A, B, C, and D. Contrary to the lower frequency f_1, the maximum difference of the theoretical RSS between with and without the received gain is lower for location D, circa 9 dB. But as the distance increases, the difference is increased as well. Location C experiences a maximum RSS difference of circa 20 dB, and for location B the RSS difference is circa 15.4 dB. Finally, for

location A the RSS difference is reduced again to circa 8.4 dB. Overall, the measured RSS seems to fit the theoretical RSS and being able to produce a distinguishable pattern for locations C and B.

Fig. 6.2c presents the RSS patterns for frequency f_3 and locations A, B, C, and D. Comparing the maximum difference of the theoretical RSS between with and without the received gain in locations D, C, B, A, results to a difference of circa 15.2 dB, 9.8 dB, 13.8 dB, and 17.3 dB respectively. Hence, the effect of the pattern is much larger in all locations compared to the other two frequencies. Moreover, again the measured RSS is evident that follows the theoretical RSS and the pattern is distinguishable in all three frequencies.

Taking into consideration the findings of measurements in this stage of research, it was evident that the different RSS patterns from MF can be utilised. The low frequency f_1 experienced RSS variations of circa 15 dB because of the receiving antenna gain pattern when the transmitter was closely located to the receiver. The middle frequency f_2 experienced RSS variations of 20 and 15.4 dB for locations B and C, while for the high frequency f_3 the RSS variations were always above 9.8 dB for all locations.

The different patterns could potentially serve as a fingerprint for each location, but further investigation was required. Since real environments experience reflections, the measurements in the anechoic chamber were not fully representative to a real case scenario. Hence, a second set of RSS measurements was performed outdoors, where at least a single reflection was present, and the reflection coefficient can be estimated.

6.2 Outdoor RSS measurements

This Section presents the theoretical model and results of the second set of RSS measurements performed in an outdoor environment. First, Subsection 6.2.1 presents the two-ray theoretical model which represents the outdoor environment and it is used to compare with the measured results. Subsection 6.2.2 is dedicated to the details of the measurements environment, while Subsection 6.2.3 presents the results from the the RSS patterns measured in the outdoor environment and compares them with the theoretical model

6.2.1 Two-ray theoretical model

In real world environments the transmitted signal finds more than a single path to reach the transmitter. Thus, in terrestrial communications the two-ray model can be used. In an outdoor environment, as the transmitted signal propagates to the receiver apart from the direct LOS at least a single ground reflection appears as shown in Fig. 6.3. This creates a more complex pathloss model since the two received rays can be either added constructively or destructively. The outcome of the ray addition (constructive or destructive) is determined by the reflection coefficient Γ, and the phase of the received ray, which is determined by the distance covered by the ray, d_1 or d_2.

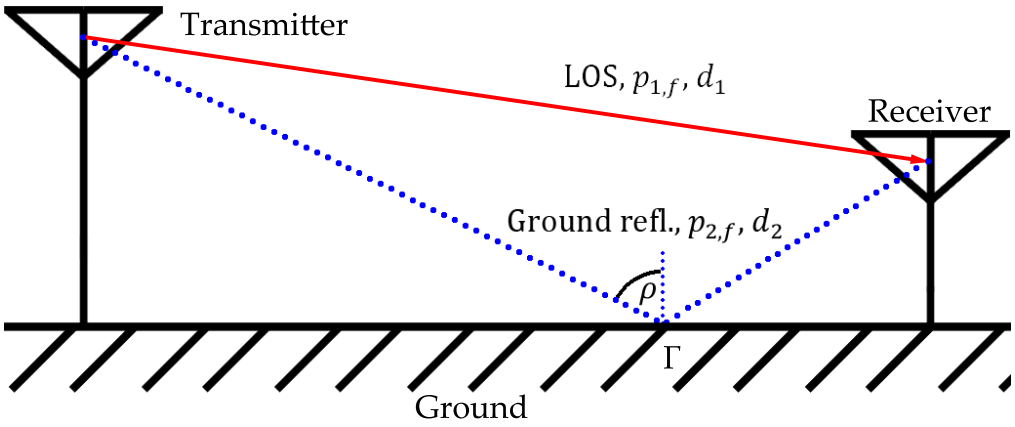

Figure 6.3: Example of a two-ray model where the transmitted wave propagates as two rays (red LOS, and blue ground reflection) before reaching in the receiver.

To further understand the constructive or destructive addition, both rays (or paths), p_1 for the LOS and p_2 for the ground reflection, are represented as continuous time waves,

$$p_1(t) = Re\left\{\frac{\lambda}{4\pi}\sqrt{G_1^{TX}}\,x(t)\frac{e^{-j2\pi d_1/\lambda}}{d_1}\right\} \tag{6.3}$$

$$p_2(t) = Re\left\{\frac{\lambda}{4\pi}\sqrt{G_2^{TX}}\,\Gamma(\rho)\,x(t-\tau)\frac{e^{-j2\pi d_2/\lambda}}{d_2}\right\} \tag{6.4}$$

where, $Re\{\cdot\}$ is the real part of $\{\cdot\}$, $\sqrt{G_1^{TX}}$ and $\sqrt{G_2^{RX}}$ are the antenna gains for the LOS and ground reflection rays, $\Gamma(\rho)$ is the reflection coefficient of the ground at an angle ρ, $x(t)$ is the transmitted signal, τ is the excess time that the ground reflection takes to reach the receiver (known as delay spread), and the term $e^{-j2\pi d/\lambda}$ determines the phases of the received ray based on d_1 and d_2, which are the path distances of LOS and ground reflection respectively. Because the continuous time waves are represented in Euler form, the use of $Re\{\cdot\}$ is necessary to negate the imaginary product.

To simplify the two-ray model we assume a narrow band signal, relative to the inverse delay spread $1/\tau$, so $x(t) \approx x(t-\tau)$. By averaging the transmitted signal $x(t)$ in time $P^{TX} = E\{|x(t)|^2\}$, and assuming the same gain for both rays $G^{TX} = G_1^{TX} = G_2^{TX}$, the received power P^{RX} can now be defined as,

$$P^{RX} = P^{TX}\left(\frac{\lambda}{4\pi}\right)^2\left|\frac{e^{-j2\pi d_1/\lambda}}{d_1} + \Gamma(\rho)\frac{e^{-j2\pi d_2/\lambda}}{d_2}\right|^2 G^{RX}G^{TX} \Longleftrightarrow \tag{6.5}$$

$$P^{RX} = P^{TX}\left(\frac{\lambda}{4\pi}\right)^2\left|\frac{1}{d_1} + \Gamma(\rho)\frac{e^{-j\Delta\phi}}{d_2}\right|^2 G^{RX}G^{TX} \tag{6.6}$$

where, $\Delta\phi = 2\pi(d_2 - d_1)/\lambda$ is the phase difference between the two rays. With the same

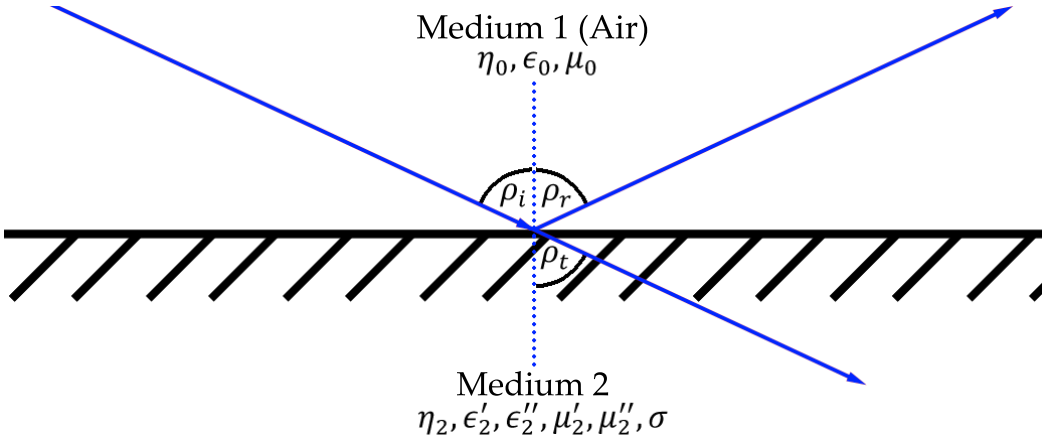

Figure 6.4: Example of a wave reflection and transmission and its analogous electromagnetic properties.

fashion as the (6.2), the pathloss P^{LS} for the two ray model is defined as,

$$P^{\text{LS}} = 20\log_{10}(d_2\ d_1\ f) - 20\log_{10}\left(\left|d_1 + d_2\ \Gamma(\rho)\ e^{-j\Delta\phi}\right|\right) - 147.6 \qquad \text{(dB)} \tag{6.7}$$

It is now evident that for the two-ray model the pathloss is not only affected by distances and frequency but by the reflection coefficient $\Gamma(\rho)$ as well. Thus, it is necessary to investigate the reflection coefficient and understand it in order to understand the pathloss when reflections occur.

The reflection coefficient Γ is defined as the ratio of the reflected wave to the incident wave, and can be described as a transmission line equation for impedance to Γ conversion [114],

$$\Gamma = \frac{Z_2 - Z_1}{Z_2 + Z_1}, \tag{6.8}$$

where, Z_1 and Z_2 are the characteristic impedances of medium 1 and 2 respectively. Using Snell's law, the characteristic impedances of the first and second medium are defined as [114],

$$Z_1 = \begin{cases} \eta_1 \cos\rho_i & \text{for parallel polarisation.} \\ \eta_1 / \cos\rho_i & \text{for perpendicular polarisation.} \end{cases} \tag{6.9}$$

$$Z_2 = \begin{cases} \eta_2 \cos\rho_t & \text{for parallel polarisation.} \\ \eta_2 / \cos\rho_t & \text{for perpendicular polarisation.} \end{cases} \tag{6.10}$$

where, η_1 and η_2 are the intrinsic impedances of the medium 1 and 2 respectively, ρ_i is the incident angle and ρ_t is the transmitted angle on medium 2 as seen in Fig. 6.4.

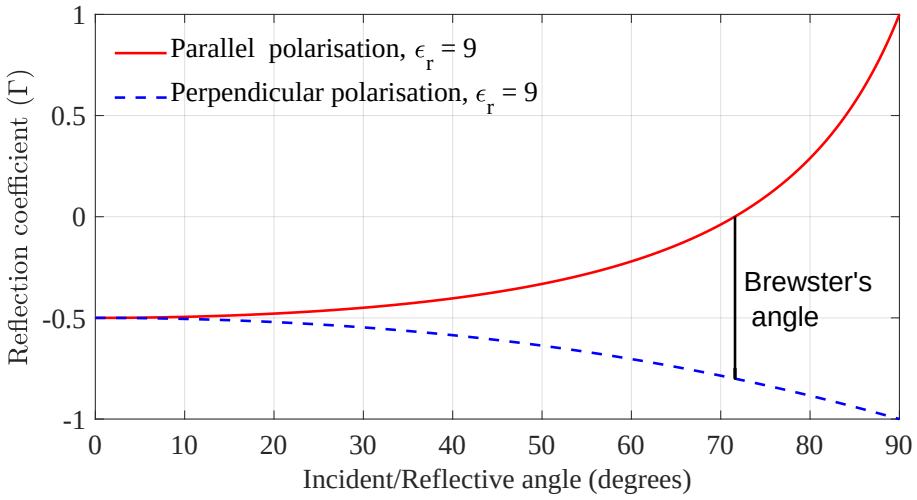

Figure 6.5: Reflection coefficient of vertically polarised antenna, as a function of incident angle and antennas with parallel (red) and perpendicular (blue dashed) polarisation.

Since medium 1 is air, the permeability is $\mu_1 = \mu_0 = 4\pi 10$ µH/m, and permittivity is $\epsilon_1 = \epsilon_0 = 8.85$ pF/m.

Furthermore, the intrinsic impedance is defined by the surface electromagnetic properties and for a complex surface is defined as [114],

$$\eta = \sqrt{\frac{j\omega(\mu' - j\mu'')}{\kappa + j\omega(\epsilon' - j\epsilon'')}}, \tag{6.11}$$

where, ω is the angular frequency of the propagating signal, μ' and μ'' are the real and imaginary magnetic permeability of the medium, ϵ' and ϵ'' are the real and imaginary permittivity of the medium, and κ is the conductivity of the medium. Thus, the intrinsic impedance of medium 1 is $\eta_1 = \eta_0 = 120\pi\ \Omega$.

The complex permeability and permittivity that define the intrinsic impedance η_2 of medium 2 can be calculated as ratios of their relative counterparts, which are defined respectively as [114],

$$\mu_r = \frac{\mu' - j\mu'}{\mu_0}, \quad \epsilon_r = \frac{\epsilon' - j\epsilon''}{\epsilon_0}. \tag{6.12}$$

The electromagnetic properties of the reflected surface play an important role in the overall intrinsic impedance. Thus, the overall received power is varied based on the reflection coefficient Γ which is defined by the surface electromagnetic properties, the carrier frequency, and the incident angle ρ_i. The permeability and permittivity ratios of different materials that are found in the environment are well researched in literature and the different values can be found [114].

Fig. 6.5 presents the reflection coefficient Γ of a vertical polarised antenna with parallel

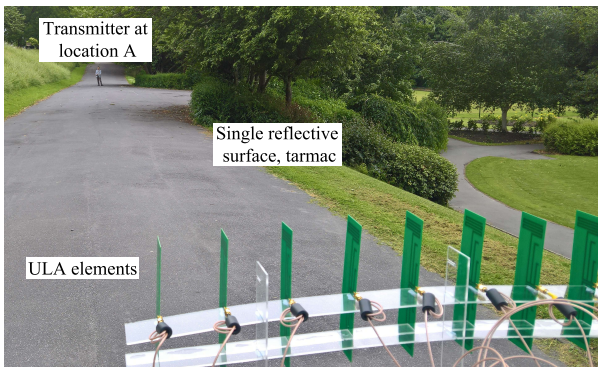

(a) ULA receiver and transmitter at location A, with a single reflective tarmac surface.

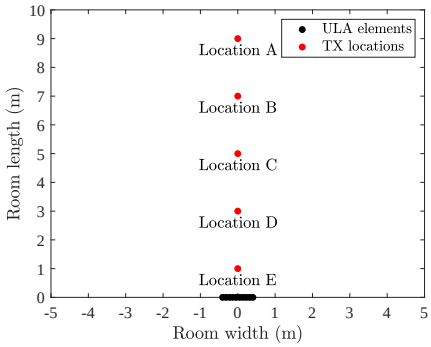

(b) Map of the outdoor environment, with the exact locations of the transmitter and the ULA.

Figure 6.6: Details of the second RSS measurements in an outdoor environment. Fig. 6.6a presents the receiving ULA and the transmitting antenna during the measurements, and Fig. 6.6b shows a detailed map of the receiving ULA and the different transmitting locations.

and perpendicular incident angles, with relative permittivity ϵ_r = 9 and relative permeability μ_r = 1. For a wave with perpendicular polarisation, as the incident angle increases, the reflection coefficient increases as well. On the other hand, for the parallel polarisation at a specific incident angle the reflection coefficient can vanish (Γ = 0). This point is also known as the Brewster's angle. Furthermore, as the incident wave increases beyond Brewster's angle the reflected wave does not rotate as the reflection coefficient changes from negative to positive.

Finally, the two-ray model is often adequate to represent outdoor terrestrial environments. The two-ray model was used in this research to simulate outdoor environment and compare it with with the measurements presented in Section 6.2. Furthermore, to test our hypothesis an even more complex channel model was required as indoor environments experience the reflection of multiple rays.

6.2.2 Outdoor measurement environment

This Subsection presents the RSS measurements performed outdoors. The purpose of doing measurements outdoors was to introduce a real environment with a single controlled reflection and investigate its effect. The reflective surface was tarmac, with a permittivity ratio of $e_r = 4.3$. The employed transmitter was the ADF4351 and the designed tri-band PCB antenna, presented in Section 4.1. The transmit power was attenuated by -50 dB across all frequencies to supply a transmission power inside the dynamic range of the receiver. The receiving ULA employed was a RTL-SDR receiver that is not presented, since it was later replaced by the RSP2 receiver presented in Section 5.3. The ULA elements and the transmitter at a distance of 9 m in the outdoor environment can be seen in Fig. 6.6a.

A detailed map of the ULA static position and five different transmitting locations can be seen in Fig. 6.6b. The ULA was set in the middle of the bottom side at a height of 1.5m,

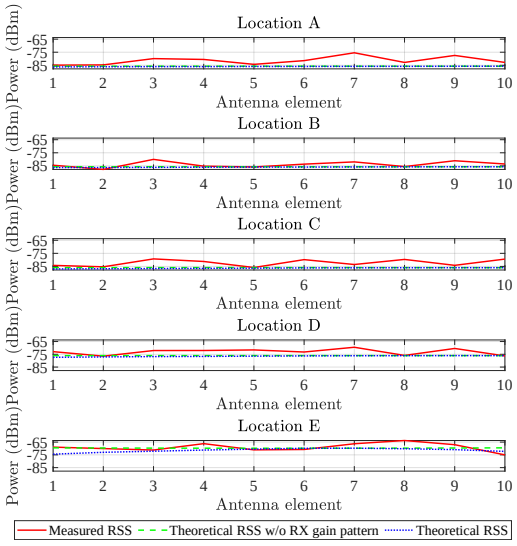

(a) RSS patterns for $f_1 = 434$ MHz in four locations A, B, C, D, and E.

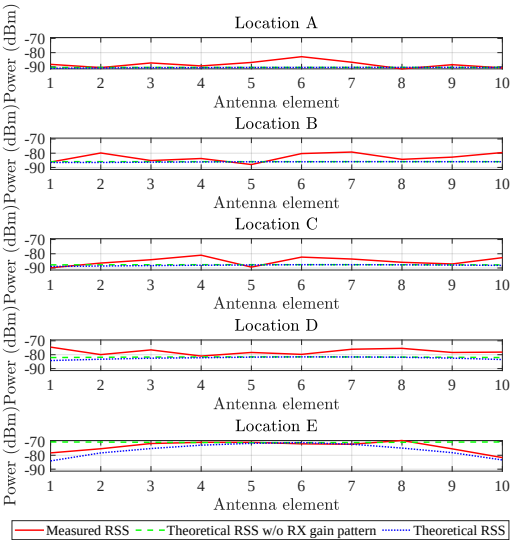

(b) RSS patterns for $f_2 = 869$ MHz in four locations A, B, C, D, and E.

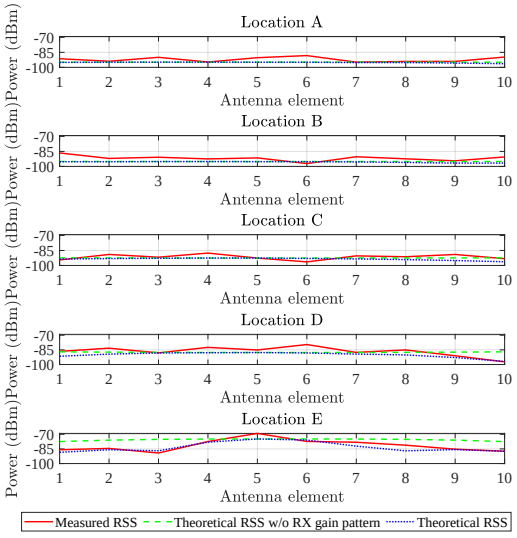

(c) RSS patterns for $f_3 = 1595$ MHz in four locations A, B, C, D, and E.

Figure 6.7: RSS patterns of the four locations A, B, C, D, E, and the three frequencies, f_1 in Fig. 6.7a, f_2 in Fig. 6.7b, and f_3 in Fig. 6.7c.

while the transmitter was always in the middle of the side as well, at a height of 1.5 m and a length distance of 9 m in location A, 7 m in location B, 5 m in location C, 3 m in location D, and 1 m in location E. The different length offsets were chosen to show the effect of the receiving RSS patterns in the three different frequencies with the presence of a reflection.

6.2.3 RSS pattern measurements

This Subsection presents the RSS patterns of the measurements. For every location and frequency in Fig. 6.7 three RSS patterns are presented. The RSS in the outdoor environment is measured first, then the theoretical RSS without the receiving ULA gain patterns, and finally the theoretical RSS with the receiving ULA gain patterns taken into consideration. The theoretical RSS is estimated with the two-ray model equation (6.6). The RSSs are presented vertically, with the top being the farthest and the bottom being the closest to the ULA.

Fig. 6.7a presents the RSS patterns for frequency f_1 and locations A, B, C, D, and E. Similarly to the previous measurements, even in the location E, where the transmitter is the closest to the receiver, the maximum difference of the theoretical RSS with and without the received gain is circa 5 dB. As the transmitter gets farther away, the difference of the two RSS patterns becomes negligible. Therefore, the outdoor environment reduces the pattern difference, compared to the anechoic chamber. Overall, the measured RSS is well within the expected of range of theoretical RSS.

Fig. 6.7b presents the RSS patterns for frequency f_2 and locations A, B, C, D, and E. In the middle frequency and location E, the maximum difference of the theoretical RSS with and without the received gain is circa 14 dB. Compared to the anechoic chamber it has increased by 5 dB, making the RSS pattern more evident. Moreover, for the remaining locations no patterns are evident, contrary to the anechoic chamber measurements, where a pattern is evident even when the transmitter is 3 m away from the receiver. Furthermore, the measured RSS is able to obtain a distinguishable pattern for the location E, and overall to follow the correct theoretical RSS values. The lack of patterns in longer range was studied extensively and it was found that it was due to the placement of the transmitter. For the measurements performed in an anechoic environment, the transmitter had an offset from the centre of the ULA. On the outdoor measurements, the transmitter was in the middle. Through simulation it was found that vertical offset allowed the formulation of more complex RSS patterns due to different angles.

Fig. 6.7c presents the RSS patterns for frequency f_3 and locations A, B, C, D, and E. Comparing the maximum difference of the theoretical RSS with and without the received gain in locations E, and D, results to a difference of circa 11 dB, 10 dB, respectively. As the transmitter gets farther away for locations C, B, and A, the RSS patterns become flat. As explained above, the reason was the placement of the transmitter and the lack of horizontal offset. Therefore, the overall performance is similar to the anechoic chamber measurements, where the pattern is visible up to a 4 m vertical distance from the ULA. As for the measured RSS it is evident that is able to obtain the correct patterns for locations E and D, and obtain RSS values close to the theoretical for locations A, B and C.

The measurements performed in the outdoor environment, showed that the received gain patterns were not visible in the low and middle frequencies, while they were on the high frequency. Comparing the measurements of the outdoor environment with the anechoic chamber, the high frequency f_3 was the only one that could obtain a received

gain pattern for a length offset of 4 m. Therefore, it was evident that the single ground reflection did not help the pattern formulation, and moreover, the overall pattern was not attainable when a transmitter got farther away from the receiver.

The main difference between the outdoor and anechoic chamber measurements could be attributed to the transmitting locations. In the anechoic chamber, the transmitter had a horizontal offset of 0.7m, while for the outdoor measurements there was no offset. Therefore, the results of the two measurements were not directly comparable, but it did show that the presence of a ground reflection did not formulate more complex patterns. To further investigate the effects of the reflections, in the next Subsections the indoor environment will be studied, first by simulation and the by measurements.

6.3 Theoretical RSS patterns in an indoor environment

This Section presents the theoretical model, simulation and the results of an indoor multi-ray environment. This Section is critical to understand how the extraction of AoA from frequency diverse RSS patterns is possible. First, Subsection 6.3.1 presents the theoretical model for the indoor environment, while Subsection 6.3.2 introduces the indoor environment used in the simulation. Subsection 6.3.2 is dedicated to the theoretical RSS patterns in a cluster, while Subsection 6.3.3 presents the theoretical RSS patterns in back row of the indoor environment. Finally, Subsection 6.3.4 is dedicated to presenting the RSS in the indoor environment as a function of distance to show why RSS indoor localisation is difficult and to justify decisions made in the following Section.

6.3.1 Multi-ray theoretical model

In an indoor environment more than a single reflection exist, hence a multi-ray propagation model needs to be defined. An example of a multi-ray indoor environment can be seen in Fig. 6.8, where there are multiple rays ($R = 5$) that propagate from the transmitter to the receiver. Apart from the LOS (red), the wave reflects on the ground ceiling and two walls (blue) with each one of the these surfaces having a different reflection coefficient Γ.

Continuing from the two-ray model, (6.5) is expanded to represent a total of R rays,

$$P^{\mathrm{RX}} = P^{\mathrm{TX}}\left(\frac{\lambda}{4\pi}\right)^2 \left|\frac{e^{-j2\pi d_1/\lambda}}{d_1} + \Gamma_2(\rho_2)\frac{e^{-j2\pi d_2/\lambda}}{d_2} + \cdots + \Gamma_R(\rho_R)\frac{e^{-j2\pi d_R/\lambda}}{d_R}\right|^2 G^{\mathrm{RX}}G^{\mathrm{TX}} \tag{6.13}$$

where, $\Gamma_R(\rho_R)$ is the reflection coefficient of ray R with an incident angle ρ_R, and d_R is the distance that ray R propagates from the transmitter to the receiver. For the R rays, r_1 is always the LOS, and the remaining rays $r \in [2, R]$ are reflections from real surfaces, such as the ground, ceiling and walls, where the transmitted wave impacts on a surface and redirects to the receiver.

To simplify the mathematical representation, each ray has a reflection coefficient Γ_r, thus, the notation of the angle ρ is removed from the reflection coefficient, assuming

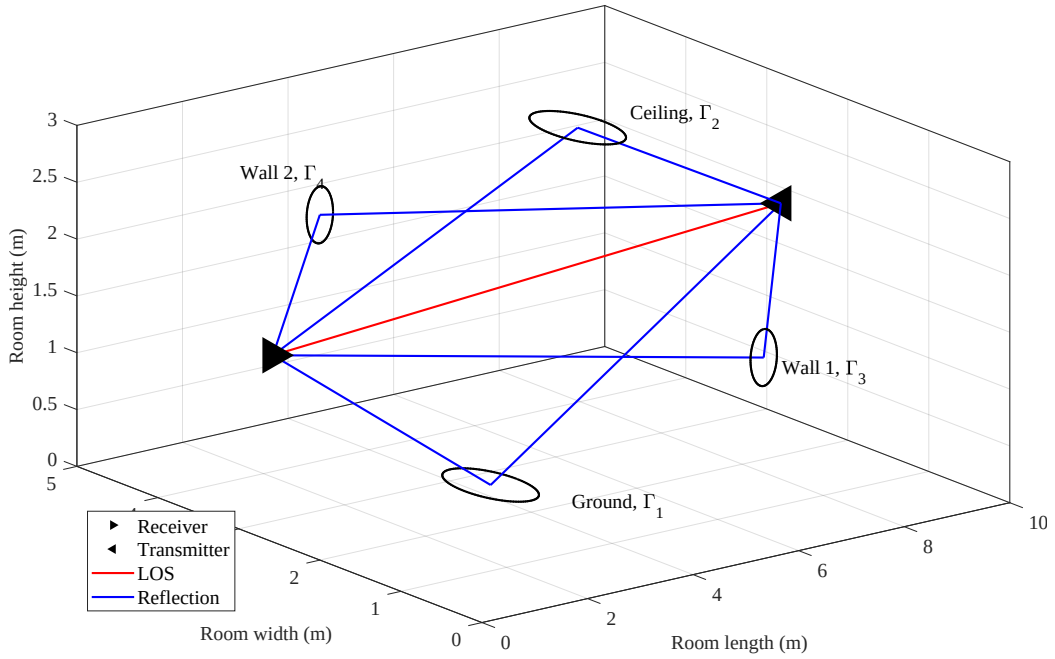

Figure 6.8: Multi-ray indoor environment where the transmitted signal finds multiple paths such as LOS (red), ground, ceiling and walls (blue), to reach the receiver.

$\Gamma_r = \Gamma(\rho_r)$. Moreover, the reflection coefficient for the LOS case ($r = 1$) is defined as $\Gamma_1 = 1$, and (6.13) can be simplified to,

$$P^{RX} = P^{TX}\left(\frac{\lambda}{4\pi}\right)^2 \left|\sum_{r=1}^{R} \Gamma_r \frac{e^{-j2\pi d_r/\lambda}}{d_r}\right|^2 G^{RX} G^{TX} \tag{6.14}$$

where, d_r is the distance between transmitter and receiver that ray r traverses, Γ_r is the reflection coefficient of the surface that ray r intercepts, and the exponential term $e^{j2\pi\frac{d_r}{\lambda}}$ represents the received phase of the ray r.

Finally, for the purpose of this research, the pathloss for the multi-ray model assuming $G^{RX} = G^{TX} = 1$ dBi is defined as,

$$P^{LS} = 20\log_{10}(f) - 20\log_{10}\left(\left|\sum_{r=1}^{R} \Gamma_r \frac{e^{-j2\pi d_r/\lambda}}{d_r}\right|\right) - 147.6. \quad \text{(dB)} \tag{6.15}$$

This equation represents the complexity of modelling an indoor environment and it was derived in the scope of this research. It shows that the overall pathloss is still proportional to the distance d_r of the rays and frequency f squared, but the phase $e^{j2\pi\frac{d_r}{\lambda}}$ caused by the summation of all rays can have the same affect. Thus, when a small shift on the transmitter location occurs, the phase of the received rays will change and this can greatly affect the pathloss.

To understand the relationship between pathloss and distance a simulation was established. The simulation took into consideration the three pathloss models presented, free

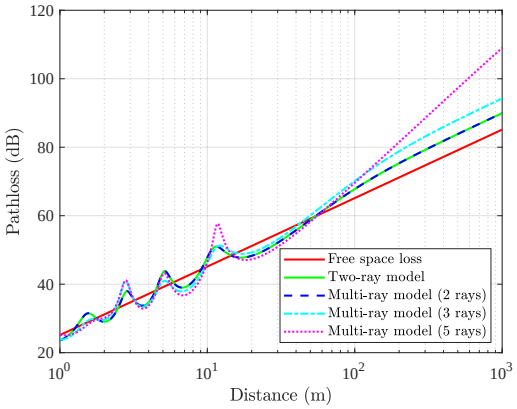

(a) Pathloss comparison between different models for frequency $f_1 = 434$ MHz.

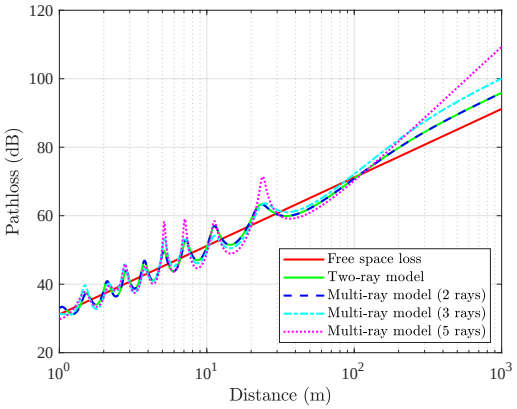

(b) Pathloss comparison between different models for frequency $f_2 = 869$ MHz.

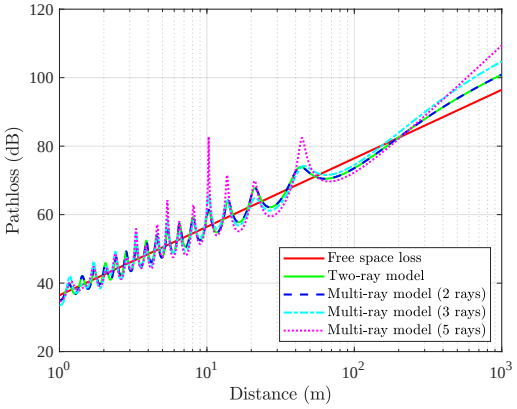

(c) Pathloss comparison between different models for frequency $f_3 = 1595$ MHz.

Figure 6.9: Pathloss comparison between the free space model, the two-ray model, and the multi-ray model with 2, 3, and 5 rays for f_1 in Fig. 6.9a, f_2 in Fig. 6.9b, f_3 in Fig. 6.9c.

space loss, two-ray model and multi-ray model, with the multi-ray model expanding over 2 rays, 3 rays, and 5 rays. Both transmitter and receiver were positioned at a height of 2 m and the change of distance was achieved by moving the transmitter in a straight line with logarithmic steps. For the 2 ray model, the ground material was set to concrete with a permittivity ratio of $\epsilon_1 = 6.2$. For the ceiling reflection (3 rays) the maximum height of the room was set to 3 m and the material was set to ceiling tiles with a permittivity ratio of $\epsilon_2 = 2.5$. While for the wall reflections, the two side walls were set to 2 meters and the material was set to drywall with a permittivity ratio of $\epsilon_3 = \epsilon_4 = 2.1$. The results of the simulation are present in Fig. 6.9.

Starting with f_1 in Fig. 6.9a, it is evident that the presence of rays formulate a variation in the pathloss. Overall four peaks are formulated between the distance of 1 m and 20 m, with a maximum variation of 10 dB compared to free space loss. Moreover, the two-ray model produced the same result with the multi-ray model with 2 rays as expected. What is interesting, is that at a distance of circa 20 meters, the pathloss variation settles

and the pathloss is constant. This point known as the critical distance d_c and it can be estimated using the height of the transmitter h_r and receiver h_r. The critical distance can be estimated using,

$$d_c = 4h_r h_t / \lambda. \tag{6.16}$$

By applying the equation 6.16, the critical distance for this case results to $d_c = 23.1$, supporting that the simulation is correct.

Furthermore, f_2 in Fig. 6.9b presents nine peaks between the distances of 1 m and 40 m, with a maximum variation of circa 12.6 dB compared to the free space loss. Therefore, it is also evident that as the frequency increases the variation increases as well. For this frequency, the critical distance is estimated to be 46.3 m, which supports the simulation results. Finally, for f_3 in Fig. 6.9c the number of peaks increase even further with fifteen peaks before the critical distance. The maximum variation is increased as well being at circa 26 dB compared to the free space loss. This results to the conclusion that high frequency signals suffer the most from reflections due to the short wavelength. Moreover, for f_3 the cutoff distance is 85 m, which is also visible from the figure.

What is also interesting from Fig. 6.9 is that after the critical distance, the pathloss is the same no matter the frequency. For example, for a distance of 100 m, the pathloss for f_1 is 69.6 dB, for f_2 is 70.2 dB, and for f_3 is 72.3 dB. Furthermore, as the distance increases the differences become even less apparent. This is due to the distances of reflections. As the distance increases the difference between the reflection distances is even smaller, resulting to a stable pathloss slope.

The multi-ray model was used in this research to simulate the indoor environment presented in Section 6.3. Furthermore, it was used to simulate and understand the MF AoA measurements performed in Chapter 7.

6.3.2 Theoretical environment

This Subsection presents the theoretical indoor environment designed for the simulation, before making measurements. The purpose of doing a simulation, was to understand what effect does the different rays have on the RSS patterns, as a function of location and material properties. For the simulation results presented in this Subsection, the first ray was the LOS while the second ray was from the ground reflection of concrete, with a permittivity of $e_2 = 6.2$. Moreover, the third ray was from the ceiling surface of tiles, with a permittivity of $e_3 = 2.5$. The fourth and fifth rays were the two side walls, in both cases assumed to be drywall, with a permittivity of $e_4 = e_5 = 2.1$. The transmit power was set at -50 dBm across all frequencies.

A detailed map of the ULA static position and 81 different transmitting locations can be seen in Fig. 6.10. The ULA was set in the middle of the bottom side at a height of 1.5 m, while the transmitter was moved at a width or length offset 0.5 m to keep a distance of 0.5 m the nearest side, at a height of 1.5 m. Moreover, the two walls that the reflection were considered were highlighted in Fig. 6.10. Finally, the two locations that the RSS patterns were investigated in Subsection 6.3.2 were highlighted in sky blue, and in Subsection 6.3.3

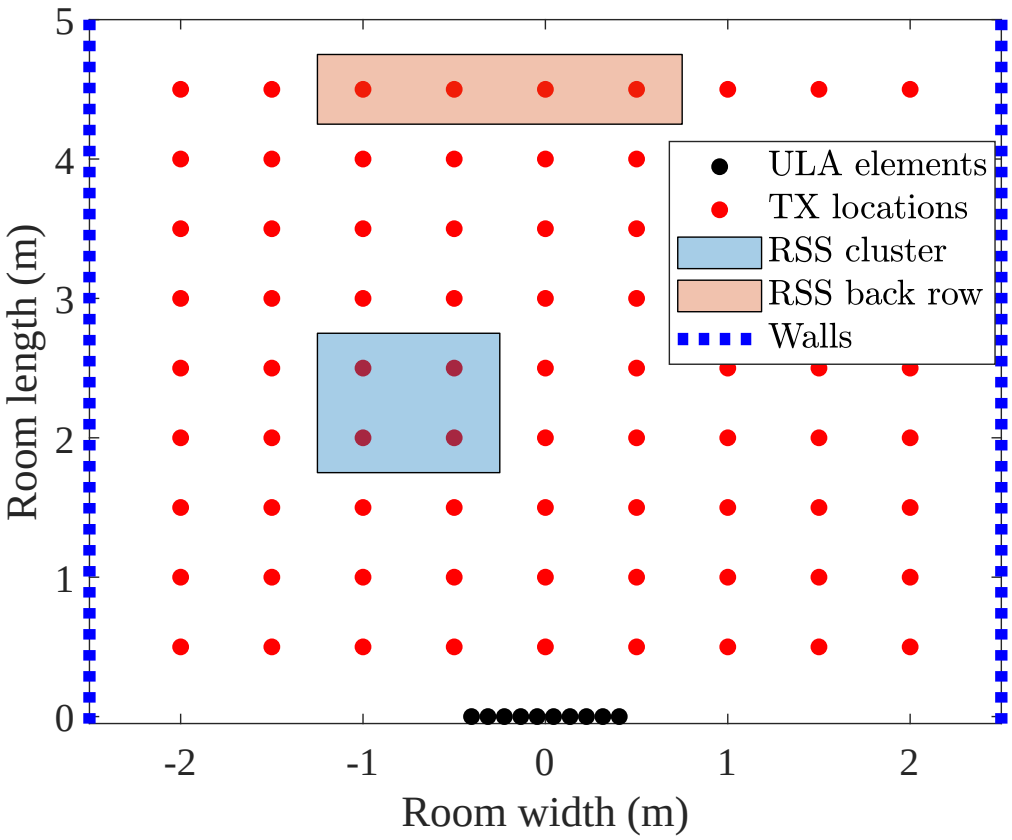

Figure 6.10: Map of the indoor theoretical environment, with the exact locations of the transmitter, ULA, walls, RSS cluster and back row locations.

was highlighted in light brown.

6.3.3 Theoretical RSS patterns in a cluster

This Subsection presents the RSS patterns of the simulation at the cluster, highlighted in 6.10. In contrast with the previous Subsections, now the theoretical RSS is presented in all frequencies for four locations, where the transmitter is shifted by 0.5 m vertically or horizontally in the room width or length, respectively. The theoretical RSS is obtained through the multi-ray equation (6.14), and the antenna gains were presented in Chapter 4.

For the low frequency f_1 in Fig. 6.11, it is evident that the patterns are different in all four locations. Therefore, even if the offset in space is only 0.5 m, the received RSS pattern can be distinguished in two out of four locations. Starting from the top of Fig. 6.11, the RSS variations between the elements are circa 3 dB, 2 dB, 17 dB, and 7 dB respectively. The only two cases that the patterns are different are at length 2.5. The other two locations offer distinguishable RSS patterns. Overall, with two out of four patterns being distinguishable in a small space, f_1 seems to be able to provide a pattern recognition diversity when the transmitter is close to the receiver.

Furthermore, regarding the middle frequency f_2, Fig. 6.11 shows that the RSS patterns

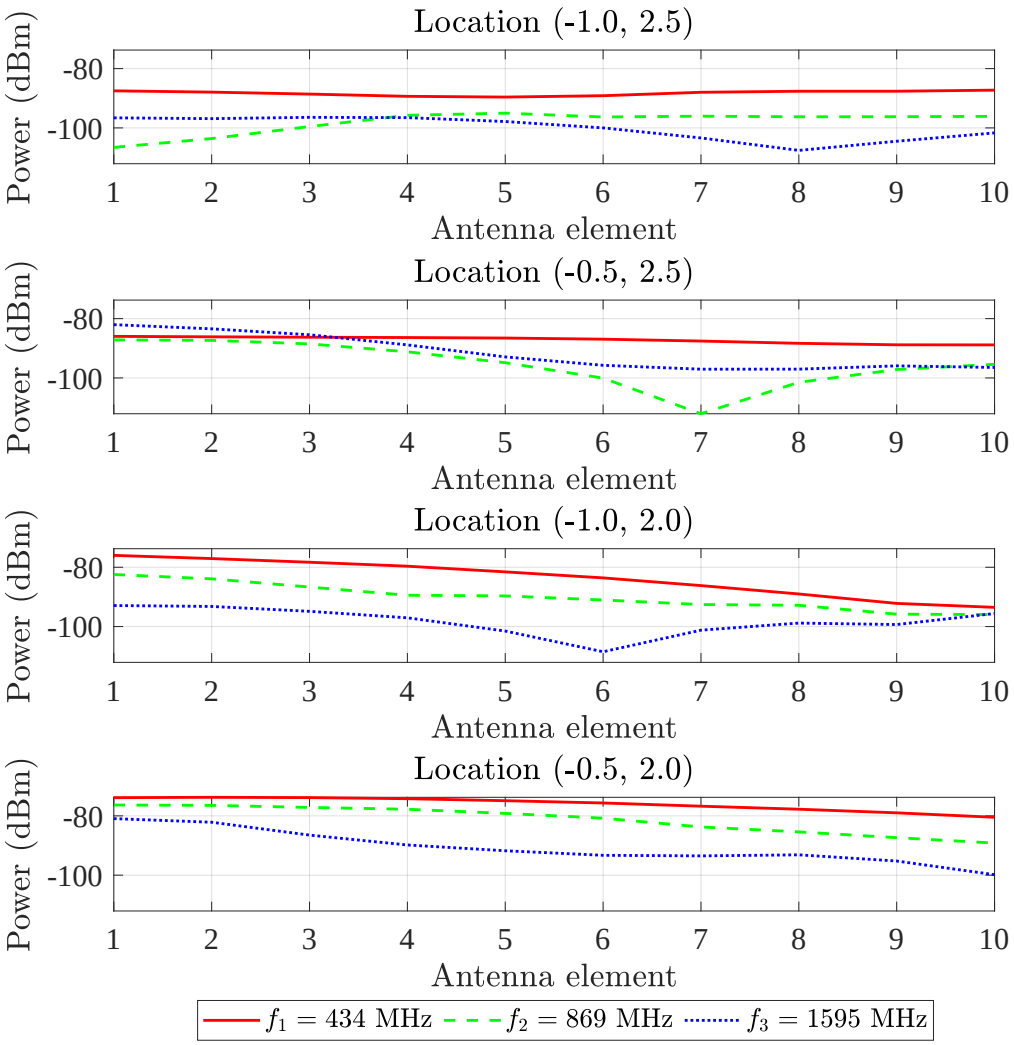

Figure 6.11: Four RSS patterns in a cluster with width and length offset of 0.5 m, and three frequencies f_1, f_2, and f_3.

are more diverse compared to the low frequency. Specifically, starting the top of Fig. 6.11, the RSS variations between the elements are circa, 10 dB, 25 dB, 13.6 dB, and 13 dB. With the middle frequency presenting at least 10 dB RSS variation between the maximum and minimum RSS, it is evident that a pattern based localisation is feasible.

For the high frequency f_3 in Fig. 6.11, it is evident that the patterns are diverse like f_2. For example, while the transmitter is at a length of 2.5 m, the RSS variations between the elements are circa 11 dB and 15 dB at an offset of -1 and 0.5 m respectively. When the transmitter gets closer to 2 m, the RSS variations between the elements increase to 15.3 dB and 19 dB at a offset of -1 and 0.5 m respectively. Hence, with the middle and high frequency patterns, location could be possible just with the use of the RSS.

Finally, this Subsection shows that the multi-frequency in an indoor environment provides a novel metric that has not been used before. The RSS patterns generated from

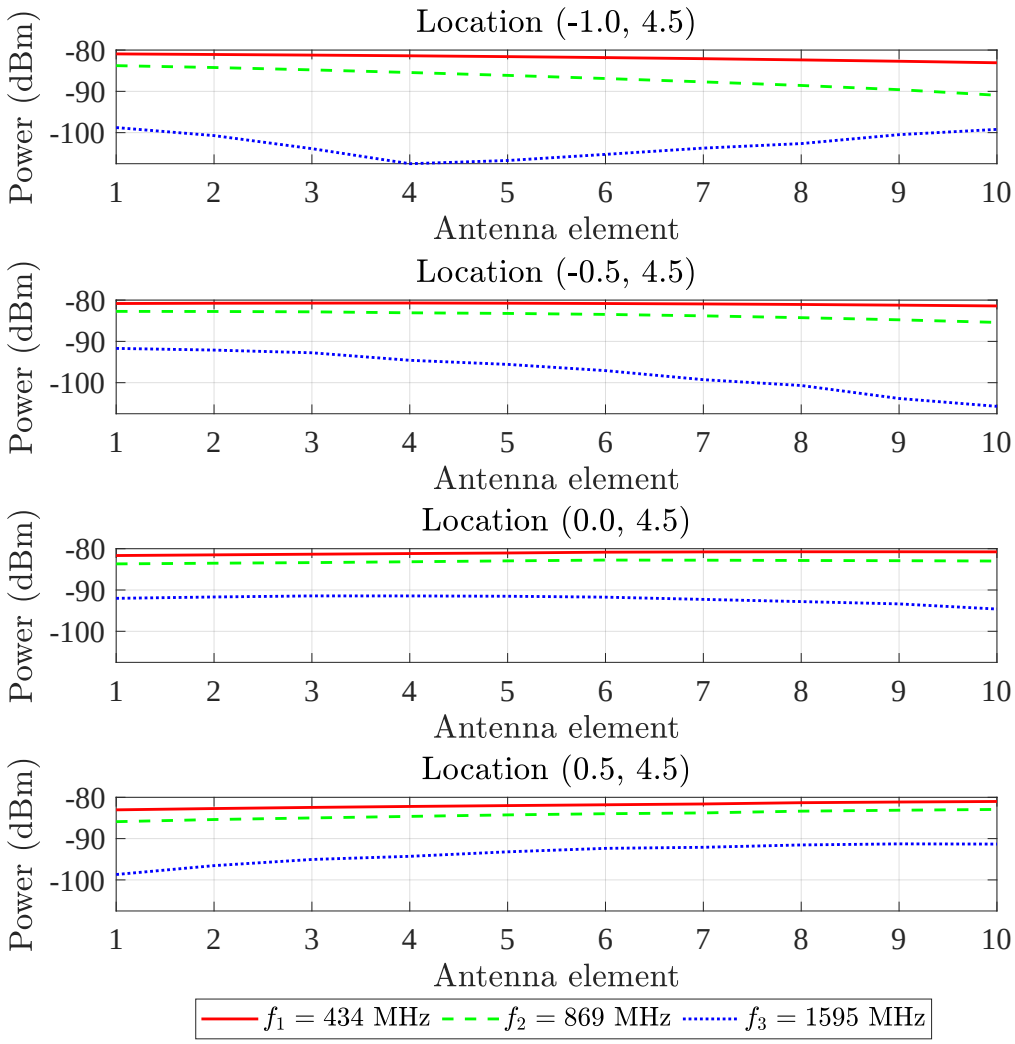

Figure 6.12: Four RSS patterns in the back row with width offset of 0.5 m, and three frequencies f_1, f_2, and f_3.

three broadly spaced frequencies in a small space are very different. This diversity could be utilised to enable localisation by comparing the measured RSS pattern in an unknown location with the RSS pattern of a known location. In the following Subsection 6.3.3, the RSS patterns of the back row are investigated.

6.3.4 Theoretical RSS pattern in the back row

This Subsection presents the RSS patterns of the simulation at the back row, as highlighted in 6.10. The purpose of this Subsection is to present the cases where the transmitter is located away from the receiving ULA. As seen in the previous Subsections, when the transmitter is circa 6 m away from the receiving ULA, the RSS pattern are almost flat. Hence, this Subsection investigates the effects of the indoor environment with five rays, which four are reflections.

For the low frequency f_1 in Fig. 6.12, it is evident in the back row the RSS patterns are non existing. The RSS variations between the elements in all cases are circa 2 dB, which in a realistic system is impossible to attain due to noise. Moreover, in the same figure, the middle frequency f_2 shows the same effect. For this frequency, the RSS variations between the elements in all cases are now circa 3 dB, which are hard to be detected by a real system.

For the high frequency f_3 in Fig. 6.12, all the locations presented in the figure have diverse patterns. Starting from the top of Fig. 6.11, the RSS variations between the elements are circa 9 dB, 14 dB, 3.5 dB, and 7.5 dB respectively. As the transmitter moves from left to right, the variation increases; but when the transmitter is directly at 90 degrees, the gain patterns provide only a small variation of 3.5 dB. As the transmitter moves another step to the right, the pattern is evident again.

Overall, from this simulation, it is evident that the indoor reflection has a bigger effect on the RSS patterns of the high frequency f_3. But that does not mean that the lower frequencies f_2, and f_3 are not useful. As shown in the previous Subsection 6.3.2, they can assist the localisation when the transmitter is closer to the receiver. In this stage of research, it is established that the RSS patterns can be diverse to allow localisation by comparing them. The following Subsection presents the mean ULA RSS as a function of distance.

6.3.5 RSS as a function of distance

This Subsection presents the theoretical mean ULA element RSS received in different locations, as presented in Fig. 6.10. The "mean RSS of ULA receiver" is the average RSS out of all ten ULA elements, which from now on will be referred to as the mean RSS. The mean RSS for all three frequencies f_1, f_2, and f_3 is presented in Fig. 6.13. From this figure, is evident that the function of RSS and distance is neither linear or exponential. As the transmitter is placed in different locations, the mean RSS can change drastically. For example, when the distance is at circa 1.5 m, the mean RSS increases for f_1 is 15 dB, for f_2 is 20 dB, and for f_3 is 7.5 dB.

This change of mean RSS is shown to first highlight the difficulty of the indoor environment and second to show the unreliability of the RSS metric. Even if the transmitter is placed at 1.5 m away from the ULA, the absolute level of RSS is similar to being in 0.5 m or 2 m away. Therefore, since the RSS patterns provide diversity in terms of establishing the location of the transmitter, mean RSS or absolute RSS level is not taken into consideration.

6.4 Extracting AoA from RSS in indoor environments

This Section presents the results of the third set of RSS measurements performed in an indoor environment, and proposes two techniques to utilise the RSS patters to obtain the AoA. First, Subsection 6.4.1 is dedicated to the two techniques developed to extract the AoA from the RSS. The following Subsection 6.4.2 presents the measurement environment,

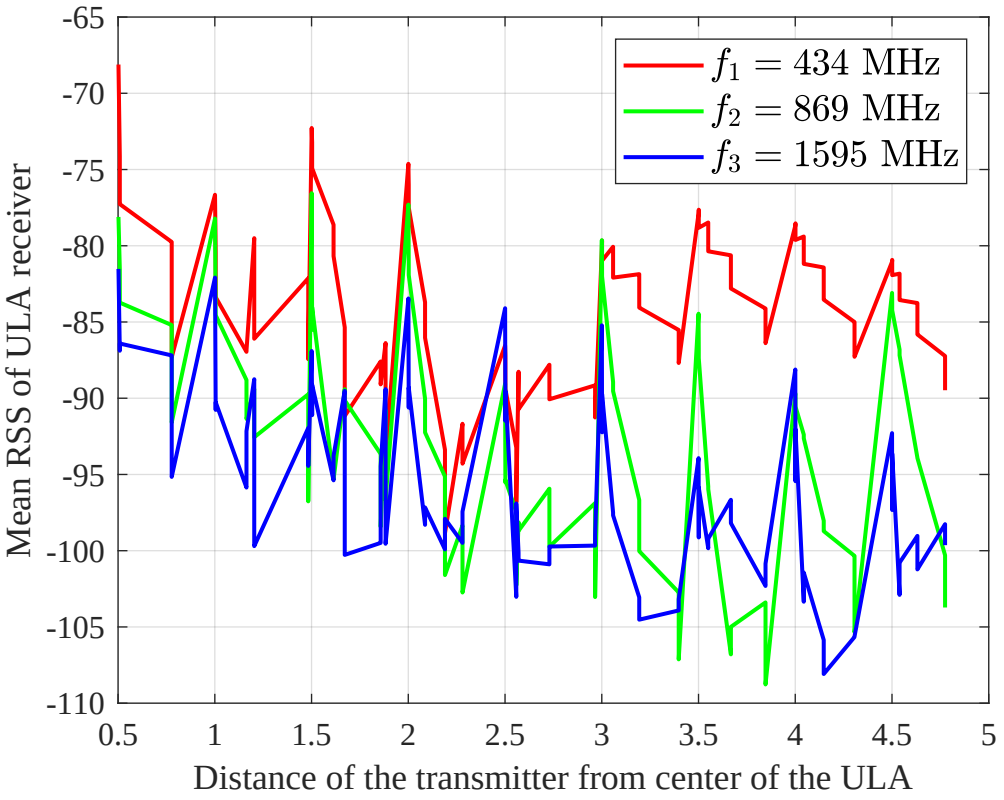

Figure 6.13: Mean RSS received by all the ULA as a function of distance.

while Subsection 6.4.3 is dedicated to the performance evaluation of estimating the AoA from the RSS. Subsection 6.4.4 investigates the performance of the proposed technique with a varying number of antenna elements, while the final Subsection 6.4.5 performs a comparison with the state of the art systems that estimate the AoA from the RSS.

6.4.1 Techniques of extracting the AoA from the RSS

In this Subsection, the process of comparing different RSS patterns is explained. The received power in a multi-ray environment has been explained in Subsection 6.3.1. Therefore, two techniques can be explained after obtaining the results of equation (6.14). For the sake of MF and the non uniform gain patterns of the receiver, the received power $P_{m,i}^{\mathrm{RX}}$ of the element m and frequency i is expressed as,

$$P_{m,i}^{\mathrm{RX}} = P_i^{\mathrm{TX}} G_i^{\mathrm{TX}} \left| \sum_{r=0}^{R} \sqrt{G_{m,i}^{\mathrm{RX}}(\theta_r, \phi_r)} \frac{\lambda_i}{4\pi d_{m,r}} \Gamma_r e^{j2\pi \frac{d_{m,r}}{\lambda_i}} \right|^2, \tag{6.17}$$

where, P_i^{TX} and G_i^{TX} are respectively the transmitted power and antenna gain of the transmitter in the frequency i, $G_{m,i}^{\mathrm{RX}}(\theta_r, \phi_r)$ is the gain of the receiver antenna in frequency i that the ray r intercepts on the element m at the angles (θ_r, ϕ_r) which are the azimuth and elevation angles respectively, λ_i is the wavelength of the frequency i, and $d_{m,r}$ is the distance

that the ray r travels to reach the element m. The *estimated* RSS pattern for frequency i is defined as,

$$\widetilde{RSS_i} = [P^{\mathrm{RX}}_{1,i}, P^{\mathrm{RX}}_{2,i}, \ldots, P^{\mathrm{RX}}_{M,i}] - \overline{\langle P^{\mathrm{RX}}_{1,i}, \ldots, P^{\mathrm{RX}}_{M,i} \rangle}. \tag{6.18}$$

where, $\widetilde{RSS_i}$ is the *estimated* RSS pattern in frequency i, and $\overline{\langle \cdot \rangle}$ is the average of $\langle \cdot \rangle$.

The two techniques of merging the *estimated* $\widetilde{RSS_i}$ for the i frequencies, developed in the scope of this research, can now be introduced. For both techniques, $n \in [1, N]$ *reference* $RSS_{n,i}$ patterns are measured, with the angle information already known.

The first method named xCorr correlates the *estimated RSS* with all known N *reference* $RSS_{n,i}$, and then sums the correlation result for each frequency as,

$$\widetilde{AoA} = \arg\max_{n} \sum_{i}^{I} \varrho\big(\widetilde{RSS_i}, RSS_{n,i}\big) \tag{6.19}$$

where, ϱ symbolises the correlation. The highest correlation is selected as the transmission location and $\widetilde{AoA}$ is estimated.

The second method, MF RMS, applies RMS for each ULA element and then sums the RMS result for reach frequency as,

$$\widetilde{AoA} = \arg\min_{n} \sum_{i}^{I} \sqrt{\frac{1}{M}\Big(\sum_{m=1}^{M} \widetilde{P^{\mathrm{RX}}_{m,i}} - P^{\mathrm{RX}}_{n,m,i} \Big)^2} \tag{6.20}$$

where the lowest RMS is selected as the transmission location $\widetilde{AoA}$. In case of a single frequency RMS, the step of summation is ignored and the selection is performed by the RMS metrics for the single frequency.

6.4.2 Indoor measurement environment

To evaluate the performance of the proposed technique, 110 measurements were performed in three frequencies, in a lab environment. The ULA was located in the bottom side of the room, as seen in Fig. 6.14. The overall size of the measurement area was 6x4 m, with 22 *reference* RSS measurements in three frequencies taken in diamond shape pattern with a distance of 1 m between them. The transmitter was at 1.6 m height, and maintained approximately 1 m distance from side walls due to benches. For the *estimated* $\widetilde{RSS}$ measurements in three frequencies, 88 transmission locations were selected randomly from the cyan grid as seen in Fig. 6.14, with the transmitter antenna at 1.6 m height. A 10 cm height offset between *reference* RSS and *estimated* $\widetilde{RSS}$ was investigated, showing no impact on the overall performance.

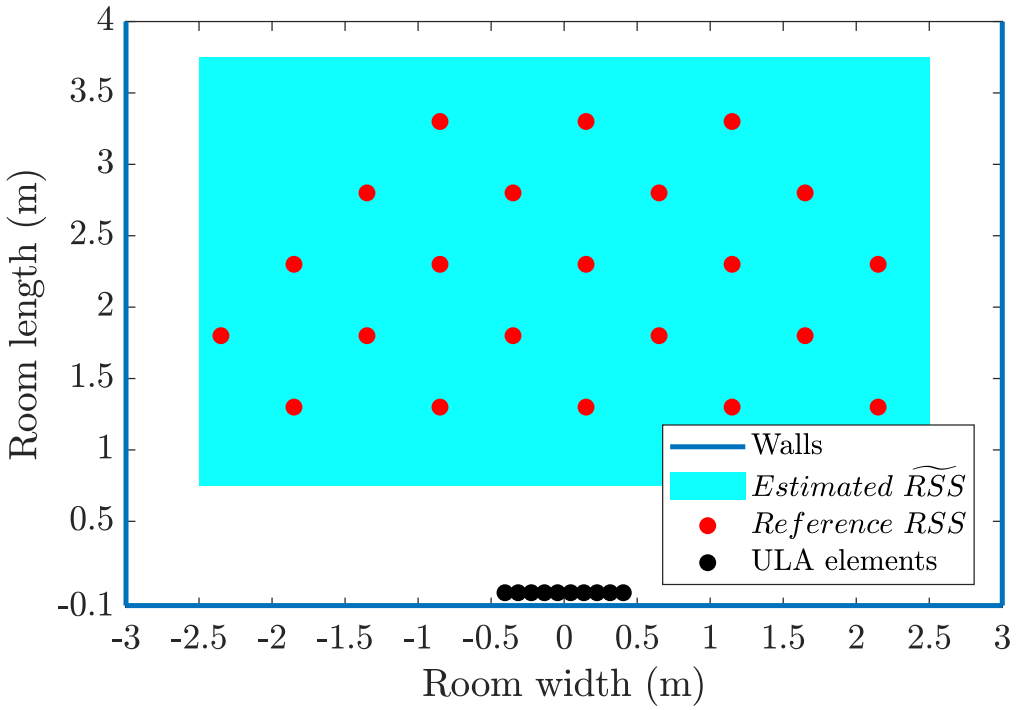

Figure 6.14: Map of the indoor environment, with the exact locations of the *reference* RSS, ULA, and walls.

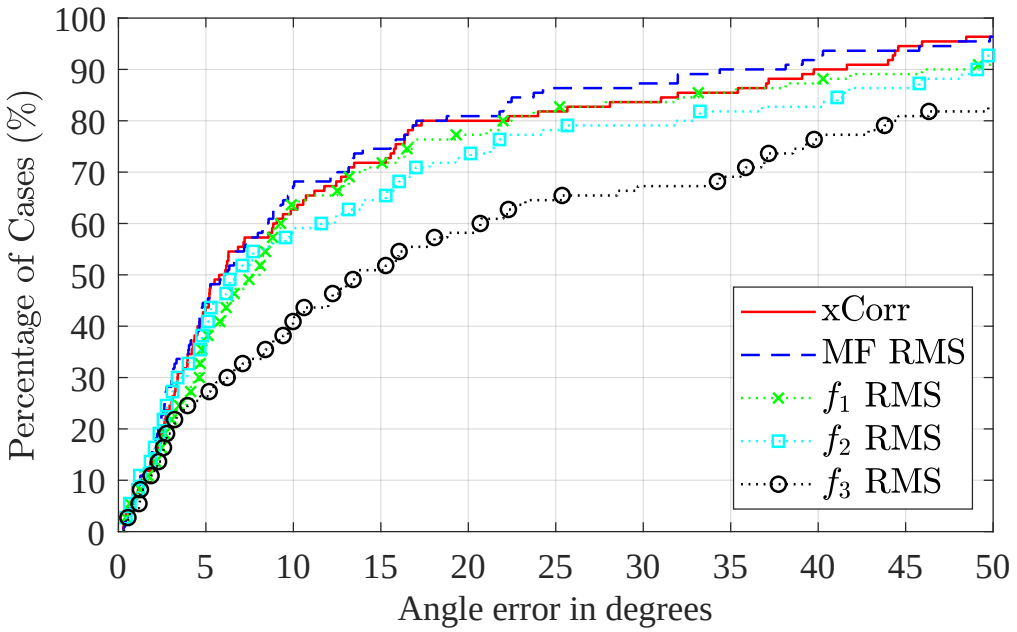

Figure 6.15: CDF of absolute error between true and estimated AoA for indoor measurements for the two MF metric fusions, xCorr and MF RMS, and single frequency RMS.

6.4.3 Performance evaluation of AoA estimation from RSS

Fig. 6.15 presents the experimental CDF of the two fusion techniques xCorr and MF RMS, as well as the RMS of every single frequency. The CDF is defined as the absolute error between estimated AoA $\widetilde{\theta}$ and true AoA θ, CDF($|\widetilde{\theta} - \theta|$). The mean error of xCorr is 5.7 degrees, MF RMS 6.2 degrees, f_1 RMS 8 degrees, f_2 RMS 6.6 degrees, and f_3 13.4 degrees. The mean improvement of xCorr compared to MF RMS is 0.5 degrees and compared to the single frequency RMS f_2 by 0.9 degrees. For 75% of the cases, both xCorr and MF RMS experience an error of circa 15.5 degrees, while f_1 is at 16.8 degrees and f_2 at 21.5 degrees. Even if f_2 has only 0.9 degrees difference for 50% of cases, for the 75% of cases the difference is 6 degrees; hence it is evident that MF is necessary to maintain a low error for a high percentage of cases.

Furthermore, from Fig. 6.15 it is evident that f_3 is the worst performing single frequency, therefore it is necessary to question its necessity. Therefore, xCorr and MF RMS are reevaluated without the presence of f_3. By removing f_3, the mean error of xCorr increases to 6.2 degrees, while for 75% of the cases the error increases to 16.8 degrees. On the contrary, the mean error of MF RMS increases to 6.3 degrees, while for 75% of the cases the error increases 15.5 degrees. Therefore, for MF RMS the mean error was increased only by 0.1 degrees and for 75% of the cases the error remains the same. From this comparison, it is evident that the best performing technique, xCorr, is affected by the presence of f_3 while MF RMS is not.

Hence, the following conclusions were drawn. It was evident that, due to multipath and wavelength, the lower frequencies f_1, and f_2 performed better compared to f_3. The smaller the wavelength, the smaller shift in space was required to change the received RSS pattern. Thus, high frequency *reference* RSS are only valid when a small shift in space occurs. If the grid of *reference* RSS becomes tighter then the result would improve. Furthermore, even though the theoretical model with four reflection presented in Section 6.3 showed that the lower frequencies did not produce diverse patterns, the measurement results show the opposite. This is due to the effects of a real environment. As the transmitter changes locations the reflective surfaces change, formulating more diverse RSS patterns. Therefore, in real environments the lower frequencies that have a higher wavelength formulate complex and diverse RSS patterns. Finally, from the results it was evident that the xCorr performance benefited from the use of MF regardless of the RMS performance of f_3. But on the contrary, MF RMS performance was the same regardless the inclusion of f_3 RMS. Therefore, the proposed system could be simplified by removing the high frequency f_3, and with the use of MF RMS the error would increase by 0.5 degrees.

6.4.4 Performance evaluation with varying number of ULA elements

Fig. 6.16 shows the experimental CDF of MF RMS for different number of ULA elements, where M is the number of elements. The mean performance error for $M = 10$ is 6.2 degrees, $M = 9$ is 7.6 degrees, $M = 8$ is 7.9 degrees, and $M = 6$ is 8.2 degrees. For 75% of the cases, the error for $M = 10$ is 15.5 degrees, $M = 9$ is 21.7 degrees, and for both

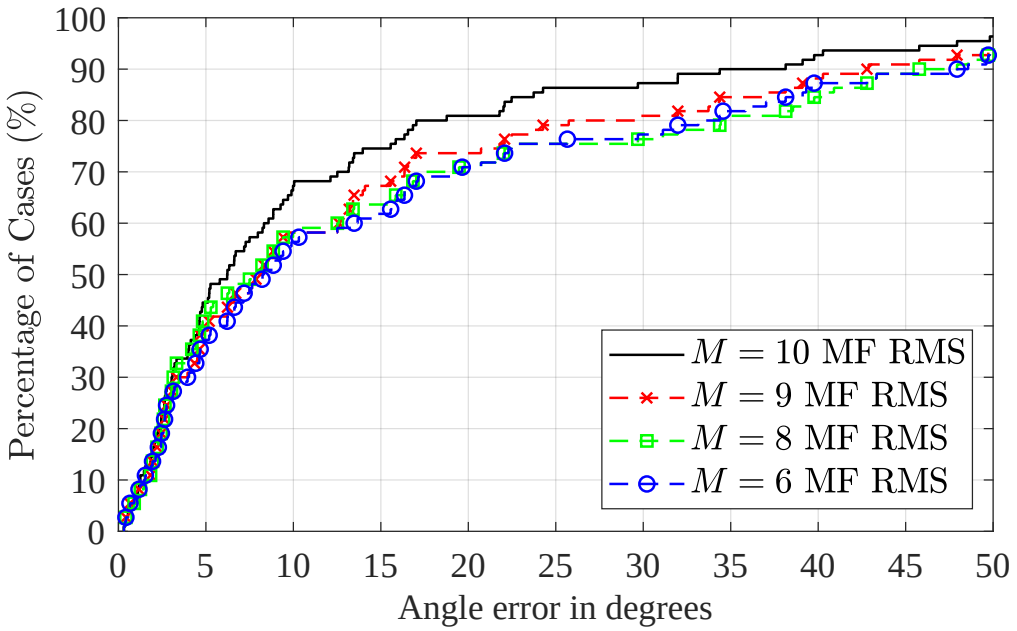

Figure 6.16: CDF of absolute error between true and estimated AoA for indoor measurements for MF RMS and different ULA elements.

$M = 8$ and $M = 6$ the error is 22.3 degrees. From Fig. 6.16, it is evident that the mean performance is not greatly affected by the reduction of the ULA elements, and that even with $M = 8$ elements, the error increases only by 1.7 degrees. On the contrary, for the 75% of the cases, even by reducing the overall number of elements by one the error increases by 6.2 degrees. Overall, the results of the experimental CDF show that MF RMS is robust in terms of mean performance. Hence, the overall number of elements could be reduced from 10 to 6 decreasing the overall system complexity, and that would increase the mean error by only 2 degrees.

6.4.5 Comparison with the state of the art systems, on estimating AoA from RSS

Table 6.1 compares the research output with the state of the art systems that utilise SBA or ESPAR and were introduced in Chapter 1. Compared to the other systems, the proposed technique sacrifices 360 degrees of detection by implementing a simple passive ULA. But, the ULA significantly reduces the hardware complexity and cost compared to SBA and ESPAR systems. Compared with [45] the proposed technique introduces 1.3 degrees improvement in accuracy. Moreover, compared to [46] and the dual-band WiFi estimation, the difference in mean CDF error is only 0.3 degrees, but the measurements of [46] were made is an anechoic chamber, with a single artificially created reflection. Hence the mean error in real indoor environments was not accurately represented. Finally, compared to the proposed systems of [47, 48], the ESPAR utilises more antenna elements, require the presence of an anchor, and the pre-calibration requirement is more exhaustive.

Table 6.1: Comparison between the proposed technique and [45], [46], [47], [48], in terms of domain, antenna type, number of elements, pre-calibration, measurement scenario, and CDF mean error.

	Domain	Antenna type	Number of elements	Pre-cal.	Scenario	CDF mean error	Complexity
This work	180°	ULA	10	Yes	Indoor measurements	5.7°	Low
Ahmed A. *et al*. [45]	360°	SBA	4	Yes	Indoor measurements	7°	Middle
Maddio S. *et al*. [46]	360°	SBA	8	No	Anechoic chamber	5.4°	Middle
Rzymowski M. *et al*. [47]	360°	ESPAR	12	Yes	Indoor measurements	1.6°	High
Kulas L. [48]	360°	ESPAR	12	Yes	Anechoic chamber	(RMSE) 2°	High

For example, the results cited in [48] require a 1994 seconds pre-calibration. Reducing the pre-calibration to 934 seconds, the error increases to 4 degrees, for an SNR of 20 dB. On the contrary, the proposed technique does not fall in this compromise, as the overall time required for pre-calibration in the presented environment is circa 660 seconds compared 934 seconds.

To provide an insight to the complexity reduction that the proposed technique imposes, these measurements could be performed using a simple RTL-SDR receiver. The cost of such an array receiver is circa £200 and requires no complex hardware configuration, pre-calibration, or switching. Furthermore, the cost of the proposed array could reduced even further by reducing the total number of elements to 6, and the mean CDF error would only increase by circa 3 degrees. Therefore, this is a very cheap solution that could be implemented in a very wide scale, compared to the other systems. Finally, the suggested technique could be potentially applied to indoor cellular APs, where they cover a wide band of cellular frequencies. The proposed technique is a simple yet effective way to perform indoor localisation, extracting AoA information from RSS.

6.5 Conclusions

This Section concludes the findings of this Chapter. In the first Section 6.1, the RSS measurements in an anechoic chamber were presented. Findings showed that the RSSs in all frequencies were effected by the ULA gain patterns, when the transmitter was located 1 m away from the receiver. As the transmitter moved farther away, the ULA gain patterns became less evident in the lower and middle frequencies f_1 f_2 due to the AoA and theULA gain patterns. On the contrary, even when the transmitter was located at 4 m away from the receiving ULA, the RSS in high frequency f_3 RSS was still affected.

In the following Section 6.2, the outdoor RSS measurements were presented. The findings of these measurements were similar to those from of the anechoic chamber. The ULA gain patterns were evident for all frequencies at a 1 meter distance, but only the high

frequency f_3 obtained diverse patterns at 4 m of distance. In fact, the middle frequency did not experience a diverse pattern at a distance of 3 m compared to the anechoic chamber. This was due to the placement of the transmitter, having no horizontal offset with the receiving. Overall, it was evident that the ground reflection did not have a great effect in the pattern formulation, and therefore the indoor environment should be investigated.

Section 6.3, presented a simulation of the indoor environment, where it was made evident that the indoor environment could produce diverse and distinguishable patterns in indoor environments. Moreover, it was shown that the mean RSS experienced large absolute change. Therefore, it was decided that the developed techniques would take into consideration only the pattern of the received signal and not the absolute level. Furthermore, in Section 6.3 the two techniques to extract AoA from RSS were presented; xCorr and MF RMS, followed by the indoor environment used for the measurements. The performance evaluation of the two techniques showed that xCorr achieved a mean error of 5.7 degrees, while MF RMS a mean error of 6.2 degrees. For the 75% of the cases, the error increased to 15.5 degrees for both techniques.

Comparing xCor with f_1 RMS, xCorr reduced the mean error by 2.3 degrees while for the 75% the error decreased by 1.3 degrees. Moreover, comparing xCor with f_2 RMS, xCorr reduced the mean error by 1 degree, while for the 75% the error decreased by 6 degrees. Therefore, it was evident that even the performance of the SF RMS changed, xCorr was always able to outperform the SF RMS. Next, the proposed technique was compared with the state of the art systems that estimate the AoA from the RSS. Compared with the complex SBA systems introduced in Chapter 1, the mean error performance of xCorr was better than [45] by 1.3 degrees and worse than [46] by a 0.3 degrees. Even though [46] performed better than xCorr, the authors performed measurements in anechoic chamber and their system was not tested in a real environment compared to the proposed technique. Furthermore, compared to the much more complex ESPAR systems, the mean error performance of xCorr was higher by 4 degrees [47] and 3.7 degrees [48]. The real benefit of the MF ULA compared to SBA and ESPAR was the overall complexity reduction in terms of pre-calibration requirements, hardware complexity and cost.

Chapter 7

Novel direct AoA estimation utilising frequency diverse antenna array

This Chapter presents two novel techniques for performing localisation utilising MF and estimating the direct ray AoA. Section 7.1 is dedicated to the introduction of MF algorithms. Section 7.2 serves an introduction to indoor environment used for measurements, while Section 7.3 presents the performance of the SF MUSIC subspace algorithms, and explains the importance of MF. Section 7.4 presents the performance evaluation of the MF direct ray AoA algorithms and its robustness in terms of frequencies, antenna elements and methods of matrix decomposition. Section 7.6 presents the comparison of the proposed system and algorithm with state of the art systems, that were discussed in Chapter 1, SpotFi [19], LTEye [31] and CUPID [32]. Finally Section 7.7, discusses the overall results and draws conclusions on why MF is the only way on detecting the direct ray AoA with high certainty.

7.1 MF MUSIC algorithms and theoretical direct AoA estimation

This Section introduces the two novel subspace algorithms that were developed for the purpose of this research. Subsection 7.1.1 introduces the MF SF MUSIC algorithm, while the following Subsection 7.1.2 presents the MF PE MUSIC algorithm.

7.1.1 Multi-frequency Spatial Fusion (MF SF) algorithm

The first developed algorithm is based on the SF FB SS MUSIC algorithm presented in Subsection 2.1. The MUSIC spatial spectrum is estimated using 2.12 for each individual frequency, after applying FB SS. For the sake of clarity and understanding, the FB SS MF

algorithm is described for i frequencies. Moreover, as described before, FB SS is applied to enable the detection of coherent signals [41], and to increase the number of detectable coherent signals [42].

The example of FB SS is presented in Fig. 2.5, where the M antenna elements ULA are divided into $L = M - M_{sps} + 1$ sub-arrays in frequency i, and M_{sps} is the number of the sub-array elements. Apart from reducing the number of the ULA elements to M_{sps}, the FB SS algorithm formulates two receiving arrays; the forward $\overrightarrow{y}_i$, and the backward $\overleftarrow{y}_i$ array, for every frequency i. This reduces the overall number of ULA elements from $2R$ to $\lfloor 3R/2 \rfloor$, when R coherent signals are detected [42].

The forward and backward covariance matrices of sub-array l are formulated as, $\overrightarrow{\boldsymbol{R}}_{l,i} = E[\overrightarrow{\boldsymbol{y}}_{l,i} \overrightarrow{\boldsymbol{y}}_{l,i}{}^{\mathsf{T}}]$ and $\overleftarrow{\boldsymbol{R}}_{l,i} = E[\overleftarrow{\boldsymbol{y}}_{l,i} \overleftarrow{\boldsymbol{y}}_{l,i}{}^{\mathsf{T}}]$ respectively. After summing all the covariance matrices generated by the l sub-arrays, the forward $\overrightarrow{\boldsymbol{R}}_i$ and backward $\overleftarrow{\boldsymbol{R}}_i$ covariance matrices are formulated. The final covariance matrix used in the MUSIC algorithm is expressed as [42],

$$R_i = \frac{\overrightarrow{\boldsymbol{R}}_i + \overleftarrow{\boldsymbol{R}}_i}{2L} \tag{7.1}$$

where, the covariance matrix $\boldsymbol{R}_i$ in frequency i is averaged by the number of sub-arrays times two, due to the forward and backward array.

By applying SVD on the $\boldsymbol{R}_i$, the number of signals can be estimated, and the noise subspace is extracted as [42],

$$\text{SVD}[\boldsymbol{R}_i] = \boldsymbol{U}_i \boldsymbol{\Sigma}_i \boldsymbol{V}_i^{\mathsf{T}}, \tag{7.2}$$

where, $\boldsymbol{U}_i$ are the noise and signal subspace, and $\boldsymbol{\Sigma}_i$ contains the eigenvalues of the covariance matrix. The number of received signals R_i that is taken into consideration for frequency i is determined by the eigenvalues as [42],

$$\boldsymbol{R}_i = \min\Big(\text{sum}\big(\boldsymbol{\Sigma}_i > \max(\boldsymbol{\Sigma}_i)/10\big), R_{max}\Big) \tag{7.3}$$

where, R_{max} is the number of maximum coherent signals allowed to be detected, which can be deduced empirically from the environment. By estimating the number of coherent signals, the noise subspace is now defined as [42],

$$\boldsymbol{U}_i = [\boldsymbol{Ux}\ \boldsymbol{Un}] = [\boldsymbol{U}_1, \ldots, \boldsymbol{U}_{R_i}\ \boldsymbol{U}_{R_i+1}, \ldots, \boldsymbol{U}_M] \tag{7.4}$$

where, $\boldsymbol{Ux}$ is the signal subspace, and $\boldsymbol{Un}$ is the noise subspace. Finally, the spatial spectrum $P_i^{\text{MUSIC}}(\theta)$ for the FB SS MUSIC algorithm in frequency i is given by [42],

$$P_i^{\text{MUSIC}}(\theta) = \frac{1}{\boldsymbol{A}_i^{\mathsf{T}}(\theta) \boldsymbol{Un}_i \boldsymbol{Un}_i^{\mathsf{T}} \boldsymbol{A}_i(\theta)}. \tag{7.5}$$

A step by step explanation of the FB SS MUSIC algorithm is presented in Alg. 7.1.

The MF SF algorithm continues the process from this point. After all the MUSIC power spectra are estimated, they are fused. The main idea is that, in every single frequency of

Algorithm 7.1 FB SS MUSIC [42]

Inputs: Received signal vectors $\boldsymbol{y}_i(t)$; Number of frequencies I; FB SS sub-arrays L; Number of maximum of coherent signals R_{MAX}

for i = 1 until I **do**
  Initialise: $\overrightarrow{\boldsymbol{R}}_i = \overleftarrow{\boldsymbol{R}}_i$ = zeros(M_{sps} by M_{sps}) matrix
  for l = 1 until $L = (M - M_{sps} + 1)$ **do**
    Forward cov. matrix: $\overrightarrow{\boldsymbol{R}}_i = \overrightarrow{\boldsymbol{R}}_i + E[\overrightarrow{\boldsymbol{y}}_{l,i}\,\overrightarrow{\boldsymbol{y}}_{l,i}{}^{\mathsf{T}}]$
    Backward cov. matrix: $\overleftarrow{\boldsymbol{R}}_i = \overleftarrow{\boldsymbol{R}}_i + E[\overleftarrow{\boldsymbol{y}}_{l,i}\,\overleftarrow{\boldsymbol{y}}_{l,i}{}^{\mathsf{T}}]$
    $l = l + 1$
  end for
  Estimate the covariance matrix: $\boldsymbol{R}_i$ (7.1)
  Apply SVD and obtain: $\boldsymbol{U}_i$, $\boldsymbol{\Sigma}_i$ (7.2)
  Determine number of coherent signals: R_i (7.3)
  Define the noise subspace: $\boldsymbol{Un}_i$ (7.4)
  Obtain MUSIC spatial spectrum: $P_i^{\text{MUSIC}}(\theta)$ (7.5)
  $i = i + 1$
end for

Algorithm 7.2 MF SF MUSIC

Inputs: Received signal vectors $\boldsymbol{y}_i(t)$; Number of frequencies I; Spatial smoothing array size M_{sps}; Number of maximum of coherent signals R_{MAX}

Run: Algorithm 1 with inputs, $\boldsymbol{y}_i(t)$, M_{sps}, I_{MAX}
Obtain the MF SF spatial spectrum: $P_i^{\text{MFSF}}(\theta)$ (7.6)

the FB SS MUSIC spatial spectrum, the direct AoA is the only ray that is expected to be present. The other rays will either appear on different angles; therefore they will not be present, or will have different amplitudes. The cause of this effect is the different reflective surfaces, and the electromagnetic propagation of different frequencies [114] and also observed by the measurements. Hence, the spatial spectrum for each frequency is expected to be different. By fusing the FB SS MUSIC spectra, the direct AoA is expected to be distinguished.

The process of MF SF continues after Alg. 7.1 is completed, where the spatial spectrum $P_i^{\text{MFSF}}(\theta)$ can be calculated. Since each spatial spectrum has a different power, their fusion is not equally weighted. Hence, $P_i^{\text{MUSIC}}(\theta)$ needs to be normalised so that the maximum power in every spatial spectrum will be equal. The final MF SF spatial spectrum $P_i^{\text{MFSF}}(\theta)$ is the product of the normalised $P_i^{\text{MUSIC}}(\theta)$, expressed as,

$$P_i^{\text{MFSF}}(\theta) = \prod_{f=1}^{F} \frac{P_i^{\text{MUSIC}}(\theta)}{\max\left(P_i(\theta)\right)}. \tag{7.6}$$

A step by step explanation of the MF SF MUSIC algorithm is presented in Alg. 7.2.

7.1.2 Multi-frequency Phase Entanglement (MF PE) algorithm

MF PE is the second algorithm developed which entangles the phase information of each frequency and resolves it with the purpose of distinguishing the direct AoA. With

Algorithm 7.3 MF PE MUSIC

Inputs: Received signal vectors $\boldsymbol{y}_i(t)$; Number of frequencies I; FB SS sub-arrays L; Number of maximum of coherent signals R_{MAX}

Initialise: $\overrightarrow{\boldsymbol{R}} = \overleftarrow{\boldsymbol{R}}$ zeros(FM_{sps} by FM_{sps}) matrix
for l = 1 until $L = (M - M_{sps} + 1)$ **do**
  Formulate forward received sub-array $\overrightarrow{\boldsymbol{V}}_l$ (7.7)
  Formulate backward received sub-array $\overleftarrow{\boldsymbol{V}}_l$ (7.8)
  Forward cov. matrix: $\overrightarrow{\boldsymbol{R}} = \overrightarrow{\boldsymbol{R}} + E[\overrightarrow{\boldsymbol{V}}_l \overrightarrow{\boldsymbol{V}}_l^{\mathsf{T}}]$
  Backward cov. matrix: $\overleftarrow{\boldsymbol{R}} = \overleftarrow{\boldsymbol{R}} + E[\overleftarrow{\boldsymbol{V}}_l \overleftarrow{\boldsymbol{V}}_l^{\mathsf{T}}]$
  $l = l + 1$
end for
Estimate the covariance matrix: $\boldsymbol{R}$ (7.9)
Apply SVD and obtain: $\boldsymbol{U}$, $\boldsymbol{\Sigma}$ (7.2)
Determine number of coherent signals: R (7.3)
Define the noise subspace: $\boldsymbol{Un}$ (7.4)
Obtain MUSIC spatial spectrum: $P_i^{\text{MFPE}}(\theta)$ (7.11)

MF PE, the merge of MF signals is performed in the time domain of the sampled data, rather the MUSIC spatial spectrum which MF SF does. The benefit is that random spatial spectrum errors do not affect the final estimation, since only the phase information of each signal is utilised.

The algorithm initially concatenates the normalised received vector of multiple frequencies and a virtual array is formulated. In practice FB SS covariance matrix of the virtual array entangles the phase from the different frequencies. Since the steering matrix is orthogonal to the noise subspace, the steering matrix of the virtual array will resolve the direct AoA as primary. If the direct LOS ray is barely received, it still exists in the noise subspace without being the main peak. When the different frequencies are entangled the direct LOS ray exist in the noise subspace of all the MF signals. On the contrary, that does not hold true for the main peak, because the source is the LOS and not a reflection from the environment. Since each frequency experiences its environment differently, different main peaks are expected. Therefore, by formulating the appropriate steering matrix the true direct AoA can be revealed, because it is orthogonal to the noise subspace that contains the direct AoA phase information.

The MF PE algorithm begins by formulating the forward $\overrightarrow{\boldsymbol{V}}$ and backward $\overleftarrow{\boldsymbol{V}}$ virtual arrays from the received vectors in frequencies $f \in [f_1, \ldots, F]$, and sub-array l as,

$$\overrightarrow{\boldsymbol{V}}_l = \left[\frac{\overrightarrow{\boldsymbol{y}}_{l,1}}{\|\overrightarrow{\boldsymbol{y}}_{l,1}\|}, \frac{\overrightarrow{\boldsymbol{y}}_{l,2}}{\|\overrightarrow{\boldsymbol{y}}_{l,2}\|}, \ldots, \frac{\overrightarrow{\boldsymbol{y}}_{l,i}}{\|\overrightarrow{\boldsymbol{y}}_{l,i}\|} \right]^{\mathsf{T}}, \tag{7.7}$$

$$\overleftarrow{\boldsymbol{V}}_l = \left[\frac{\overleftarrow{\boldsymbol{y}}_{l,1}}{\|\overleftarrow{\boldsymbol{y}}_{l,1}\|}, \frac{\overleftarrow{\boldsymbol{y}}_{l,2}}{\|\overleftarrow{\boldsymbol{y}}_{l,2}\|}, \ldots, \frac{\overleftarrow{\boldsymbol{y}}_{l,i}}{\|\overleftarrow{\boldsymbol{y}}_{l,i}\|} \right]^{\mathsf{T}}, \tag{7.8}$$

where, $\overrightarrow{\boldsymbol{y}}_{l,i}$ denotes the forward received vector of sub-array l and frequency i, $\overleftarrow{\boldsymbol{y}}_{l,i}$

denotes the backward received matrix, and $\|*\|$ is the 2-norm or also known as the maximum singular value of matrix $*$. The 2-norm is essential to the process as it equally weights all the eigenvalues. Since the pathloss is related to the frequency, the maximum eigenvalue for each frequency will be different and the different scaling of the eigenvalues will apply a weighting on the final AoA estimation.

Furthermore, the forward $\overrightarrow{\boldsymbol{R}}$ and backward $\overleftarrow{\boldsymbol{R}}$ covariance matrices are estimated by the summation of the L sub-arrays. The normalised covariance matrix $\boldsymbol{R}$ of the virtual array $\boldsymbol{V}$ is expressed as,

$$\boldsymbol{R} = \frac{\overrightarrow{\boldsymbol{R}} + \overleftarrow{\boldsymbol{R}}}{2L} \tag{7.9}$$

where, $\boldsymbol{R} = \text{diag}\{\sigma_r^2, \ldots, \sigma_R^2\}$, σ_r^2 is the eigenvalue of the ray $r \in [1, R]$. The covariance matrix $\boldsymbol{R}$ contains the signal and noise subspace (7.4), but since each frequency has a different phase effect on the ULA, the phases are entangled. Therefore, the appropriate steering matrix $\boldsymbol{A_V}$ needs to be formulated that resolves the entangled phase information because it is orthogonal to the noise subspace. The appropriate steering matrix is defined as,

$$\boldsymbol{A_V} = [\boldsymbol{A}_1, \boldsymbol{A}_2, \ldots, \boldsymbol{A}_i]^T, \tag{7.10}$$

where, $\boldsymbol{A}_f$ is the steering vector of frequency $f \in [1, F]$. By applying SVD, the noise subspace $\boldsymbol{Un}$ can be obtained and the MF PE MUSIC spatial spectrum is expressed as,

$$P^{\text{MFPE}}(\theta) = \frac{1}{\boldsymbol{A_V}(\theta)^T \boldsymbol{Un} \boldsymbol{Un}^T \boldsymbol{A_V}(\theta)}. \tag{7.11}$$

A step by step explanation of the MF PE MUSIC algorithm is presented in Alg. 7.3.

7.2 Indoor environment used for performance evaluation measurements

To understand how well the SF FB SS MUSIC and the developed MF algorithms perform in distinguishing the direct ray AoA in a real indoor environment, measurements were performed in a seminar room and its peripheral rooms. The receiving ULA was stationed at the middle of a side wall, at a height of 1.6 m. The transmitter was moved to 36 different locations, transmitting a CW in three frequencies, $f_1 = 434$ MHz, $f_2 = 869$ MHz, $f_3 = 1595$ MHz, for a total of 108 measurements, at a height of 1.5 m. Out of the total 36 transmitter locations, 19 were in the same room with the ULA receiver. In 8 of the locations there was a single wall obstructing the direct AoA, while for the final 9 locations there were two walls obstructing the direct AoA.

A detailed floor plan of the measurements can be seen in Fig. 7.1, where the black star represents the centre of the ULA, the red dots represent the unobstructed locations where the LOS is present. The blue squares represent the one wall obstruction, while the green diamonds are the measurement locations when the signal was obstructed by two walls. To measure the true location of the transmitter, a laser distance measurement device was

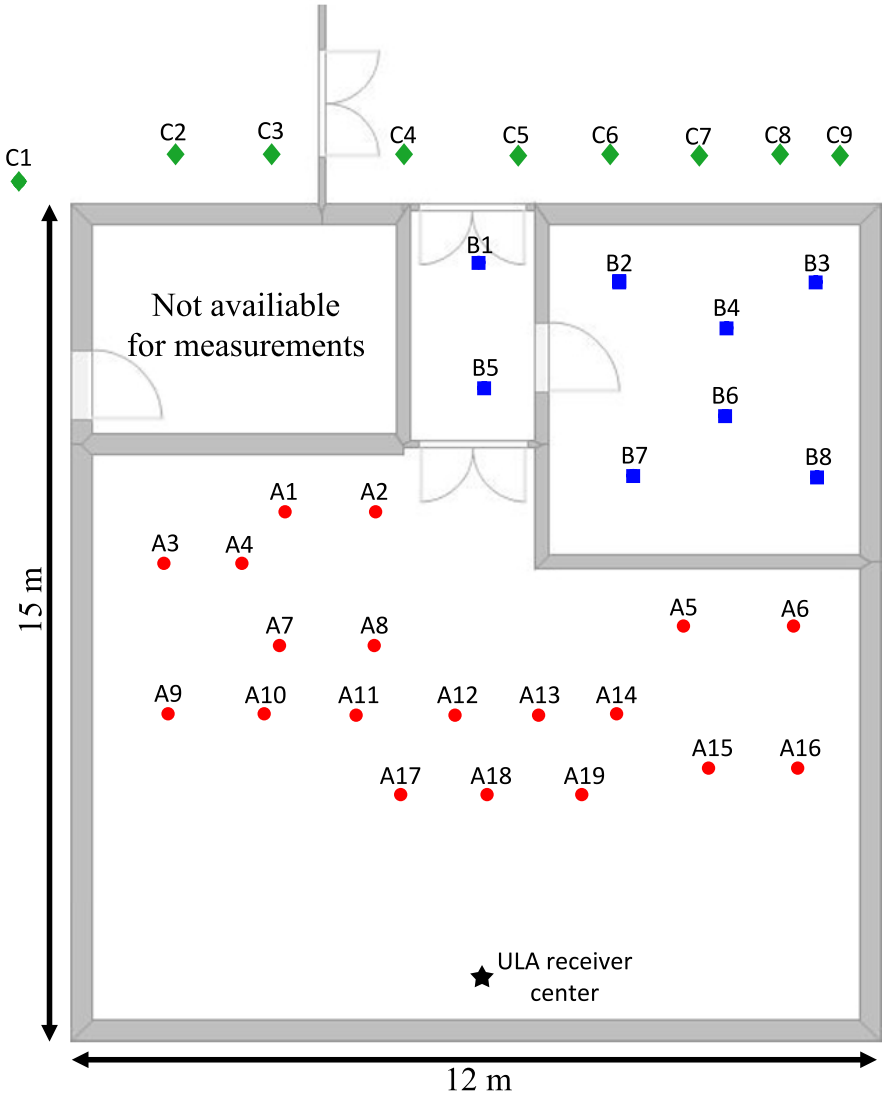

Figure 7.1: Indoor measurement environment with specific locations.

used with a measurement accuracy of 1.5 mm and maximum distance of 40 m.

To confirm flat fading, the MUSIC algorithm were applied in the first 2000 and the last 2000 samples of the received sample block, which contained 2 million samples. The MUSIC power spectra was the same for the first and the last 2000 samples, therefore, flat fading was confirmed. The sample rate was set to 2 Msps, the transmit power was set to -30 dBm, and the gain of the RSP2s was set to 0 dB. The SNR was measured for each location and ULA element and then averaged. Table 7.1 presents the average SNR. The transmitting locations were chosen to be at least 2 m apart with each other and 1 m away from walls. The distance of 2 m apart between measurements was applied to enable diverse AoA results, while the 1 m spacing between transmitter and walls was applied to allow the formulation of a reflecting ray from the wall. If the transmitter was placed right next to the wall then no reflection could be formulated. Specifically, for the measurement

Table 7.1: Average SNR measured at different locations and frequencies.

	f_1	f_2	f_3	
SNR with direct LOS	27	25	19	dB
SNR with 1 wall obstruction	17	18	12	dB
SNR with 2 walls obstruction	12	13	7	dB

at location C1, the transmitter was placed at 50 cm off the horizontal wall and 1 m off the vertical wall to investigate the different frequency interaction with the walls and nearby door, of the space that was unavailable for measurements.

7.3 Performance evaluation of the SF direct AoA estimation

This Section presents the results of the SF direct AoA estimation performance evaluation. To understand how the SF FB SS MUSIC behaves in the different scenarios, Section 7.4.1 presents the spectral results of the SF FB SS MUSIC algorithms with LOS obstruction. Section 7.4.2 is dedicated with the spectral results of one wall obstructing the LOS, while Section 7.4.3 presents the results of two walls obstructing the LOS. Finally, Section 7.4.4 is dedicated on the statistical performance by presenting the CDF of all cases.

7.3.1 Results and discussion of SF direct AoA for no wall obstruction

The first evaluation is on how accurately the developed algorithms determine the direct AoA when there are no obstructions. Fig. 7.2 presents the SF FB SS MUSIC spatial spectrum of four different locations to discuss how the developed algorithm combats the issues that emerge from multiple rays. The exact location of the measurements is presented in Fig. 7.1, Subsection 7.2. Moreover, to simplify the name of the algorithm SF FB SS MUSIC, it will be referred to as f FB SS, where f is the frequency of the MUSIC spectrum.

For location A3, Fig. 7.2a; the power spectra of f_1, and f_3 frequencies are shifted to the right with 8 degrees and 5.7 degrees of error respectively. Meanwhile, f_2 is on the opposite side with a high error, at 14 degrees. Therefore it is evident that the f_1, and f_3 are close to the direct AoA estimation, but the multipath that f_2 experiences does not allow a direct AoA detection.

Moreover, for the location A8, Fig. 7.2b; it is evident that the f_1 and f_2 spectra are broad, with errors of 12 degrees and 19 degrees respectively, while f_3 has a sharp peak with an error of 6.2 degrees. Also, a second peak is formulated, at circa -7 dB lower at the other side of the power spectra, meaning that there is at least on reflection from that angle. In this location, the overall error increases and the peaks become broader. As explained in Section 2.5 this is occurring due to the steering matrix being tainted.

Furthermore, in location A12, Fig. 7.2c; f_1 detects a wall reflection as a direct AoA at 38.7 degrees error, while the direct AoA peak is at circa -7 dB. On the other hand, the f_2

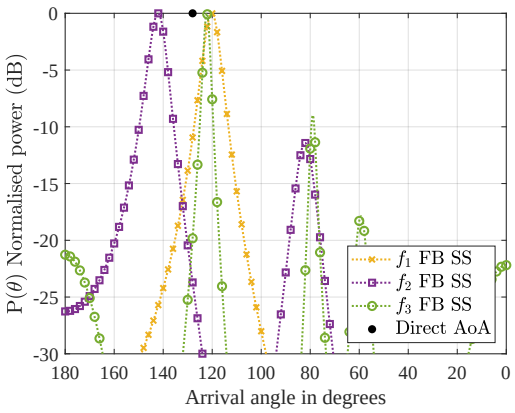

(a) MUSIC power spectra at A3. Direct AoA: 128 degrees.

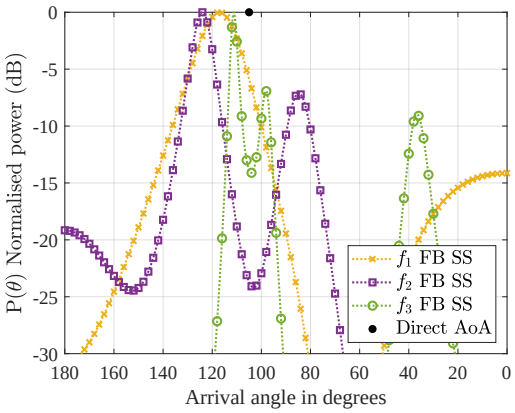

(b) MUSIC power spectra at A8. Direct AoA: 105 degrees.

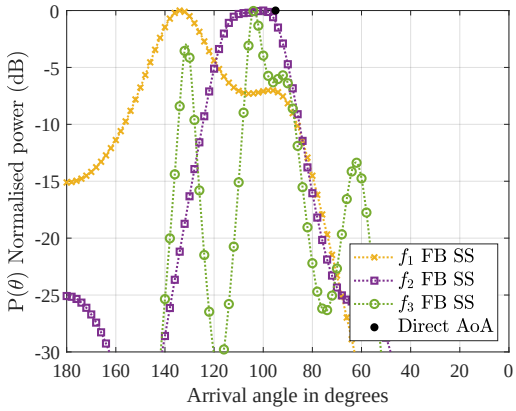

(c) MUSIC power spectra for A12. Direct AoA: 95 degrees.

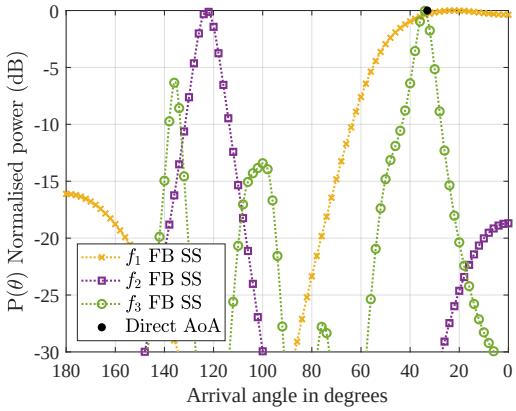

(d) MUSIC power spectra for A16. Direct AoA: 33 degrees.

Figure 7.2: The MUSIC power spectra for single frequency algorithm in cases where the direct AoA is not obstructed for locations, A3 (Fig. 7.2a), A8 (Fig. 7.2b), A12 (Fig. 7.2c), A16 (Fig. 7.2d).

spectrum is broad, and the f_3 spectrum detects a direct AoA 105 degrees but a secondary peak is detecting the direct AoA at circa -6 dB. The error for both f_2, and f_3 are at 5.3 and 8.7 degrees respectively. Even though their estimation error is lower, the power peaks are broad, suggesting that the phase information is uncertain to point on the direct AoA.

Finally, an example with an extreme angle detection is presented in location A16, Fig. 7.2d. We can see that f_1 is on the right side with an error of 11.4 degrees, while f_2 is at the other side of the spectrum with an error of 89.8 degrees, and f_3 is closer to a correct estimation with an error of 1.4 degrees. In this case, it is evident that the f_2 measurement is not accurate due to a reflection, and the result of f_1 is very broad suggesting the presence of AoA noise. On the contrary, f_3 is able to perform an accurate estimation, with a reflection at circa 138 degrees. Moreover, in all four locations presented in Fig. 7.2, it is evident that f_3 is the frequency that detects the direct AoA with the lowest error, and highest certainty.

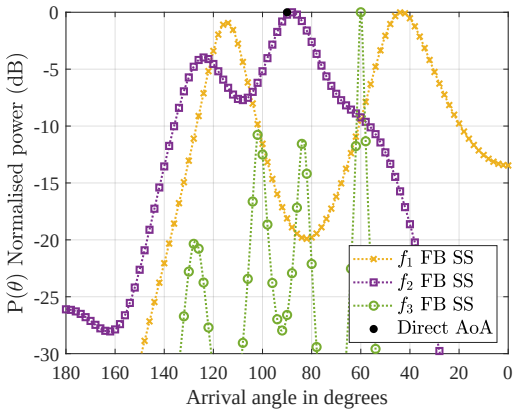

(a) MUSIC power spectra at B1. Direct AoA: 90 degrees.

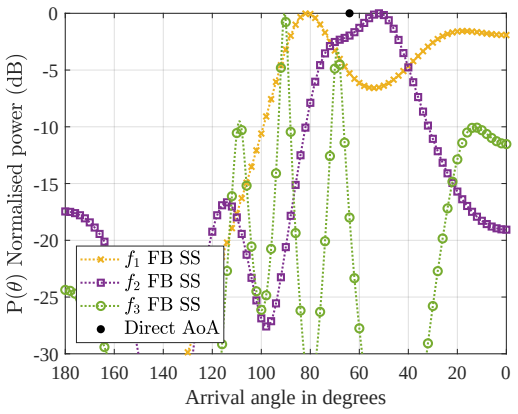

(b) MUSIC power spectra at B3. Direct AoA: 64 degrees.

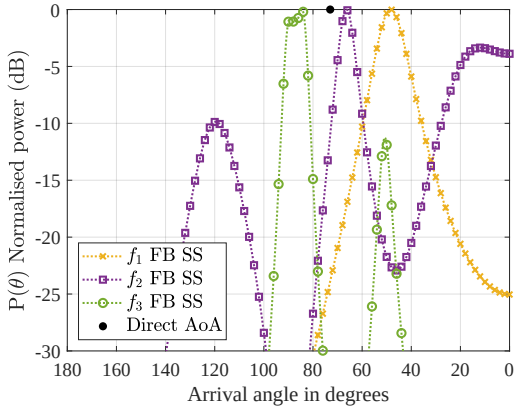

(c) MUSIC power spectra for B7. Direct AoA: 73 degrees.

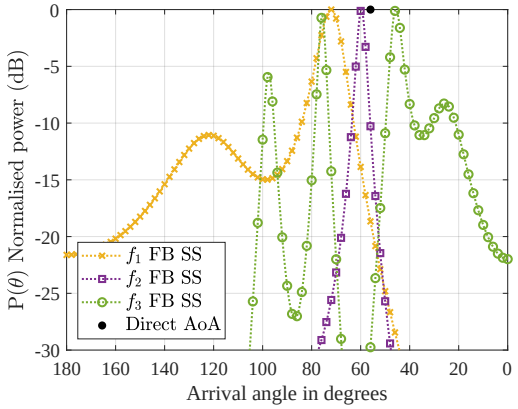

(d) MUSIC power spectra for B8. Direct AoA: 57 degrees.

Figure 7.3: The MUSIC power spectra for single frequency algorithm in cases where the direct AoA is obstructed by a single wall for locations, B1 (Fig. 7.3a), B3 (Fig. 7.3b), B7 (Fig. 7.3c), B8 (Fig. 7.3d).

7.3.2 Results and discussion of SF direct AoA for one wall obstruction

In this Subsection the accuracy of the FB SS MUSIC is evaluated when the direct AoA is obstructed by a wall. Fig. 7.3 presents the MUSIC power spectra of four different locations to discuss the issues that emerge from multiple rays with a single wall obstruction when SF MUSIC is applied.

For location B1, Fig. 7.3a; where the transmitter is positioned directly between the doors only f_2 is able to determine the direct AoA, with an error of 2.4 degrees. On the contrary, f_1 has a reflection as the primary peak with an error of 46.8 degrees; but a secondary peak at circa -1 dB lower has a lower error. While f_3 has an error of 30 degrees, it produces a correct estimation at circa -11 dB, 6.5 degrees away from the direct AoA. In this example, it is evident that with a single wall obstruction, only f_2 can detect the direct AoA. Overall, again f_1 and f_2 have broad peaks meaning that the steering matrix is tainted.

Moreover, for location B3, Fig. 7.3b; all three frequencies produce a peak close to the direct AoA. Frequencies f_1 and f_2 have a 17 degrees and 12.2 degrees error respectively, while f_3 produces the primary peak at 90.5 degrees, but at -3 dB lower a second peak appears only 4.9 degrees from the direct AoA. Therefore, even if the peaks are close, the lowest error is at 12.2 degrees. Comparing f_3 with the other two frequencies, f_3 formulate a sharp power peak close to the direct AoA suggesting that the information is correct. On the other hand, even though the estimation has a high error, f_2 and f_3 power peaks are broad, especially close the direct AoA, suggesting that the phase information is uncertain regarding the direct AoA. Hence, an algorithm that utilises the phase information from all the frequencies could improve the direct AoA estimation.

Furthermore, for location B7, Fig. 7.3c; we can see another example where all single frequency metrics produce different peaks with a high error. The errors are at 24.5 degrees for f_1, 6.7 degrees for f_2, and 11.5 degrees for f_3. Again, it is evident that all the frequencies have broad peaks, meaning that information regarding the direct AoA exists, but it is not certain.

Finally, for an extreme angle detection in location B8, Fig. 7.3d; only f_2 is close with an error of 3.7 degrees and a sharp peak, meaning that the phase information is clear. The other two remaining frequencies f_1, and f_3 have an error of 16.1 degrees and 10.4 degrees respectively. The peaks of f_1 and f_3 are again broad and contain some information in the direct AoA. Moreover, as with B1, f_2 is the only frequency in these four locations presented in Fig. 7.3 that is closer on detecting the direct AoA and overall achieves the best performance.

7.3.3 Results and discussion of SF direct AoA for two walls obstruction

In this Subsection the accuracy of the FB SS MUSIC is evaluated when the direct AoA is obstructed by two walls. In Fig. 7.4, the MUSIC spatial spectrum of four different locations is presented, to discuss the issues that emerge from multiple rays with two walls obstruction when SF MUSIC is applied.

For location C1, Fig. 7.4a; we can see that both f_1 and f_3 appear to have the direct AoA at circa 133 degrees. Looking back at Fig. 7.1, we can see this is the location of the door. Therefore, it is evident that both frequencies detect a reflection coming from the door, while the AoA for f_2 seems to be shifted even further appearing at 139 degrees. The overall errors are 13.9 degrees, 19 degrees, and 12 degrees, for f_1, f_2, and f_3 respectively. The overall direct AoA estimation is the worse so far, with f_1 having a broad peak suggesting a tainted steering matrix, and both f_2, f_3 having secondary peaks lining up at 84.5 degrees.

On the contrary, for location C3, Fig. 7.4b; the steering matrix of f_1 and f_3 seem to contain correct phase information. Frequency f_1 is off 9.1 degrees while f_3 is off 9.4 degrees with a secondary peak at -0.3 dB. The low frequency f_2 produces a broad peak, while the high frequency f_3 produces multiple peaks due to multipath. Furthermore, f_2 is unable to perform an estimation due to uncertain phase information. As shown Section 2.5 when the steering matrix is tainted the peaks become broad, even if the SNR is above 0

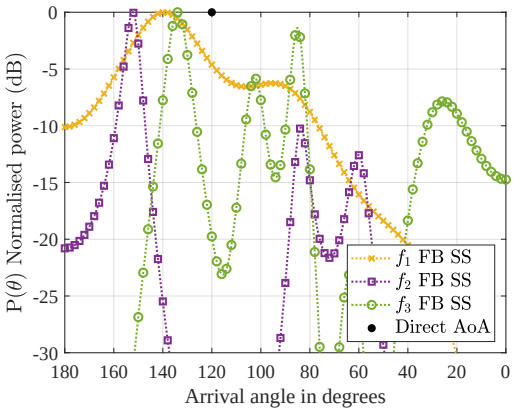

(a) MUSIC power spectra at C1. Direct AoA: 120 degrees.

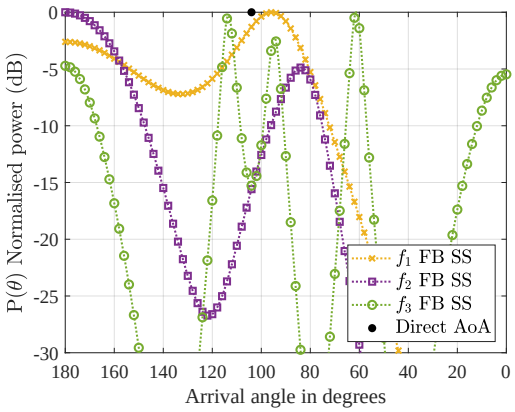

(b) MUSIC power spectra at C3. Direct AoA: 104 degrees.

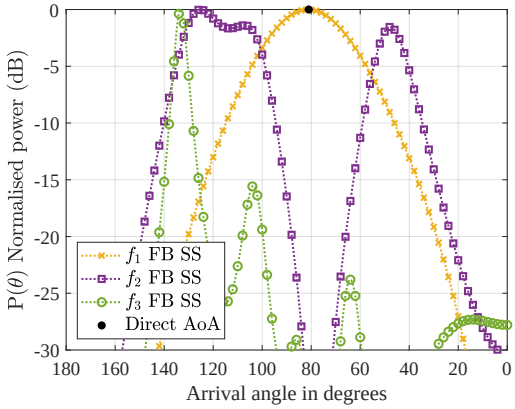

(c) MUSIC power spectra for C6. Direct AoA: 81 degrees.

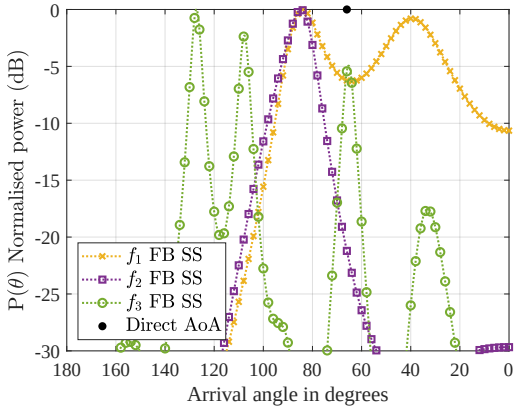

(d) MUSIC power spectra for C9. Direct AoA: 66 degrees.

Figure 7.4: The MUSIC power spectra for single frequency algorithm in cases where the direct AoA is obstructed by two walls for locations, C1 (Fig. 7.4a), C3 (Fig. 7.4b), C6 (Fig. 7.4c), C9 (Fig. 7.4d).

dB. In this case there could be multiple signals from 180 degrees (as bot f_1 and f_3 power spectra suggests) and therefore an estimation was impossible.

Moreover, for location C6, Fig. 7.4c; we can see that only f_1 is able to perform a correct estimation with an error of 0.2 degrees, but the peak is broad. Both f_2 and f_3 have a false detection at 125 and 133 degrees respectively. Looking back at Fig. 7.1, we can see that there is a horizontal wall blocking the direct line of sight. The wavelength of f_1 seems to not be directly affected by the presence of that wall; but the other two frequencies with smaller wavelengths are affected. Even though the power spectra of locations C5 or C7 is not presented, it is worth noting that during the measurements, as the transmitter moved closer to either C5 or C7, the AoA power spectra error was significantly reduced.

Finally, for location C9, Fig. 7.4d; we can see that f_1 produces two false estimations at 84 degrees and 40 degrees, but the overall spectrum does not drop below -6 dB. At f_2, a broad peak at 84.5 degrees suggests a tainted steering matrix, while the third peak of f_3 is at the direct AoA at -5 dB. Overall, the direct AoA errors for f_1, f_2, and f_3 are 18 degrees,

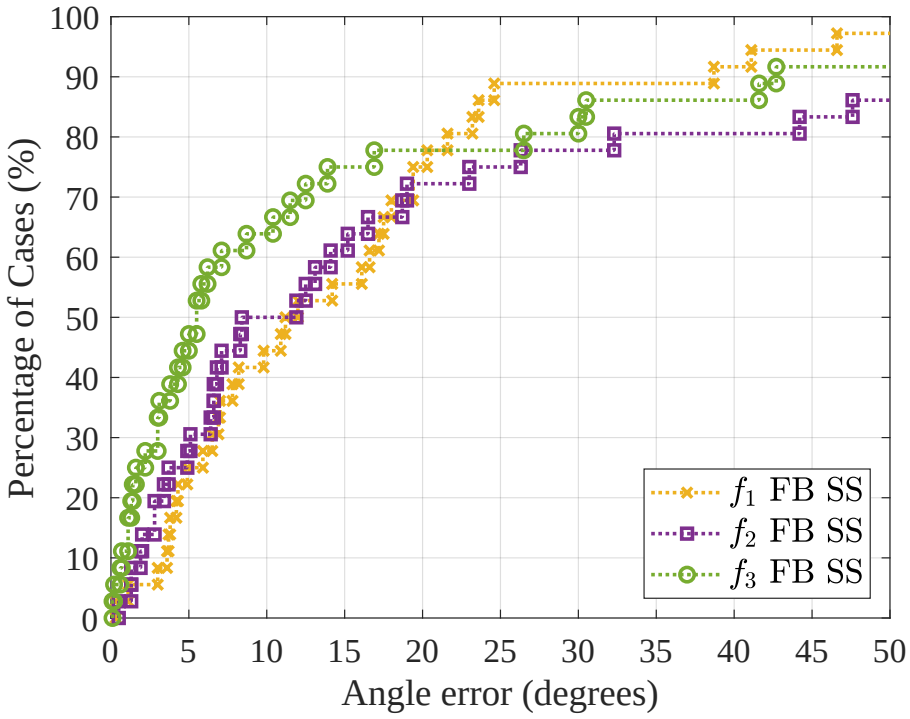

Figure 7.5: Empirical CDF plot of angular error for FB SS MUSIC in frequencies, f_1, f_2, f_3.

18.5 degrees, and 127.2 degrees respectively. Overall, f_1 is the only frequency in these four locations presented in Fig. 7.4 that is closer on detecting the direct AoA and overall achieves the best performance.

7.3.4 Statistical performance results and discussion of SF direct AoA estimation

In Fig. 7.5, the empirical CDF of the absolute error between direct AoA θ and estimated direct AoA ($\widetilde{\theta}$) from the 108 measurements in all 36 locations is presented, CDF($|\widetilde{\theta} - \theta|$). For a direct AoA estimation only the strongest peak was taken into consideration. For the high frequency f_3, the mean error is 5.3 degrees; while for the middle frequency f_2, the mean error is 11.9 degrees. Finally, for the low frequency f_1, the mean error is 12 degrees. As for 75% of the measurements, f_3 exhibits an error of 16.7 degrees, for f_2 the error is 23 degrees, and for f_1 is 20.3 degrees. In this point, it is clear that f_1 starts to outperform the middle frequency f_2 with a small error margin. Finally, for the 95% of the measurements, f_1 attains a lower error than f_2 for the first time at 41.1 degrees, while f_1 and f_3 errors are over 50 degrees.

In terms of RMSE, for the single frequency FB SS MUSIC algorithms, the error is 22.5 degrees, 33.9 degrees, and 21.7 degrees, for f_1, f_2, f_3 respectively. Showing that the lower and highest frequencies exhibit the lowest RMSE error. Both CDF and RMSE results showed that each frequency of the FB SS MUSIC has advantages and disadvantages. In terms of CDF performance, it is evident that the high frequency f_3 should be favoured

since it achieves the lowest error in 50% and 75%. The lower error is due to the number of measurements done in LOS and no obstructions. As the measurements showed, for the high frequency the direct LOS outperforms the lower frequencies. On the contrary, when walls obstruct the direct ray, the lower frequency outperforms the high frequency. This is reflected by the RMSE result where the errors of f_1 and f_3 are very close.

Moreover, the measurements showed that even if the SF estimation contains a high error, the correct phase information still exists in the signals. Therefore, a MF approach that fuses the phase information could potentially estimate the correct direct AoA. The following Subsection explains the two novel algorithms developed that fuse the MF information to detect the direct AoA.

7.4 Performance evaluation of the MF direct AoA estimation

This Section presents the results of the MF direct AoA estimation performance evaluation. To understand how the MF algorithms work, in Section 7.4.1 the spectral results of the MF algorithms are presented with no wall obstruction. Section 7.4.2 is dedicated to the spectral results with one wall obstructing the LOS, while Section 7.4.3 presents the results with two walls obstructing the LOS. Finally, Section 7.4.4 is dedicated on the statistical performance by presenting the CDF of all cases.

7.4.1 Results and discussion of MF direct AoA for no wall obstruction

The first evaluation is on how accurately the developed algorithms determine the direct AoA when there are no obstructions. Fig. 7.6 presents the MUSIC spatial spectrum of 4 different locations to discuss how the developed MF algorithms combat the issues that emerge from multiple rays. The exact locations of the measurements are presented in Fig. 7.1, Subsection 7.2.

For location A3 in Fig. 7.6a, the proposed MF SF algorithm obtains an error of 5.7 degrees, while MF PE that utilises the phase information results to a correct estimation with 0.4 degrees of error. Compared to the best SF, which is f_3 with an error of 5.7 degrees, there is a 5.3 degrees of improvement. From the first example, it is evident that MF PE is able to resolve the direct AoA using the phase information of the signals received in MFs. On the contrary, MF SF performs a similar estimation with the SF f_3, which offers no improvement.

Moreover, for location A8, Fig. 7.6b; by fusing the spectrum, MF SF has an error of 6.7 degrees and MF PE is able to ascertain the direct AoA, with an error of 0.2 degrees. But since the single frequency measurements contained phase uncertainty, a second peak appears around 130 degrees at circa -2 dB. Compared to the best SF result of f_3 and 6.2 degrees of error, the overall improvement is 6 degrees. Again, MF SF does not obtain better result than the SF f_3.

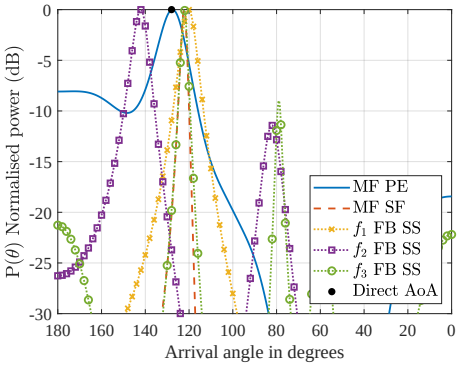

(a) MUSIC power spectra at A3. Direct AoA: 128 degrees.

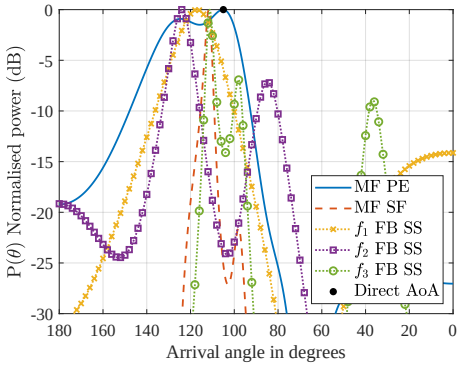

(b) MUSIC power spectra at A8. Direct AoA: 105 degrees.

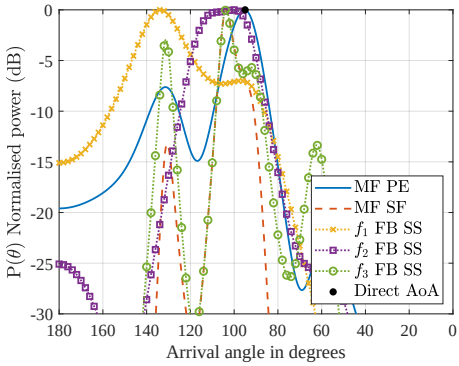

(c) MUSIC power spectra for A12. Direct AoA: 95 degrees.

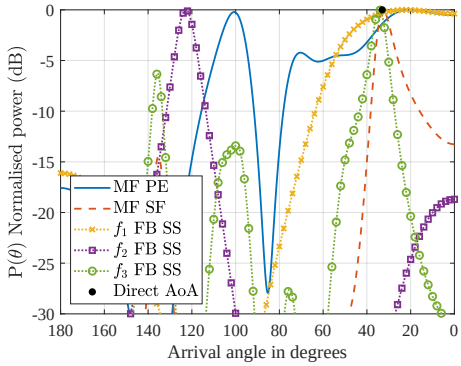

(d) MUSIC power spectra for A16. Direct AoA: 33 degrees.

Figure 7.6: The MUSIC spectra for single and multi frequency algorithms in cases where the direct AoA is not obstructed for locations, A3 (Fig. 7.6a), A8 (Fig. 7.6b), A12 (Fig. 7.6c), A16 (Fig. 7.6d).

Furthermore, in location A12, Fig. 7.6c; where the SF FB SS MUSIC algorithms resulted in broad peaks due to phase uncertainty, we can see that MF SF estimation has 8.7 degrees of error, while MF PE has a 0.3 degree error. It is evident that the phase information allows MF PE to achieve a correct estimation, improving the best result of f_2, by 5 degrees. The most important result of this example is that the MF PE is able to estimate the direct AoA with high certainty. Even though a second peak is formulated at circa 130 degrees, it is at circa -9 dB, allowing a correct estimation of the direct AoA.

Finally, the example with an extreme angle detection is presented in location A16, Fig. 7.6d. By having two peaks of the SF close to the the true AoA, MF SF performs the best with an error of 0.4 degrees, while MF PE estimates the direct AoA with an error of 13 degrees and a second peak at 100 degrees at circa 0.3 dB lower. This is the first example where one of the measurements is not accurate (f_2) and at the same time the result of f_1 is broad, suggesting phase uncertainty. This example provides an insight on why the overall estimation performance of the MF PE is compromised, and how MF PE is applied in the real world.

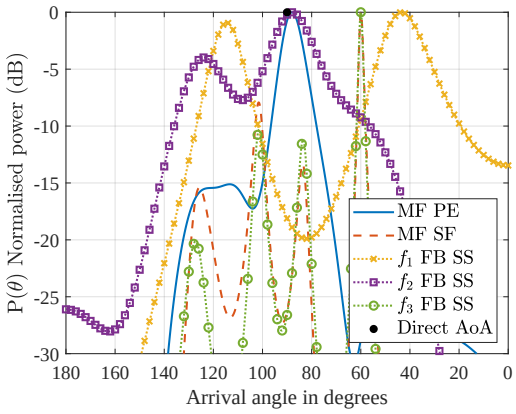

(a) MUSIC power spectra at B1. Direct AoA: 90 degrees.

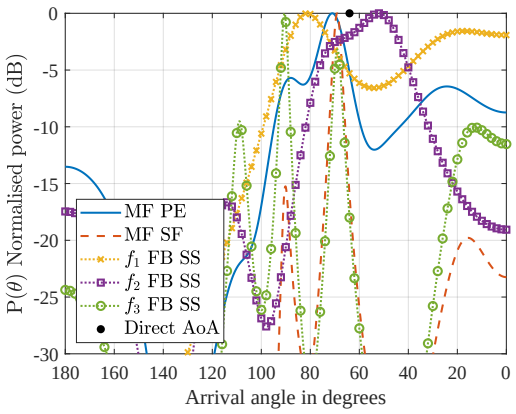

(b) MUSIC power spectra at B3. Direct AoA: 64 degrees.

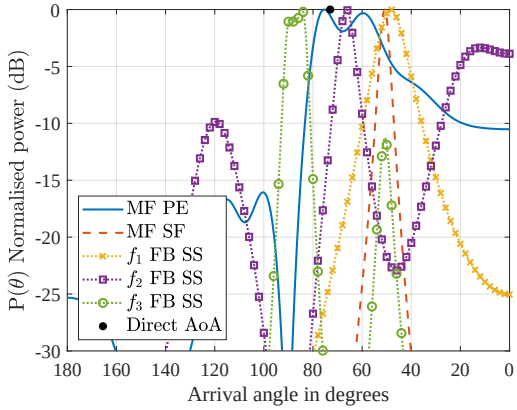

(c) MUSIC power spectra for B7. Direct AoA: 73 degrees.

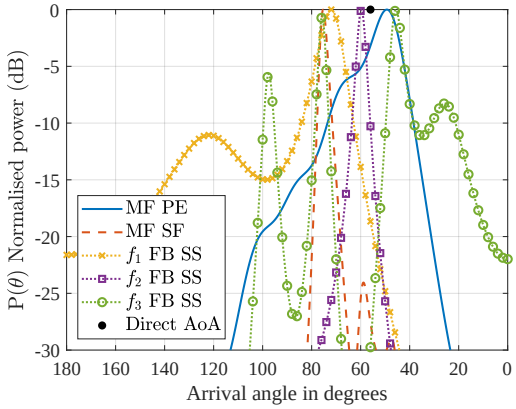

(d) MUSIC power spectra for B8. Direct AoA: 57 degrees.

Figure 7.7: The MUSIC spectra for single and multi frequency algorithms in cases where the direct AoA is obstructed by a single wall for locations, B1 (Fig. 7.7a), B3 (Fig. 7.7b), B7 (Fig. 7.7c), B8 (Fig. 7.7d).

7.4.2 Results and discussion of MF direct AoA for one wall obstruction

In this Subsection the accuracy of the developed algorithms is evaluated when the direct AoA is obstructed by a wall. In Fig. 7.7, the MUSIC spatial spectrum of 4 different locations is presented to discuss how the developed algorithms combat the issues that emerge from multiple rays and a single wall obstruction.

For location B1, Fig. 7.7a; MF SF produces a similar result with f_3, as the other two frequencies f_2 and f_3 produce broad peaks due to phase uncertainty. MF PE is able once again to determine the direct AoA with an error of 2 degrees, since even f_1 contains correct phase information at the true AoA even though it is at -20 dB. Compared to the best SF f_2, there is no improvement in this scenario. Overall, a 2 degree accuracy is very good, and can result to a high localisation accuracy.

Moreover, for location B3, Fig. 7.7b; both MF SF and MF PE algorithms have similar performance experiencing an error of 5 degrees, and 7 degrees respectively, as the power

spectra and phase information diverges close to the secondary peak of the f_3. This example is very difficult to produce a very accurate localisation because all the peaks of the SF are located at completely different angles. But since all signals have phase information close to the direct AoA, MF PE can improve the direct AoA estimation by 7.2 degrees.

Furthermore, for location B7, Fig. 7.7c; again all single frequency metrics produce different results. MF PE is able to determine the direct AoA. The estimation contains an error of 2.5 degrees, but a second peak appears at 60 degrees at circa -0.3 dB. MF SF produces a peak with an error of 22.2 degrees, while a smaller peak appears from the f_3 at circa -11 dB power. Again, it is evident that MF PE has the best performance, and improves the direct AoA detection by 4.2 degrees.

Finally, for an extreme angle detection in location B8, Fig. 7.7d; only f_2 is close with an error of 3.7 degrees. The other two remaining frequencies f_1, and f_3 experience a higher error of over 10 degrees and therefore MF SF is affected as well. The secondary peak from f_3 increases the error to circa 19.3 degrees, while MF PE takes advantage of the phase information from f_2 and f_3 and produces at peak with an error of 6.7 degrees. This is the first example where a SF FB SS MUSIC out performs MF PE, increasing the error by 3 degrees. From the spectral result at Fig. 7.7d we can see that the direct AoA phase information is very low for frequencies f_1 and f_3. The sharp peak of f_2 allows a semi-accurate estimation, preventing a coarse error.

7.4.3 Results and discussion of MF direct AoA for two walls obstruction

In this Subsection the accuracy of the developed algorithms is evaluated when the direct AoA is obstructed by two walls. In Fig. 7.8, the MUSIC spatial spectrum of 4 different locations is presented to discuss how the developed algorithms combat the issues that emerge from multiple rays and two walls obstructions.

For location C1, Fig. 7.8a; as shown in Subsection 7.4.2, the majority of the SF algorithms detected the direct AoA being at circa 133 degrees. As shown in Fig. 7.1, this is the location of a door, therefore the signal propagates through the door with higher power, than through the walls. This is evident in f_1 exhibiting a broad peak suggesting phase uncertainty, while both f_2 and f_3 have secondary peaks at circa 84.5 degrees. MF SF is located to the other side of the spectra at 84.4 degrees, with an error of 35.5 degrees. Also, it is evident that MF PE is unable to distinguish the direct AoA since no other frequency contains correct information regarding the direct AoA resulting to an estimation of 132 degrees. Overall, MF PE is able to improve the estimation by one degree, which can be judged insignificant. This performance is due to the lack of phase information at the direct AoA. From Fig. 7.8a, it is evident that the SF f_2 and f_3 lack phase information, therefore direct AoA detection is impossible for MF PE.

On the contrary, for location C3, Fig. 7.8b; where the phase information is available, MF PE is able to ascertain the direct AoA with an error of 1.2 degrees. In fact, f_1 and f_3 seem to contain phase information relevant to the AoA. That is a circa 8 degrees improvement compared to the best SF f_1 performance. Due to the poor performance of f_2, MF PE is

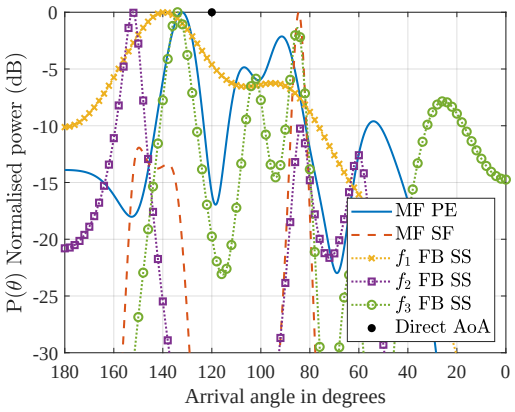

(a) MUSIC power spectra at C1. Direct AoA: 120 degrees.

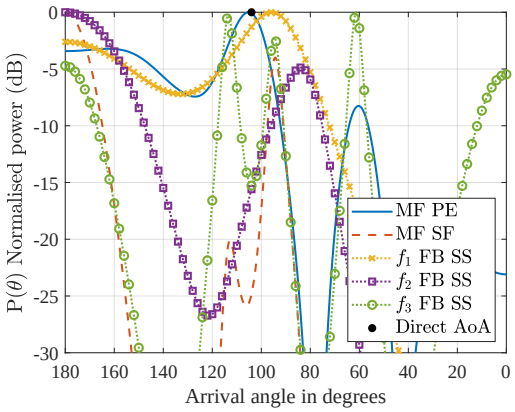

(b) MUSIC power spectra at C3. Direct AoA: 104 degrees.

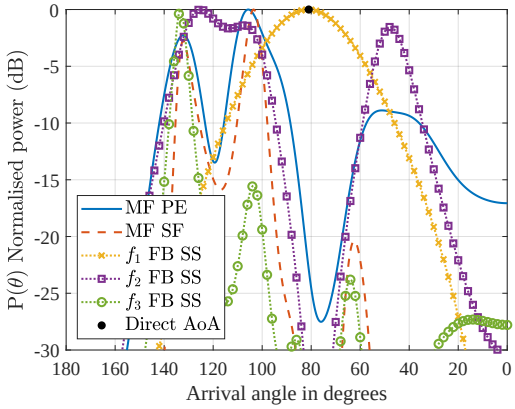

(c) MUSIC power spectra for C6. Direct AoA: 81 degrees.

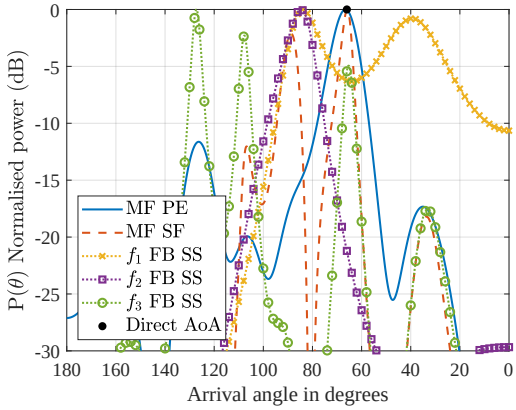

(d) MUSIC power spectra for C9. Direct AoA: 66 degrees.

Figure 7.8: The MUSIC spectra for single and multi frequency algorithms in cases where the direct AoA is obstructed by two walls for locations, C1 (Fig. 7.8a), C3 (Fig. 7.8b), C6 (Fig. 7.8c), C9 (Fig. 7.8d).

unable to perform an estimation due to phase uncertainty.

Moreover, for location C6, Fig. 7.8c; both MF SF and MF PE perform a wrong estimation. This is the worst performing result out of all 36 locations. The direct AoA error observed for MF PE is 24.7 degrees. In this example, the application of MF SF results to an error of 24.5 degrees. Looking back at Fig. 7.1, we can see that there is a horizontal wall blocking the direct line of sight. The wavelength of f_1 seems to not be directly affected by the presence of that wall but the other two frequencies with smaller wavelengths are affected. As the receiver moves close to either C5 or C7 the AoA power spectra becomes clearer.

Finally, for location C9, Fig. 7.8d; we can see that both MF SF and MF PE are able to resolve the direct AoA with an error of 0.2 and 0.5 degrees respectively. Compared to the best SF f_1, the improvement on the direct AoA detection is 84 degrees. This example, proved that only MF can detect the direct AoA. The phase information exists in all SF, but non of them has a peak close to the direct AoA. Both MF SF and MF PE are able to

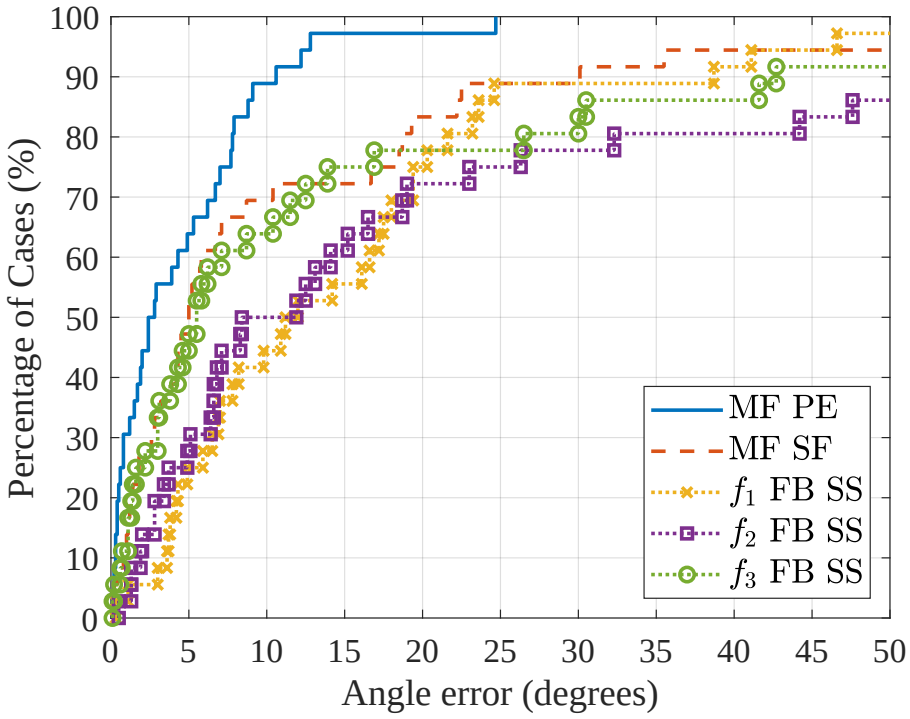

Figure 7.9: Empirical CDF plot of angular error for FB SS MUSIC in frequencies, f_1, f_2, f_3, and MF SF, MF PE algorithms.

perform correct estimations.

7.4.4 Statistical performance results and discussion of MF PE direct AoA estimation

Fig. 7.9 presents the empirical CDF of the absolute error between direct AoA θ and estimated direct AoA ($\widetilde{\theta}$) from the 108 measurements in all 36 locations is presented, CDF($|\widetilde{\theta} - \theta|$). We can see that the mean error of MF PE is 2.4 degrees, while the second best is MF SF with a mean error of 5 degrees. Regarding the SF, f_3 has an error of 5.3 degrees, f_2 has 8.4 to 11.9 degrees of error, and the error of f_1 is at 12 degrees. As for 75% of the measurements, the MF PE achieves an error of 7 degrees, while MF SF and f_3 are both at circa 16.7 degrees. Finally, for the 95% of the measurements MF PE is able to maintain an error below 12.8 degrees, MF SF error is at 35.5 degrees, and f_1 at 41.1 degrees. The only case that the error is greater than 15 degrees for MF PE is highlighted at Subsection 7.4.3, for the measurement in location C6 Fig. 7.8c.

In terms of RMSE, for the single frequency FB SS MUSIC algorithms the error is 22.5 degrees, 33.9 degrees, and 21.7 degrees, for frequencies f_1, f_2, f_3 respectively. While MF SF error is at 23.4 degrees, and MF PE error is at 6.7 degrees. In terms of RMSE performance, f_1, f_2, and MF SF performances are equal with an error difference circa 1.7 degrees. Overall, we can see that MF PE is able to reduce the RMSE error by 15 degrees, even if the single frequencies experience a high error.

With these results, it is evident that the MF PE algorithm is the only way to distinguish the direct AoA. The most critical finding of this research is that the performance of the MF PE relies on the the phase information. As shown Section 2.5 the SNR, the number of ULA elements, and and existence of AoA noise play an important role. Moreover, findings showed that if at least two out of the three frequencies contain the phase information on the direct AoA, the error is reduced drastically. In the next subsection, the robustness of the MF PE is investigated. The robustness takes into consideration, the number of frequencies used, the number of antenna elements, and the performance of the MF PE by obtaining the noise subspace (7.2) and applying QR instead of SVD.

7.5 Investigation of the MF direct AoA robustness

This Section investigates the robustness of the MF PE algorithm. In the first Subsection 7.5.1, the effect of the number of frequencies is investigated by applying the MF PE with a different set of frequencies. In the following Subsection 7.5.2, the importance of the antenna elements is investigated by pruning the number of elements in the array. In the final Subsection 7.5.3, the use of the SVD is questioned by evaluating the performance of MF PE when the noise subspace is obtained by the QR decomposition methods 1 and 2, as shown by Tayem [58] in Subsection 3.2.1.

7.5.1 Performance evaluation with varying number of frequencies

This Subsection discusses the effects of different frequencies in the performance of MF PE. Fig. 7.10 presents the empirical CDF error performance of MF PE by reducing the number of frequencies used for estimation. The mean error of only utilising the frequencies f_1, f_2 is 11.3 degrees, f_1, f_3 is 5.6 degrees, and f_2, f_3 is 6.9 degrees. As for the 75% of the measurements, in the same order, the error is 18.7 degrees, 16 degrees, and 18.5 degrees respectively. Taking into consideration the percentile error, we can see that the performance is similar; but seeing the CDF curve at Fig. 7.10, it is evident that the performance of f_1, f_3 is slightly better. Thus, when ranking the importance of the frequencies in the overall MF PE performance, the most important frequencies are f_3, f_1, and f_2, confirming the single frequency performance shown in Subsection 7.3.2.

The main reason that we see f_3 outperforming the other two frequencies is due to the number of measurements in the LOS. As it is highlighted in Subsection 7.3.2, the high frequency performs better in the direct AoA scenario with no obstruction. Since half of the measurements performed are with LOS, it is expected that the high frequency performs better. Moreover, that is another reason why the majority of research is focused on high frequencies (e.g. WiFi) as shown in the literature review presented in Chapter 1.

Comparing the best results of Fig. 7.10 with the previously presented CDF of single frequency in Fig. 7.9, it is evident that the performance of f_3 is equal and in some percentile better than MF PE. This might be confusing but taking into consideration the spectral results of Fig. 7.6, 7.7, 7.8, in some instances, not all frequencies contains accurate phase

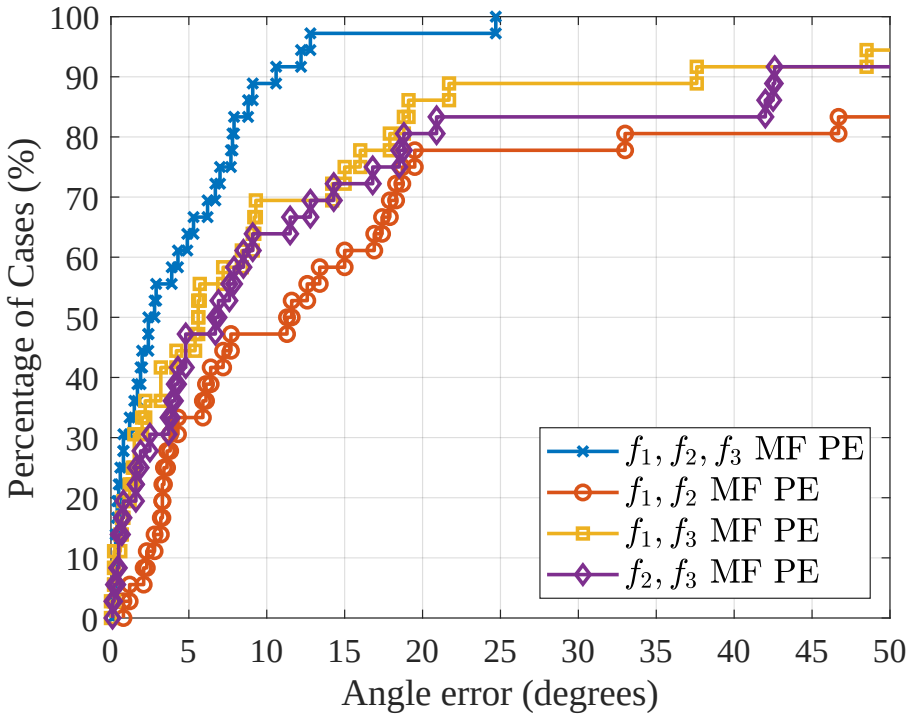

Figure 7.10: Empirical CDF plot of angular error for MF PE utilising all frequencies, frequencies f_1 and f_2, frequencies f_1 and f_3, and frequencies f_2 and f_3.

information. Entangling the phase information from two frequencies when only one is accurate, it is only natural that the result will be worse. Therefore, in order for MF PE to be effective, all three frequencies are required.

7.5.2 Performance evaluation with varying number of ULA elements

This Subsection discusses the effect that the number of antenna elements has in the performance of MF PE. To measure the effect, the number of elements is pruned before the application of the algorithms. Fig. 7.11 presents the empirical CDF error performance of MF PE if the ULA had fewer elements. As the number of antenna elements M decreases from 10 to 9, the mean error increases from 2.8 degrees to 4.2 degrees. Moreover, for 8 and 7 antenna elements, the mean error is 5.9 degrees and 9.8 degrees respectively. It is evident that when we decrease the number of elements from 10 to 8, the reduced phase information does not affect the result greatly since the error increases by only 3.1 degrees. But when the number of elements is pruned to 7, the error increases to 8 degrees which is significantly higher compared to the 3.1 degrees.

Concerning the performance in the 75% of the measurements, the relationship between a 10, 9, 8, 7 antenna elements and the error is 7 degrees, 14.2 degrees, 18.1 degrees, and 44.8 degrees respectively. Hence, it is evident that a high number of antenna elements is vital for the performance of MF PE. Looking at the 97% of the measurements, only the 10 antenna elements performance produce a result with less than 25 degrees of error.

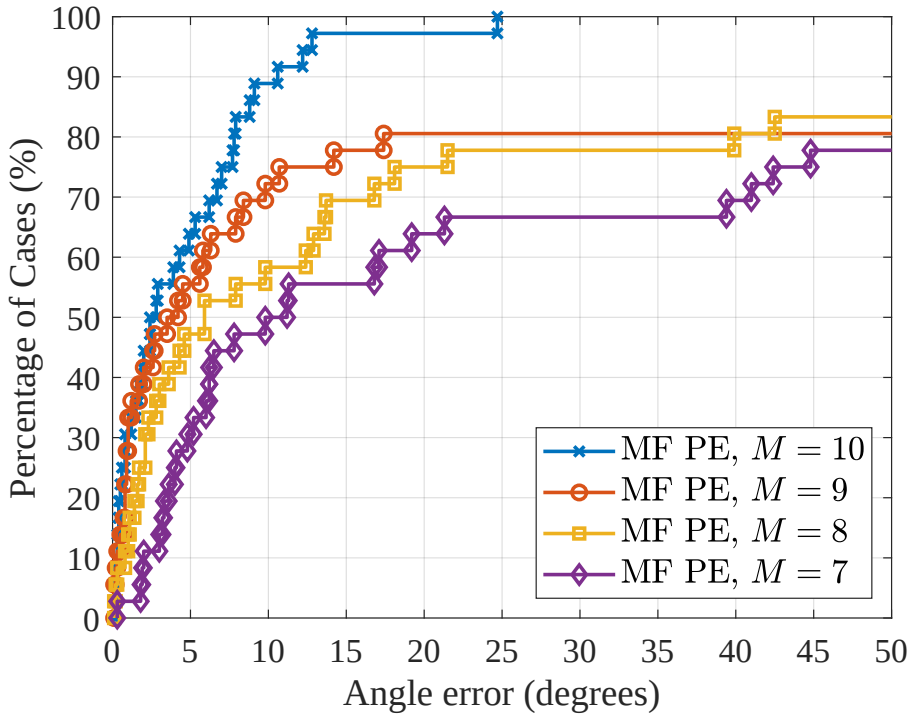

Figure 7.11: Empirical CDF plot of angular error MF PE with $M = 10$, $M = 9$, $M = 8$, $M = 7$, antenna elements.

Also, at the 80% of the measurements, as we can see from Fig. 7.11, the error performance of the reduced antenna elements starts to converge. As shown from the simulation in Section 2.5, as the number of elements increase, the measured floor imposed by noise drops because the size of the received information is increased. Therefore, it is believed that this is happening due to the limit in the phase information, having a measured noise floor imposed by noise. To put the percentile in perspective, 28 out of 36 measurements require the presence of one additional element so that they can be resolved with an error less than 50 degrees. Therefore, if the mean performance is more important in the overall application, the number of elements can be pruned down to 9 or even 8 depending on the accuracy requirements.

On the contrary to what the literature suggests [7, 19], the direct AoA detection performance of MF PE is increased as the number of antenna elements increases. This is due to the criteria of direct AoA estimation and the fact that only a single metric is utilised for estimation. In both examples [7, 19], the systems fuse information from multiple receivers and specifically in [19] from multiple metrics as well. Therefore, even if the true direct AoA estimation is not correct, the back-end algorithms can still resolve it with fewer antenna elements. The benefits of applying MF in a real system is to reduce the overall number of receivers in an area. As this research has show, MF provides the ability of detecting the direct ray even behind two walls with high accuracy. Therefore, fewer receivers are required to cover an area, reducing the overall cost. A more extensive comparison between MF PE and the state of the art systems will be performed in Subsection 7.6.

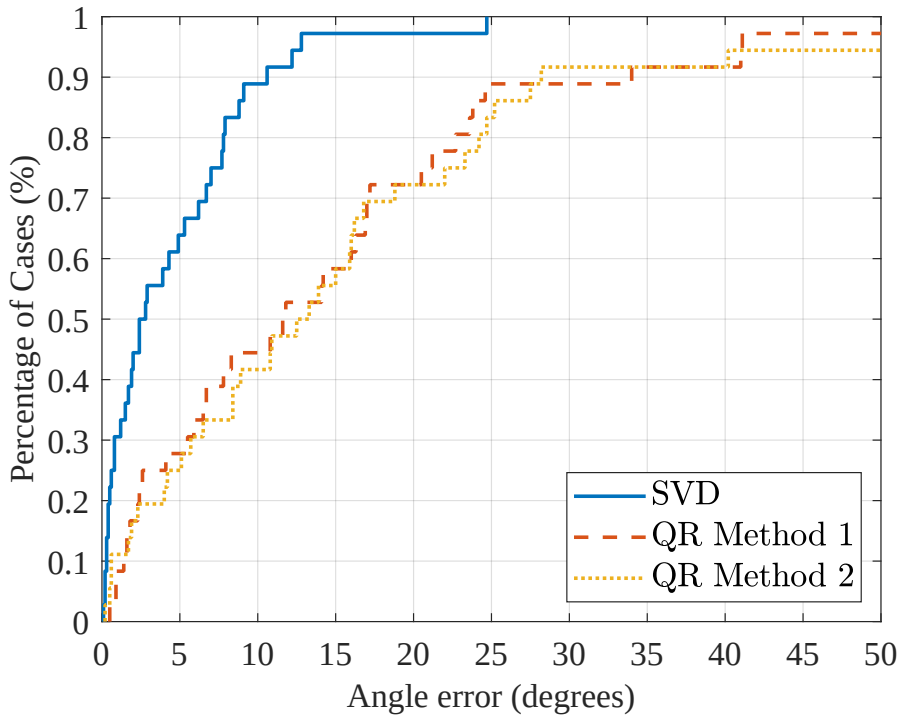

Figure 7.12: Empirical CDF plot of MF PE by obtaining the noise subspace with SVD or QR decomposition **method 1**, and **method 2** from [58] with $M = 10$.

7.5.3 Performance evaluation of MF PE utilising QR

This Subsection presents the performance of the MF PE by adopting the QR decomposition methods presented in [58]. As explained in Subsection 3.2.1, the complexity of the QR decomposition using the Householder transform is $\mathcal{O}((mn2 - n3)/3)$, while SVD has a complexity of $\mathcal{O}(mn2 + n3)$. Therefore, by utilising QR decomposition instead of SVD, the algorithmic complexity is reduced.

Fig. 7.12 presents the empirical CDF error performance of MF PE using SVD, and methods 1 and 2, presented in Subsection 3.2.1, developed by [58]. The mean error performance of QR method 1 is 11.8 degrees, while the error of QR method 2 is 12.5 degrees. For 75% of the measurements, the error of QR method 1 increases to 21.2 degrees, while the error of QR method 2 is 22 degrees.

Overall, from Fig. 7.12 it is evident that the performance of the MF PE with the adoption of the QR decomposition suffers in both the mean performance and in the 75% of the measurements. The increase for the mean error is 9.2 degrees, while for 75% of the measurements is 15 degrees. The issue with the performance of QR decomposition is due to the lack of phase information. The reason for the error increase is due to the fact that SVD subspace estimation is more complex but maintains the phase information in the signal and noise subspace. On the contrary, the findings show that the less complex QR decomposition sacrifices the subspace phase information. This realisation is made by looking at the individual MUSIC spectra, as shown in Subsection 7.3, and Subsection 7.4.

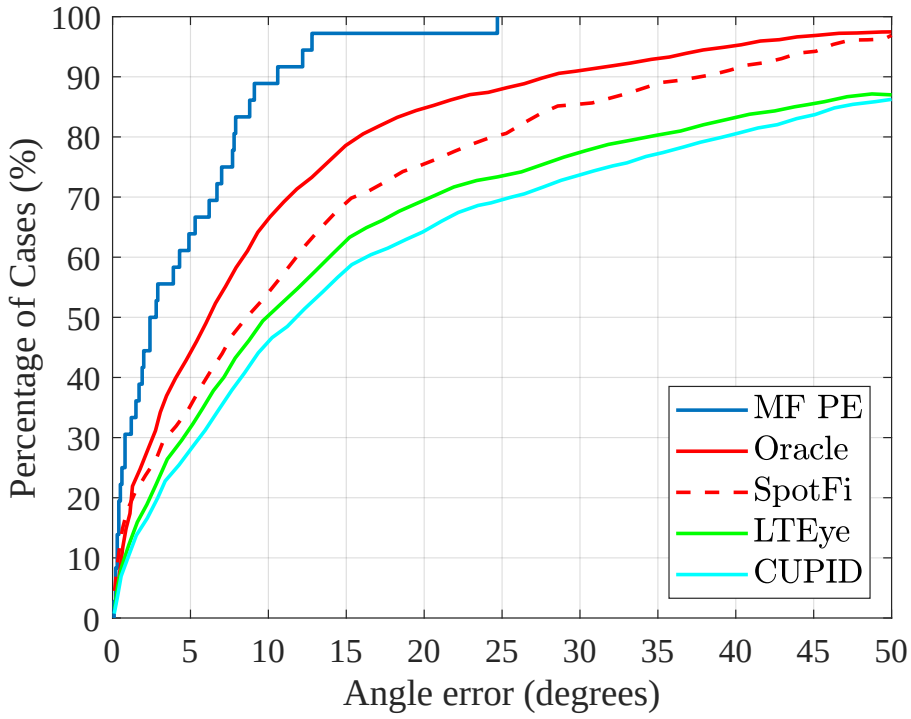

Figure 7.13: Empirical CDF plot comparing MF PE, Oracle, SpotFi [19], LTEye [31], and CUPID [32], in regards to direct AoA selection.

7.6 Comparison with the state of the art systems, on detecting the direct AoA

This Section presents a comparison of the best performing MF algorithm, MF PE and state of the art systems SpotFi [19], LTEye [31], and CUPID [32], in regards to direct AoA selection. Fig. 7.13 presents the empirical CDF error performance of MF PE, Orcale, SpotFi, LTEye and CUPID. The Oracle algorithm presented in the figure is not a real system. It is an ideal scenario of SpotFi, where Oracle selects the AoA closest to the direct AoA from SpotFi, therefore in some sense, is the best performance that SpotFi can achieve in theory.

The mean error performance of MF PE is 2.4 degrees while Oracle and SpotFi are 6.1 and 8.6 degrees respectively. The mean error of LTEye is 9.9 degrees, while the mean error of CUPID is at 11.8 degrees. Therefore, regarding mean performance, MF PE reduced the error by 3.7 degrees compared to Oracle and 6.2 degrees compared to SpotFi. Moreover, the error performance in the 75% of the measurements is 7 degrees for MF PE, 13.5 degrees for Oracle, 19.7 degrees for SpotFi, 27.1 degrees for LTEye, and 31.8 degrees for CUPID. For the 75% performance, the error is reduced by 6.5 and 12.7 degrees comparing MF PE with Oracle and SpotFi respectively. Finally, to highlight the exceptional performance of MF PE, for the 95% of the measurements the error is 12.8 degrees while for Oracle and SpotFi the error is 39.8 and 45.9 degrees respectively. The 95% of the error provides provides an insight on the excellent performance of MF PE. By utilising MF and applying

MF PE the error is reduced by 27 degrees compared to Oracle, and 33.1 degrees compared to SpotFi. Therefore, it is evident that the implementation of multiple frequencies and MF PE can improve the localisation accuracy compared to the state of the art localisation systems.

7.7 Conclusions

This Section concludes the findings of this Chapter. Section 2.5 serves as an introduction to the Chapter providing further insight on how the MUSIC power spectra works. Three simulations are introduced, where the MUSIC power spectra is presented as a function of SNR, as a function of number of ULA elements, and as a function of AoA noise. In the following Section 7.2, the environment where measurements took place was presented, with three different location scenarios highlighted. In the first measurement scenario, the LOS was present and the direct ray was not obstructed; in the second measurement scenario the direct ray was obstructed by a single wall, and in the third measurement scenario the direct ray was obstructed by two walls. Then, the spectral and statistical results of the SF FB SS MUSIC were presented in Section 7.3. The spectral results showed that in the first measurement scenario the high frequency f_3 outperformed the lower frequencies f_1 and f_2, while for the other two measurement scenarios the lower frequencies f_1 and f_2 performed slightly better than the high frequency f_3. Overall, the findings showed that phase information regarding the direct AoA still existed on the majority of the measurements, but it was not high enough to perform a correct estimation. The results of the empirical CDF for the high frequency f_3 showed a mean performance error of 5.3 degrees and for 75% of the measurements 16.7 degrees.

In Section 7.1, the developed MF algorithms were introduced. The purpose of MF SF was to fuse the spatial spectrum all frequencies, while the purpose of MF PE was to entangle the phase information on the sampled time domain, maintaining the phase information, and untangle them with the appropriate steering matrix. The spectral and statistical findings of Section 7.4 proved that MF PE outperformed MF SF and all the SF FB SS MUSIC results. Spectral results showed that when two out of three frequencies had phase information regarding the direct AoA, MF PE was able to estimate the direct AoA with high accuracy. The improvement that MF PE achieved compared to the best performing SF FB SS MUSIC in the CDF was 2.9 degrees for 50% of the measurements, 9.7 degrees for the 75% of the measurements, and 22.7 degrees for the 95% of the measurements. Therefore, it was evident that MF was able to achieve significant improvement in all percentiles of measurements.

In Section 7.5, the robustness of the MF PE was investigated. First, the number of required frequencies was examined by applying the MF PE algorithm with a different set of frequencies. The best performing frequencies were found to be f_3 and f_1, but still the mean error increased 5.6 degrees. Hence, it was evident that all frequencies were important in order the MF PE can have an exceptional performance. The reason the performance degradation was because all frequencies have valuable phase information. By

reducing the number of frequencies, the phase information was reduced, therefore the estimation of the direct AoA was worse. Then, the required number of ULA elements was examined by pruning the size of the array. By pruning the number of elements to 9, the mean error increased by 1.4 degrees while for 8 elements the mean error was increased by 3.9 degrees. The mean increase of error was small; but for the 75% of the measurements and 9 elements, the error increased by 7.2 degrees while for 8 elements increased by 11.1 degrees. Thus, if the mean performance was the main concern of the system, the number of elements could be potentially decreased. In the final robustness test, the QR decomposition [58] was applied instead of the SVD to obtain the signal and noise subspace. The findings showed that the QR decomposition reduced the phase information in the subspace. The mean error was increased to 9.2 degrees, while for the 75% of the measurements the error was increased by 15 degrees. Hence, the simplification of the algorithm by applying QR decomposition would not help the overall system performance.

Moreover, Section 7.6 was dedicated on the comparison of the MF PE with the state of the art systems highlighted in Chapter 1, SpotFi [19], LTEye [31], and CUPID [32]. Findings showed that MF PE was the only algorithm that was able to obtain the direct AoA with very high certainty. The mean error performance of MF PE compared to Oracle (an ideal version of SpotFi) improved the direct AoA estimation 3.7 degrees while for 75% of the measurements improved the estimation by 6.5 degrees, and for 95% of the measurements improved the estimation by 27 degrees.

The findings of this Chapter proved that MF PE was able to obtain a very high accuracy in direct AoA estimation compared to the state of the art systems. These findings indicated that the use of MF could decrease the number of receivers required, because MF PE was able to estimate the direct AoA with high accuracy. Moreover, the low error of the direct AoA estimation was achieved when at least two out of three signals contained relevant phase information in their subspace. Therefore, the use of at least three frequencies was important. Furthermore, if the mean performance was the main concern of the system, the overall number of elements could be reduced from 10 to 8, but the use of SVD was crucial to the excellent performance, because it was able to maintain phase information, that QR decomposition does not.

Chapter 8

Conclusions and future research

This Chapter summarises the findings of this research, draws conclusions based on the findings and highlights potential future research. Section 8.1 presents the findings of each Chapter with detailed results and explanations, while Section 8.2 provides a brief description on future research this research could generate.

8.1 Summary

The first Section is dedicated to the conclusions of the presented research by summarising the context and findings of each Chapter. In Chapter 1, it was made evident that localisation is a research topic with no universal solution. Outdoor localisation research is focused on GPS, while indoor localisation systems require an unrealistic number of receivers or exhaustive pre-calibration. Then it highlights the novelty of this research, which is the use of frequency diverse RF antenna arrays for AoA estimation. This Chapters concludes by listing the research contributions and the organisation of this thesis.

Chapter 2 was dedicated on the necessary background information. First, the analytical model of the receiver was presented. It was followed by the most basic method of estimating the AoA from the received phase, interferometry. Then, the MUSIC and ESPRIT subspace algorithm were introduced, which are more advanced methods and they are based on the orthogonality between the noise and the signal subspaces to resolve the AoA. Moreover, decorrelation methods were introduced such as SS and FB SS, which are used by state of the art systems. Finally, multiple simulations are presented to provide an insight on the MUSIC power spectra and how it is affected as a function of SNR, number of ULA elements, and AoA noise.

Chapter 3 is were the state of the art localisation systems are presented. The list is categorised based on the metrics that are utilised to achieve that. Some of the papers were highlighted and later compared with the outputs of this research in Chapters 6 and 7. Through the literature review, it was made evident that the majority of the systems were bound by protocols and therefore, the use of multiple broadly spaced frequencies had not been researched before. Hence that was one of the reasons that this research avenue was

followed.

Chapter 4 introduces the novel tri-band PCB antenna design, measurements and simulation. Measured results show that the the return losses were all within the design parameters, and the design antenna was employed for both transmitter and receiver array. Moreover, measurements and simulation of the PCB antenna as a ULA showed that the reflection coefficients of the targeted frequencies were within design parameters and that there was no effect of mutual coupling.

Chapter 5 presented the design of both transmitter and receiver used for the measurements in Chapters 6 and 7. Transmitter characterisation showed that the missmatch losses for all frequencies not exceeding -0.6 dB and resulted that the overall the transmitter design was adequate for its purpose, being able to perform measurements for approximately 20 hours of continuous use. Furthermore, the RSP2 receiver array was presented with a detailed explanation on how the array was synchronised and calibrated. Frequency synchronisation was achieved by connecting the output of the sampling clock of the first RSP2 to the following RSP2, while time synchronisation took advantage of the two ports. A signal was injected on Port B of the RSP2 and the same signal could be seen in Port A with zero phase difference but attenuated by 14 dB. Finally, receiver array characterisation was presented, with the dynamic range of the RSP2 receiver array measured to be -130 dBm to -50 dBm for f_1, -120 dBm to -50 dBm for f_2, and -110 dBm to -40 dBm for f_3. Also the impedances of the RSP2 were measured and the highest missmatch loss was estimated to be -3.9 dB, -5.1 dB, and -1.9 dB, for f_1, f_2 and f_3 respectively. This did not have a great affect on the dynamic range of the receiver, and therefore the receiver array was adequate to perform the final measurements.

In Chapter 6, the first major contribution of this research was presented; the extraction of AoA from MF RSS measurements [29]. In these first measurements performed in an anechoic chamber, the ULA gain patterns were evident in the RSS when the transmitter was close to the receiver. As the transmitter got farther away, the RSS patterns of the lower frequencies f_1 and f_2 became flat. After additional measurements in an outdoor environment, the ground reflection introduced did not affected the RSS patterns. On the contrary, multi-ray simulation of an indoor environment found that the wall reflections affected the RSS patterns. Therefore, two novel techniques were developed, named xCorr, and MF RMS to extract AoA from RSS patterns. Measurements were performed in an indoor environment to evaluate the two techniques and then they were compared with the state of the art systems that estimate the AoA from RSS, introduced in Chapter 1. The state of the art systems employ either a SBA or ESPAR antennas which both increase the overall cost and system complexity. Compared with SBA systems, the proposed technique xCorr, in some cases reduced the mean error by 1.3 degrees [45], or slightly increased it by 0.3 degrees [46]. Compared with ESPAR systems, the proposed technique always increased the error by 4 degrees [47] and 3.7 degrees [48]. The real benefit of the proposed technique was the significantly reduced system complexity that was required.

Chapter 7 presented the second major contribution of this research, where the AoA was estimated by fusing signals from MF [30]. First, the indoor environment that was

used for measurements was introduced followed by the performance evaluation of the SF MUSIC algorithm presented in Chapter 2. The issues of each individual frequency were highlighted and it was made evident that merging the three proposed frequencies could potentially improve the AoA estimation. Then, two algorithms were introduced; MF SF that fuses all the SF spectra formulating a single spectrum, and MF PE which entangles the phases on a signal level, formulates the appropriate steering vector and estimates the AoA. Using the same measurements, the MF algorithms were evaluated. Findings showed that MF PE algorithm improved the direct AoA estimation in all cases reducing the overall error for 50% of the measurements to 2.4 degrees, in 75% of the measurements to 7 degrees, and in 95% of the measurements to 12.8 degrees. Then, the robustness of MF PE was tested by reducing the number of frequencies and it was found that all frequencies were required to maintain the low error performance. Moreover, by reducing the number of ULA elements from 10 to 9, the mean error performance was increased by 2.8 degrees to 4.2 degrees, while for 75% of the cases the error increased by 7 degrees. Hence, reducing the number of elements greatly affected the 75% performance. Also, the use of QR decomposition instead of SVD was investigated, as suggested in Chapter 1 [58]. It was found that QR decomposition affected the performance of MF PE because it reduced the phase information obtained from the subspace. Finally, MF PE was compared with the state of the art localisation system SpotFi on estimating the direct AoA. Findings showed that MF PE reduced the mean error by 6.2 degrees; moreover, for 75% of the cases the error was reduced by 12.7 degrees, and for 95% of the cases the error was reduced by 33.1 degrees.

The findings of Chapters 6 and 7, proved that MF can provide a plethora of benefits. MF reduced the overall hardware cost, and achieved the same or slightly worse result. Furthermore, it showed through measurements that MF PE can dramatically improve the direct AoA estimation, compared to state of the art systems. With the needs of localisation being highlighted in Chapter 1, MF is the only approach that can achieve universal localisation with high accuracy. The lower frequencies enable long range communications, while the diversity of the MF signals in indoors provide a unique advantage over the state of the art localisation systems.

8.2 Future research

This Section presents possible future research that can be generated from this work. Subsection 8.2.1 presents a novel idea for a circularly polarised MF antenna which could be employed by both transmitter and receiver, while Subsection 8.2.2 is dedicated on explaining a novel application of Genetic Algorithm (GA) to estimate the properties of the rays that reach the receiver. Finally, Subsection 8.2.3 presents an autonomous localisation system that could potentially employ a self evolving algorithm that would autonomously learn the propagating environment and perform localisation.

8.2.1 Circularly polarised transmitting and receiving antenna

It is known that diversely polarised antennas for AoA detection allow the detection of closely spaced signals [21]. The authors in [21] showed that the use of MUSIC with a polarisation angle of 10 degrees was able to resolve the AoA of two signal separated by 1 degree degree, with an error of 0.1 RMS, for 12 dB SNR. On the contrary, a linearly polarised array was unable to separate the two signals. Hence, the use of diverse polarised antennas can reduce the AoA noise. Taking that into consideration, the design of a tri-band Circularly Polarised (CP) antenna started, at the end of the research. The purpose was to utilise a CP antenna, repeat the measurements with CP and linear antennas with MF, and evaluate the benefits. The design process is described in detail below.

In [115], the authors presented a reduced size CP antenna for 434 MHz with meandered bow-tie elements and a quadrifilar feed. The designed antenna solved the issue of the size requirements of 434 MHz and reduced the overall size to 11.24 cm. Moreover, circular polarisation was achieved with a feed network using lump element components. By following a similar design, a tri-band circularly polarised antenna could designed and simulated for frequencies that are used in this research. An example of such design is show in Fig. 8.1. The four meandering elements are the radiating parts of the antenna, while the square in the centre could house the matching circuit and create the phase offset required for each element. To create the phase offset on board the antenna, the employment of an ADL5390 could be considered [116]. ADL5390 is an Intermediate Frequency (IF)/RF vector multiplier. The ADL5390 consists of two RF inputs and two broadband variable gain amplifiers (20 MHz, to 2.4 GHZ) whose outs are summed. The maximum output can be controlled to a maximum of +5 dB or minimum of -30 dB, while the phase can be shifted over 360 degrees. The adjustable modulation bandwidth is up to 230 MHz, with a noise floor of -148 dBm/Hz.

Finally, the CP antenna that would be employed in a real system, as a transmitter or receiver. The ADL5390 has the ability to control the gain, which will be a great feature for the transmitter, enabling OOK or pulse modulation, which could be used to improve AoA accuracy. To increase the information that the transmitter provides, an OOK modulated signal could be transmitted with sensor data, instead of a CW. The designed CP antenna could potentially serve multiple different bands, simply by changing the matching circuit. Therefore, the design of such CP antenna could have a wider research impact.

8.2.2 Genetic Algorithms for localisation without fingerprinting

Evolutionary Algorithm (EA) is a large family of heuristic problem solving algorithms that have found applications in real world problems [117, 118]. GA specifically, is a subset of EAs. In GA problem, a population is evolved toward a better solution. Each individual of the population has a set of unique set of properties which can be mutated. The evolution begins from a random population, where each individual is evaluated through a fitness function. The fitness function is the optimisation problem expressed in a form of an equation. After the population is evaluated, the best solutions of the fitness function are

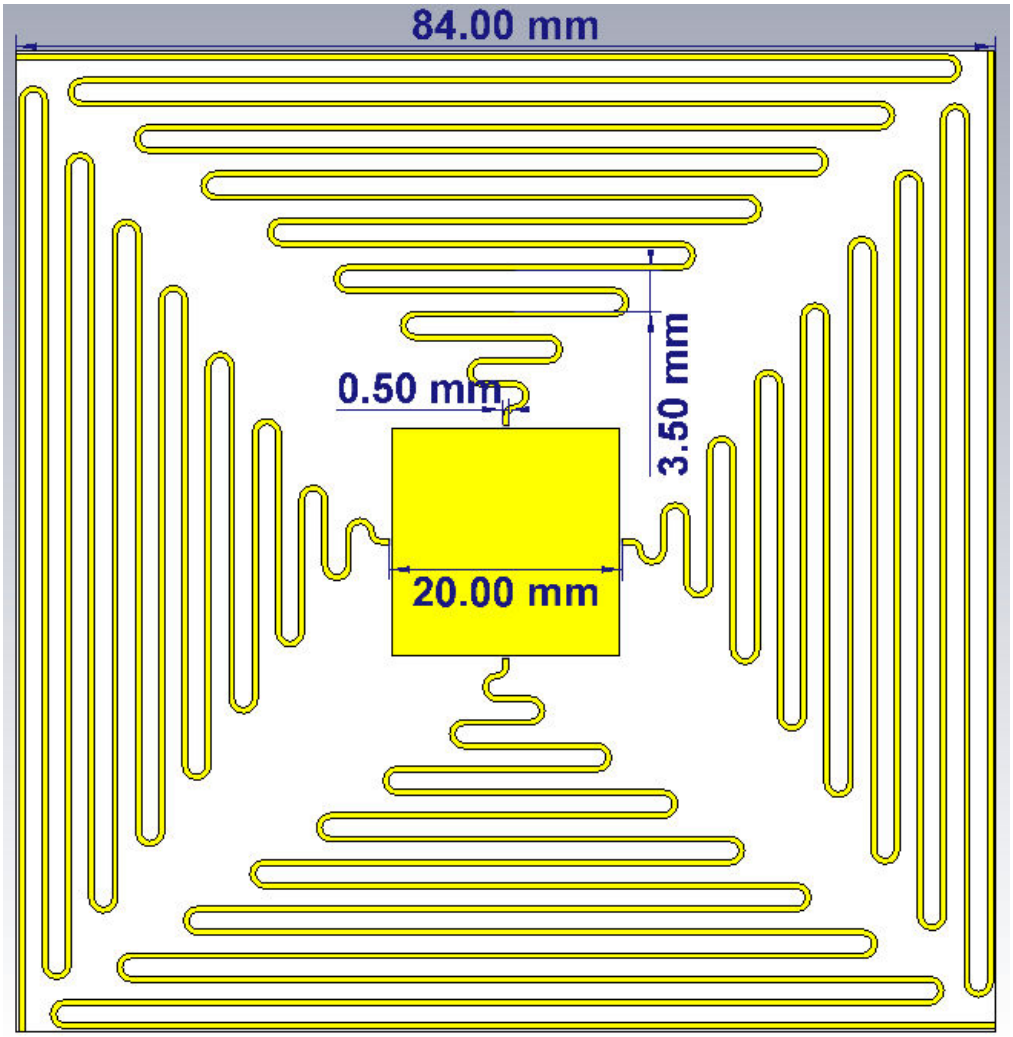

Figure 8.1: Example of a tri-band CP antenna.

selected to breed a new population, forming the next generation. The iterative process continues with the new generation being evaluated with the same fitness function; then, the best performing individuals are selected to breed the next generation. The iterative process continues for a predetermined number of generations or until certain criteria of the GA are met. Advanced GA takes mutation into consideration, where randomly a number of the population is mutated and has its unique properties changed randomly.

Every GA requires a genetic representation and a fitness function. Genetic representation is the way of representing the individual of the population, while fitness function is the objective function used to summarise the performance of an individual. Therefore, having a genetic representation and a fitness function, the optimisation problem can be solved heuristically. The benefit of heuristic algorithms is the trade-off between accuracy or precision for speed. Therefore, the GA finds a shortcut to a solution, being convex or non-convex. Therefore, GA are structured to solve very wide range of problems, en-

gineering and computer science [119], earth sciences [120], finance and economics [121], and social sciences [122].

As this research has indicated, indoor localisation can be extremely difficult. Therefore, an application of a GA can help produce a system that performs localisation on complex environments, such as indoors. The multi-ray model which was explained in this research, can serve as the objective function. Since the RSS is a function of rays and distances that depend on the location of the transmitter, the GA could heuristically attempt to resolve the location to mach the measured RSS. The use of GA has been studied before for outdoor environments and cellular transmission [123]. Findings showed that GA ray-tracing can achieve significant reduction in computation time.

Moreover, by applying GA ray-tracing in an indoor environment would eliminate the requirement for fingerprinting RSS values. Therefore, the pre-calibration requirements of the method introduced in Chapter 6 would be eliminated. Finally, an example that GA could be applied is with multiple low cost RSS receivers distributed in an area, performing RSS measurements. Each receiver would apply a local GA to estimate the location of the transmitter. Their results would be shared on a single device in an IoT network and then by running a local algorithm or machine learning network, the final estimation would be made.

8.2.3 Autonomous localisation system

This Subsection is dedicated to the ideal goal of the future research. Machine learning research spending is expected to grow from £9.4B in 2018 to £45B by 2021. Advancements in research and development of machine learning algorithms and integrated circuits will have an impact on the future localisation systems, effecting accuracy and speed. Therefore, the next step of this research should investigate the use of different DNN, that will utilise multiple metrics, such as the traditional RSS, AoA, and the MF which was introduced in this research. A DNN is a broad family of machine learning algorithms based on Artificial Neural Network (ANN), and they can be either supervised or unsupervised.

With the flexibility of being both supervised and unsupervised, the system should incorporate a supervised DNN first. The supervised DNN would accept metrics from the localisation system, then attempt to localise the transmitter, and finally apply corrections. The corrections could be either human input or images from cameras that can pin point the exact location of the transmitter. The idea behind this system is that it could be set in an environment and for a short time with human or camera corrections the DNN would be trained. After the DNN is trained, the human or camera corrections can be removed, therefore the overall cost of the system is reduced. If low cost cameras are implemented they could remain in position and continue the training the DNN in key locations.

The following step would be to remove the corrections. That would be possible by replacing the human and camera corrections with sensor data. The use of sensor data such as magnetic field, accelerometer, and gyroscopic data, has been used before, in Simultaneous Localisation and Mapping (SLAM) systems. For example, in [124] the author

used sensor data from the phone, and attempts to localise the location by setting boundaries made by opportunistic transmission of signals such as Very High Frequency (VHF) signals, Frequency Modulation (FM) radio, cellular, and television data. The result was a low accuracy system when the locations are not revisited periodically. Therefore, by formulating a DNN that utilises metrics from MFs instead of opportunistic signals, which offer accuracy, the overall performance is expected to be improved. Such system would be unsupervised and learn its environment by it self, as the transmitter navigates through the space.

Bibliography

[1] Ahmad Raza, Shafqat Hameed, and Tim Macintyre. *Global Positioning System – Working and its Applications*, pages 448–453. Springer Netherlands, Dordrecht, 2008.

[2] Microsoft Indoor Localization Competition - IPSN 2015. `https://www.microsoft.com/en-us/research/event/microsoft-indoor-localization-competition\-ipsn-2015/`, 2015. Accessed: 2019-06-27.

[3] Microsoft Indoor Localization Competition - IPSN 2016. `https://www.microsoft.com/en-us/research/event/microsoft-indoor-localization-competition\-ipsn-2016/`, 2016. Accessed: 2019-06-27.

[4] Microsoft Indoor Localization Competition - IPSN 2017. `https://www.microsoft.com/en-us/research/event/microsoft-indoor-localization-competition\-ipsn-2017/`, 2017. Accessed: 2019-06-27.

[5] Dimitrios Lymberopoulos, Jie Liu, Xue Yang, Romit Roy Choudhury, Souvik Sen, and Vlado Handziski. Microsoft Indoor Localization Competition: Experiences and Lessons Learned. *GetMobile: Mobile Comp. and Comm.*, 18(4):24–31, Jan. 2015.

[6] Moustafa Youssef and Ashok Agrawala. The Horus WLAN Location Determination System. In *Proceedings of the 3rd International Conference on Mobile Systems, Applications, and Services*, MobiSys '05, pages 205–218, New York, NY, USA, 2005. ACM.

[7] Jie Xiong and Kyle Jamieson. ArrayTrack: A Fine-Grained Indoor Location System. In *In Proc. of NSDI*, 2013.

[8] X. Wang, L. Gao, S. Mao, and S. Pandey. CSI-Based Fingerprinting for Indoor Localization: A Deep Learning Approach. *IEEE Transactions on Vehicular Technology*, 66 (1):763–776, Jan. 2017.

[9] J. L. Wang and M. C. Loui. Privacy and ethical issues in location-based tracking systems. In *2009 IEEE International Symposium on Technology and Society*, pages 1–4, 2009.

[10] Othman Khalifa, Jalel Chebil, Aisha Hashim, and Shihab Hameed. Ethical issues in monitoring and based tracking systems. *IIUM Engineering Journal*, Spcial, 01 2011.

[11] Sam Lucero. IoT platforms: enabling the Internet of Things. Technical report, IHS Technology, Mar. 2016. URL https://cdn.ihs.com/www/pdf/enabling-IOT.pdf.

[12] Securing Smart Cities. Cities around the world are getting smarter, but are they being designed with security in mind? Trend Micro's Forward-looking Threat Research (FTR) team. https://www.trendmicro.com/vinfo/us/security/news/internet-of-things/securing-smart-cities, 2017. Accessed: 2019-06-27.

[13] IndoorAtlas - Making Indoor Worlds Discoverable. http://www.indooratlas.com/, 2012. Accessed: 2019-06-27.

[14] Q-Track - Enable "Knowing Where: Anywhere". http://q-track.com/, 2002. Accessed: 2019-06-27.

[15] iBeacon - Give your iOS apps the ability to determine its proximity to iBeacon-enabled hardware with Core Location APIs. https://developer.apple.com/ibeacon/, 2013. Accessed: 2019-06-27.

[16] Jiang Xiao, Zimu Zhou, Youwen Yi, and Lionel M. Ni. A Survey on Wireless Indoor Localization from the Device Perspective. *ACM Comput. Surv.*, 49(2):25:1–25:31, Jun. 2016.

[17] S. Salous. *Radio Propagation Measurement and Channel Modelling*. Wiley, 2013.

[18] J.S. Seybold. *Introduction to RF Propagation*. Wiley, 2005.

[19] Manikanta Kotaru, Kiran Joshi, Dinesh Bharadia, and Sachin Katti. SpotFi: Decimeter Level Localization Using WiFi. *SIGCOMM Comput. Commun. Rev.*, 45(4):269–282, Aug. 2015.

[20] H. S. Lui and H. T. Hui. Direction-of-Arrival Estimation: Measurement using compact antenna arrays under the influence of mutual coupling. *IEEE Antennas and Propagation Magazine*, 57(6):62–68, Dec. 2015.

[21] E. Ferrara and T. Parks. Direction finding with an array of antennas having diverse polarizations. *IEEE Transactions on Antennas and Propagation*, 31(2):231–236, Mar. 1983.

[22] Eddie Ball and Athanasios Vasileiadis. Wireless as Enabler of Innovation in 21st Century Health and Social Care. In *Harnessing the Power of Technology to Improve Lives, Proceedings of the 14th European Conference on the Advancement of Assistive Technology, AAATE Conf. 2017, Sheffield, UK, September 12-15, 2017*, pages 80–85, 2017.

[23] *PXI Chassis*. National Instrument, Jul. 2019. URL http://www.ni.com/pdf/product-flyers/pxi-express-chassis.pdf.

[24] *Transceiver Adapter Module for FlexRIO*. National Instrument, Jul. 2019. URL http://www.ni.com/pdf/product-flyers/flexrio-custom-instrumentation.pdf.

[25] *RTL-SDR Blog V3 Datasheet*. RTL-SDR Blog, 2018. URL `https://www.rtl-sdr.com/wp-content/uploads/2018/02/RTL-SDR-Blog-V3-Datasheet.pdf`. v3.

[26] A. Vasileiadis and E. A. Ball. A cost-effective technique for concurrent IQ stream capture for prototyping phased arrays. In *Loughborough Antennas Propagation Conference (LAPC 2017)*, pages 1–4, Nov. 2017.

[27] *Radio Spectrum Processor 2 - RSP2*. SDRplay, Mar. 2018. URL `https://www.sdrplay.com/docs/RSP2andRSP2proDatasheetv2.2.pdf`. v2.2.

[28] E. A. Ball and A. Vasileiadis. Constant Envelope Transceivers in Millimetre-Wave Massive MIMO: EVM and Link Budget Considerations. In *2018 IEEE 10th Sensor Array and Multichannel Signal Processing Workshop (SAM)*, pages 84–88, Jul. 2018.

[29] Athanasios Vasileiadis and Eddie Ball. Extracting AoA information from RSS utilizing multiple frequencies and non uniform gain patterns of a ULA. Manuscript submitted for publication in Transactions on Circuits and Systems Part II: Express Briefs, 2019.

[30] Athanasios Vasileiadis and Eddie Ball. Direct ray AoA estimation utilising multi-frequency in indoor multi-ray environments. Manuscript submitted for publication in The Journal of Engineering, 2019.

[31] Swarun Kumar, Ezzeldin Hamed, Dina Katabi, and Li Erran Li. LTE Radio Analytics Made Easy and Accessible. In *Proceedings of the 6th Annual Workshop on Wireless of the Students, by the Students, for the Students*, S3 '14, pages 29–30, New York, NY, USA, 2014. ACM.

[32] Souvik Sen, Jeongkeun Lee, Kyu-Han Kim, and Paul Congdon. Avoiding Multipath to Revive Inbuilding WiFi Localization. In *Proceeding of the 11th Annual International Conference on Mobile Systems, Applications, and Services*, MobiSys '13, pages 249–262. ACM, 2013.

[33] J.G. Proakis. *Digital Communications*. Electrical engineering series. McGraw-Hill, 2001.

[34] G.D. Durgin. *Space-time Wireless Channels*. Prentice Hall communications engineering and emerging technologies series. Prentice Hall PTR, 2003.

[35] Andreas Molisch. *Wireless Communications*. Wiley-IEEE Press, 2005.

[36] C. Nguyen and S. Kim. *Theory, Analysis and Design of RF Interferometric Sensors*. SpringerBriefs in Physics. Springer New York, 2012.

[37] R. Schmidt. Multiple emitter location and signal parameter estimation. *IEEE Transactions on Antennas and Propagation*, 34(3):276–280, Mar. 1986.

[38] R. Roy, A. Paulraj, and T. Kailath. Direction-of-arrival estimation by subspace rotation methods - ESPRIT. *ICASSP '86. IEEE International Conference on Acoustics, Speech, and Signal Processing*, 11:2495–2498, Apr. 1986.

[39] Z. Chen, G. Gokeda, and Y. Yu. *Introduction to Direction-of-arrival Estimation*. Artech House signal processing library. Artech House, 2010.

[40] A. Kaw. *Introduction to Matrix Algebra*. www.autarkaw.com, 2008.

[41] M. Wax T. Shan and T. Kailath. On spatial smoothing for direction-of-arrival estimation of coherent signals. *IEEE Transactions on Acoustics, Speech, and Signal Processing*, 33(4):806–811, Aug. 1985.

[42] S. U. Pillai and B. H. Kwon. Forward/backward spatial smoothing techniques for coherent signal identification. *IEEE Transactions on Acoustics, Speech, and Signal Processing*, 37(1):8–15, Jan. 1989.

[43] J. Wang, Y. Zhao, and Z. Wang. A MUSIC like DOA estimation method for signals with low SNR. In *2008 Global Symposium on Millimeter Waves*, pages 321–324, April 2008.

[44] Don H. Johnson and Dan E. Dudgeon. *Array Signal Processing: Concepts and Techniques*. Simon & Schuster, Inc., New York, NY, USA, 1992. ISBN 0130485136.

[45] A. U. Ahmed and M. T. Islam and M. Ismail. Estimating DoA From Radio Frequency RSSI Measurements Using Multi-Element Femtocell Configuration. *IEEE Sensors Journal*, 15(4):2087–2092, Apr. 2015.

[46] S. Maddio, A. Cidronali, M. Passafiume, G. Collodi, M. Lucarelli, and S. Maurri. Multipath Robust Azimuthal Direction of Arrival Estimation in Dual-Band 2.45–5.2 GHz Networks. *IEEE Transactions on Microwave Theory and Techniques*, 65(11):4438–4449, Nov. 2017.

[47] M. Rzymowski, P. Woznica, and L. Kulas. Single-Anchor Indoor Localization Using ESPAR Antenna. *IEEE Antennas and Wireless Propagation Letters*, 15:1183–1186, 2016.

[48] L. Kulas. RSS-Based DoA Estimation Using ESPAR Antennas and Interpolated Radiation Patterns. *IEEE Antennas and Wireless Propagation Letters*, 17(1):25–28, Jan. 2018.

[49] P. Bahl and V. N. Padmanabhan. RADAR: an in-building RF-based user location and tracking system. In *Proceedings IEEE INFOCOM*, volume 2, pages 775–784 vol.2, Mar. 2000.

[50] Paramvir Bahl, Venkata N. Padmanabhan, and Anand Balachandran. Enhancements to the RADAR User Location and Tracking System. Technical report, MSR-TR-2000-12, Microsoft Research, 2000.

[51] Y. Wen, X. Tian, X. Wang, and S. Lu. Fundamental limits of RSS fingerprinting based indoor localization. In *2015 IEEE Conference on Computer Communications (INFOCOM)*, pages 2479–2487, Apr. 2015.

[52] S. Tomic, M. Beko, and R. Dinis. RSS-Based Localization in Wireless Sensor Networks Using Convex Relaxation: Noncooperative and Cooperative Schemes. *IEEE Transactions on Vehicular Technology*, 64(5):2037–2050, May. 2015.

[53] J. Xiao, K. Wu, Y. Yi, and L. M. Ni. FIFS: Fine-Grained Indoor Fingerprinting System. In *2012 21st International Conference on Computer Communications and Networks (ICCCN)*, pages 1–7, Jul. 2012.

[54] Mauro Brunato and Roberto Battiti. Statistical Learning Theory for Location Fingerprinting in Wireless LANs. *Comput. Netw.*, 47(6):825–845, Apr. 2005.

[55] A. Cidronali and S. Maddio and G. Giorgetti and G. Manes. Analysis and Performance of a Smart Antenna for 2.45-GHz Single-Anchor Indoor Positioning. *IEEE Transactions on Microwave Theory and Techniques*, 58(1):21–31, Jan. 2010.

[56] E. Taillefer, A. Hirata, and T. Ohira. Direction-of-arrival estimation using radiation power pattern with an ESPAR antenna. *IEEE Transactions on Antennas and Propagation*, 53(2):678–684, Feb. 2005.

[57] M. Tarkowski and L. Kulas. RSS-Based DoA Estimation for ESPAR Antennas Using Support Vector Machine. *IEEE Antennas and Wireless Propagation Letters*, 18(4):561–565, Apr. 2019.

[58] Nizar Tayem. Real Time Implementation for DOA Estimation Methods on NI-PXI Platform. *Progress in Electromagnetics Research B*, 59:103–121, Apr 2014.

[59] M. Scherhäufl, M. Pichler, E. Schimbäck, D. J. Müller, A. Ziroff, and A. Stelzer. Indoor Localization of Passive UHF RFID Tags Based on Phase-of-Arrival Evaluation. *IEEE Transactions on Microwave Theory and Techniques*, 61(12):4724–4729, Dec. 2013.

[60] M. Scherhäufl, M. Pichler, D. Müller, A. Ziroff, and A. Stelzer. Phase-of-arrival-based localization of passive UHF RFID tags. In *2013 IEEE MTT-S International Microwave Symposium Digest (MTT)*, pages 1–3, Jun. 2013.

[61] M. Scherhäufl, M. Pichler, and A. Stelzer. UHF RFID Localization Based on Phase Evaluation of Passive Tag Arrays. *IEEE Transactions on Instrumentation and Measurement*, 64(4):913–922, Apr. 2015.

[62] M. Scherhäufl, M. Pichler, and A. Stelzer. Robust localization of passive UHF RFID tag arrays based on phase-difference-of-arrival evaluation. In *2015 IEEE Topical Conference on Wireless Sensors and Sensor Networks (WiSNet)*, pages 47–49, Jan. 2015.

[63] M. Cremer, U. Dettmar, C. Hudasch, R. Kronberger, R. Lerche, and A. Pervez. Localization of Passive UHF RFID Tags Using the AoAct Transmitter Beamforming Technique. *IEEE Sensors Journal*, 16(6):1762–1771, Mar. 2016.

[64] N. Tayem, M. Omer, and A. A. Hussain. DOA Estimation Method using R Matrix of the QR Factorized Data and its Prototype Implementation on NI-PXI Platform. In *2014 IEEE Military Communications Conference*, pages 333–337, Oct. 2014.

[65] N. Tayem, M. Omer, and A. A. Hussain. Hardware Implementation of MUSIC and ESPRIT on NI-PXI Platform. In *2014 IEEE Military Communications Conference*, pages 329–332, Oct. 2014.

[66] Gene Howard Golub and Charles F Van Loan. *Matrix computations*. Johns Hopkins University Press, 1996.

[67] R. Miesen, F. Kirsch, and M. Vossiek. UHF RFID Localization Based on Synthetic Apertures. *IEEE Transactions on Automation Science and Engineering*, 10(3):807–815, Jul. 2013.

[68] M. Scherhäufl, M. Pichler, and A. Stelzer. Localization of passive UHF RFID tags based on inverse synthetic apertures. In *2014 IEEE International Conference on RFID (IEEE RFID)*, pages 82–88, Apr. 2014.

[69] Swarun Kumar, Stephanie Gil, Dina Katabi, and Daniela Rus. Accurate Indoor Localization with Zero Start-up Cost. In *Proceedings of the 20th Annual International Conference on Mobile Computing and Networking*, MobiCom '14, pages 483–494, New York, NY, USA, 2014. ACM.

[70] J.M. Rigelsford and A. Tennant. Sidelobe reduction in a random spherical volumetric array using frequency diversity. *Applied Acoustics*, 74(6):865 – 869, 2013.

[71] V. Viikari, P. Pursula, and K. Jaakkola. Ranging of UHF RFID Tag Using Stepped Frequency Read-Out. *IEEE Sensors Journal*, 10(9):1535–1539, Sep. 2010.

[72] Luis Brás, Nuno Carvalho, Pedro Pinho, Lukasz Kulas, and Krzysztof Nyka. A Review of Antennas for Indoor Positioning Systems. *International Journal of Antennas and Propagation*, 2012, Dec. 2012.

[73] S. Maddio, A. Cidronali, and G. Manes. Smart antennas for direction of arrival indoor positioning applications. *Theory, Practice, and Advances*, 2011.

[74] A. Cidronali and G. Collodi and S. Maddio and M. Passafiume and G. Pelosi and S. Selleri. Improving phaseless DoA estimation in multipath-impaired scenarios by exploiting dual-band operations. In *2016 IEEE MTT-S International Microwave Symposium (IMS)*, pages 1–4, May 2016.

[75] R. Szumny, K. Kurek, and J. Modelski. Attenuation of multipath components using directional antennas and circular polarization for indoor wireless positioning systems. In *2007 European Microwave Conference*, pages 1680–1683, Oct. 2007.

[76] L. Kanaris, A. Kokkinis, M. Raspopoulos, A. Liotta, and S. Stavrou. Improving RSS fingerprint-based localization using directional antennas. In *The 8th European Conference on Antennas and Propagation (EuCAP 2014)*, pages 1593–1597, Apr. 2014.

[77] T. A. Thomas, F. W. Vook, and S. Sun. Investigation into the effects of polarization in the indoor mmWave environment. In *2015 IEEE International Conference on Communications (ICC)*, pages 1386–1391, Jun. 2015.

[78] P. Nepa, F. Cavallo, M. Bonaccorsi, M. Aquilano, M. C. Carrozza, and P. Dario. Experimental Analysis of RSSI-Based Indoor Location Systems with WLAN Circularly Polarized Antennas. In *Lecture Notes of the Institute for Computer Sciences, Social Informatics and Telecommunications Engineering*, pages 176–183. Springer Berlin Heidelberg, 2011.

[79] Z. Szalay and L. Nagy. Utilization of linearly and circularly polarized antennas for indoor positioning. In *2015 17th International Conference on Transparent Optical Networks (ICTON)*, pages 1–4, Jul. 2015.

[80] A. Cidronali, G. Collodi, S. Maddio, M. Passafiume, and G. Pelosi. 2-D DoA Anchor Suitable for Indoor Positioning Systems Based on Space and Frequency Diversity for Legacy WLAN. *IEEE Microwave and Wireless Components Letters*, 28(7):627–629, Jul. 2018.

[81] Y. D. Zhang, X. Li, and M. G. Amin. Target localization in multipath environment through the exploitation of multi-frequency array. In *2010 International Waveform Diversity and Design Conference*, pages 000206–000210, Aug. 2010.

[82] A. Basit, W. Khan, S. Khan, and I. M. Qureshi. Development of frequency diverse array radar technology: a review. *IET Radar, Sonar Navigation*, 12(2):165–175, 2018.

[83] M Mouhamadou, Patrick Vaudon, and Mohammad Rammal. Smart Antenna Array Patterns Synthesis: Null Steering and Multi-User Beamforming by Phase Control. *Progress in Electromagnetics Research*, 60:95–106, Feb. 2006.

[84] Paolo Rocca, Randy Haupt, and Andrea Massa. Interference Suppression in Uniform Linear Arrays Through a Dynamic Thinning Strategy. *IEEE Transactions on Antennas and Propagation*, 59:4525–4533, Dec. 2011.

[85] D. K. Barton. *Radars. Volume 6 - Frequency agility and diversity*. Dedham, Mass., Artech House, Inc., 1977. 428 p, 1977.

[86] A. M. Haimovich, R. S. Blum, and L. J. Cimini. MIMO Radar with Widely Separated Antennas. *IEEE Signal Processing Magazine*, 25(1):116–129, 2008.

[87] J. Li and P. Stoica. MIMO Radar with Colocated Antennas. *IEEE Signal Processing Magazine*, 24(5):106–114, Sep. 2007.

[88] Y. Ding, J. Zhang, and V. Fusco. Frequency diverse array OFDM transmitter for secure wireless communication. *Electronics Letters*, 51(17):1374–1376, 2015.

[89] Wen-Qin Wang. Range-Angle Dependent Transmit Beampattern Synthesis for Linear Frequency Diverse Arrays. *Antennas and Propagation, IEEE Transactions on*, 61: 4073–4081, Aug. 2013.

[90] W.-Q Wang. Phased-MIMO Radar With Frequency Diversity for Range-Dependent Beamforming. *Sensors Journal, IEEE*, 13:1320–1328, Apr. 2013.

[91] B. Chen, Y. Huang, X. Chen, G. Wang, and J. Guan. Multiple-Frequency CW Radar and the Array Structure for Uncoupled Angle-Range Indication. *IEEE Antennas and Wireless Propagation Letters*, 17(12):2203–2207, Dec. 2018.

[92] M. Guo, Y. D. Zhang, and T. Chen. Performance Analysis for Uniform Linear Arrays Exploiting Two Coprime Frequencies. *IEEE Signal Processing Letters*, 25(6):838–842, Jun. 2018.

[93] P. P. Vaidyanathan and P. Pal. Sparse sensing with co-prime samplers and arrays. *IEEE Transactions on Signal Processing*, 59(2):573–586, Feb. 2011.

[94] Y. D. Zhang, M. G. Amin, F. Ahmad, and B. Himed. DOA estimation using a sparse uniform linear array with two CW signals of co-prime frequencies. In *2013 5th IEEE International Workshop on Computational Advances in Multi-Sensor Adaptive Processing (CAMSAP)*, pages 404–407, Dec. 2013.

[95] Jonathan Rigelsford and A Tennant. Acoustic imaging using a volumetric array. *Applied Acoustics*, 67:680–688, Jul. 2006.

[96] H. Wilden. The crow's-nest radar - An omnidirectional phased array system. *NASA STI/Recon Technical Report A*, 82:253–258, 1980.

[97] R. Voles. Spherical shell and volume arrays. *IEE Proceedings - Microwaves, Antennas and Propagation*, 142:498–500(2), Dec. 1995.

[98] A. Tennant, A. F. Fray, D. B. Adamson, and M. W. Shelley. Beam scanning characteristics of 64 element broadband volumetric array. *Electronics Letters*, 33(24):2001–2002, Nov. 1997.

[99] M. Scherhäufl, M. Pichler, and A. Stelzer. UHF RFID Localization Based on Evaluation of Backscattered Tag Signals. *IEEE Transactions on Instrumentation and Measurement*, 64(11):2889–2899, Nov. 2015.

[100] Gazzah Leila, Leila Najjar, and Hichem Besbes. Selective hybrid RSS/AOA weighting algorithm for NLOS intra cell localization. In *IEEE Wireless Communications and Networking Conference, WCNC*, 04 2014.

[101] Gazzah Leila, Leila Najjar, and Hichem Besbes. Improved selective hybrid RSS/AOA weighting schemes for NLOS localization. In *International Conference on Multimedia Computing and Systems*, volume 0, 04 2014.

[102] Slavisa Tomic, Marko Beko, and Rui Dinis. Distributed RSS-AoA Based Localization with Unknown Transmit Powers. *IEEE Wireless Communications Letters*, 5:1–1, 08 2016.

[103] S. Tomic, M. Beko, R. Dinis, and P. Montezuma. A Closed-Form Solution for RSS/AoA Target Localization by Spherical Coordinates Conversion. *IEEE Wireless Communications Letters*, 5(6):680–683, Dec 2016.

[104] Stephen Boyd and Lieven Vandenberghe. *Convex Optimization*. Cambridge University Press, New York, NY, USA, 2004.

[105] *Ultimate N WiFi Link 5300*. Intel, 2015. URL `https://www.intel.com/content/dam/www/public/us/en/documents/product-briefs/ultimate-n-wifi-link-5300-brief.pdf`.

[106] Y. Huang and K. Boyle. *Antennas: From Theory to Practice*. Wiley, 2008.

[107] Sophocles J. Orfanidis. *Electromagnetic Waves and Antennas*. Distributed by Sophocles J. Orfanidis's website, Aug. 2016. URL `http://eceweb1.rutgers.edu/~orfanidi/ewa/`.

[108] *ADF4351 - Wideband Synthesizer with Integrated VCO*. Analogue Devices, 1999. URL `https://www.analog.com/media/en/technical-documentation/data-sheets/ADF4351.pdf`. Rev. A.

[109] *Atmel 8-bit Microcontroller with 4/8/16/32KBytes In-System Programmable Flash*. Atmel, Jul. 2012. URL `https://cdn-shop.adafruit.com/datasheets/ATMEGA328P.pdf`. 8271E-AVR.

[110] Athanasios Vasileiadis. Multi thread SDRplay RSP2 Matlab Toolbox, 2018. URL `https://github.com/VasAthanasios/MultiThread_SDRplayRSP2_Matlab_Toolbox`.

[111] *RSP2 Reference Clock Application Note*. SDRplay, Dec. 2016. URL `https://www.sdrplay.com/docs/SDRplay_RSPII_Reference_Clock_Application_Note_R1P0.pdf`. v1.0.

[112] *Low data rate, low power sub-1GHZ transceiver*. SPIRIT1, Apr. 2012. URL `https://datasheet.octopart.com/SPIRIT1QTR-STMicroelectronics-datasheet\-13717468.pdf`. Doc ID 022758 Rev 2.

[113] J.S. Seybold. *Introduction to RF Propagation*. Wiley, 2005.

[114] J.D. Kraus and D.A. Fleisch. *Electromagnetics: With Applications*. McGraw-Hill series in electrical and computer engineering. WCB/McGraw-Hill, 1999.

[115] T. P. Ketterl, R. A. Ramirez, and T. M. Weller. Reduced-size circular polarized antenna for 434MHz RFID systems using meandered bowtie elements with a novel quadrifilar feed. In *2015 IEEE 16th Annual Wireless and Microwave Technology Conference (WAMICON)*, pages 1–3, Apr. 2015.

[116] *ADL5390 - RF/IF Vector Multiplier*. Analogue Devices, 2017. URL `https://www.analog.com/media/en/technical-documentation/data-sheets/ADL5390.pdf`. Rev. A.

[117] W. Banzhaf, P. Nordin, R.E. Keller, and F.D. Francone. *Genetic Programming: An Introduction*. Morgan Kaufmann Series in Arti. Elsevier Science, 1998.

[118] Marco Tomassini. *Spatially Structured Evolutionary Algorithms*. Springer-Verlag, 2005.

[119] Oded Maimon and D. Braha. A genetic algorithm approach to scheduling PCBs on a single machine. *International Journal of Production Research*, 36:761–784, Nov. 2010.

[120] Karolina Stanislawska, Krzysztof Krawiec, and Timo Vihma. Genetic Programming for Estimation of Heat Flux Between the Atmosphere and Sea Ice in Polar Regions. In *Proceedings of the 2015 Annual Conference on Genetic and Evolutionary Computation*, GECCO '15, pages 1279–1286, New York, NY, USA, 2015. ACM.

[121] Stephen Zhang and Vladan Babovic. An Evolutionary Real Options Framework for the Design and Management of Projects and Systems with Complex Real Options and Exercising Conditions. *Decision Support Systems*, 51:119–129, Apr. 2011.

[122] Joost Buurman, Stephen Zhang, and Vladan Babovic. Reducing Risk Through Real Options in Systems Design: The Case of Architecting a Maritime Domain Protection System. *Risk analysis : an official publication of the Society for Risk Analysis*, 29:366–79, Mar. 2009.

[123] T. Imai. Novel ray-tracing acceleration technique employing genetic algorithm for radio propagation prediction. In *2006 First European Conference on Antennas and Propagation*, pages 1–6, Nov. 2006.

[124] R. M. Faragher, C. Sarno, and M. Newman. Opportunistic radio SLAM for indoor navigation using smartphone sensors. In *Proceedings of the 2012 IEEE/ION Position, Location and Navigation Symposium*, pages 120–128, Apr. 2012.